DYNAMICAL SIMULATION OF STRUCTURED COLLOIDAL PARTICLES

A Thesis
Presented to
The Academic Faculty

by

Matthew C. Hagy

In Partial Fulfillment
of the Requirements for the Degree
Doctor of Philosophy in the
School of Chemistry and Biochemistry

Georgia Institute of Technology
December 2013

DYNAMICAL SIMULATION OF STRUCTURED COLLOIDAL PARTICLES

Approved by:

Dr. Rigoberto Hernandez, Advisor
School of Chemistry and Biochemistry
Georgia Institute of Technology

Dr. Kenneth R. Brown
School of Chemistry and Biochemistry
Georgia Institute of Technology

Dr C. David Sherrill
School of Chemistry and Biochemistry
Georgia Institute of Technology

Dr. David S. Sholl
School of Chemical and Biomolecular Engineering
Georgia Institute of Technology

Dr. Stephen C. Harvey
School of Biology
Georgia Institute of Technology

Date Approved: November 4, 2013

ACKNOWLEDGEMENTS

There are many people that I'd like to acknowledge for their assistance in helping me complete this thesis. First, I'd like to thank my adviser—Prof. Rigoberto Hernandez—for the advice that he provided me in countless discussion as well for supporting my research. Next, I'd like to thank my committee members for the guidance they provided in constructing this thesis and in presenting the results. The advice provided by Prof. Hernandez and my committee members has aided my growth as a scientist. The many members of the Hernandez group have all provided valuable insight into studying chemical dynamics with computer simulations. They also helped me to refine my presentation skills. I thank you all for this assistance. Additionally, I'm thankful for the the many friends that I've made in the chemistry department over the years. Lastly, I'd like to thank my family for their support throughout the years. Thank you everyone!

TABLE OF CONTENTS

LIST OF TABLES

LIST OF FIGURES

SUMMARY

In this thesis, computer simulations are used to study colloidal systems with structured interactions. These are particle interactions that include both attraction and repulsion. An example of a structured colloid is a Janus particle such as polystyrene spheres with a gold coating on one hemisphere. [62] These new colloids differ from conventional colloids that have either strictly attractive or strictly repulsive particle interactions. It is anticipated that these novel interactions will give rise to new microscopic structure and dynamics and therefore new material properties. In this thesis, new models are developed to capture the interactions of three structured colloidal systems. The effect of these novel interactions on material properties are quantified through dynamical simulation. Results show that structured interactions can lead to unexpected particle ordering and novel dynamics.

The first system studied is electrostatically-stabilized depletion associating (ESDA) colloidal particles. ESDA particles have a radially structured pair interaction profile that includes short-range attraction and longer-range repulsion. This creates an energetic barrier that limits the rate of reversible pair association in colloidal gelation. It was previously unknown how this barrier height would affect the gelation dynamics of ESDA particles at moderate to high colloid volume fractions. To study this process with computer simulation we developed a new model for ESDA particles. Long-time Brownian Dynamics simulation of the ESDA model are performed to quantify gelation dynamics for a range of energetic barrier heights and colloid volume fractions. The primary finding was that an Arrhenius-like time-rescaling factor can explain how changes in the energetic barrier height affect gelation dynamics for higher volume fractions. Deviations of this theory at lower volume fraction have been explained by the significance of spatial diffusion in addition to energy diffusion on gelation dynamics. Additionally, the gel network formed in simulation—that is the graph where each particles is a node and reversible bonds are the edges—is visualized and found to contain highly connected regions in the later stages of gelation.

In the second structured colloidal system of interest, we consider dipolar Janus (DJ) colloidal

particles—that is spherical particles with two hemispheres of different chemistry such that one hemisphere is positively charged while the other in negatively charged. The structured interaction of DJ particles has attractive and repulsive terms that vary with the orientations of particles in a pair. A new model is constructed for the dynamical simulation of DJ particles in which the electrostatic surface of each particle is represented point-wise (PW). To validate this new model, cluster structures of PW particles are compared to those found in previous experimental and simulation work. Near identical cluster structures are found, which demonstrates that the PW model captures the interactions of DJ particles while also facilitating molecular dynamics simulations. Additionally, we numerically construct the partition function for an isolated pair of PW particles to quantify the relation between the surface electrostatic charge density of each DJ particle and the affinity of a pair. The partition function computations show that the effective isotropic interaction profile between pairs of DJ particles is similar to that of conventional isotropically attractive colloidal particles (e.g. depletion attracting colloids). This suggests DJ colloids may have similar properties to isotropic colloids with comparable pair affinity. This similarity is tested by also modeling DJ colloids with the isotropic interaction profiles from pair free energy computations. We call this alternative representation the coarse-grained (CG) model for DJ particles in that it is equivalent to coarse-graining over orientations.

Molecular dynamics computer simulations of DJ particle systems are performed in both the PW and the CG model to quantify the equilibrium structure of particles in each representation. These simulations are performed for the fluid-like region of the phase diagram where pair associations are reversible and neither long-range order nor arrested dynamics are present. Surprisingly, the PW and CG models have identical structure (as quantified by isotropic pair correlation functions) over a range of pair affinities and colloid volume fractions. These results suggests that DJ colloids have static properties similar to conventional isotropically attractive colloids for these conditions. In contrast, if DJ particles formed small isolated clusters or linear chains—as found in related systems—then the PW model would have different structure than the CG model. Such microscopic structure would alter the physical properties of DJ colloidal material. The significance of isolated clusters and linear chains in the PW model of DJ particles at stronger pair interactions are studied using nonequilibrium quenches. Again, neither chains nor isolated clusters are found and instead each

simulation system is found to collapse into a single large aggregate, which suggests a phase transition to solid structure. Therefore DJ colloids are only anticipated to form novel structures at two sets of conditions: in the solid region of the phase diagram and in the dilute and low temperature limit where isolated clusters will form. Rigorous thermodynamics computations show that the CG model reproduces the free energy of PW model, but not the energy and entropy balance. These results suggests that DJ colloids will have higher heat capacities than isotropically attractive colloids.

Dynamical properties of two models are also computed from molecular dynamics simulation. The dynamics of the CG model are found to be accelerated relative to those of the PW models for the same range of conditions for which both models have identical static properties. Physically, this suggests DJ colloids will have slower transport and relaxation than comparable isotropically attractive colloids. This has important implications for the processing of DJ colloidal materials in that we predicted these materials will be more prone to dynamical arrest than convention colloidal materials. The slower dynamics of the DJ particles have been explained by the observation of more long-duration reversible bonds in the PW model than found in the CG model.

Accelerated dynamics of a coarse-grained model relative to the detailed model from which it is developed has been observed in previous simulation studies with other coarse-grained models. This is believed to be a common consequence of coarse-graining. There is interest in mapping the accelerated dynamics of a coarse-grained model to the original time scale as has been previously accomplished with two methods: Langevin damping and time-rescaling. We have applied these dynamical mapping methods to the CG model to test the ability of each method to map the accelerated CG dynamics onto the PW time scale. Both methods improve time correlation functions and diffusion constants of the CG model, although neither method improves the distribution of reversible bonds durations. This demonstrates that conventional dynamical mapping methods are not reproducing the PW dynamics in the CG model for all time and length scales. Therefore new dynamical mapping methods may be needed and in this thesis considerations for such methods are discussed.

Lastly, we have generalized our dipolar Janus (DJ) colloidal particle models to striped particles with n stripes (a Janus particle is a $n = 2$ striped particle). Striped particles are interesting in that in the limit of large n one would anticipate no effective electrostatic interaction as each favorable interaction would be canceled by a near equal unfavorable term from a neighboring stripe. We

have developed PW models for $n = 3$ to $n = 7$ striped particles. The relationship between surface electrostatic density and pair affinity in each of these models has been quantified with pair partition function computations. Surprisingly, it is found that distributing the same electrostatic surface charge into more stripes does not always lead to weaker pair affinity. Simulation of striped particle systems in both the PW and CG model are performed to quantify static and dynamic properties. In general, the striped particle results mirror those of our earlier DJ study in that the CG model captures the static structure of the PW model. Further, when normalized by pair affinity, the static properties of different n striped particle systems are comparable. As earlier found with Janus particles, striped particles have slower dynamics in the PW model than in the CG model and this disparity can be large as a factor of 4. This suggests that striped surfaces can substantially alter the transport and relaxation properties of colloidal materials while preserving the structural properties of conventional isotropically attractive colloids.

CHAPTER I

INTRODUCTION

This thesis explores colloidal systems in which the particle interactions include both attraction and repulsion using dynamical computer simulations. Results provide insight into the properties of new colloidal materials. We name this combination of attraction and repulsion as structured interactions and they are challenging to simulate as they lead to large forces, particle frustration, and dynamical arrest. New models are developed for several colloid systems with structured interactions and dynamical computer simulations of these models allow us to compute the microscopic structure and particle dynamics that result from these novel interactions. Unexpected structure and novel dynamics are found as detailed throughout this thesis. Additionally, we compare structured colloids to conventional isotropically attractive colloids with the use of coarse-graining methods.

1.1 Colloidal background

Colloidal particles are essential to the chemical industry with diverse applications including paints, coatings, gels, and drug delivery. [11, 38, 95] In the context of this work, colloids can be defined as large particles with diameters on the orders of 10 nm to 10 μm dispersed in water. Colloidal systems form microscopic structure with the order between particles giving rise to gas, liquid, and solid phases in analogy to atomic systems. This structure is due to the interactions between particles, volume constraints, and thermodynamic fluxes such as temperature. Additionally, the particle interactions also influence the dynamic properties of colloids, including transport and relaxation. Colloids have substantially slower dynamics than atomic fluids as due to the large size and mass of colloidal particles.[38] This can lead to dynamical arrest and nonequilibrium states as occur in colloidal glasses and gels. For this reason, there is significant interest in understanding the dynamics of colloids. [30]

Colloidal interactions can vary greatly with different colloidal chemistry, ionic strength of solution, and the presence of surfactants or polymers.[11, 38] The physical properties of colloidal materials can be controlled by modulating these parameters and this allows the material properties

to be tuned to the needs of each application. There has been much experimental and theoretical work aiming to explain how these interactions affect the structure, dynamics, and ultimately the bulk properties of colloidal materials.[11, 38] In conventional colloidal systems, particles can be regarded as isotropic with an effective interaction that is either purely repulsive or includes an attractive well. The effects of such interactions have been studied with hard sphere[3, 112] and sticky sphere[120, 99] models respectively. There has been substantial theoretical and simulation work that explains how these interactions influence colloid properties. [29, 92, 33, 129, 11, 38, 99, 95, 4] Current theory for non-dilute colloids has focused on pair interactions based around volume exclusion (hard spheres) with augmentation for softer repulsion or an attractive well. [29, 92, 33, 129, 11, 38, 99, 95, 4] In this thesis we have extended theoretical and simulation work to colloidal particles that include both attractive and repulsive components. We label this class of colloidal particles as structured.

1.2 Motivation

There has been tremendous interest in the fabrication of new colloid particles with novel interactions over the last decade. [98, 47, 51, 97, 31, 22, 113] This has been motivated by the possibility of making new colloidal materials with new properties. This broad class of new colloidal particles are labeled anisotropic in contrast to conventional isotropic colloids. Anisotropic particles with non-uniform (i.e. patterned surfaces) can give rise structured interactions with either attractive or repulsive interactions between each pair of particles as based on their mutual orientations. Janus particles—spherical particles with two hemispheres of different chemistry—is one anisotropic colloidal structure that has attracted much attention. [123, 19, 62, 69] Experimental and simulation work have already shown that Janus particles self-assemble into novel cluster structures due to their structured interactions. [62, 121, 63, 69, 113] This suggest Janus colloidal materials may have new material properties as due to the novel microscopic ordering and dynamics.

It is not yet possible to experimentally measure the bulk properties of Janus colloids due to challenges in producing large quantities of Janus particles.[69, 74] Therefore computer simulations have played a large role in predicting the novel properties of structured colloids.[138, 26, 27, 48, 83, 49, 109, 110, 40, 107] The pioneering simulations of Glotzer and Zhang demonstrated that

novel self-assembly structures could be realized with the structured interactions of Janus and patchy particles.[138] Sciortino and coworkers have simulated amphiphilic Janus particles in which one of the hemispheres is hydrophobic while the other in hydrophilic.[109, 110, 40] Their simulation results included the discovery of novel phase behavior and thermodynamic properties as due to the formation of isolated miceullar clusters. Structured interactions have also been shown to affect colloids dynamics.[26, 27] De Michele et al. found suppressed particle transport in their simulation of tetrahedral patchy particles as due to network formation. [26, 27]

1.3 Thesis objectives

This thesis quantifies the effects of structured interactions on the static and dynamics properties of new colloidal materials with the use of dynamical computer simulation. Three different classes of colloids systems with structured interactions are studied. For each, we seek to explain the role of these novel interactions on the static and dynamic properties of the colloidal particles using computer simulation. To this end, new models are developed for each of structured colloidal systems of interest. The specific systems studied are as follows:

1.3.1 Radially structured colloidal particles (ESDA colloids)

We first consider the structured interactions in electrostatically-stabilized depletion associating (ESDA) colloids. ESDA particles have a radially structured pair interaction that includes short-range attraction and longer range repulsion. [111, 114] This results in an energetic barrier that limits the rate of pair association. Our goal is to explain how this energetic barrier affects the dynamics of gel formation in ESDA colloids. There has been limited experimental study of ESDA colloids, [111, 114] with current work focused on the creation of large energetic barriers (on the order of $20\,\mathrm{k}T$) to stabilize colloids suspensions: i.e. prevent gelation. Related theoretical work has shown that small energetic barriers (on the order of $2\,\mathrm{k}T$) can enhance network formation in Lennard Jones systems.[14] This suggests that different energetic barrier heights may affect the structure of gels formed by ESDA particles. Additionally, the energetic barrier should limit the association of particles as should alter the gelation dynamics. Therefore the first objective of this thesis to study ESDA gelation with computer simulation and analytic theory to explain the effect of the energetic barrier height in this radially structured interaction.

1.3.2 Dipolar Janus colloids

Next, we consider surface patterned structured interactions as occur in Janus colloids. There has been much experimental interest in the fabrication of Janus particles to create new colloidal materials. [123, 19, 62, 69] Previous simulations by other authors have shown how the structured interactions of amphiphilic Janus colloids can give rise to new microscopic structure. [109, 110, 40] In this thesis we focus on another class of Janus colloidal particles that has received less theoretical attention: the dipolar Janus (DJ) motif in which the surface of one hemisphere is positively charged and the other is negatively charged. The goal of this project is to understand how the structured interactions of DJ colloids affect particle ordering and dynamics. To this end, a new model of DJ colloids is constructed with only continuous terms to allow for molecular dynamics simulation. Additionally, we contrast the properties of DJ colloids to those of conventional isotropically attractive colloids. This is accomplished by coarse-grained methods as detailed in Chapter 4.

1.3.3 Striped colloids

The Janus surface patterns is an instance of a more general surface pattern consisting of stripes of alternating chemistry. There has been recent experimental interest in fabricating striped particles[66, 89, 135, 68, 82, 67] as yet another class of anisotropic colloids. We aim to study the structured interactions of these new striped colloidal particles. This is accomplished by adapting the models and methods of our Janus colloid work. As with Janus particles, we contrast striped colloidal particles to isotropically attractive colloids through the use of coarse-graining methods.

1.3.4 Coarse-grained dynamical mapping

In this thesis, coarse-grained models are found to capture the microscopic structure (i.e. particle ordering) in systems of dipolar Janus and striped colloidal particles. In contrast, the coarse-grained models are found to have accelerated dynamics relative to the detailed models. This would prevent the coarse-grained models from being used in future studies of structured colloid dynamics (e.g. simulating the gelation of dipolar Janus colloids). This problem of accelerated coarse-grained dynamics has been previously reported in other simulations work with coarse-grained methods. [80, 88, 28, 65, 81, 85, 55, 2] There is general interest in relating the accelerated dynamics of

coarse-grained models back to the original time scale so that these computationally more efficient models can be used to study dynamic properties. This is accomplished with dynamical mapping methods. [1, 93, 88, 28, 65, 55] In this thesis, we test whether these methods can be applied to our coarse-grained models for Janus and striped colloids.

1.4 Organization of thesis

This thesis is structured around four core chapters that each focus on one area of structured colloids. Each core chapter is written as a separate standalone article as prepared for journal publication. At this time, two have already been published in peer reviewed journals. Each chapter can be read separately, although later chapters do refer back to earlier chapters that include additional details of models and methods used. In addition to the core chapters, Chapter 2 focuses on the development of computer codes for the computation of correlation functions. These tools were developed for this thesis work and have broader applications to future simulation studies.

The first of these core chapters is Chapter 3, which focuses on the gelation dynamics of radially structured colloidal particles. The ESDA model for these radially structured colloidal particles with an energetic barrier to pair association is developed in this chapter. Brownian dynamics simulations are used to quantify the gelation dynamics of the ESDA model with different barrier heights and colloid volume fractions. Additionally, an analytic time-rescaling theory is constructed to explain how energetic barrier height influence gelation time scales. Theory is compared to simulation results to determine the conditions for which time-rescaling adequately describe gelation dynamics in these radially structured colloids.

The next chapter, Chapter 4, considers surface structured colloidal particles with a focus on dipolar Janus (DJ) colloids. This chapter begins by developing the pointwise (PW) model of DJ colloids: a new model that reproduces DJ particle cluster structures while also being amenable to dynamical simulation. We also consider the extent to which DJ particles can be modeled as isotropically attractive colloidal particles—as comparable to more conventional depletion attracting colloids—by modeling the pair interaction with an effective isotropic interaction. This interaction is computed by coarse-grained over pair orientation and therefore this model is named the coarse-grained (CG) model of DJ particles. Dynamical simulation are used to compute the static and

thermodynamic properties of DJ colloids in both models. Surprisingly, the static results of the CG model are near identical to those of the PW model as detailed in this chapter. This suggests DJ colloids many have much in common with more conventional isotropically attractive colloids (e.g. depletion attracting colloids). There are a few deviations between the PW and CG models, which suggests new material properties.

Chapter 5 builds off the work of Chapter 4 with a focus on the dynamics of DJ colloids. The dynamics of the PW and CG model are found to differ throughout the same range of conditions for which the two models were found to have identical static properties. Specifically, the CG model has accelerated dynamics relative to the PW model. This suggests that DJ colloids will have slower transport and relaxation than comparable isotropically attractive colloids. This has important implications for the processing of DJ colloidal materials in that they may be more prone to dynamical arrest than convention colloidal materials. The slower dynamics of DJ colloids are explained through the observation of long-duration reversible bonds in the PW model as are absent in the CG model. This chapter also considers how the dynamics of the CG model can be related to the time scale of the PW model with dynamical mapping methods. Current methods are found insufficient to capture all time and length scales and therefore new dynamical mapping methods are needed. Such methods would allow future study of DJ dynamics with the computationally efficient CG model and may have broader applications to other dynamical simulations of coarse-grained models.

The final core chapter, Chapter 6, studies structured colloidal particles with striped surface patterns. This is accomplished by generalizing the models and methods of Chapters 4 and 5 that were originally developed for dipolar Janus (DJ) particles. DJ particles are striped particles with $n = 2$ stripes and this chapter additionally considers particles with $n = 3$ to $n = 7$ stripes. New PW and CG models are constructed for each n. Simulation results are similar to that which was first found for DJ particles: n-striped particles have structure comparable to isotropically attractive colloids and slower dynamics. Further, larger values of n generally lead to slower dynamics such that higher n-striped particles have considerably slower dynamics than conventional isotropically attractive colloids. The simulation results also suggest that different n-striped colloids have substantially different phase behavior. This chapter also has a large appendix, Appendix A, that includes the full set of results obtained in the study of striped particles.

The thesis finishes with a summary of conclusions in Chapter 7. This chapter also presents possible future work that is suggested by the results of this thesis. Ellipsoidal Janus and striped colloids are introduced as additional structured colloid systems that could be explored in future simulation work. Such simulations could be performed by adapting the methods and models developed in this thesis for the study of dipolar Janus colloids. Additionally, future nonequilibrium simulations of dipolar Janus and striped colloids are proposed to explore the glasses and gels formed by these novel structured colloids. Lastly, we revisit the topic of coarse-grained dynamics and discuss how new dynamical mapping methods might be constructed to facilitate dynamics simulation with computationally efficient coarse-grained models.

CHAPTER II

COMPUTING STATIC AND DYNAMIC CORRELATIONS FUNCTIONS ON THE FLY

2.1 Motivation

The computation of static and dynamic correlation functions is essential to analyzing computer simulations of chemical systems. Conventionally, these computations are performed post-simulation using a trajectory file of configurations that was written during simulation. Only a small number of the configurations observed in simulation can be written to the trajectory file due to limitations of disk space. This impacts the quality of the computed correlation functions. The smallest time difference between adjacent configurations in the trajectory file limits the resolution of dynamic correlation functions computed. Additionally, static correlation functions may need computed at lower resolutions to ensure convergence as the computations only considers the limited number of configuration in the trajectory file.

These limitations can be overcome by computing correlations functions during simulation (i.e. on the fly). This allows each computation algorithm to consider a larger number of simulation configurations than could be writen to a trajectory file. As an example, in our study of dipolar Janus colloids each simulation would have had to write an approximately 10 GB trajectory file to compute the desired resolution time correlation functions in post processing. It would not be possible to write such trajectories files with current disk space limitations as roughly 5000 simulations were required. By computing the time correlation functions on the fly, each simulation only needed to maintain a roughly 100 MB intermediate state file. We have released the real-time correlation function computing code developed for this thesis research in an open source Python/Cython library: rtchemstats.[1] The correlation function computation algorithms implemented in this library are listed in Table 1.

This chapter provides details on how correlation functions are computed on the fly. Section 2.2

[1] https://github.com/matthagy/rtchemstats

Table 1: List of correlation function provided by rtchemstats

Name	Function	rtchemstats Computer
Isotropic pair correlation function	$h(r) = g(r) - 1$	StaticIsotropicPairCorrelationComputer
2-Dimensional pair correlation function	$h(a,b)$	Static2DPairCorrelationComputer
2-Dimensional orientation correlation function	$\langle \vec{d}_1 \cdot \vec{d}_2 \rangle (a,b)$	Static2DPairCorrelationComputer
Mean squared displacement function	$C_R(t)$	MeanSquareDisplacementComputer
Velocity autocorrelation function	$C_v(t)$	VelocityAutocorrelationComputer
Reversible bond duration distribution	$f(t_\mathrm{b})$	BondDurationAnalyzer

introduces the algorithms developed for these computations. Implementation of these algorithms in code are discussed in Section 2.3. Lastly, this section also provides some examples on using the developed library to compute static and dynamic correlation functions on the fly.

2.2 Algorithms

2.2.1 Static pair correlations

The static pair correlation function $h(r)$ for pairs of particles in simulation is computed by building a histogram of pair separation distances r. The separation distances between pairs of particles must be calculated with the consideration of periodic boundary conditions. This is efficiently performed by normalizing each i component of the direct pair separation vector $\vec{l}$ to give $\vec{r}$ by the relation

$$r_i = \begin{cases} l_i - s & \text{if } l_i > s/2 \\ l_i + s & \text{if } l_i < -s/2 \\ l_i & \text{otherwise} \end{cases} \tag{1}$$

where s is the lateral dimension of the cubic periodic box.

This histogram of separation distances n_r can be converted to a discrete density distribution ρ_r by normalizing for the total number of pair observations and the volume of the spherical shell v_r of each histogram component.

$$\rho_r = \frac{n_r}{v_r n N} \tag{2}$$

where n is the number of configurations analyzed and N is the number of particles in each configuration. The volume of each spherical shell is given by

$$v_r = \frac{4}{3}\pi\left[(r+\Delta r)^3 - r^3\right] \tag{3}$$

where r is the lower bound of the histogram bin and Δr is the bin width. The discrete pair distribution function and the pair correlation function are each given by

$$g_r = \rho_r/\rho \tag{4}$$

and

$$h_r = g_r - 1, \tag{5}$$

respectively, with ρ as the bulk density of system.

A similar procedure is used to compute the anisotropic pair correlations for particles that have a director vector (e.g. dipolar Janus particles). In this case the pair separation vector $\vec{r}$ is projected onto the two dimensional references frame of each of the particles in a pair. A two dimensional histogram of the pair separations in this references frame is constructed and a similar normalization procedure is used to compute the discrete density distribution. Additionally, a separate two dimensional histogram can accumulate the the orientation correlation for pairs of particles $\vec{d}_1 \cdot \vec{d}_2$. This is used to calculate the average orientation correlations for pairs of particles at different orientations within this two dimensional frame.

2.2.2 Time correlation functions

Computing time correlations functions (TCFs) present a particular challenge in that these computations require a history of previous simulation configurations. If the full history is maintained (in memory!) then we are no better off than if all configurations were just written to disk. The time correlation function computations algorithms are designed such that they hold on to a portion of the full history of previously seen configurations in simulation, but discard each configuration at the first available chance. To describe this strategy we consider the general structure of a time correlation function, $C_X(t)$, computation as

$$C_X(t) = \langle M_X\left[X_i(t_j), X_i(t_j+t)\right]\rangle_{i,t_j} \tag{6}$$

where M_X is some kernel function specific to each TCF and $X_i(t^*)$ is a configuration property of the i-th particle (e.g. position $\vec{R}_i$ or velocity $\vec{v}_i$) at each reference time t^* in simulation. The average is taken over all particles i and all reference times t_j. For the mean squared displacement (MSD), $C_R(t)$, the kernel function is

$$M_{\mathrm{R}}\left(\vec{R}_a, \vec{R}_b\right) = \left|\vec{R}_a - \vec{R}_b\right|^2. \tag{7}$$

Similarly for the velocity autocorrelation function (VACF), $C_v(t)$, the kernel function is

$$M_{\mathrm{v}}\left(\vec{v}_a, \vec{v}_b\right) = \vec{v}_a \cdot \vec{v}_b \tag{8}$$

The general strategy for computing each TCF, $C_X(t)$, starts by sampling configurations from simulations at a fixed rate of τ_X. With these configuration a numerical TCF is computed at $m+1$ time intervals at a resolution τ_X from 0 to a maximum time of $m\tau_X$. The value of the TCF at each time interval $k\tau_x$ is computed by averaging the the kernel function M_X over each pair of sampled configuration that are separted by k intervals (i.e. $X_i(t_j)$ and $X_i(t_j + k\tau_X)$) for all reference times t_j and for all i particles *a la* Eq. 6.

To perform this averaging, a history of the last m configurations is maintained throughout the TCF computation. At the start of TCF computation we first collect a history of the first m configurations sampled at a rate of τ_X without performing any averaging. For each subsequent configuration $X(j\tau)$ the quantity

$$\left\langle M_X\left\{X_i\left[(j-k)\,\tau_X\right], X_i\left(j\tau_X\right)\right\}\right\rangle_i \tag{9}$$

is computed with each of the k previous configurations $X\left[(j-k)\,\tau_X\right]$. This provides the instantaneous correlation at each time interval $j\tau_X$ for the current configuration with respect to each of the previous configurations as averaged over all i particles. The instantaneous correlation is averaged over all reference configurations j sampled throughout simulation to provide the average TCF. After the instantaneous correlations are computed and accumulated, the current configuration is added to the front of the configuration history and the oldest configuration is discarded.

Updating and accessing this history is most efficiently accomplished with the use of a ring buffer data structure (Figure 1). A pointer is maintained to current head which contains the most recent $X(j)$ configuration. When a new configuration is be analyzed, the history of previous configurations can be iterated starting from the head to compute the instantaneous correlations of the new

configuration with each of the previous configurations. After these computations, the pointer can be advanced such that it now points to the oldest entry in the configuration history. This entry is overwritten with the new configuration to update the history in preparation for analyzing the next sampled configuration.

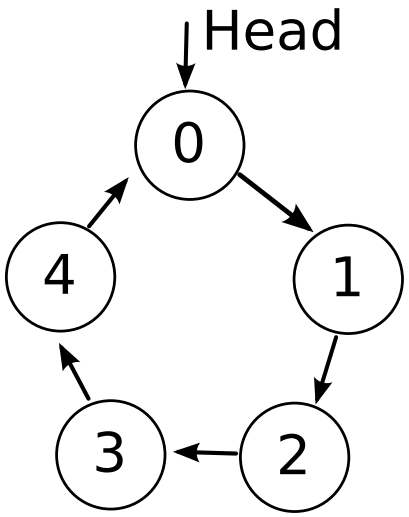

Figure 1: Schematic for a ring buffer data structure. The arrow denotes the relationships between nodes and the head node.

A modification to this general TCF computation procedure is applied to the mean squared displacement computation algorithm to account for periodic boundary conditions. Instead of keeping a history of the positions themselves, this algorithm maintains a history of the separation vectors between the positions of simulation configurations adjacent in sampled time. These separation vectors are normalized with respect to periodic boundary conditions using Eq. 1. To apply the MSD kernel in Eq. 7, the separation vectors are cumulatively summed to give the positions trajectory as normalized for periodic boundary conditions.

2.2.3 Bond durations distribution

The distribution of reversible bond durations betweens pairs of particles in simulations is a quantity that can provide insight into microscopic dynamics. The first step in computing the duration of reversible bonds is to determine the (i, j) pairs of particles that are bonded in a simulation configuration. This is accomplished by interating all pairs and comparing their separation distance r (with consideration of periodic boundary conditions using Eq. 1) against a bond cutoff distance r_{bond}. A

set b is constructed that includes all (i, j) tuples as specifies the pairs of particles that are bonded. For bond identification it is useful to order each tuple such that $i < j$.

The time at which each individual bond is formed and the time at which it is subsequently broken can be determined by monitoring the set of bonds throughout simulation at a rate of τ_b. This produces a sequence of bond sets b_k as indexed by variable k. By comparing the sets between adjacent samples, k and $k-1$, it can be determned which bonds are formed and which are broken in the k-th configuration. The set of bonds formed in the k-th configuration is given by

$$b_{\text{formed},k} = b_k - b_{k-1} \tag{10}$$

and set of bonds broken in this configuration is given by

$$b_{\text{broken},k} = b_{k-1} - b_k, \tag{11}$$

where subtraction implies taking the set relative complement: i.e.

$$a - b = a \setminus b = a^c \cap b\,. \tag{12}$$

A book keeping data structure is used to track the configuration index k at which each (i, j) bond is formed. When the bond is subsequently broken, its formation time can be looked up in this data structure to determine the duration of the bond at a resolution of τ_b. The bond durations observed in simulation are histogrammed to produce the distribution of bond durations. In practice, this histogram is generally constructed on a log-scale for bond duration.

2.3 Code implementation and usage examples

A Python library—rtchemstats—has been developed to implement these algorithms. Each correlation function computation is implemented as a "Computer" class which encapsulates the algorithm and its internal state. An "accumulate" method is provided by each computer as takes a simulation configuration and applies the correspodning algorithm. A "get_accumulated" methods returns a new object which represents the results of computation. At the moment, the rtchemstats project is hosted on github at the URL https://github.com/matthagy/rtchemstats.

For computational efficency (both CPU and memory) the core of each computation algorithm is implemented in the Cython language. Cython is a hybrid C/Python language for use in developing

Python extensions. Algorithms can acess both C-primitives (e.g. ints and pointers) as well as Python objects. These core computation components can therefore leverage the speed of C while exposing a Python interface for use in scripting.

The following examples illustrate usage of rtchemstats correlation function "Computers" and highlight some features of the library. These demonstration source files can be found in the "Demo" directory within the rtchemstats project. Examples are structured to reproduce select portions of Verlet and Levesque's [127, 128, 75] original study of Lennard Jones fluids. Details of the simulation methods and reduced variables can be found in those references. Simulations are performed using my PyLJFluid library;[2] a simple Molecular Dynamics engine developed for educating students about computer simulations. A small utility module (util.py) is used in each demonstration to intiailize and equilibrate simulations with the "get_equilibrated_simulation" function. This utility module is included in the Demo directory.

The first example shows the computation of the pair distribution function, $g(r)$, using the StaticIsotropicPairCorrelationComputer. This code is included in Code 2.1. Simulation conditions are chosen to match a system studied by Verlet in reference [127]. Lines 11 and 12 show the construction of the computer object, including the specificiation of computation parameters. In lines 13 and 14 a production loop is performed in which the simulation configuration is advanced in time using the underlying Molecular Dynamics propagator. The analysis algorithms are applied to simulation configuration in Lines 15 and 16. Under the hood, the "accumulate_positions" method is applying the algorithm of Section 2.2.1 to extract pair separation distances (with periodic boundary conditons) and accumulate a histogram of these distances. In line 17, the results of pair correlation computation are aquired as encapsulated in a Python object. Line 21 demonstrates how these results can be used; in this case to create a plot of the pair distribution function. This plot is included in Figure 2 and these results can be compard to those of Verlet for the same computation (Fig. 1 of reference [127]). It is seen that the new analysis code of rtchemstats produces identical results as validates this newly developed code.

In the second example, we compute the velocity autocorrelation function (VACF), $C_v(t)$, using the VelocityAutocorrelationComputer. The code of this example is included in Code 2.2.

[2] https://github.com/matthagy/PyLJFluid

Again, simulation conditions are chosen to match a system studied by Levesque and Verlet in reference [75]. In this example, lines 15 and 16 show the construction of the computer object with the specification of paramters for VACF computation. Similar to the pair correlation example, a production loop is performed over lines 17 and 18. On line 19 of the production loop, the VACF compuation algorithm—as described in Section 2.2.2—is applied to sampled simulation configuration. Internally, the VACF computer maintains a history of simulation velocities to facilitate these computations. The results of the computation are aquired on line 20 as are wrapped up in a Python object. An example of using these results is shown on line 25 where the normalized VACF is plotted (Figure 3). Plotting is performed in the same fashion as Levesque and Verlet plotted their results in Figure 2 of reference [75]. Comparision of our new results with Levesque and Verlet's results validates the new analysis code.

```
1  '''Compute the pair distribution function g(r) for a Lennard Jones
2     system at T=1.46 and rho=0.4. Results can be compared to Figure 1
3     of Verlet L. Phys. Rev. 165. 201. (1968)
4  '''
5  from rtchemstats.pair1d import StaticIsotropicPairCorrelationComputer
6  from util import get_equilibrated_simulation
7  import matplotlib.pyplot as pl
8
9  sim = get_equilibrated_simulation(rho=0.4, T=1.46)
10
11 gr_comp = StaticIsotropicPairCorrelationComputer(dr=0.01,
12                                                  r_max=sim.config.box_size / 2)
13 for i in xrange(200):
14     sim.cycle(10)
15     gr_comp.accumulate_positions(sim.config.positions,
16                                  sim.config.box_size)
17 gr = gr_comp.get_accumulated()
18
19 plt.figure(1)
20 plt.clf()
21 plt.plot(gr.r, gr.g)
22 plt.xlabel(r'Pair Separation, $r$ ($\sigma$)')
23 plt.ylabel(r'Pair Distribution, $g(r)$')
```

Code 2.1: Python source code to compute the static pair distribution function of a Lennard Jones system using the rtchemstats library.

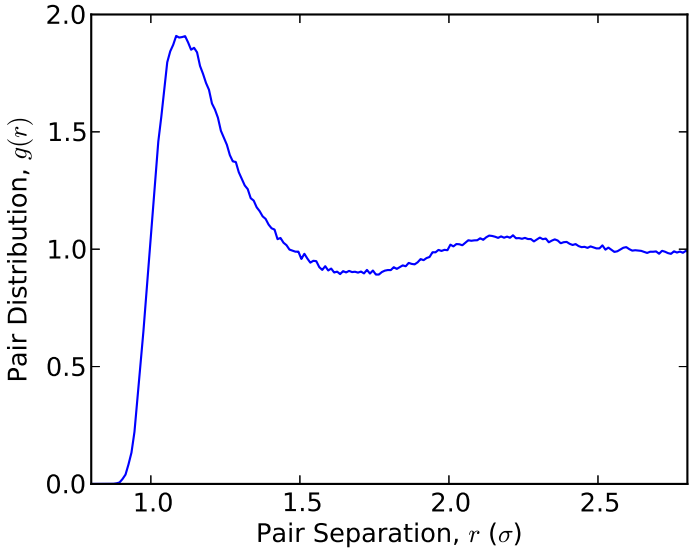

Figure 2: Pair distribution function computed with rtchemstats StaticIsotropicPairCorrelationComputer for a Lennard Jones system with temperature $T = 1.46$ and density $\rho = 0.4$. Results of Code 2.1 as can be compared against the results shown in Figure 1 of reference [128].

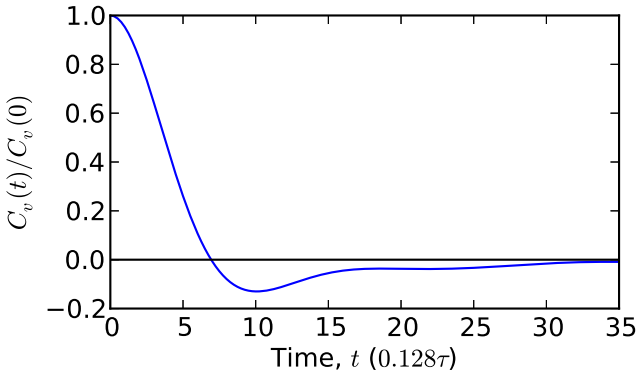

Figure 3: Normalized velocity autocorrelation function computed with rtchemstats VelocityAutocorrelationComputer for a Lennard Jones system with temperature $T = 0.76$ and density $\rho = 0.85$. Results of Code 2.1 as can be compared against results shown by a dashed line Figure 2 of reference [75].

```
'''Compute the velocity autocorrelation function C_v(t) for a
   Lennard Jones system at T=1.46 and rho=0.4. Results can be compared
   to Figure 1 of Levesque D. and Verlet L. Phys. Rev. A. 2514. 201. (1970)
'''

from rtchemstats.tcf import VelocityAutocorrelationComputer
import matplotlib.pyplot as plt

from util import get_equilibrated_simulation, dt, N

sim = get_equilibrated_simulation(rho=0.85, T=0.76)

# Compute C_v(t)
cycle_rate = 1
cv_comp = VelocityAutocorrelationComputer(window_size=250, N_particles=N,
                                          analyze_rate=dt * cycle_rate)
for i in xrange(2000):
    sim.cycle(cycle_rate)
    cv_comp.analyze_velocities(sim.config.calculate_velocities())
Cvt = cv_comp.get_accumulated()

# Plot C_v(t)
plt.figure(1)
plt.clf()
plt.plot(Cvt.t / 0.128, Cvt.Cv / Cvt.Cv[0])
plt.xlabel(r'Time, $t$ ($0.128 \tau$)')
plt.ylabel(r'Normalized Velocity Autocorrelation Function, $C_v(t) / C_v(0)$')
```

Code 2.2: Python source code to compute the velocity autocorrelation function of a Lennard Jones system using the rtchemstats library.

CHAPTER III

THE GELATION DYNAMICS OF ELECTROSTATICALLY-STABILIZED (ESDA) COLLOIDS

3.1 Introduction

The association of colloidal particles is a process of great industrial importance. [11, 38, 95] Such association is generally called flocculation when it is reversible and coagulation when it is irreversible. These processes are not merely colligative as they are controlled by both colloidal-particle and solvent parameters such as particle size, solvent ionic strength, and the presence of surfactants. There has been substantial theoretical work that provides an explanation for how these and other parameters influence colloidal flocculation and aggregation for a variety of colloid systems. [11, 38, 95, 4] In this work, we extend theory and simulation to colloidal particles with pair interactions that are neither purely attractive or repulsive and instead have an energetic barrier to pairwise association. We focus on a model of latex spheres that reversibly associate—as due to short-range depletion forces—and study how an energetic barrier—as due to longer-range electrostatic forces—influences the dynamics of colloidal flocculation.

Depletion association occurs when non-absorbing macromolecules are added to a dispersions of colloidal particles. A depletion zone of relatively low macromolecule concentration is formed around each colloidal particle. It is thermodynamically favorable for the depletion zones of different particles to overlap such that the overall free volume available to macromolecules is increased. This drives reversible association between colloidal particles in a flocculation process. It has been shown that depletion-flocculation can be inhibited (i.e the colloid dispersion can be stabilized) with electrostatic interactions between colloidal particles. [111] From a technological standpoint, this is beneficial in that the strength of the electrostatic interaction can be reduced through the addition of electrolytes to solution so as to induce flocculation. Sharma and Waltz[114] have experimentally measured the interaction profiles for pairs of electrostatically-stabilized depletion-associating (ESDA) colloidal particles using internal reflection microscopy. They have shown that varying

macromolecule concentration and electrolyte concentration allows for significant control over the overall interaction profile. This includes modulating the height of the energetic barrier that limits pair association as would allow one to control the time scales of flocculation. To our knowledge, this relationship of barrier height on the flocculation time scale has not previously been studied through either experiment or simulation for moderate colloid volume fraction of $\phi > 0.1$. In this work, we study this relationship using simulation and theory.

The flocculation of colloidal particles has previously been studied through computer simulation with a variety of methods and models. [9, 14, 41, 102] Bos and Opheusden[9] simulated the aging of colloidal gels with Lennard-Jone interactions using Brownian Dynamics and found a compactification of gel structure with time. Similarly, Santos, Campanella, and Carignano[106] also studied the dynamics of colloidal gelation with a focus on the length scale of attraction. Their results include the observation of collapsed crystalline structure for longer range attraction and spanning networks for shorter range attraction. Butler and Hanley[14] studied Lennard-Jones particles with a small barrier height of roughly $2\,k_{\mathrm{B}}T$ limiting association using Monte Carlo simulation. They found this barrier was sufficient to enhance network formation. The effects of attraction length-scale on glass formation have been simulated by Foffi and coworkers. [41] Their results suggests that kinetic arrest is the only mechanism that can lead to disordered and arrested states for short-range attractive particles. Depletion-attracting colloidal glasses were simulated by Puertas, Fuchs, and Cates[102] to study the aging of attractive glasses as was found to be similar to the aging of repulsive glasses. These authors showed there are special considerations for attraction-driven glasses in that the number of reversible bonds increases with times as affects the structure of the gel.

In this paper, we investigate the effect of reaction barrier height on the dynamics of depletion flocculation for a model of electrostatically-stabilized latex colloidal particles. We begin in Section 3.2 by constructing a model for these colloidal particles. Long-time Brownian Dynamics simulation of the model are performed to quantify the flocculation dynamics. This is accomplished with optimized and parallelized code that we have developed as discussed in Section 3.3. Additionally, in Section 3.4 an analytic theory of flocculation with an energetic barrier is developed

using population equation approach. Through an application of Kramers theory we develop a time-rescaling relationship that explains how a change in the energetic barrier height affects the flocculation time-scale. Simulation results (Section 3.5) quantify the time-scales and dynamics of floc formation for a range of colloid volume fractions and reaction barrier heights. Floc structure is visualized to show the importance of highly connected regions at certain conditions. The time-rescaling theory is tested on simulation results in Section 3.5.2. Theory explain the affect of energetic barrier height on the early and middle stages of simulated flocculation for high volume fraction. Deviations from the theory at lower volume fractions are explained by the competition between spatial diffusion and energy diffusion. In Sec.3.6 we summarize and discuss these results in regard to their implications for colloidal technologies and their relation to previous work.

3.2 The ESDA Model Potential

A colloid suspension with dissipative solvent is modeled as a collection of identical Brownian spheres that interact through additive pairwise forces. Specifically, we consider latex particles of radius $R_p = 67.5\,\text{nm}$ in water at $T = 300\,K$. The pair potential between particles in this model is developed from a physically-motivated theory designed specifically to describe latex particle interactions.[72] It ensures that the length-scale of the repulsive barrier is properly proportional to particle diameter. To account for the lyophobic nature of such particles, the pair potential is developed from DLVO theory with the addition of a hydrophobic attraction as reviewed by Kostansek.[72] The base equation for this pair potential is as follows:

$$u_{\text{DLVO}}(h) = 2\pi\varepsilon_r\varepsilon_0 R_p \Psi^2 \ln\left(1+e^{-\kappa h}\right) - AR_p/12h - FR_p e^{-h/L} \tag{13}$$

where h is the distance separating the surfaces of two particles (*i.e.*, $h = r - 2R_p$ where r is the center-to-center separation distance). The first two terms in Eq. 13 correspond to the electrostatic repulsion and van der Waals attraction respectively of a standard DLVO potential. The third term describes the close range hydrophobic attraction between two colloid particles. The physical meaning of the parameters in this expression are explained thoroughly in Ref. [72] and references therein. We have chosen values (presented in Table 2) to model latex particles. Solvent ionic strength is chosen to give a moderate barrier height in the initially considered potential. The height of this energetic barrier is $E_\text{b} = \max[u_{\text{DLVO}}(h)] = 10.3\,k_\text{B}T$.

Table 2: The value of pair potential parameters in Equation 13.

Variable	Value	Value in SI units	Significance
R_p	$67.5\,\mathrm{nm}$	$6.75\times10^{-8}\,\mathrm{m}$	Particle radius
A	$10^{-13}\,\mathrm{erg}$	$10^{-20}\,\mathrm{N}$	Hamaker constant
ε_r	80	80	Relative permittivity of water
Ψ	$55\,\mathrm{mV}$	$55\times10^{-3}\,\mathrm{kg\,m^2/A\,s^3}$	Particle surface potential
κ	$(2\,\mathrm{nm})^{-1}$	$5\times10^{8}\,\mathrm{m^{-1}}$	Debye screening length
F	$5\times10^{-11}\,\mathrm{N}$	$5\times10^{-11}\,\mathrm{kg\,m/s^2}$	Structural contact force
L	$1\,\mathrm{nm}$	$1\times10^{-9}\,\mathrm{m}$	Hydrophobic decay length

Short-range attraction is modeled by a harmonic well. This is introduced into the pair potential by defining a switching distance of $h_\mathrm{s} = 3.4\,\mathrm{nm}$, inside of which the harmonic well replaces the potential of Eq. 13

$$u_0(h) = \begin{cases} u_\mathrm{DLVO}(h) & \text{if } h \geq h_\mathrm{s} \\ c_2h^2 + c_1h + c_0 & \text{if } h < h_\mathrm{s} \end{cases} \tag{14}$$

The harmonic well is constructed to be both continuous and smooth with the original potential at the cutoff distance and to have a well of depth $E_\mathrm{w} = -5.3\,k_\mathrm{B}T$ relative to the non-interacting infinite separation $u_\mathrm{DLVO}(h\to\infty) = 0$. This value is chosen to simulate a colloidal floc in which particles can dissociate on a physically relevant (and simulation accessible) time scale.

To investigate the effect of pair potential barrier height E_b independent of the well region, linear scaling is used to modulate the repulsive region of the potential ($h > 2.7\,\mathrm{nm}$). This region of the potential is rescaled by the factor f such that the barrier height is given by $E_\mathrm{b} = fE_\mathrm{b,0}$ where $E_\mathrm{b,0} = 10.3\,k_\mathrm{B}T$ is the barrier height of the base potential. Forces are calculated from the resulting non-analytic potential using numerical differentiation. Before performing numerical differentiation, minor Gaussian smoothing is applied to the entire potential so to ensure continuity in the forces. Five pair potentials with barriers heights of $E_\mathrm{b} = 1.03$, 3.09, 5.15, 7.21, and $10.3\,k_\mathrm{B}T$ are used in this study; they correspond to scaling values $f = 0.1$, 0.3, 0.5, 0.7, and 1, respectively. These five potentials are shown in Figure 4. The general shape of the pair potentials — including the relative length scales of the attractive and repulsive components — is comparable to that experimentally measured for electrostatically-stabilized depletion-associating colloids in Ref. [114]. Larger colloidal particles were used in this experimental study. When scaled by particle diameter, the length scales of the repulsive and attractive components in these potentials are comparable to those found

in experiment.

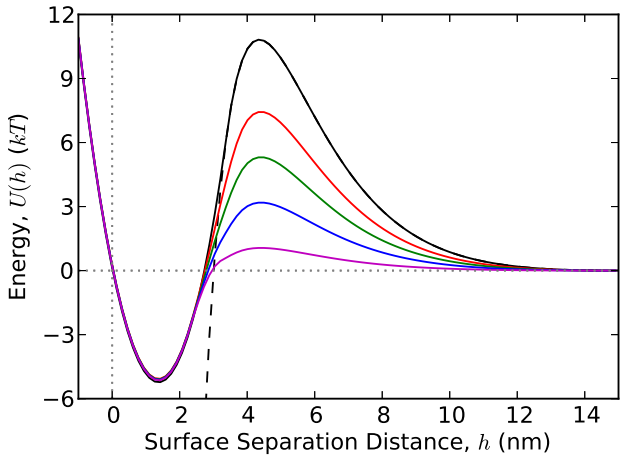

Figure 4: Colloid particle pair-interaction potentials used in simulations where $k_{\mathrm{B}}T$ is defined at $T = 300$ K. The dashed line shows the original latex colloid particle potential in Equation 13 that diverges to $-\infty$ at close separation. The black curve shows the potential of Equation 14 in which short range reversible attraction is modeled with a harmonic well. The remaining curves are examples of linear scaling of the repulsive region of the potential to modulate the barrier height independent of the attractive well depth. Shown curves correspond to barrier heights of $E_{\mathrm{b}} = 1.03$, 3.09, 5.15, 7.21, and $10.3\,k_{\mathrm{B}}T$

3.3 Simulation

The dynamics of colloidal particles are treated herein using Brownian Dynamics simulations propagated according to the Ermak algorithm.[36] The equation of motion is effectively a Langevin equation in the limit of inertialess particles moving through a fast relaxing solvent. The well-known free draining approximation is used in treating hydrodynamics. The total force on a given colloidal particle at any point in time is assumed to be described completely by the sum of pairwise forces: a viscous-solvent frictional force, and a stochastic force. With the condition of inertialess particles, a force balance equation leads to an instantaneous velocity for each particle that is characteristic of the translation over a specified small interval of time Δt. The resulting equation of motion for each i-th particle's coordinate $\mathbf{r_i}$ over each finite time step of duration Δt is

$$\Delta \mathbf{r}_i(t) = \mathbf{F}_i(t)\frac{\Delta t}{\gamma} + \Delta \mathbf{W}_i\,, \tag{15}$$

where $\mathbf{F}_i$ is the net pairwise force on particle i, and γ is the viscous drag coefficient on the particle in solution. For the spherical colloidal particles in this model, γ is calculated from the particle radius

R_p and water viscosity, $\eta = 8.9 \times 10^{-4}$ Pa s ,by Stokes law, $\gamma = 6\pi\eta R_p$. The stochastic influence of the solution is introduced through the vector $\Delta\mathbf{W}$ in which every element—with respect to particle number i and direction α—is uncorrelated. Each element of this random force is characterized by a Gaussian distribution centered about zero with variance $\langle \Delta W_{i,\alpha}^2 \rangle = 2\Delta t k_B T/\gamma$. This relationship between the extent of stochastic thermal fluctuation and friction is given by the fluctuation dissipation theorem.

Simulation are performed at times scales on the order of ten seconds. The high volume fractions and the large forces experienced by the colloidal particles in the simulations necessitated the choice of small time step, $\Delta t = 1$ ns. This leads to simulations that require billions of integration cycles and hence computational efficiency is a high priority. To this end, typical optimization techniques have been implemented in the code. This includes linear interpolation tables for the efficient evaluation of the analytically complex pair forces, neighbor tables to minimize unnecessary force evaluations, vectorized random number generation, and parallelization through a standard Message Passing Interface (MPI). Even with these optimizations, each simulation took on the order of three months using all eight cores of a Dell 1950 with dual quad-core Intel Xeon E5410 CPUs. This high computational resource demand has limited the current investigation to a single trajectory for each set of parameters considered. This a common limitation when simulating colloid flocculation. [9, 106] As a result, we limit our analysis to the computation of structural properties that average over multiple particles per a configuration with the assumption that a single configuration is representative of the full ensemble.

Using our parallel and optimized Brownian Dynamics code, long-time simulations are performed in a cubic box with periodic boundary conditions. Each simulated system contains $N = 1000$ particles with the box size adjusted for the target volume fraction ϕ. Volume fraction is calculated by modeling each particle as sphere of diameter 145 nm. This corresponds to distance at which the initial pair potential $u_0(h)$ takes a value of approximately $1\,k_B T$. Volume fractions of $\phi = 0.05$, 0.2, 0.35, and 0.5 are investigated. Each simulation is initialized from a configuration with no flocculation (i.e. no pair of particles is within the attractive well of the pair potential). The following procedure is used to create each initial non-flocculated configuration. First, a maximum-packing-fraction hexagonal-close-packed (HCP) lattice is generated. Particles are removed randomly as

needed to reach the target volume fraction. This ordered particle system is thermally equilibrated using Brownian Dynamics simulation with each particle modeled as a soft sphere using the following purely-repulsive pair potential

$$u_{\text{rep}}(h) = k_{\text{B}}T \exp\left(-\frac{h/\,\text{nm} - 10}{0.5}\right). \tag{16}$$

Upon thermal equilibration, this purely-repulsive interaction is replaced by the model pair potential described in Section 3.2. A long-time Brownian Dynamics trajectory is then simulated with configurations saved to disk for subsequent analysis. We note that this was necessary as this study was performed before the development of *rtchemstats* library (Chapter 2). Had *rtchemstats* been available, analysis could have been performed in real-time, without the need to write trajectories to disk.

We primarily consider the formation of reversible bonds between pairs of particles in analyzing the flocculation dynamics from simulation. A reversible bond is defined as a pair of particles that are within the attractive well of the pair potential $h < 3.4\,\text{nm}$. The coordination number $n_i(t)$ is defined as the number of reversible bonds formed by the i-th particle at time t in simulation. Mean coordination number $\langle n(t) \rangle$—as averaged over all particles in simulation at time t—-provides a bulk description of the extent of flocculation with time. Additionally, visualization of the bonding network—the graph formed by representing particles as nodes and reversible bonds as edges—allows for the inspection of the flocculation structure. In particular, it allows us to see if highly connected regions are being formed.

3.4 Theory

In this section, we develop a theory to justify a near-Arrhenius dependence of the rate of depletion flocculation on the reaction barrier height E_{b}. The degree of flocculation of the particles can be characterized using the time-dependent probability distribution of particle coordination numbers,

$$P_n(t) = \frac{1}{N} \sum_i \delta_{n,n_i(t)} \tag{17}$$

where $P_n(t)$ is the fraction of particles with a coordination number n at time t, $n_i(t)$ is the coordination number of the i-th particle at time t, and N is the total number of particles. The equation of

motion for the distribution $P_n(t)$ can be recast into a master equation (using a population balance equation approach),

$$\frac{d}{dt}P_n(t) = -(k_n^{\mathrm{f}} + k_n^{\mathrm{b}})P_n + k_{n-1}^{\mathrm{f}}P_{n-1} + k_{n+1}^{\mathrm{b}}P_{n+1}\,, \tag{18}$$

where k_n^{f} and k_n^{b} are the forward (association) and backward (dissociation) rates, respectively. These rate constants will change with time as they are dependent on the flocculation structure.

In accordance with Kramer's theory,[73] the backward rate can be estimated as

$$k_n^{\mathrm{b}} \approx \frac{\omega_0\omega_{\mathrm{b}}}{2\pi\gamma/m}\exp\left(-\frac{E_{\mathrm{b}}+E_{\mathrm{w}}}{k_{\mathrm{B}}T}\right) \tag{19}$$

where m is the mass of a particle; ω_0 is the frequency of oscillations near the potential minimum; $\omega_{\mathrm{b}} \equiv -u''(h_{\mathrm{barrier}})/m$ is that for the top of the potential barrier; and $E_{\mathrm{b}} + E_{\mathrm{w}}$ is the height of the potential as seen from the point of the attractive well.

The forward rate is proportional to the number of collisions and, thus, to the overall concentration C of particles

$$k_n^{\mathrm{f}} = Ck_a \tag{20}$$

where the association constant k_a in dense systems can also be evaluated with the help of Kramers theory:

$$k_a \approx V\frac{\omega_1\omega_{\mathrm{b}}}{2\pi\gamma/m}\exp\left(-U_{\mathrm{b}}/k_{\mathrm{B}}T\right)\,. \tag{21}$$

Here V is the "reaction" volume in the vicinity of the potential barrier and ω_1 represents the effective oscillation frequency outside the barrier. In crowded systems such oscillations are always present due to permanent collisions with particles from the second solvation shell.

From Equations 19 and 21, it is apparent that changes in the reaction barrier height affect only E_{b} (ipso facto) and ω_{b}. Other parameters remain unaffected. We assume that the second derivative of the reaction barrier is proportional to E_{b},

$$\frac{\omega_{\mathrm{b}}^{rma}}{\omega_{\mathrm{b}}^{rmb}} \approx \frac{E_{\mathrm{b}}^{\mathrm{a}}}{E_{\mathrm{b}}^{\mathrm{b}}}. \tag{22}$$

Thus, if the barrier is changed from $E_{\mathrm{b}}^{\mathrm{a}}$ to $E_{\mathrm{b}}^{\mathrm{b}}$, then new values of the backward and forward rates become

$$k_n^{\mathrm{b}}\big|_f = \chi\, k_n^{\mathrm{b}}\big|_{f=1} \tag{23}$$

$$k_n^{\mathrm{f}}\big|_f = \chi\, k_n^{\mathrm{f}}\big|_{f=1} \tag{24}$$

where χ is given by

$$\chi = \frac{E_{\mathrm{b}}^{\mathrm{b}}}{E_{\mathrm{b}}^{\mathrm{a}}} \exp\left(\frac{E_{\mathrm{b}}^{\mathrm{a}} - E_{\mathrm{b}}^{\mathrm{b}}}{k_{\mathrm{B}}T}\right) \tag{25}$$

Changing all the rates in Eq. (18) in accordance with the same law is equivalent to rescaling time by the factor χ. Therefore, if one has a solution $P_n^{\mathrm{a}}(t)$ for a given barrier height $E_{\mathrm{b}}^{\mathrm{a}}$, then a solution for the distribution $P_n^{\mathrm{b}}(t)$ at barrier height $E_{\mathrm{b}}^{\mathrm{b}}$ can be found as

$$P_n^{\mathrm{b}}(t) = P_n^{\mathrm{a}}(t/\chi) \tag{26}$$

The utility of this theory lies in reducing the effort for determining the solutions, at a given volume fraction, for arbitrary barrier heights to the determination of the solution (from simulation or experiment) at a single barrier height. In addition, this scaling factor is roughly equal to the Arrhenius factor

$$\exp\left(\frac{E_{\mathrm{b}}^{\mathrm{a}} - E_{\mathrm{b}}^{\mathrm{b}}}{k_{\mathrm{B}}T}\right) \tag{27}$$

which would be expected from physical intuition alone. This provides a simple description of the effect of E_{b} on the dynamics of depletion flocculation in electrostatically-stabilized colloids. The time-rescaling theory will be applied to simulation results in Section 3.5.2 as a test of its validity.

3.5 Results

3.5.1 Simulated gelation dynamics

The timescales and flocculation dynamics for the Brownian relaxation of an initially unassociated suspension of ESDA colloidal particles into an associated floc network is illustrated through the snapshot of a single such trajectory in Fig. 5. In these snapshots particles are color coded according to their coordination number as detailed in the caption. This figure includes a snapshot at the very long time of $t = 10\,\mathrm{s}$ which is accessible using our optimized and parallel codes. The long-time snapshot shows highly connected crystalline domains in which particles are associated with as many as 11 or 12 neighbors.

To quantify the extent of flocculation in each trajectory with time, the mean coordination $\langle n(t)\rangle$ is considered as averaged over all particles of a configuration at time t. Figure 6 shows the time dependence of $\langle n(t)\rangle$ at four volume fractions for the highest and lowest barrier heights considered

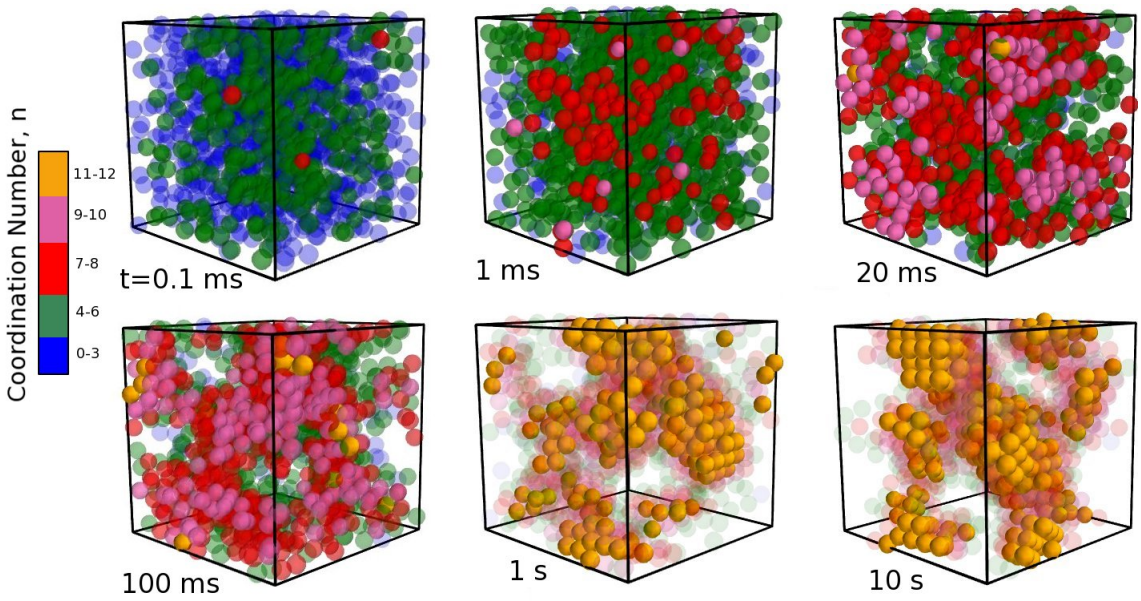

Figure 5: Snapshots of simulation configurations for $\phi = 0.35$ and $E_b = 1.03\,k_BT$ throughout time. Particles are color coded by coordination number, n, with $0 \leq n \leq 3$ - blue, $4 \leq n \leq 6$ - green, $7 \leq n \leq 8$ - red, $9 \leq n \leq 10$ - pink, $11 \leq n \leq 12$ - orange. In each snapshots, lower coordination number particles are rendered partially transparent and the transparency is adjusted to show the structure of higher coordination number particles. In the later two snapshots particles with $n \leq 10$ are rendered more transparent to better show the highly connected crystalline domains with $n \geq 11$.

in this work. For the high barrier height, $E_b = 10.3\,k_BT$, the effect of ϕ is straightforward: suspensions with higher volume fractions flocculate faster. At this high barrier height, $\langle n(t) \rangle$ approaches a value near 6 towards the end of the trajectory though not all of them have clearly plateaued within the observation window. This suggests that they have not yet fully equilibrated.

At the lower barrier height, $E_b = 1.03\,k_BT$, the time-dependence in the mean coordination number, shown in Figure 6, differs considerably between different values of ϕ. At short times, $t < 10\,\text{ms}$, $\langle n(t) \rangle$ shows the same trend as seen for $E_b = 10.3\,k_BT$ in that systems with higher volume fraction flocculate faster. At longer times, the dynamics begin to slow down and then suddenly accelerate when $\langle n(t) \rangle \gtrsim 7$ by the end of simulation for all of these low barrier trajectories. The time at which the dynamics accelerates increases with increasing ϕ. In fact, the $\phi = 0.5$ results show a significant region of log-time for which flocculation dynamics have slowed. At the latest stages of the observed flocculation, $t > 1\,\text{s}$, there is no clear trend as to the effect of volume fraction on $\langle n(t) \rangle$. The cause of flocculation acceleration at intermediate times for $E_b = 1.03\,k_BT$ will be considered in Section

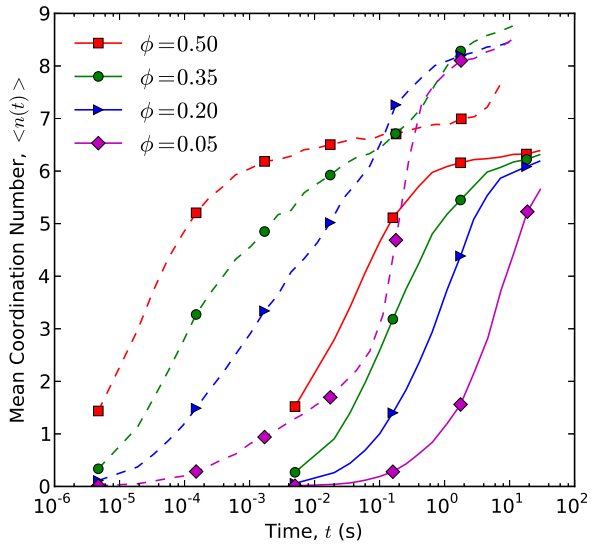

Figure 6: The effect of volume fraction ϕ on the flocculation dynamics of long-time Brownian Dynamics simulations as quantified by mean coordination number $\langle n(t) \rangle$. Results are shown for four different volume fraction with $\phi = 0.5$, 0.35, 0.2, and 0.05 as shown by red squares, green circles, blue triangles, and magenta diamonds, respectively. Solid lines show the results for a barrier height of $E_b = 10.3\,k_B T$ where as dashed lines are for $E_b = 1.03\,k_B T$. Markers are only included at select data points to denote the different curves.

3.5.3 when we consider the structure of the flocculation network.

The effect of E_b on the flocculation dynamics is also studied by comparing $\langle n(t) \rangle$ for five different barrier heights. These results are shown in Fig. 7 for two different volume fractions. In all cases, smaller E_b leads to faster flocculation dynamics as could be anticipated. For $\phi = 0.5$, all of the curves are qualitatively similar by a shift in log-time with the exception of the $t > 1\,s$ for $E_b = 1.03\,k_B T$. This suggests the time-rescaling relationship developed in Section 3.4 may relate these curves and this is further explored in Section 3.5.2. The $\phi = 0.2$ curves are not as qualitatively similar to each other. Additionally, the $\phi = 0.2$ results show a greater extent of flocculation for times of $t > 0.1\,s$ in the results for the three smaller barrier heights of $E_b = 1.03$, 2.09, and $5.15\,k_B T$ than found in any of the $\phi = 0.5$ results with values of $\langle n(t) \rangle > 7$ observed.

3.5.2 Time scale invariance in gelation dynamics

In this section we investigate the regimes in which the time-rescaling theory developed in Section 3.4 is applicable to floc dynamics. This test is performed by scaling all $\langle n(t) \rangle$ results at the same

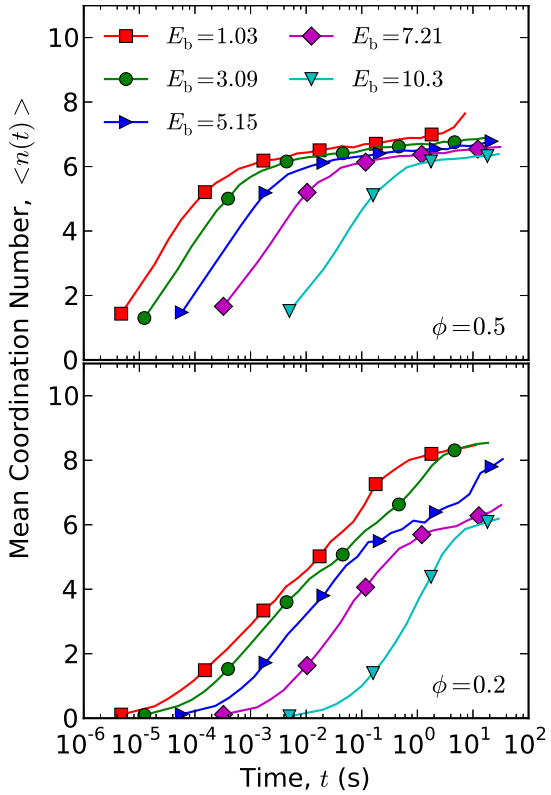

Figure 7: The effect of barrier height E_b on the flocculation dynamics of long-time Brownian Dynamics simulations as quantified by mean coordination number $\langle n(t) \rangle$. Results are shown for five different energetic barrier heights with $E_b = 1.03, 3.09, 5.15, 7.21$, and $10.3\,k_BT$ as shown by red squares, green circles, left-blue triangles, magenta diamonds, and cyan down-triangles, respectively. Upper panels shows results for $\phi = 0.5$ where as lower panel is for $\phi = 0.2$. Markers are only included at select data points to denote the different curves.

volume fraction with different barrier heights E_b to a common time scale. The common time scale of the $E_b = 10.3\,k_BT$ results is chosen for comparison. These scaled flocculation dynamics results are shown in Figure 8. For $\phi = 0.5$ and $\phi = 0.2$ simulation are performed for five values of E_b where as for $\phi = 0.35$ and $\phi = 0.05$ simulation are only performed for $E_b = 1.03$ and $10.3\,k_BT$. If the scaling theory is correct, all curves for a single volume fraction with different barrier heights (same color with different markers) would overlap exhibiting (near) universal behavior. The time-rescaling theory is found to work well for $\phi = 0.5$ with a deviation only observed for $E_b = 1.03\,k_BT$ at longer rescaled-times of $\chi t > 2 \times 10^3$ s. For $\phi = 0.35$ and 0.5 the rescaling theory is moderately successful, with all rescaled curves being within a decade of rescaled-time of each other. Larger deviations are observed for $\phi = 0.05$ where the two rescaled curves are qualitatively different.

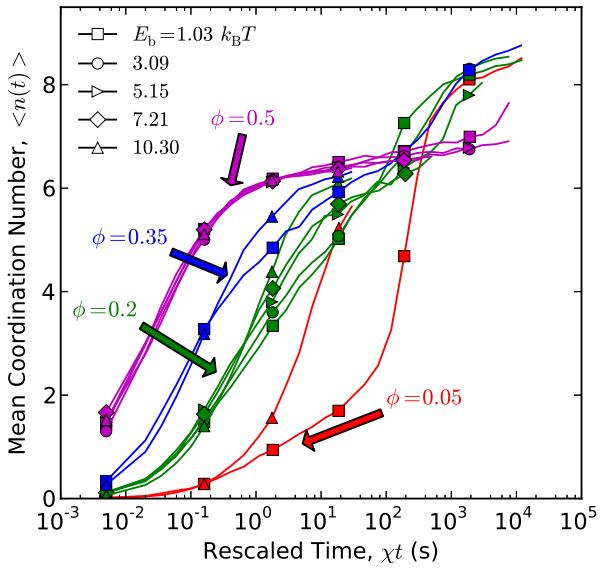

Figure 8: Mean coordination number dynamics plotted by rescaled-time χt where χ is given by Eq. 25. Rescaling factor χ is chosen to map the dynamics to the $E_b = 10.3\,k_BT$ time scale. Different barrier heights are denoted by the symbols: $E_b = 1.03\,k_BT$ (□), 3.09 (◯), 5.15 (▷), 7.21 (◇), and 10.3 (△). Additionally, different volumes fractions are identified by curve color as labeled on plot.

To understand the deviations of the time-rescaling theory, we study the distribution of coordination numbers $P_n(\chi t)$ in simulation for systems at the same volume fraction with different values of E_b at roughly the same rescaled time χt. These results are shown in Fig. 9. Panel A and D show results for $\phi = 0.5$ for two rescaled times of $\chi t \approx 2.3$ s and $\chi t \approx 1.1 \times 10^3$ s, respectively. In each of these two panels the P_n results for different values of E_b are comparable. This demonstrates that the time-scaling theory explains well the time evolution of $P_n(t)$ for this high volume fraction of $\phi = 0.5$. In contrast, panel B demonstrates that this theory is inadequate for $\phi = 0.2$ near $\chi t \approx 2.25$ s. In this case, $P_n(t)$ is found to vary for all five barrier heights investigated. Specifically, the $P_n(t)$ results for smaller values of E_b are shifted to lower values of n relative to the results for $E_b = 10.3\,k_BT$. Panel E shows results for the same volume fraction at later rescaled time of $\chi t \approx 1.1 \times 10^3$ s. Only the three lowest barrier heights trajectories can be extended out to this later rescaled-time. It is interesting that the $P_n(t)$'s appear to be more similar at this later stage of time than what is seen for the earlier time results of panel B. More trajectories are needed to determine whether this is a statistically relevant result.

The $P_n(t)$ results are also analyzed for $\phi = 0.05$ and $\phi = 0.35$ at later rescaled times of $\chi t \approx 9\,\mathrm{s}$ in panels C and F, respectively. At these volume fractions simulation are only performed for $E_\mathrm{b} = 1.03\,k_\mathrm{B}T$ and $E_\mathrm{b} = 10.3\,k_\mathrm{B}T$. For $\phi = 0.05$ the $P_n(t)$ results for these two barrier heights are qualitatively quite different with far higher coordination numbers observed for $E_\mathrm{b} = 10.3\,k_\mathrm{B}T$. This could be explained by the importance of spatial diffusion at low concentrations. The scaling theory only considers energy diffusion and therefore does not account for the additional time needed for particle to diffuse into each others vicinity at lower volume fractions. In contrast, similar $P_n(t)$ results are found in $\phi = 0.35$ for $E_\mathrm{b} = 1.03\,k_\mathrm{B}T$ and $E_\mathrm{b} = 10.3\,k_\mathrm{B}T$ at $\chi t \approx 9\,\mathrm{s}$.

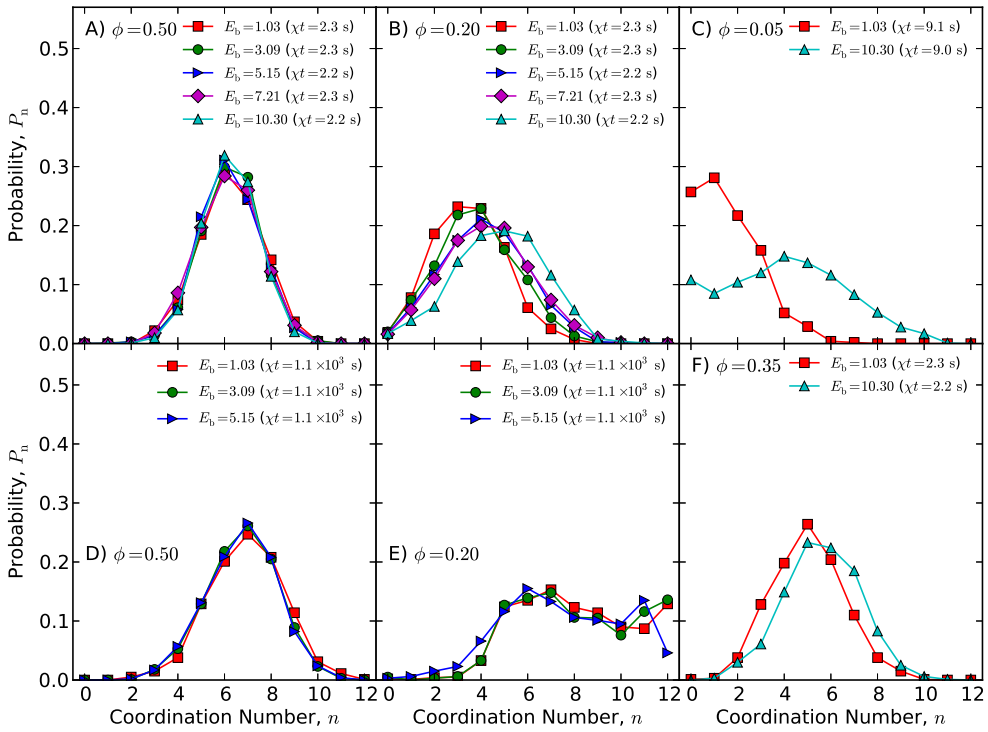

Figure 9: Probability distribution of particle coordination numbers P_n from simulation for systems that differ in E_b. In each panel, results are shown for configurations that are at roughly the same rescaled time χt to test the time-rescaling theory. Time is rescaled to a barrier height of $E_\mathrm{b} = 10.3\,k_\mathrm{B}T$. The value of E_b and the rescaled time of the analyzed configuration for each curve are specified in the legend of each panel.

3.5.3 Gelation network structure

The topological network structure formed during simulated flocculation can also reveal some of the differences in the the flocculation process as it depends on macroscopic characteristics. This network is a graph with the particles being nodes and the bonds as edges. As a preliminary study of the network structure we visualize the flocculation graphs using the Graphviz NEATO program.[34] These visualization only show the graph structure (particle bonding connections) and are not related to the spatial positioning of particles. Figure 10 shows the structure of the flocculation networks for several volume fractions near the end of simulation $t \approx 10\,\mathrm{s}$.

We first consider the different network structures formed with the low barrier height $E_\mathrm{b} = 1.03\,k_\mathrm{B}T$ in contrast to a high barrier height $E_\mathrm{b} = 10.3\,k_\mathrm{B}T$. Panels 10(a) and 10(b) show the structures for the high barrier height at volumes fractions of $\phi = 0.05$ and $\phi = 0.5$, respectively. These visualizations show isolated clusters for the lower volume fraction and a highly-connected spanning network at the high volume fraction. These results can be contrasted to the same volume fractions with the low barrier height as show in panels 10(c) and 10(f). The lower volume fraction systems shows a higher extent of connectivity for this lower barrier height than that observed for the higher barrier height as anticipated from mean coordination number results. Additionally, this systems shows several regions of high connectivity. The high volume fraction system with the lower barrier height shows a highly connected spanning network as also observed in the higher barrier height system at this volume fraction.

Panels 10(d) and 10(e) show the network structure near the end of simulation with the low barrier height for the volume fractions of $\phi = 0.2$ and $\phi = 0.35$, respectively. Both structures show highly connected regions within a spanning network. The highly connected regions are similar to that which was seen for $\phi = 0.05$ with the low barrier height. In general it appears that highly connected regions are important in the flocculation structures for the low barrier height of $E_\mathrm{b} = 1.03\,k_\mathrm{B}T$ for volume fractions $\phi \lesssim 0.35$.

The flocculation network structure also explains the difference in the flocculation process with different values of E_b for the lower volume fraction of $\phi = 0.2$. Network structure are shown in Figure 11 for three different barrier heights, each for a configuration with roughly the same mean

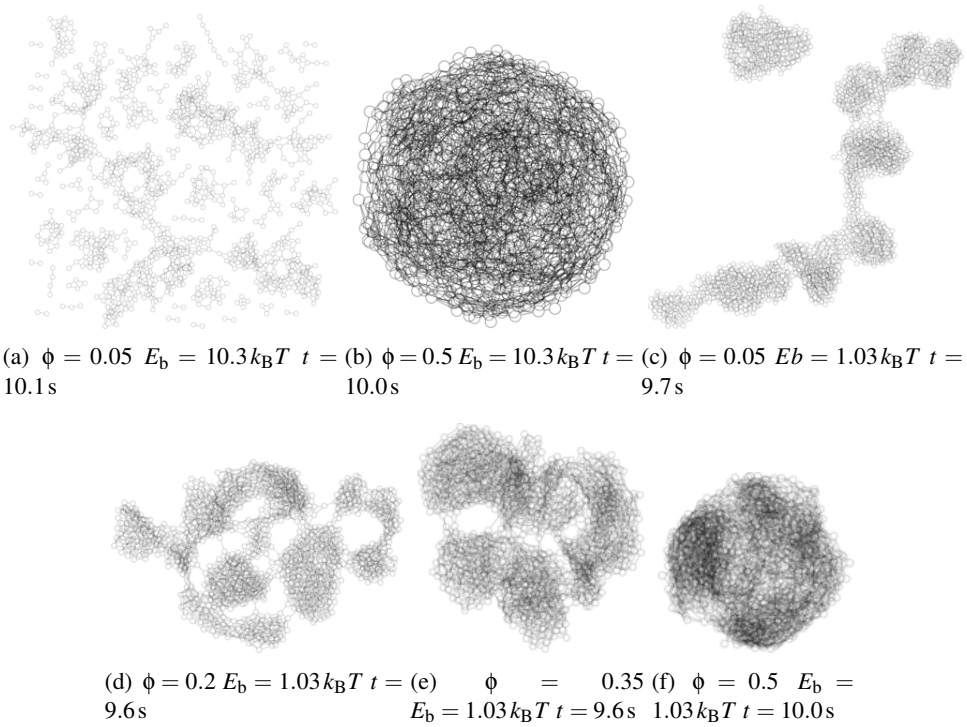

(a) $\phi = 0.05$ $E_b = 10.3\,k_BT$ $t =$ 10.1 s (b) $\phi = 0.5$ $E_b = 10.3\,k_BT$ $t =$ 10.0 s (c) $\phi = 0.05$ $Eb = 1.03\,k_BT$ $t =$ 9.7 s

(d) $\phi = 0.2$ $E_b = 1.03\,k_BT$ $t =$ 9.6 s (e) $\phi = 0.35$ $E_b = 1.03\,k_BT$ $t = 9.6$ s (f) $\phi = 0.5$ $E_b = 1.03\,k_BT$ $t = 10.0$ s

Figure 10: Structure of the flocculation networks at time $t \approx 10$ s. Volume fraction, barrier height, and the time of the shown configurations are denoted below each panel. For panels 10(c) to 10(f) the rescaled-times (to $E_b = 10.3\,k_BT$) are roughly $\chi t \approx 10^4$ s.

coordination number of $\langle n(t) \rangle \approx 5$. From visual inspection, it appears that a more compact structure is formed for lower values of E_b. This suggests that changes in barrier height can lead to different flocculation pathways with different intermediate structures.

3.5.4 Preliminary shear results

Colloidal gels are known to exhibit viscoecstatic properties [115] and shearing can influence the gelation of isotropically attractive colloid particles. [105] Previous computer simulations have provided valuable insight into the effects of shearing on colloidal gelation. [101] This begs the question: how does shearing influence colloidal gelation with an energetic barrier to pair association as occurs in the ESDA model. This section provides preliminary results for the effect of shearing on the flocculation dynamics of ESDA particles.

Shearing is simulated with the introduction of a linear velocity profile, which occurs in couette flow. The shear profile is simulatd along the z direction of the simulation box with flow in the x

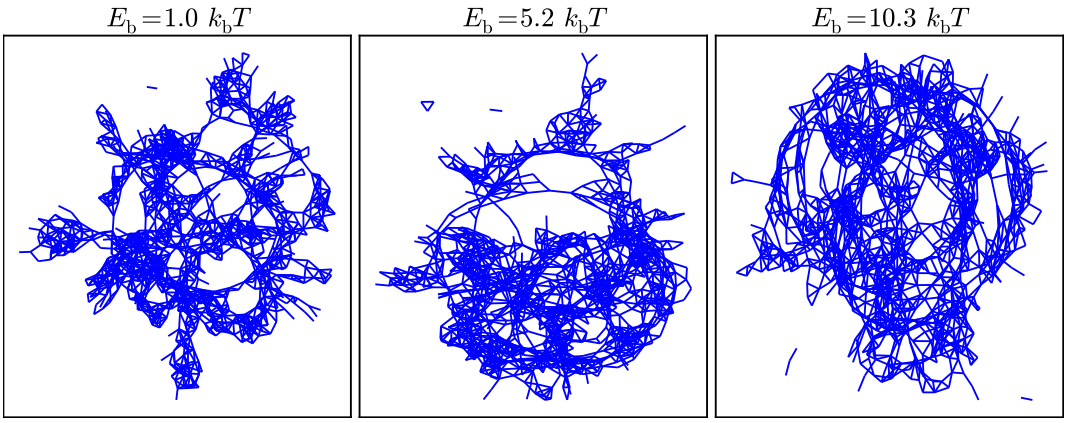

Figure 11: Flocculation network structure from simulation for $\phi = 0.2$ with different values of E_b shown in each panel. Simulation configuration are chosen to each have a coordination number of $\langle n(t) \rangle \approx 5$. The time of each configuration are $t = 0.016$, 0.074, and 2.8 s for $E_b = 1.0$, 5.2, and $10.3\,k_BT$, respectively.

direction. This is implemented by adding velocity $v_{x,s}$ to the instance velocity along the x direction for each particle.

$$v_x = v'_x + v_{x,s}. \tag{28}$$

The linear velocity profile along the z direction is specified by

$$v_{x,s} = \alpha(z - l/2), \tag{29}$$

where α is the shear rate and l is the length of the periodic simulation box.

Preliminary shearing simulation have been performed for the full barrier height potential for a range of shear rates. The effect of shearing on gelation dynamics of quantified by computing the time-dependent mean coordination number, $\langle n(t) \rangle$. These preliminary results are shown in Figure 12. Results show that moderate shear rates of $\alpha = 100s^{-1}$ have negligible effects on the flocculation dynamics. In contrast, larger shear rates of $\alpha = 10000s^{-1}$ accelerate the early stages of flocculation. This can be explained by addition of kinetic energy to particles by shear as allows them to surmount the energetic barrier. Additionally, the larger shear rate is found to limit extent of structure formed at the later stages of flocculation for volume fractions of $\phi = 0.5$ and $\phi 0.35$. This is likely due to shear forces breaking up larger structures. These preliminary results show that shearing can influence the flocculation dynamics of ESDA colloids.

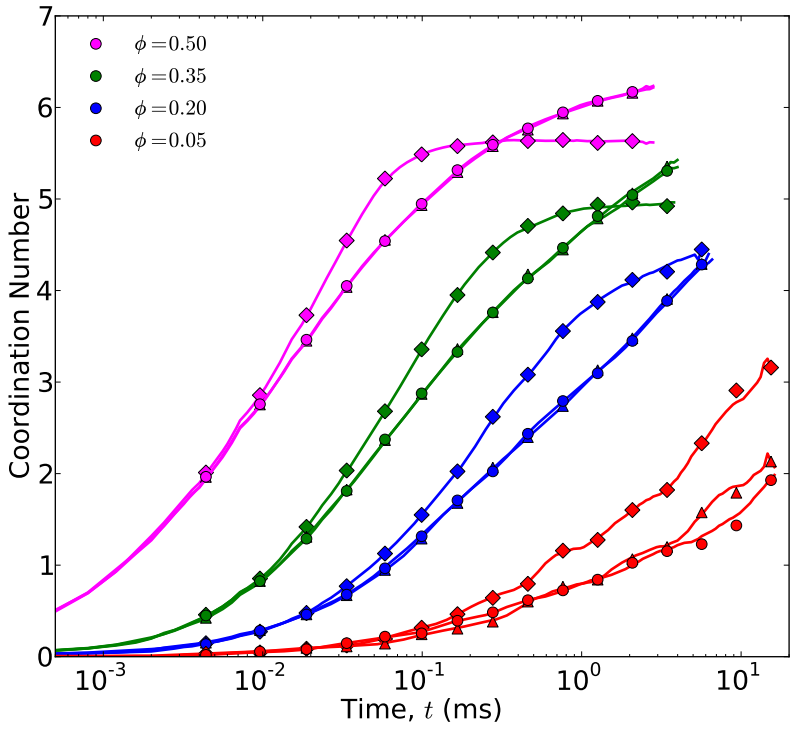

Figure 12: Preliminary results for the effect of shearing on the flocculation dynamics of ESDA particles. Simulations are performed for the full barrier height potential at a range of colloid volume fractions ϕ and shear rates α. Results are shown for three different shear rates $\alpha = 0s^{-}1$ ◯, $\alpha = 100s^{-1}$ △, and $\alpha = 10000s^{-1}$ ◇ for volume fractions of $\phi = 0.5$ - magenta, $\phi = 0.35$ - green, $\phi = 0.2$ - blue, and $\phi = 0.05$ - red.

3.6 Discussion

An Arrhenius-like time-rescaling theory has been found to capture flocculation dynamics of ESDA colloidal particles in the activated regime, namely when the energetic barrier height is of the order $1\,k_{\mathrm{B}}T \lesssim E_{\mathrm{b}} \lesssim 10\,k_{\mathrm{B}}T$, on the flocculation dynamics of dense colloids for a moderate extent of flocculation. This time-rescaling theory does not just capture the mean coordination number, but also explains the time-dependent distribution of particle coordination number $P_n(t)$ for these conditions. Deviation from this theory are found at lower colloid volume fractions of $\phi \lesssim 0.2$. The latter is not entirely a negative result in that it shows that there is a complex relationship between E_{b} and the flocculation dynamics for these conditions, and that there exists a second regime in which the

flocculation dynamics are determined by a different mechanism. Moreover, analysis of the flocculation network structure in simulation suggests that different flocculation pathways are followed at different barrier heights. This includes more highly connected regions when the particle flocculate with a weaker energetic barrier.

These results can be compared to previous simulation studies of colloidal flocculation. Butler and Hanley observed that a small barrier height on the order of $2k_{\mathrm{B}}T$ was sufficient to observe enhanced network formation in system of Lennard-Jones particles. [14] Similarly, we find that more open networks are formed in colloidal flocculation with higher barrier heights. Bos and Opheusden found a compactification of colloidal gel structure with time in their simulation of Lennard Jones particles.[9] Similarly, the flocculation structure in our simulations shows compactification with highly connected regions. This simulated flocculation dynamics does slow with time, but does not reach a steady state value as suggest the formation of a colloidal glass. Therefore it is anticipated that these ESDA particles are forming a colloidal glass, which may have similarities to the attraction driven colloidal glasses studied by Puertas, Fuchs, and Cates.[102]

In summary, we have constructed the ESDA model for electrostatically-stabilized depletion associating particles. With this model, the effects of energetic barrier height on the flocculation dynamics of colloid particles has been studied with long-time Brownian Dynamics simulation and population balance theory. Through simulation we have quantified the flocculation dynamics—as measured by mean coordination number—for a range of energetic barrier heights and colloid volume fractions. Additionally, we have visualized the flocculation network to determine the significance of highly connected regions in the floc structure. An Arrhenius-like time-rescaling relationship was developed to explain the change in flocculation time scales upon a change in energetic barrier height. Simulation results show that this relationship works well at high volume faction of $\phi = 0.5$. This suggests an activated process dominates the dynamics at these conditions. Deviation at lower volume fractions of $\phi \lesssim 0.2$ demonstrate the complex relationship of energetic barrier height on the flocculation dynamics. Simulation results show that for these lower volume fractions, system with different barrier heights flocculate through different pathways with lower barrier heights systems showing more highly connected regions.

CHAPTER IV

STATIC PROPERTIES OF DIPOLAR JANUS PARTICLES

4.1 Introduction

Recent advances in mesoscale fabrication have allowed for the construction of anisotropic colloidal particles that are anticipated to self assemble into novel structures so as to unlock new material properties. [98, 47, 51, 97, 31] One example is the prediction of richer phase behavior for anisotropic colloidal materials[46, 48, 109] as can exist in gas, liquid, crystalline, or amorphous phases due to the order between particles in analogy with atomic materials. The Janus structure — where spherical particles have two chemically distinct hemispheres — is one such anisotropic colloid particle structure that has warranted much experimental, [18, 123, 43, 59, 19, 20, 122, 62, 61, 63, 69] theoretical, [35, 32, 69] and simulation [35, 62, 48, 63, 109, 83, 110, 49, 69, 103] attention.

Janus particles where first prepared by Veyssié et al.[18] by protecting one hemisphere of a glass sphere (with diameter circa $50\,\mu$m to $90\,\mu$m) with a cellulose film so as to allow the modification of the other hemisphere. This concept of hemisphere protection has been used in several subsequent techniques for Janus particle production. [123, 43, 59, 19, 20, 62, 61, 63, 69] Takei and Shimizu[123] developed a procedure where a dense monolayer of latex spheres is formed on a solid surface in vacuum. Gold is then deposited onto the top hemispheres while the bottom hemispheres remain inaccessible due to their dense packing within the monolayer. This gold layer can subsequently be modified with thiol chemistry. Takei's method has allowed the production of Janus particles with a diameter as small as 110 nm. [59] Fujimoto and coworkers[43] have developed a procedure for Janus particle fabrication that employs a colloid monolayer at liquid interfaces allowing for liquid surface modification chemistry. Dipolar Janus colloids were produced by Paunov and coworkers[19] using a microcontact printing technique whereby ionic surfactants are deposited on top of a monolayer of particles with opposite charge. These same authors have also engineered a technique using gel trapping to protect particle surfaces similar to Veryssié's early technique, but

with applications to particles an order of magnitude smaller. [20] Unfortunately, limited quantities of Janus particles can be produced with these methods as they all treat a single monolayer of particles.

One approach to producing larger quantities of nonuniform surface particles has been developed by Ikeda and coworkers.[90, 122] They aggregate silica particles and modified only the accessible parts of particles on the cluster surface. This method can produce gram size quantities of nonuniformly coated particles, although there is little control over the geometry of the surface coverage. A method for the production of large quantities of Janus particles has been developed by Granick et al.[61] by partially trapping colloidal particles at the surface of wax particles. This method provides good control over the extent of colloidal particle surface that is exposed for chemical modification and has the potential to be scaled up to produce gram-scale quantities of Janus particles.

Due to current challenges of scaling up Janus particle fabrications techniques, there have been limited experimental studies of Janus colloidal systems [62, 63] and bulk materials properties have yet to be studied to our knowledge. Granick and coworkers have studied clusters formed by Janus particles for two different types of Janus chemistries: dipolar Janus (DJ) particle clusters,[62] and amphiphilic Janus particle clusters.[63] Using epifluoresence microscopy they imaged the structure of the clusters containing between $N = 2$ and $N = 12$ particles. Additionally, they found these same structures were predicted by the Monte Carlo simulations of Janus colloid models that they developed. The authors demonstrated how anisotropic interactions could lead to novel cluster structures that differ from isotropic particle clusters and also that computer simulation models can describe Janus colloid systems effectively. Unfortunately, to our knowledge there has been no experimental work on the bulk properties of Janus colloidal materials. This gap has thus far been filled through computer simulations using simple, but instructive, models [48, 109, 83, 49, 110] and the present work is aimed at advancing our understanding of bulk systems further.

Sciortino and coworkers simulated the interactions of patchy particles with interactions comparable to amphiphilic Janus colloids. [109, 110] They treated these interactions using the patch model developed by Kern and Frenkel to describe generic highly-anisotropic interactions using discontinuous potentials.[71] Sciortino et al.[109, 40] found the formation of isolated clusters of amphiphilic Janus particles similar to those observed by Granick et al.[63] The clusters are found

to play a key role in the phase behavior of the patchy particle systems that Sciortino and coworkers simulated. [109, 110] Specifically, they discovered a region of the phase diagram in which clusters form a gas phase — with limited interactions between clusters — as coexists with a fluid phase. This leads to unconventional phase behavior as the gas phase is energetically favored and the liquid phase is entropically favored. [109, 110] Rosenthal et al.[103] have studied systems of amphiphilic Janus particles using smooth potentials within the Tarazona model[119] and they also found cluster structures to play a significant role in phase behavior. Even at high densities, the isolated clusters did not condense together, but instead adopted denser cluster structures. A similar model was also addressed earlier by Erdmann et al.[35] through both integral equation theories and Monte Carlo simulations. They found that nematic-like order can arise in liquid phases of amphiphilic Janus particles given sufficiently strong anisotropies in the pair interaction. They also found that polar phases for systems of DJ particles can favor pairwise parallel axis alignment.[35]

Hall et al.[48, 49] characterized the interactions of DJ colloids through a model consisting of hard spheres with two embedded point charges. By discretizing the point charge interactions and using discontinuous molecular dynamics, the authors were able to map out the phase behavior of both monodisperse systems[48] and binary mixtures. [49] Their results predict rich phase behavior for DJ particles, including multiple crystalline phases in monodisperse systems and the phase behavior can either simplify or grow richer in binary mixtures as dependent on whether the components differ in size or interaction strength respectively. A key result of their study is the observation of string-like chain structures within a liquid phase. At lower temperatures the authors found that the strings gave rise to a percolating network as consistent with a colloidal gel. Miller and coworkers observed similar results in their simulation of dipolar dumbbells.[83] These authors specifically focused on lower densities consistent with colloidal gels and they also found a transition from chain structures to a percolating network as temperature was decreased. The observation of chain structures is comparable to that which has been seen in the point dipole models of simple polar fluids: namely the dipolar hard sphere model[133] and Stockmayer fluids. [24] Thus the known structure of simple polar fluids [24, 96, 42, 117, 133, 15] appears to be relevant to the behavior of DJ colloids.

In contrast, Granick et al.[62] have emphasized that DJ colloidal particles are not well approximated by point dipoles as the size of the particles greatly exceeds the electrostatic screening length.

Instead, they propose a point charge model of DJ colloidal particles whereby the pair potential between particles is rigorously calculated as the sum interaction between point sites uniformly spaced across the surface of each sphere in their study of Janus particle clusters. It is therefore of interest to study whether a system of DJ particles modeled in high detail will also exhibit structural properties comparable to dipole models. In this chapter, we develop such a detailed model. We do not find any significant chain formation in our simulations. Indeed, those simulations with the strongest pair interactions proceed towards highly connected aggregates.

Additionally, the present model uses only continuous potential terms so as to accommodate classical dynamics integrators directly. This is in contrast to previous discontinuous models for anisotropic particles, which require non-Hamiltonian methods for dynamical propagation.[26, 48, 49] The use of a molecular dynamics propagating engine allows one to better understand dynamical correlations that may occur in complex environments such as those we have seen in the case of motion of rods in spherical environments[124, 125] or spherical probes through rods of varying degree of order.[126] To this end, we have developed a model potential in which the potential is continuous and the forces are well-defined everywhere. While this serves a significant role in the benchmark studies on equilibrium properties described here, this continuity will be even more important in future studies of the dynamics.

At sufficiently high temperature and low densities, the anisotropic nature of DJ particles are minimized and they are well approximated as simple isotropic particles with an orientation averaged potential of mean force. Such isotropically interacting particles are well understood at both a conceptual and theoretical level for atomic fluids.[21, 54] In colloids, such isotropically attractive colloids can arise from polymer depletion interactions[38] with attractive well depths on the order of $1\,k_{\mathrm{B}}T$ to $5\,k_{\mathrm{B}}T$ as found in experiment.[104] Quantifying the conditions under which this approximation breaks down is necessary to determine in which regimes new colloidal material properties can be expected. These new material properties can then be attributed to multibody orientation correlations that cannot be captured by such a pairwise potential of mean force. On the other hand, it may be useful to process DJ colloids under conditions at which they behave as conventional isotropic colloidal materials so that existing techniques can be applied reliably. It is therefore important to know under which conditions multibody orientation correlations.

In this chapter, we construct a detailed model of DJ colloidal particles and study their equilibrium static properties using molecular dynamics. In Sec. 4.2.1, the new pointwise (PW) DJ particle model is defined. We also consider the conditions under which DJ particles can be modeled as simple isotropically attractive particles by constructing an isotropically coarse-grained (CG) model of DJ particles in Sec. 4.2.2. Numerical methods for simulation and computations are explained in Section 4.3. Perhaps surprisingly, the CG model often reproduces the equilibrium structure (Section 4.4.1) and ensemble free energies (Section 4.4.4) of the PW model. This agreement suggests that multibody orientation correlationsare insignificant in DJ colloids with pair free energetics on the order of $A_{\mathrm{p}} \gtrsim -3\,k_{\mathrm{B}}T$ for moderate volume fractions of $0.1 \leq \phi \leq 0.4$. Equilibrium simulations of stronger interacting systems are not possible with current methods, but the time-dependent relaxation is studied Section 4.4.5 and the results suggest the existence of phase transitions to solid structures. The discussion in Section 4.5 compares our models and results with previous studies of Janus colloids and simple polar fluids. It is notable that the current results for the PW model show no signs of chain structures in liquid regimes as were observed earlier in dipole models.

4.2 Dipolar Janus colloid models

To study the static properties of DJ colloids, two particle models are constructed. Both models include only continuous potentials so as to facilitate the simulation of dynamics as studied in Chapter 5. A detailed and computationally expensive model is used to rigorously study the properties of DJ particles using a decomposition of the particle surface into point charges (pointwise or PW model). Additionally, we develop a coarse-grained (CG) model where an isotropic potential of mean force is constructed by averaging over pair orientations. Beyond greatly reducing the computational expense, the CG model additionally allows us to consider the importance of multibody orientation correlationsin DJ particles and how their properties are related to isotropically attractive particles.

4.2.1 Pointwise (PW) model

A rigorous model for the interactions of DJ particles is constructed by dressing softly-repulsive isotropic particles with an orientation dependent electrostatic interaction

$$u_{\mathrm{PW}}(r,\omega_i,\omega_j) = u_{\mathrm{repl}}(r) + u_{\mathrm{elec}}(r,\omega_i,\omega_j) \tag{30}$$

where $u_{\mathrm{repl}}(r)$ is an isotropic (dependent only the separation distance of the particle centers r) repulsive interaction and the term $u_{\mathrm{elec}}(r,\omega_i,\omega_j)$ includes the DJ-geometry electrostatic interactions which are dependent upon the orientations ω_i and ω_j of the two particles in each pair. In this model $u_{\mathrm{repl}}(r)$ takes the form of a Lennard-Jones potential that is shifted and truncated at the energy minimum to be purely repulsive and to give an effective diameters of 220 nm; $u_{\mathrm{repl}}(r = 220\,\mathrm{nm}) = 1\,k_{\mathrm{B}}T$.

$$u_{\mathrm{repl}}(r) = \begin{cases} 0 & r \geq 2^{1/6}\sigma_{\mathrm{lj}} + \Delta_r \\ u_{\mathrm{lj}}(r-\Delta_r) - u_{\mathrm{lj}}(2^{1/6}\sigma_{\mathrm{lj}}) & r < 2^{1/6}\sigma_{\mathrm{lj}} + \Delta_r \end{cases} \tag{31}$$

$$u_{\mathrm{lj}}(x) = 4\varepsilon_{\mathrm{lj}}\left[\left(\frac{\sigma_{\mathrm{lj}}}{x}\right)^{12} - \left(\frac{\sigma_{\mathrm{lj}}}{x}\right)^{6}\right]$$

with $\sigma_{\mathrm{lj}} = 50\,\mathrm{nm}$, $\Delta_r = 170\,\mathrm{nm}$, and $\varepsilon_{\mathrm{lj}} = 1\,k_{\mathrm{B}}T$. (We note here that this entire study is performed at $T = 300\,K$.)

Ideally, one would construct an analytic form for $u_{\mathrm{elec}}(r,\omega_i,\omega_j)$ by integrating over the surfaces of the hemispheres of each DJ particle. As these integrals are not analytically tractable for all pair orientations, they are numerically approximated as the Coulomb interactions between n_{p} point charges evenly distributed across the spherical surfaces of each particle in a pair. [138, 62] In this manner, $u_{\mathrm{elec}}(r,\omega_i,\omega_j)$ takes the form

$$\begin{aligned} u_{\mathrm{elec}}(r,\,\omega_i,\omega_j) &= \frac{q^2}{4\pi\varepsilon_0\varepsilon_r}\sum_{i}^{n_{\mathrm{p}}}\sum_{j}^{n_{\mathrm{p}}} s_i s_j\, c\,(|\vec{p}_i - \vec{p}_j|) \\ &= \frac{\sigma^2 d^4 \pi}{4\varepsilon_0\varepsilon_r}\left\langle s_i s_j\, c\,(|\vec{p}_i - \vec{p}_j|)\right\rangle_{i,j} \end{aligned} \tag{32}$$

$$c(x) = \begin{cases} 0 & x \geq r_c \\ \frac{1}{x} - \frac{1}{r_c} & x < r_c \end{cases}$$

with the point charges located at $\{\vec{p}_i\}$ and $\{\vec{p}_j\}$ for the respective particles of a pair. Each point has a charge magnitude of q and a charge sign of $s = \pm 1$ to model fthe positive and negative

hemispheres of a DJ particle. The second line in Equation 32 gives u_{elec} in terms of the particle surface charge density $\sigma = n_{\text{p}} q/\pi d^2$, where the n_{p} point charges are evenly distributed across a sphere of diameter $d = 200\,\text{nm}$. The point charge Coulombic interaction is cutoff at a distance of $r_c = 30\,\text{nm}$ and this leads to a DJ pair potential that vanishes for $r \geq 230\,\text{nm}$. This truncation of the Coulombic potential is only valid in solvent of sufficient ionic strength so as to screen longer ranged electrostatics ($I \approx 0.1\,\text{mM}$ for a Debye length of 30 nm). For simplicity, ionic screening isn't modeled with appropriate point charge potential modifications and the relative dielectric of the medium corresponds to pure water $\varepsilon_r = 80.1$. Therefore this model corresponds to DJ particles in an aqueous solution with low ionic strength. Example pair interaction potentials are shown in panel (a) of Fig. 13.

The structures of DJ colloid clusters have been studied through both experiment and simulation of a similar model with discontinuous potentials by Granick et al. [62] and we use their results in testing this new model. Their model differs from ours in that point charges interact through attractive or repulsive square potentials of a single magnitude and the particle cores are modeled as hard spheres.[62] The authors found cluster structures through simulated annealing and therefore the specific square potential magnitude does not influence cluster structures. Monte Carlo simulated annealing to a temperature of $0\,K$ is used to sample the lowest energy configurations of clusters in the PW model (select structures shown in Figure 14). The pair potential between particles corresponds to a charge density of $\sigma = 2.22 \times 10^3\, e_0/\mu\text{m}^2$, although the length scales of pair interactions are not significantly affected by charge density and therefore these clusters can be taken as characteristic for all non-trivial charge densities. The lowest energy structures for all clusters we investigated — $N \in \{2,3,4,5,7,9,10,12\}$ — are consistent with those reported in reference [62]. It is significant that the lowest energy cluster structures all have a net asymmetric distribution of charge over the surface of the cluster as first reported by Granick et al.,[62] which suggests a tendency for systems of DJ colloids not to form isolated clusters.

4.2.2 Coarse-Grained (GC) isotropic model

The PW model constructed in the previous section is computationally expensive as it requires the calculation of a large number of point charge interactions to determine the potential of a single pair

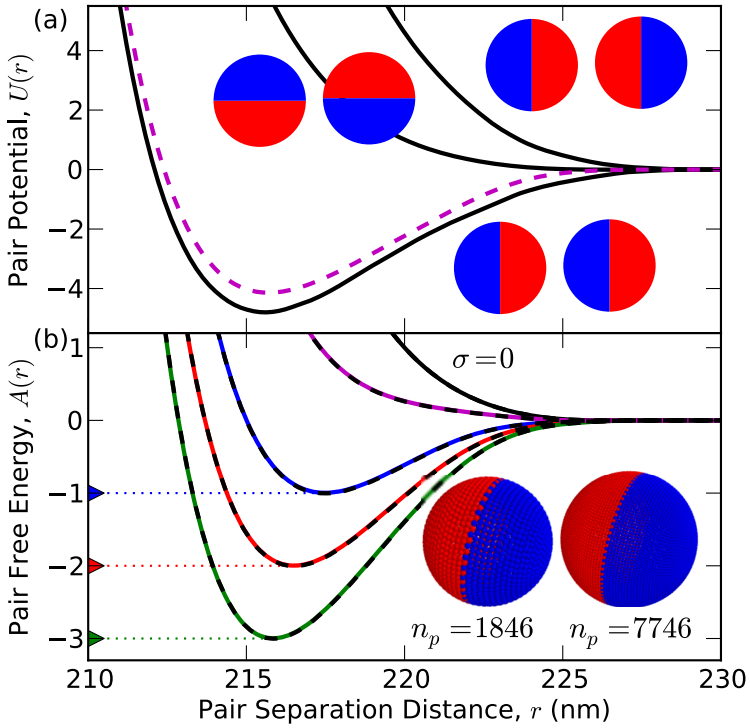

Figure 13: Panel (a): solid lines show examples of the pair interaction potential in the PW model for three pair orientations as indicated by the schematics on the plot. Shown potential corresponds to $A_{\mathrm{p}} = -3kT$ ($\sigma = 2.22 \times 10^3\, e_0/\mu\mathrm{m}^2$) and $n_{\mathrm{p}} = 1846$ point charges. The dashed magenta line shows the mean energy profile as Boltzmann averaged over pair orientations. Panel (b): the potentials of mean force $A(r)$ for a pair of particles in the CG model. Shown profiles have marked minima of $-A_{\mathrm{p}} = 1kT$, (blue) $2kT$, (red) and $3kT$ (green) and correspond to charge densities of $\sigma = 1.93 \times 10^4\, e_0/\mu\mathrm{m}^2$, $2.09 \times 10^4\, e_0/\mu\mathrm{m}^2$, and $2.22 \times 10^4\, e_0/\mu\mathrm{m}^2$ respectively. Additionally, the free energy profile for $\sigma = 1.5 \times 10^4\, e_0/\mu\mathrm{m}^2$ is shown in magenta and the free energy (and also energy) of the uncharged repulsive particles ($\sigma = 0$) is shown as the black line. Solid lines indicate free energy profiles computed with the electrostatic term $u_{\mathrm{elec}}(r, \omega_i, \omega_j)$ approximated by $n_{\mathrm{p}} = 1846$ points charges across each sphere surface and dashed black lines show near identical results with $n_{\mathrm{p}} = 7746$ point charges. Units of the y-axis for both plots are kT (at $T = 300\,K$).

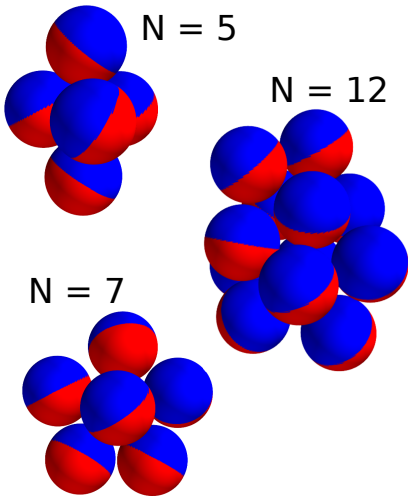

Figure 14: Lowest energy structures for select sized clusters in the PW model as found through Monte Carlo simulated annealing. Observed structures are consistent with those reported in reference [62] by Granick et al.

of DJ particles. Therefore it is of interest to determine how coarse-graining can be used to reduce the computational expense. Specifically, we consider averaging over the orientational degrees of freedom for each pair of DJ particles to construct an isotropic potential of mean force. This CG model additionally allows us to determine how DJ particles are related to comparable isotropically attractive particles and the significance of multibody orientation correlationsin DJ colloids.

To compute the isotropic potential of mean force between a pair of DJ particles, the canonical partition function $Q(r)$ for a pair of particles in one-dimension is constructed. This is accomplished by evenly sampling $n_k = 32,768$ pair orientations for each r separation distance with even distribution assured by enumerating pair orientations through internal coordinates.

$$Q(r) = f \sum_{k}^{n_k} e^{-\beta u\left(r, \omega_{i,k}, \omega_{j,k}\right)} \tag{33}$$

with the sum over the sampled orientations k, $\beta = 1/k_B T$, and normalization constant f.

The potential of mean force, the Helmholtz free energy $A(r)$, is simply found as

$$A(r) = -\beta^{-1} \ln \left\langle e^{-\beta u\left(r, \omega_{i,k}, \omega_{j,k}\right)} \right\rangle_k \tag{34}$$

with the brackets denoting an average over the k orientations and thereby the normalization constant in Equation 33 is set to $f = k^{-1}$ by the condition $A(r \geq 230\,\text{nm}) = 0$.

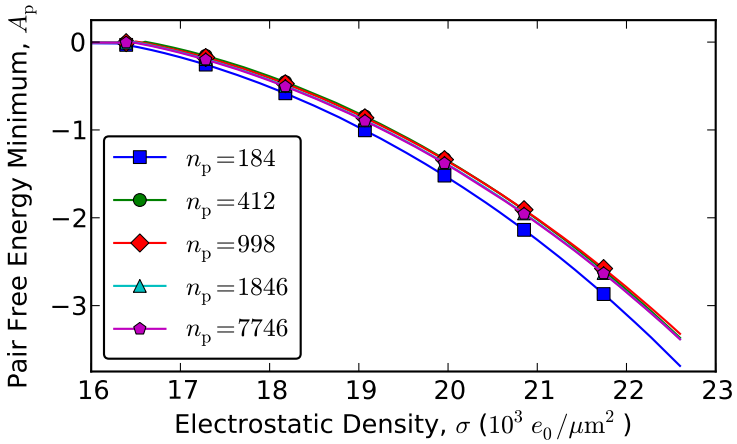

Figure 15: Relationship between the electrostatic charge density across a DJ particle surface σ and the free energy minimum for a pair of DJ particles A_p (in units of kT). The function $A_p(\sigma)$ is computed with different numbers of point charges n_p approximating the charged surface of each DJ colloid in the pair as labeled on the plot. Markers are included at an interval of 10 computed points. The surface area of each DJ particle in this model is $0.15\,\mu m^2$ such that number of elemental charges e_0 on each particle is roughly an order of magnitude less than σ.

Illustrative pair free energy profiles $A(r)$ are shown in panel (b) of Figure 13. The free energy minimum A_p of each profile is taken as characteristic of the pair affinity at a specific particle surface electrostatic density σ. The relationship between σ and A_p is depicted in Figure 15 for several surface discretization resolutions. As the profiles $A(r)$ and the relation $A_p(\sigma)$ are found to be independent of the number of points charges for $n_p \gtrsim 1000$, $n_p = 1846$ is used in simulation of the PW model.

4.3 Numerical methods

4.3.1 Simulation

The pairwise and continuous PW model for particle interactions developed in Sec. 4.2.1 has been implemented with an integrator for particle dynamics so as to obtain the equilibrium structure of these systems. A periodic cubic box (cf. Figure 16) is filled with $N = 1000$ DJ particles at varying densities (by way of changing the box length). In these simulations, the forces and torques on each colloidal particle are calculated using the analytic gradients of the pair potential $u(r, \omega_i, \omega_j)$ in Eq. 30. Terms accounting for dissipative solvent and hydrodynamic interactions are not included. The effect of a dissipative solvent is not included in this current study so that the effects of the

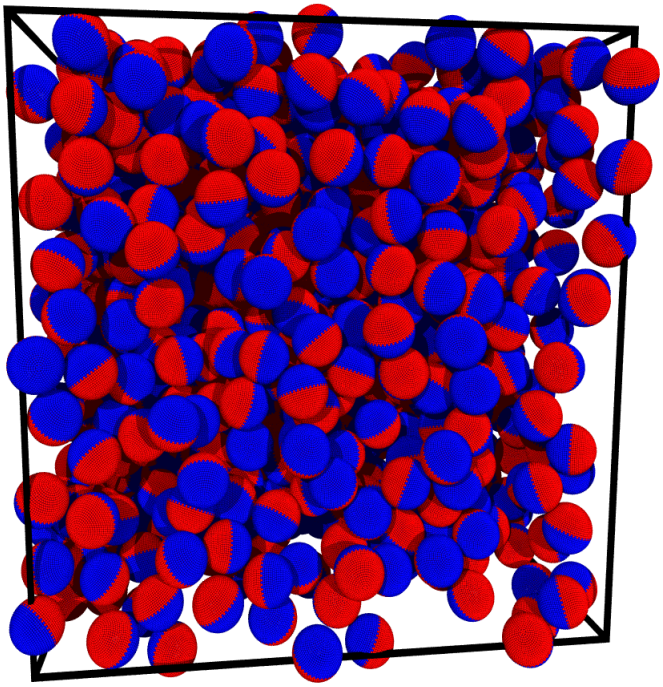

Figure 16: Snapshot of a simulated PW system for $\phi = 0.4$, $\sigma = 2.22 \times 10^3\, e_0/\mu\text{m}^2$ ($A_\text{p} = -3\,kT$). The 1000 colloid particles were each rendered as $n_\text{p} = 1846$ points across the surface of each sphere, although they appear near perfectly smooth at this scale.

DJ interaction on static and dynamic properties can be isolated. Additionally, such simple vacuum models have played a key role in understanding features of colloid dynamics such as attractive melting. [99]

In addition to varying the charge density, three colloid volume fractions $\phi \in \{0.1, 0.2, 0.4\}$ are investigated. The volume fraction $\phi = \pi N l^3/6V$ is calculated according to the volume occupied by N hard spheres with a specified diameter l in a simulation box of volume V. The diameter of the DJ particles is fixed at $l = 220\,\text{nm}$ ignoring the possible change in the effective diameter due to charge. In order to specify timescales in the particle dynamics integrator, the particle mass must also be specified. Each colloid is assigned a mass $M = 4.2 \times 10^{-24}\,\text{kg}$ corresponding to a sphere of diameter 200 nm with the density of water.

Equilibrium quantities are obtained through an average over a trajectory after equilibration. Starting from a random initial configuration of $N = 1000$ non-overlapping hard spheres, a Nose-Hover thermostat is used to thermally equilibrate each simulated PW system at $T = 300\,K$ for up to

4 ms with an integration time step of $\Delta t = 1$ ns. After the total energy of the system is found to be stable (less than %1 change in total energy over the course of 1 ms), the thermostat is removed and a 5 ms NVE trajectory is simulated for the sampling of static and dynamic properties. Although any dynamical artifacts of the thermostat are not integral to the current work, their exclusion ensures that dynamical correlations (and relaxations) can be correctly studied as will be pursued in future work.

All simulations are performed using the molecular dynamics package LAMMPS, specifically the integration algorithms "fix nvt/asphere" and "fix nve/asphere". [100] Particle were represented by a center of mass location and orientation quaternion as dynamically propagated by the LAMMPS integration algorithms. The electrostatic component of the force field for the PW model is implemented as a new pair potential module that calculates forces and torques from the analytic gradients of Equation 32. This module can support arbitrary arrangements of point charges to model $u_{\text{elec}}(r, \omega_i, \omega_j)$. It therefore accommodates more structured coverings which would be of use in simulating patchy particles in future work.

Simple rotational and translational transformations are used to calculate the $\{\vec{p}_i\}$ and $\{\vec{p}_j\}$ point charge location sets associated with each particle in a pair. As a significant optimization, this transformation code can cheaply determine $\vec{p}_i$'s that are sufficiently far away from the other particle's center of mass so as to not interact with any $\vec{p}_j$'s of the other particle. Such points are excluded from the calculated set of points that enter into Equation 32 for the calculation of the PW potential and gradients. In practice this reduces the number of point charge pair interactions by a factor of between 100 to 300 and provides a substantial speed up in force field calculations. As an example, for a pair of DJ particle separated by a distance of $r = 216$ nm with $n_{\text{p}} = 1846$ base point charges, each calculated point charge set is reduced in size to around $n_{\text{p}}^* \approx 130$ and thereby the number of point charge pair terms is reduced from $n_{\text{p}}^2 \approx 3.4 \times 10^6$ to just $n_{\text{p}}^{*2} \approx 1.7 \times 10^4$. In contrast, this optimization could not efficiently be used in a GPU-based PW force field that was also developed and as a result the GPU code was slower. We also note that a spherical harmonics expansion of $u_{\text{elec}}(r, \omega_i, \omega_j)$ (as detailed in reference [50]) required too many terms to offer any computational savings.

Comparable simulations are performed for the CG model. The gradients of the non-analytic

$A(r)$ functions are computed by numerical differentiation using spline fitting from which linear interpolation tables are generated. No numerical stability problems are observed with the Hamiltonians constructed in this fashion; the NVE simulations conserve energy with numerical errors less than 0.02% over the course of each NVE trajectory. While this isotropic interaction does not provide torques, the same rotating particle integration algorithms are used for consistency. Stronger interacting systems ($\sigma > 19\, e_0/\mu\text{m}^2$) in the CG model require longer equilibration times of up to 500 milliseconds. A contrast of equilibration in the PW model versus the CG model for these stronger interacting systems is briefly studied in Section 4.4.5.

For each (ϕ, σ) value in each of the two models, one-hundred different simulations are performed starting from different random configurations. After equilibration each trajectory contributes $20,000$ configurations sampled once every 250 nanoseconds (250 integration steps) to yield an averaged value of a given observable. This effectively provides one-hundred different observations from which we then obtain an average. Additionally, the uncertainty in a given quantity is calculated from the standard deviation of the observable. As a check of the equilibration procedure, the kinetic energy distribution of the NVE trajectories is computed for the ensemble of sampled configurations for each (ϕ, σ) value in each model. Excellent agreement with the Maxwell-Boltzmann distribution is observed with the mean temperature being within $\langle T \rangle = 300 \pm 2\, K$ for each (ϕ, σ) value in each model.

The possibility that finite size effects affect the equilibrium observables is investigated using simulations of $N = 4,000$ particles. The most challenging scenario occurs for the strongest studied pair interaction strength $A_\text{p} = -3\, k_\text{B} T$ at each of the three volume fractions in both the PW and CG models. Ten trajectories have been simulated for each system. Although not shown, the equilibrium potential energy and isotropic pair correlation functions $h(r)$ were computed and found to be near identical to those for the $N = 1,000$ particle systems. We thus conclude that $N = 1,000$, as used through this study, is sufficient to obtain convergence without significant finite size effects.

4.3.2 Free energy computations

It is of interest to study the influences of DJ interactions on the thermodynamic state functions — chiefly the free energy — in colloids. This is essential for the study of phase behavior and material

properties over a range of conditions. The regions of ϕ, T space where the PW and CG models agree is of particular interest because DJ colloids can be expected to behave as isotropically attractive colloids under such conditions. Deviations of the PW model from the CG model — as could arise from multibody orientation correlations— would correspond to new phase behavior arising from the DJ interaction.

The computation of free energy is not as straightforward as other quantities as it requires knowledge of the partition functions Q_1 and Q_2 to determine the free energy difference $\Delta A_{1,2}$ between the systems 1 and 2.

$$\Delta A_{2,1} = A_2 - A_1 = -\beta \ln \frac{Q_2}{Q_1} \tag{35}$$

In the present case, we are interested in the free energy difference between two DJ particle systems that differ only in charge density σ (both systems are of the same particle model and the same volume fraction)

$$\Delta A_{\sigma_2,\sigma_1} = A_{\sigma_2} - A_{\sigma_1} = -\beta \ln \frac{Q_{\sigma_2}}{Q_{\sigma_1}} \tag{36}$$

where Q_{σ_x} is the canonical partition function for the particle system with charge density σ_x.

Directly computing Q_{σ_x} for each simulated system is an inefficient means of computing free energy differences. Of the various methods that have been developed for computing Q_2/Q_1 in simulation, the Bennett Acceptance Ratio[5] method (BAR) is selected as this method has been shown to provide the most computationally efficient means of estimating the free energy difference between two simulated systems.[116] BAR is based around the relation

$$e^{-\beta(\Delta A_{2,1}-C)} = \frac{\langle f[\beta(U_2 - U_1 - C)]\rangle_1}{\langle f[\beta(U_1 - U_2 + C)]\rangle_2} \tag{37}$$

where U_1 and U_2 denote the potential energy of a configuration $\mathbf{q}$ calculated with the potential functions $U_1(\mathbf{q})$ and $U_2(\mathbf{q})$ of systems 1 and 2 respectively and where $f(x)$ is the Fermi-Dirac function $f(x) = (1+e^x)^{-1}$. The average in the numerator is taken over the set of configurations sampled in the simulation of system 1 with the potential $U_1(\mathbf{q})$ and the denominator average is likewise performed for simulated configurations with potential $U_2(\mathbf{q})$. Bennett proved this relationship holds for all values of C and it is therefore straightforward to numerically solve for the value of C which makes the ratio in equation 37 equal to 1 and thereby $C = \Delta A_{2,1}$. [5]

It is essential that the two systems compared in Equation 37 have significant configuration overlap for an accurate estimate of $\Delta A_{2,1}$. This implies that $U_1(\mathbf{q})$ and $U_2(\mathbf{q})$ cannot differ greatly and in our application of BAR we find this necessitates the comparison of systems with only a small change in σ. By sampling configurations at many different values of σ, the free energy difference of adjacent systems $\Delta A_{\sigma_i,\sigma_{i-1}}$ is computed through BAR. Thereby the free energy of of any system relative to the reference repulsive particle system ($\sigma = 0$) at the same volume fraction is calculated as the sum of free energy differences between adjacent systems.

$$\Delta A_{\sigma^*} = A_{\sigma=\sigma^*} - A_{\sigma=0} = \sum_{i}^{\sigma_i=\sigma^*} \Delta A_{\sigma_i,\sigma_{i-1}} \tag{38}$$

Additional NVT simulations are used to generate the large sets of configurations needed for each of the many values of σ at each volume fraction and in each of the two models. These NVT simulations are initialized and equilibrated by the same procedure described earlier and then configurations are sampled every 500 nanoseconds for a total of 10000 configuration per a trajectory. For each (ϕ,σ) value in each model, 5 such NVT trajectory are collected starting from different random initial configurations to account for possible artifacts of the deterministic Nose-Hover thermostat. An estimate of uncertainty in $\Delta A_{\sigma_i,\sigma_{i-1}}$ is computed using the method presented in reference [116] and in all cases the uncertainty was less than 0.1%.

4.4 Results

4.4.1 Isotropic pair density correlations

To understand how DJ interactions affect the reversible structure of colloid systems, the static properties of equilibrated configurations have been obtained. We begin by computing the isotropic density correlation function

$$h(r) = g(r) - 1 \tag{39}$$

where $g(r) = \phi(r)/\phi$ is the reduced density function. The computation of pair-separation-distance histograms with bin sizes of $\Delta r = 1\,\text{nm}$ is used to construct $\phi(r)$. Although not shown, the first peak is the predominant feature of $h(r)$; it is found to occur near $r \approx 215\,\text{nm}$ in all cases. As should be expected, the strength of this peak increases with increasing volume fraction ϕ and increasing charge density σ. Perhaps surprisingly, the CG model is found to reproduce the results of the PW model.

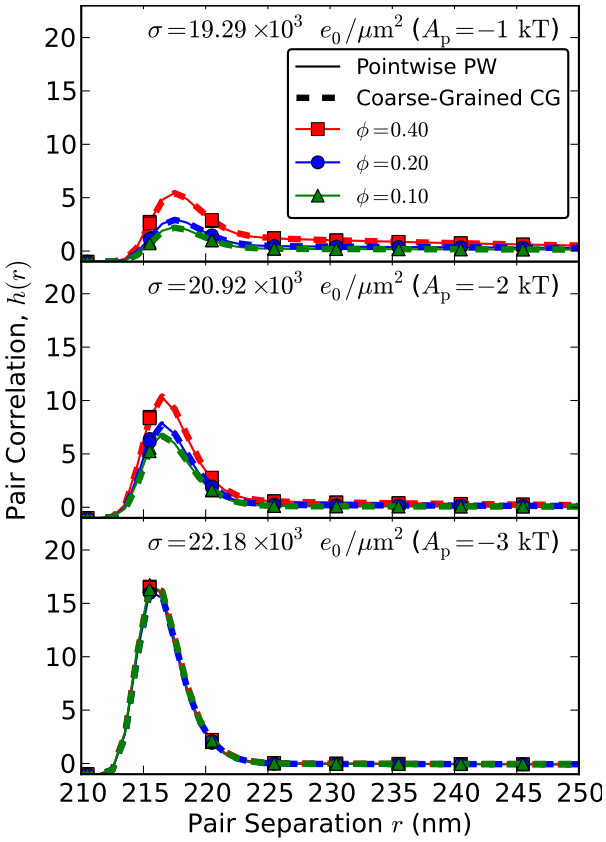

Figure 17: Static isotropic pair correlations functions $h(r)$ computed for simulations of both DJ models: the PW model results are shown as solid lines and the CG results as dashed lines. Figures focus on the first peak in $h(r)$. Each panel is obtained for different charge densities σ (and corresponding pair affinity A_p) as listed above. In each panel, the curves correspond to different volume fractions ϕ with values 0.10, 0.20 and 0.40 corresponding to green triangles, blue circles and red squares, respectively. The data markers are used only to indicate the curves which connect the generated points obtained at intervals of 1 nm. Uncertainty in results are comparable to the plotting line width.

This suggests that multibody orientation correlationsdo not strongly affect the static translational microstructure of DJ colloids with pair affinities as strong as $A_\text{p} = -3\,k_\text{B}T$ at the studied densities.

The Fourier transform of the pair correlation function $\hat{h}(k)$ provides another vantage point from which to analyze the reversible microstructures by considering their periodicity at different length scales. The dimensionless $\hat{h}(k)$ is

$$\hat{h}(\vec{k}) = \rho \int \exp\left(-i\vec{k}\cdot\vec{r}\right) h(\vec{r})\, \mathrm{d}\vec{r} \tag{40}$$

$$\hat{h}(k) = \frac{4\pi\rho}{k} \int \sin(kr)\, h(r)\, r\, \mathrm{d}r \tag{41}$$

where ρ is the number density $\rho = N/V$. The static structure factor is simply related by $S(k) =$

$1+\hat{h}(k)$.

In computing $\hat{h}(k)$ from $h(r)$, it is common to extend the range of $h(r)$ using the Ornstein-Zernike relationship with iterative numerical methods to accurately compute $\hat{h}(k)$ for small values of k. [127] In many situations these computations are found to diverge for the sampled $h(r)$ functions as can be explained by the lack of long range forces and the severe peak in some $h(r)$ functions. Therefore $\hat{h}(k)$ can only be computed down to a minimum value $k_{\min} = 2\pi/r_{\text{box}}$ as limited by the lateral dimension of the simulation box r_{box}.

In Figure 18, the computed $\hat{h}(k)$ functions are compared for DJ systems with varied charge densities at each investigated volume fraction. As with $h(r)$, the CG model reproduces the periodic structures in $\hat{h}(k)$ for the investigated DJ systems. The consistent shifting of short range structure, $kl \gtrsim \pi$, to shorter wavelengths with increasing charge density is explained by the corresponding decrease in the range of the repulsive components of the potential of DJ particles in this model; i.e. a decrease in the effective particle diameter. Additionally, the long wavelength structure, $kl \lesssim \pi$, is found to be qualitatively changed by the strength of by the attractive components of the pair potential for lower volume fractions. These observations are consistent with the WCA liquid theory of simple fluids that predicts such universal periodic structure properties as due solely to harshly repulsive components of the pair potential.[132]

4.4.2 Anisotropic pair density correlations

Due to spherical asymmetry, the reduction of the structure to $h(r)$ is perhaps too severe, and it is useful to consider the generalized pair correlation function $h(\vec{r})$. We use the Janus particle frame with the z-axis as the axial direction between Janus hemispheres and its center at the origin. In this frame the system retains azimuthal symmetry, and hence we average over the angle about this axis to obtain a pair correlation function $h(r_{\text{e}}, r_{\text{a}})$ where the vectors r_{a} and r_{e} denote the position along the axial and equatorial directions in this plane. We need only consider a single quadrant as displayed in Figure 19 because of the symmetry of pairwise quantities within this frame.

The density of particles at different orientations about each particle in the PW model is analyzed by constructing the static pair density correlation function $h(r_{\text{e}}, r_{\text{a}})$. Similar to the computation of $h(r)$, this function is also computed through the construction of a histogram of pair separation

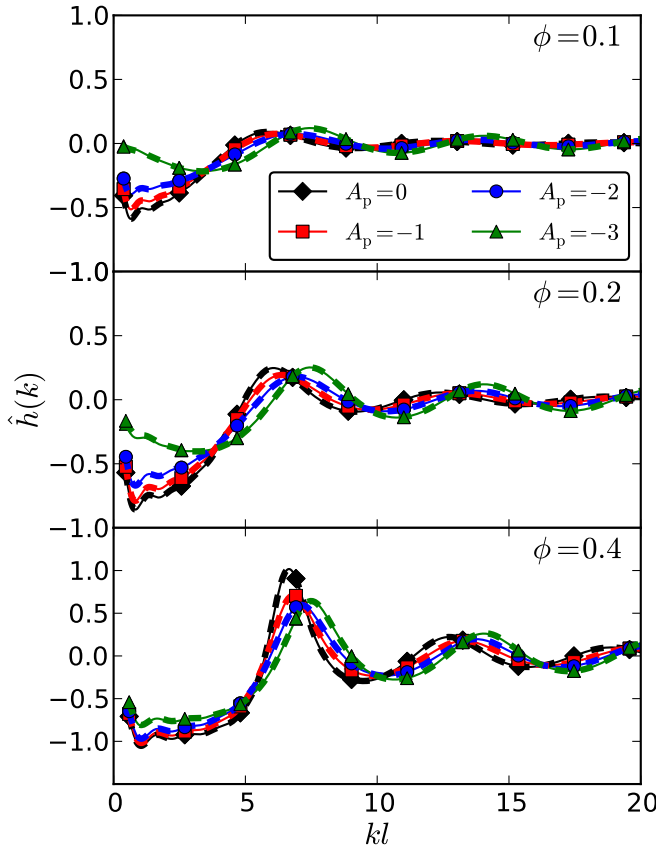

Figure 18: Fourier transform of the pair correlation function $\hat{h}(k)$ of DJ systems plotted with wave number k scaled by the diameter of the bare repulsive particles $l = 220\,\text{nm}$. Each panel is obtained for different volume fractions ϕ as listed above. The curves correspond to different charge densities σ (and corresponding pair affinity, A_p) with values $A_p = 0\,k_B T$ ($\sigma = 0\,e_0/\mu\text{m}^2$), $A_p = -1\,k_B T$ ($\sigma = 19.29\,e_0/\mu\text{m}^2$), $A_p = -2\,k_B T$ ($\sigma = 20.92\,e_0/\mu\text{m}^2$), and $A_p = -3\,k_B T$ ($\sigma = 22.18\,e_0/\mu\text{m}^2$) corresponding to black diamonds, red squares, blue circles, and green triangles respectively. The data markers are used only to indicate the curves which connect the generated points obtained at intervals of $0.04kl$. PW results are shown in solid lines and the CG results in dashed lines, although there is near perfect agreement between the two curves in all cases. Uncertainty in results are comparable to plotting line width.

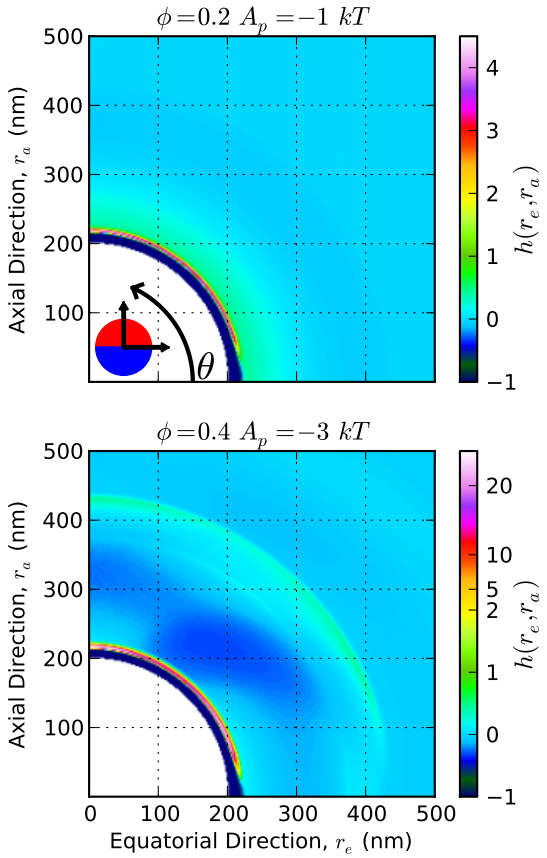

Figure 19: Static density correlations $h(r_{\rm e}, r_{\rm a})$ within the Janus particle frame for two representative PW systems as labeled on each plot. Within this frame the axial direction $r_{\rm a}$ measures distances along a direction spanning the hemisphere tips and the equatorial direction $r_{\rm e}$ goes through the intersection of the hemispheres. The two plots have the same color-scale for the range $[-1:2]$. This color-scale continues for the $\phi = 0.2$, $A_{\rm p} = -1\,k_{\rm B}T$ plot, whereas for the $\phi = 0.4$, $A_{\rm p} = -3\,k_{\rm B}T$ plot a different scale is used for $(2:25]$.

distances at different orientations using square bins of size 2 nm x 2 nm. Figure 19 displays $h(r_{\rm e}, r_{\rm a})$ at two representative (ϕ, σ) values in the PW model. In both plots the first neighbor shell is clearly seen as a thin band near $r \approx 215$ nm. A depletion zone near the particle equator — where the hemispheres are joined — is observed in this shell for both systems. Additionally, for $\phi = 0.4$, $A_{\rm p} = -3\,kT$ a second depletion zone is also observed at approximately 60° from the $r_{\rm a}$ axis. This denser and more strongly interacting system also shows a less pronounced and broader second neighbor shell near $r \approx 430$ nm and a corresponding broad depletion band between shells at around $r \approx 330$ nm. These features also vary with angle θ.

To further study the ordering in the first neighbor shell, integrated angular cross sections $h(\theta)$ of

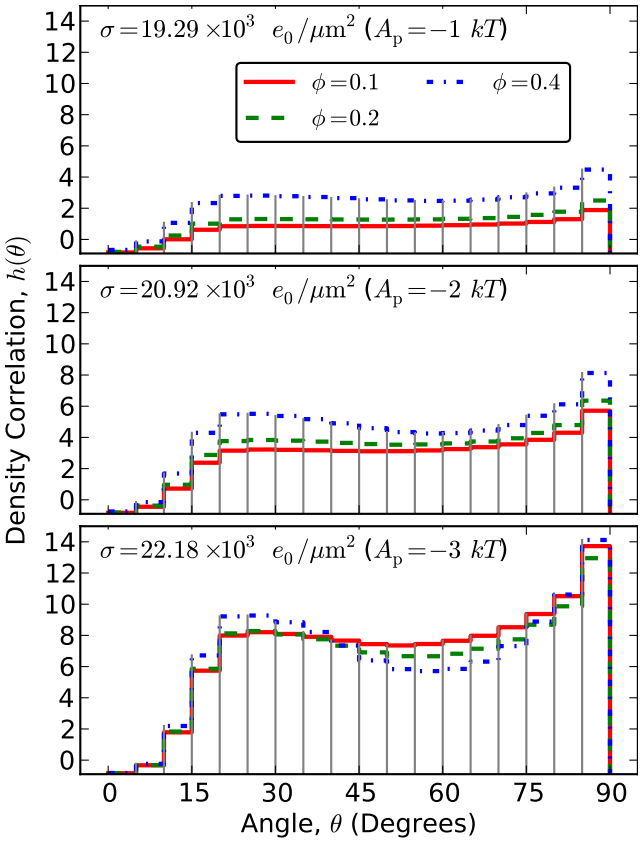

Figure 20: Angular cross sections of the static density correlations as calculated within the Janus particle frame for PW systems. The angle $\theta = \arctan(r_a/r_e)$ is defined relative to the equatorial direction with 90 degree being at a hemisphere tip. Each angular cross section shows the average pair correlation within the distances $210\,\text{nm} \leq \sqrt{r_e^2 + r_a^2} \leq 222\,\text{nm}$ as averaged in bins of size $\Delta\theta = 5^\circ$. Each panel is for a different charge density σ across the colloid surface and results are shown for the three different volumes ϕ as denoted by line color and style. Uncertainty in results are comparable to the plotting line width.

$h(r_e, r_a)$ with $\theta = \arctan(r_a/r_e)$ are obtained by averaging over the the radii within this shell, namely for $r = \sqrt{r_e^2 + r_a^2}$ such that $210\,\text{nm} < r < 222\,\text{nm}$. Results are shown in Fig. 20 and it is clearly seen that all investigated structures exhibit a depletion zone near the equator of the hemispheres ($\theta = 0$). At lower volume fractions and weaker charge densities (e.g. $\phi = 0.1$, $\sigma = 1.93 \times 10^4\, e_0/\mu m^2$, $A_p = -1.0\, k_B T$) the depletion zone gradually gives rise to a roughly stable plateau by $\theta \approx 20^\circ$. With stronger charge densities and/or higher volume fractions, this plateau is replaced by two smooth peaks joined by a depletion zone near $\theta \approx 60^\circ$. In all cases this second depletion zone becomes more predominant with an increase in density.

This ordering in neighbor shells is not just the result of the pair potential, but also strongly

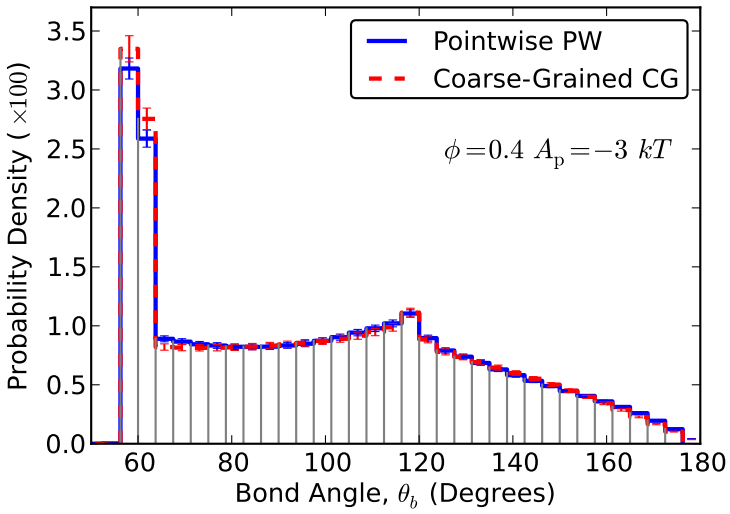

Figure 21: Distribution of angles between particles bonded to a common central particle, where a bond is defined by $r \leq 230\,\text{nm}$. Results are shown for the PW model (solid line) and the CG model (dashed line) for $\phi = 0.4$, $A_p = -3\,k_B T$ ($\sigma = 2.22 \times 10^3\, e_0/\mu\text{m}^2$). Histograms have bin sizes of $\Delta\theta = 3.75^\circ$ and error bars are shown.

influenced by packing constraints. Therefore the neighbor shell structures in both the PW and CG models are compared to determine the effect of packing constraints. To quantify order in the first neighbor shell, the distribution of bond angles between particles bonded to a single common particle are computed, where a bonded pair is defined by $r \leq 230\,\text{nm}$. Figure 21 shows the distribution of bond angles for both the PW and CG models at $\phi = 0.4$ and $A_p = -3\,k_B T$; the parameters for the strongest observed ordering. These distributions agree within the uncertainty of the computation. They both show a strong peak near $\theta_b \approx 60^\circ$ and a smaller peak near $\theta_b \approx 120^\circ$. Distributions for other (ϕ, A_p) values are also highly similar in both models and are not shown. This simple metric describing first shell ordering suggests that the structure of the neighbor shell is identical in both the PW and CG models for the range of investigated parameters. This implies that the anisotropic density correlations found in $h(r_e, r_a)$ are due solely to a biasing in how each DJ particle orients itself within its neighbor shell.

4.4.3 Pair orientation correlations

An investigation of the correlation in orientation between pairs of DJ particles can reveal whether there is additional structure in these systems not seen in the pair density correlations. Particle orientation is identified through the orientation vector $\vec{d}$ that spans from the center of each particle to the top of the red hemisphere (along the axial direction defined in Section 4.4.1). The correlation of the orientations of two particles, $\vec{d}_1$ and $\vec{d}_2$, are averaged for particles at different positions (r_e, r_a) relative to the Janus frame of particle 1. We need only consider a single quadrant as discussed before and also displayed in Figure 22 because of the symmetry of pairwise quantities within the Janus frame. As in $h(r_e, r_a)$, the pair orientation correlation function $\langle \vec{d}_1 \cdot \vec{d}_2(r_e, r_a) \rangle$ has been obtained using histograms with bin sizes of 2 nm x 2 nm.

The orientation correlations for two representative DJ systems are shown in Figure 22. Significant orientation correlations are only observed within the first neighbor shell for the lower volume fraction system with weaker interactions ($\phi = 0.2, A_p = -1\, k_B T$). In contrast, significant orientation correlations are observed within the second neighbor shell for $\phi = 0.4, A_p = -3\, k_B T$. The associated band at the third neighbor shell exhibits weak and diffuse correlations. The length scales of these orientation correlations significantly exceeds the length scales of the density correlations, which are found to be quite weak at the second shell. Further, both the first and second shell orientation correlations are found to be angularly dependent, with stronger correlations observed near the tips of a DJ particle than near the equator.

It also worth noting the weak, but not negligible, anti-correlation observed near the tip of a DJ particle for $230\,\text{nm} \lesssim r \lesssim 255\,\text{nm}$ in the $\phi = 0.4$, $A_p = -3\, k_B T$ system. This unexpected anti-correlation occurs outside of the range of pair interactions and therefore isn't correlated with any pair energetics; such anti-correlation near the tips would be energetically unfavorable within the pair interaction range. It is therefore reasonable to attribute this orientational anti-correlation to multibody interactions as due the effect of a third particle on the correlation of a pair. While this weak anti-correlation of orientations isn't associated with any significant density correlation, it does signify weak multibody orientation correlationsbetween DJ particles.

As with density correlations, the structures of the first shell orientation correlations are further

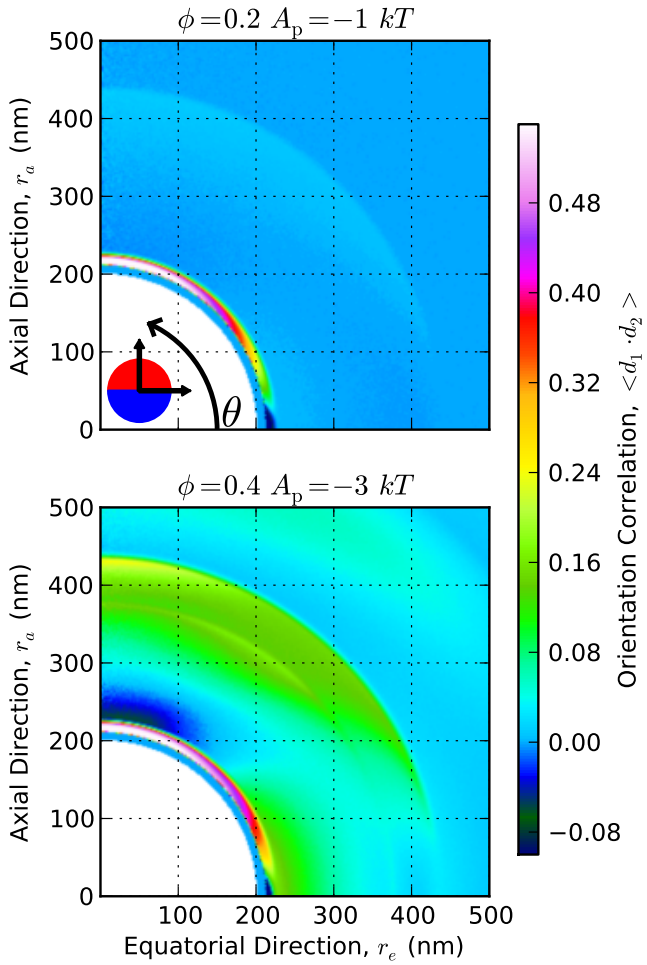

Figure 22: Correlation of the orientations of the director vectors d_1 and d_2 for pairs of DJ particles within the Janus frame for two PW systems.

analyzed by calculating angular cross sections (Figure 23). It is first observed that a weak anti-correlation at $\theta \approx 0$ is found for all system except $\phi = 0.4$, $A_p = -3k_BT$. This anti-correlation correspond to pairs with unlike hemispheres in close proximity as is energetically more favorable than correlated orientations at the equator of a DJ particle. These same systems also exhibit comparable monotonic increases in orientation correlations from the equator until near the tip ($\theta \approx 80^\circ$). It is found that the $\phi = 0.4$ curve becomes increasingly removed from the other two curves as the charge density is increased. With the highest charge density, consistent with $A_p = -3k_BT$, the $\phi = 0.4$ curve shows the largest disparity with other curves. This may suggest a minor reorganization in how a DJ particle orients itself within its first neighbor shell as to facilitate weak multibody

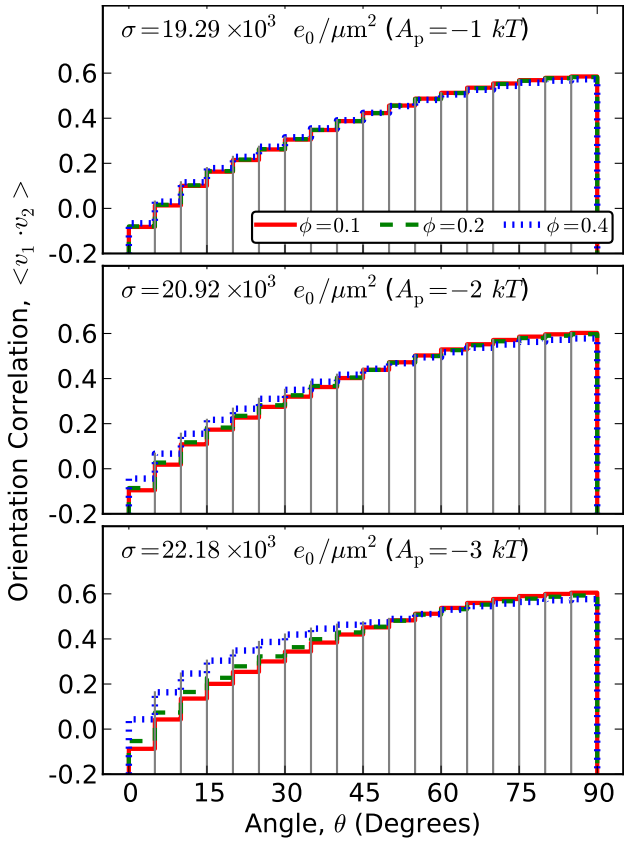

Figure 23: Angular cross sections of the static pair orientation correlations as calculated within the Janus particle frame for PW systems. The angle θ is defined relative to the equatorial direction with 90 degree being at a hemisphere tip. Each angular cross section shows the average pair orientation correlation within the distances $210\,\text{nm} \leq \sqrt{r_e^2 + r_a^2} \leq 222\,\text{nm}$ as averaged in bins of size $\Delta\theta = 5^\circ$. Each panel is for a different charge density σ across the colloid surface and shows results for the three different volume fractions ϕ denoted by color and line style. Uncertainty in results are comparable to the plotting line width.

orientation correlations.

4.4.4 Thermodynamics

The free energies calculated by methods detailed in Section 4.3.2 are shown in Figure 24. It is found that there is near perfect agreement between the free energies calculated in the PW and CG models. There are only minor systematic deviations of the CG model from the PW model on the order of 1% as seen in the plotting of $\Delta A_{CG} - \Delta A_{PW}$. These results demonstrate that multibody orientation correlationsare insignificant in determining the static state for the range of DJ interaction strengths and densities investigated in this study.

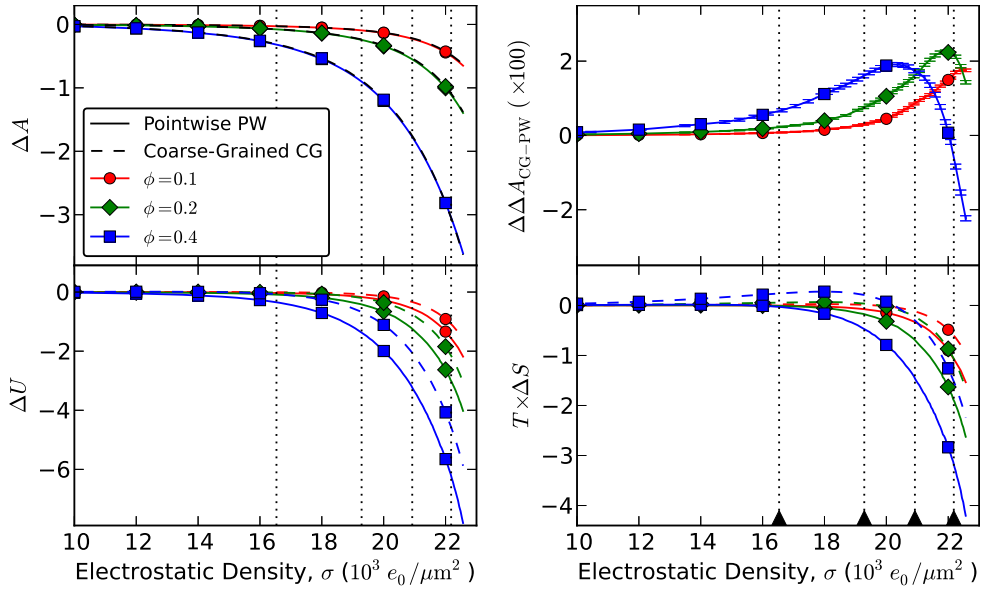

Figure 24: Thermodynamic state functions of DJ systems for the PW model (solid lines) and CG model (dashed lines). All state functions are in units of kT/particle at $T = 300\,K$ and calculated relative to the uncharged repulsive particle system ($\sigma = 0$) for each volume fraction. Each panel shows a different state function: free energy ΔA, model free energy differences $\Delta\Delta A_{\mathrm{CG-PW}} = \Delta A_{\mathrm{CG}} - \Delta A_{\mathrm{PW}}$, internal energy ΔU, and entropy $T \times \Delta S$. Results for the three investigated volume fractions are denoted by different color curves and plotting marker symbol as labeled on the figure. Markers are only included every $\Delta\sigma = 2\,e_0/\mu\mathrm{m}^2$ to denote curves which are computed at increments of $\Delta\sigma = 0.1\,e_0/\mu\mathrm{m}^2$. In the ΔA panel the CG model curves are plotted in black to better show their near perfect overlap on top of the PW curves. Uncertainties are negligible (less than 0.1%) and therefore error bars are only shown in the $\Delta\Delta A_{\mathrm{CG-PW}}$ plot where the y-axis is enhanced by a factor of 100. Four vertical dotted lines denote the charge densities corresponding to the following pair affinities in order left-to-right: $A_{\mathrm{p}} = -0.01\,k_{\mathrm{B}}T$, $A_{\mathrm{p}} = -1\,k_{\mathrm{B}}T$, $A_{\mathrm{p}} = -2\,k_{\mathrm{B}}T$, and $A_{\mathrm{p}} = -3\,k_{\mathrm{B}}T$.

Decomposing each system free energy into a potential and an entropic part allows us to examine the effect of orientational correlations at the pair vs. system level (Figure 24). For weak interactions, $\sigma \lesssim 2.1 \times 10^3\,e_0/\mu\mathrm{m}^2$ ($A_{\mathrm{p}} \gtrsim -1\,k_{\mathrm{B}}T$), the CG model shows an increase in entropy with increasing charge density as can be attributed to a net decrease in particle size and increased free volume. In contrast, the PW model always shows a decrease in entropy with higher charge densities, although this is offset by a larger decrease in internal energy. In this perspective orientational averaging can be seen as determining the balance between the entropic loss and energetic gain of orientational correlations at a pairwise level. This method — consistent with the assumption that orientational correlations can be pairwise averaged — appears sufficiently accurate within the scope of the current study.

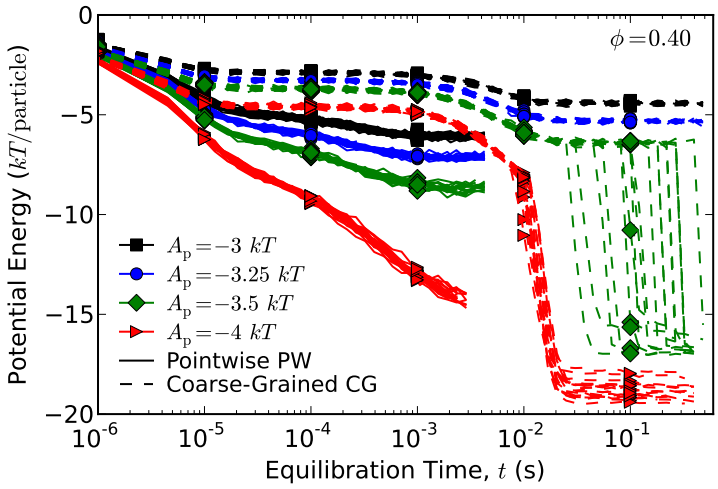

Figure 25: The progression of equilibration – quantified by potential energy – is shown for 20 trajectories for each of the select systems. Results for the PW model are shown with solid lines and the corresponding systems in the CG model are plotted with dashed lines. Line color and plotting marker are used to denote different surface charge densities: $\sigma = 22.18\, e_0/\mu\text{m}^2$, $A_\text{p} = -3\, k_\text{B}T$ black squares; $\sigma = 22.46\, e_0/\mu\text{m}^2$, $A_\text{p} = -3.25\, k_\text{B}T$ blue circles; $\sigma = 22.73\, e_0/\mu\text{m}^2$, $A_\text{p} = -3.5\, k_\text{B}T$ green diamonds; $\sigma = 23.23\, e_0/\mu\text{m}^2$, $A_\text{p} = -4\, k_\text{B}T$ red triangles. Among the shown systems, only the $A_\text{p} = -3\, k_\text{B}T$ and $A_\text{p} = -3.25\, k_\text{B}T$ systems are considered to have reached equilibrium.

4.4.5 Nonequilibrium relaxation of stronger interactions

Simulation of stronger interacting DJ system (higher σ's) were attempted, but were not found to equilibrate. While this prevents the computation of static properties through simulation, some properties of these stronger interacting system can be inferred by studying their equilibration trajectories; i.e. their nonequilibrium relaxation from an initial hard sphere configuration. The progression of equilibration — as quantified by excess internal energy — is shown in Figure 25. Results for the $A_\text{p} = -3\, k_\text{B}T$ and $A_\text{p} = -3.25\, k_\text{B}T$ systems are included for comparison as these systems did equilibrate in both models. The role of frustration in the equilibration of stronger interacting systems is immediately obvious for the PW systems, although the final CG systems are also unstable with respect to internal energy even after long equilibration runs. Additionally, the wide spread of internal energies for the CG model at the end of relaxation also signifies dynamical arrest. It is found the strongest interacting systems have substantially larger drops in internal energy. This is quite evident for the CG model of the $A_\text{p} = -3.5\, k_\text{B}T$ and $A_\text{p} = -4\, k_\text{B}T$ systems where sudden and drastic drops are observed. This is taken as a sign of a liquid-to-solid transition as would be associated with the

discontinuity in the equilibrium internal energy as a function of charge density.

A sudden drop in internal energy during equilibration is not observed in any of the PW systems. Nonetheless, these non-equilibrating PW systems also show large decreases in internal energy relative to the equilibrating ones. A similar discontinuity in internal energy with respect to interaction strength is also apparent for the PW model. The trajectories are insufficiently long to determine if the simulations will pass through regions of dynamical arrest with a large spread in energies between trajectories as observed in the CG model. The more gradual and continuous progression toward equilibrium in the PW model versus the CG model is interesting and may suggest different mechanisms of dynamical reorganization in quenching DJ colloids as compared to isotropically attractive colloids.

In previous work on DJ particles with strong dipole characteristics [48, 83] and simple polar fluids, [24, 133] significant chain formation has been reported. However, the DJ systems simulated in the present work do not exhibit much chain formation because they appear to favor the formation of complex aggregates. This can be quantified through a reversible aggregation graph for individual particle configurations along the equilibration trajectories. This graph is defined through nodes and edges representing particles and reversible bonds between them, respectively. Particles are connected through a bond when their separation distance r is less than 230 nm. Each isolated component of this graph represents an isolated reversible cluster with a well-defined size and topology.

We therefore characterize the significance of chain topology by determining the fraction of particles in each simulated configuration that are involved in chain-like aggregates. We use a weak definition for chains by allowing aggregates that include at most one cross-link — that is, when the corresponding node contains more than 2 edges — and only consider graph components with at least 10 nodes. Figure 26 shows the fraction of particles in these so-called chain-like aggregates throughout the nonequilibrium simulations. The chain fraction is less than 1% on average and is found not to depend on the extent of equilibration. In the $\phi = 0.4$ simulations, no chain-like aggregates are ever seen.

Indeed, the aggregation appears to proceed towards the formation of large clusters instead of forming chains. This can be seen in Figure 27 wherein the size of the largest cluster is shown as a function of equilibration time. At the highest volume fraction $\phi = 0.4$, all of the particles in a

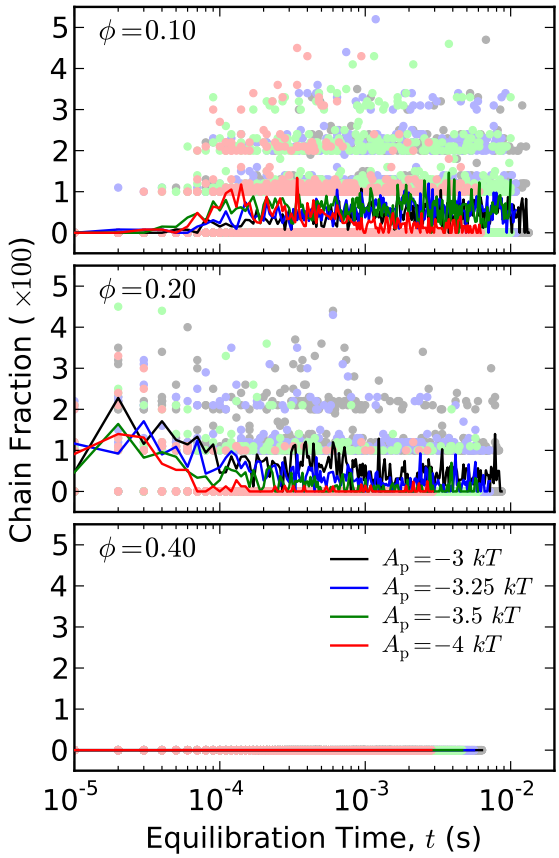

Figure 26: The average fraction of particles contained in *chain-like* aggregates — that is, those aggregates which include at least 10 particles and include at most 1 cross linker — are displayed as a function of equilibration time. Transparent dots indicate the values for each of 10 trajectories of the propagated PW model, and solid curves indicate the average fraction across this set of trajectories. Each panel corresponds to different volume fraction ϕ as labeled in the top left corner and each color curve is for a different pair affinity using the same labeling scheme as Fig. 25.

simulated system persist in a single large aggregate due to the minimal free volume from the outset. For the non-equilibrating potential strengths ($A_p \leq -3.5\, k_B T$) at volume fractions of $\phi = 0.2$ and $\phi = 0.4$, the late stages of equilibration proceed by reorganization of a single highly connected aggregate. This is frustrated by the large number of neighbors around each particle as well as the finite dimensions of the box which may not support periodic spanning structures as would occur in crystalline phases.

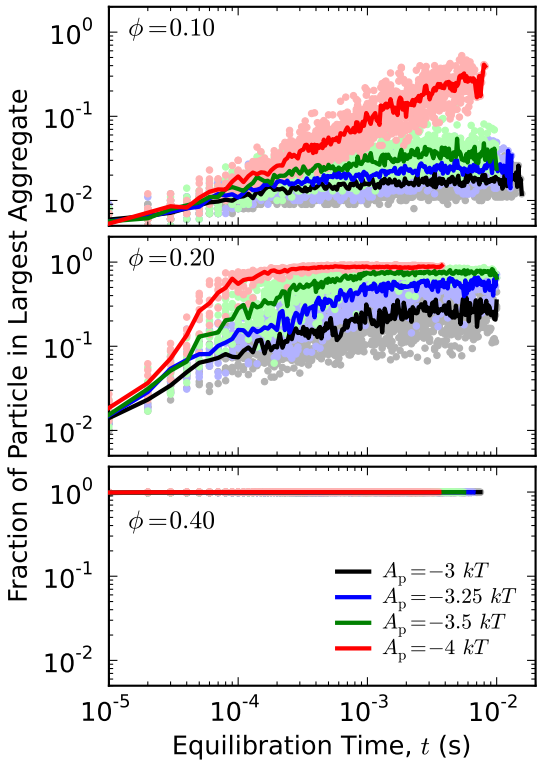

Figure 27: The fraction of particles involved in the largest aggregate, regardless of topology, in each configuration is shown as a function of equilibration time in the propagated PW trajectories. Transparent dots indicate the values for each of 10 trajectories of the propagated PW model, and solid curves indicate the average fraction across this set of trajectories. Each panel corresponds to different volume fraction ϕ as labeled in the top left corner and each color curve is for a different pair affinity using the same labeling scheme as Fig. 25.

4.5 Discussion

The ability of the orientation-averaged CG model to capture the static and thermodynamic properties of DJ particles as calculated in the PW model is the primary result of this study. It suggests that multibody orientation correlationsare unimportant in DJ particle systems with densities up to $\phi = 0.4$ and pair affinities of up to $A_p = -3k_BT$. Within this regime, DJ colloids are therefore expected to exhibit phase behavior and thermodynamic properties identical to comparable isotropically attractive colloids. Granick et al. [62] have estimated that their DJ colloids have pair affinities on the order of $-5k_BT$ to $-10k_BT$. It would therefore not be too difficult to create colloidal dispersions with smaller magnitude affinities so as to test our finding that their structure would be similar to that of a corresponding isotropically attractive colloidal dispersion.

In this study, DJ particles are found to have a preferred orientation within their neighbor shell, although the structure of this shell is identical to that of comparable isotropically attractive particles. The preferred orientation is exhibited through a density correlation that is strongest near the DJ particle tips and that exhibits a depletion zone near the equator between the two hemispheres. This alignment within neighbor shells leads to significant orientational correlations between DJ particles that can extend out to the third neighbor shell. Pair orientation correlations also provide evidence for the emergence of weak multibody orientation correlationsin the strongest interacting and densest equilibrium PW system studied.

At sufficiently high densities and/or high charge densities (or low temperatures) multibody orientation correlationsare expected to significantly influence DJ particle properties. This leads to divergence in the properties of DJ and isotropically attractive colloids at comparable conditions. Unfortunately, these regions of (ϕ,σ) space are inaccessible through the numerical methods used here because of a combination of the limitations in computer power and the very large integration times that would be required. DJ systems with slightly higher charge densities (pair affinities $A_{\mathrm{p}} \lesssim -3.5\,k_{\mathrm{B}}T$) did not equilibrate with current methods. Nevertheless, their time-dependent relaxation from an initial hard sphere configuration towards equilibration were simulated. A substantially larger drop in internal energy was seen in the partial equilibration of these systems when simulated using both the PW and CG models as compared to the equilibrating systems. These results suggest a discontinuity in the internal energy with respect to charge density as would correspond to a liquid-to-solid phase transition. It is therefore predicted that DJ systems with interactions of the order $A_{\mathrm{p}} \lesssim -3.5\,k_{\mathrm{B}}T$ will exist in a solid state. Current results can make no predictions as to whether the solid state would be crystalline or amorphous. The structural changes in these time-dependent relaxations could be quantified in the same manner as Debenedetti et al. in reference [37] to determine if these systems are approaching crystal structure.

We therefore predict that the static properties of DJ and isotropically attractive colloids will only diverge within solid regions of phase space. This hypothesis is supported by current results for liquid state systems near the predicted liquid/solid boundary which shows DJ particle systems to be identical to comparable isotropically attractive particle systems. This is in agreement with Poisson-Boltzmann cell model predictions for colloids with non-uniform charge distributions.[32] Within

this model, Eggen and van Roij[32] theoretically proved that there does not exist a nonuniform charge distribution that will produce orientational ordering in the absence of long-range translational order. In contrast, amphiphilic Janus colloid models display unconventional phase behavior in the liquid and gas regions of phase space due to the formation of isolated clusters. [109, 110, 40] Similar phase behavior wouldn't be expected for DJ particles. This is due to DJ clusters having a net asymmetric distribution of charge that promotes the formation of larger structures.[62] Isolated cluster formation for DJ particles has not been observed in our results, although such structure would be expected at lower volume fractions than presently studied.

Similar to the AJ colloid particle studies, [109, 110, 40, 103] DJ particles can also be modeled using the Kern-Frenkel patch potential [71] or the Tarazona model.[119] This would provide a more coarse-grained approach to the DJ interaction than developed in the PW model while still incorporating orientational dependence as dropped in our CG model. Such a DJ model would be particularly amenable to Monte Carlo simulation for the study of phase behavior. Time-dependent quantities for the patch model can also be calculated using an event-driven molecular dynamics approach as previously demonstrated.[26] The recent extension of the Tarazona model by Rosenthal et al[103] so as to include smooth coarse-grained potentials to describe the self-assembly of AJ particles could also be employed in a like manner for DJ. However, the present model has the advantage of being scalable with respect to possible substructure in the Janus particle surface.

Our PW model can also be contrasted to Hall et al.'s[48, 49] and Miller et al.'s[83] models of DJ particle which have a stronger dipole character and include long-range electrostatics. Both of those models are found to exhibit chain formation[48, 83, 49] as also seen in models of simple polar fluids[24, 133] and not seen in the PW model. For isochores on the phase diagram comparable to current work, Hall et al., [48] find that cooling of the fluid phase first leads to the formation of a significant population of chains within the fluid phase giving rise to percolating networks upon further cooling. At even lower temperatures, the authors found BCT lattice structures with voids. [48] The simulated equilibrium liquid phase of the PW models has structure comparable to isotropically attractive particle systems and our nonequilibrium relaxation simulations proceed towards highly connected aggregates and solid structure is predicted. Hence there is a disparity between their model and ours. The DJ particle models of Hall et al. and Miller et al. should be more accurate

than our PW model in the absence of electrostatic screening where the dipole character dominates and the long range electrostatic interactions promote chain formation. Our model does specifically truncate electrostatics, albeit at a length scale characteristic of low ionic strength $I \approx 0.1\,\mathrm{mM}$. In the absence of long range electrostatics, the specific nature of the short-range geometry in the DJ interaction will dominate as is well captured by the PW model. The absence of chain structures in the PW model may also be a consequence of this cutoff in the electrostatic term. As a corollary, simple polar fluid models may also well describe DJ particles in the absence of electrostatic screening, but may fail for even weak electrostatic screening due to the large length scales of colloidal particles relative to the screening length.

The simple polar fluid models do have similar anisotropy as DJ colloids, and therefore methods that have been successfully applied to the dipolar hard sphere model and Stockmayer fluid may be of use to study DJ colloids. The mean-spherical approximation (MSA) integral equation solution for dipolar hard sphere static properties has been given by Wertheim. [134] In this solution, the translational structure is assumed to be identical to the comparable density hard sphere system. Orientational correlations are introduced as due to the embedded dipoles through a generalization of the Ornstein-Zernike relation. The MSA solution of the dipolar hard sphere model is found to agree with the results of Monte Carlo simulations[96] and more rigorous integral equation computations —such as reference hypernetted-chain (RHNC)[42]— for weaker dipole strengths and/or higher temperatures —that is, conditions for which the excess potential energy is of the order $U_{\mathrm{ex}}/N \gtrsim -0.5\,k_{\mathrm{B}}T$. The breakdown of the MSA for stronger interactions can be at least partially explained by translational structure changes resulting from the embedded dipole interaction as observed in Monte Carlo simulations. [96] Therefore such an MSA treatment is not applicable to our PW model because we observed changes in the translational structure with increasing charge density. As more rigorous integral equations methods are found to capture dipolar hard sphere properties well for stronger dipole strengths ($U_{\mathrm{ex}}/N \approx -4\,k_{\mathrm{B}}T$),[42] they may find success in predicting DJ particle static properties. Such methods have already been successfully applied to the Kern-Frenkel one-patch particle model with large self-associating patches as comparable to amphiphilic Janus particles. [45]

In conclusion, we have constructed a new model for DJ particles and studied its static and thermodynamic properties with molecular dynamics computer simulations. An orientation-averaged isotropic CG model was found to reproduce the computed properties of the rigorous PW model demonstrating the insignificance of multibody orientation correlationsinside the range of parameters studied ($\phi \leq 0.4$ and $A_{\mathrm{p}} \geq -3\,k_{\mathrm{B}}T$). This suggests that DJ colloids will have identical equilibrium properties as comparable isotropically attractive colloids within this region of the phase diagram. Nonequilibrium relaxation simulations of stronger interacting systems show no signs of chain formation. Additionally, these nonequilibriums results suggest a phase transition to solid structures and also show deviations in the properties of the PW and CG models. Therefore multibody orientation correlationsare predicted to be insignificant in DJ colloids within the liquid phase. The significance of multibody orientation correlationsin nonequilibrium DJ colloids (e.g. gels or colloids under shear forces) is the subject of future work.

CHAPTER V

DYNAMIC PROPERTIES OF DIPOLAR JANUS PARTICLES

5.1 Introduction

Surface modification of colloidal particles has received significant attention because such tunable anisotropic particles may give rise to new colloidal materials. [98, 47, 51, 97, 31] Janus particles are a subclass of such anisotropic particles. They are spherical, with each of of two hemispheres decorated by a different chemistry. [18, 123, 62, 69] In the present work, we study dipolar Janus (DJ) particles that have two hemispheres of opposite sign and equal magnitude in charge. There has been limited experimental [62, 69] and theoretical [48, 83] work on DJ particles, particularly with regards to dynamics. [83]

Previous theoretical studies have shown novel dynamics for anisotropic particles. [26, 27, 83] Sciortino and coworkers observed several interesting features in the dynamics of tetrahedrally patchy particles, including a non-monotonic dependence of the diffusion constant on volume fraction as due to the formation of a network at an optimal volume fraction. [26, 27] Hansen et al. discovered a two-step gelation process in their dumbbell model of dipolar particles.[83] We have previously developed a model for dipolar particles that focuses on the geometry of their electrostatic interactions through a pointwise (PW) decomposition of the particles surface [52] and in this paper we provide a study of the dynamics of this model.

We also consider the dynamics of an isotropic coarse-grained (CG) model of DJ particles that we have previously shown to capture the static equilibrium properties of DJ particles for a significant range of conditions. [52] The dynamics of the CG model are found to be accelerated relative to the detailed model. Such accelerations have previously been seen in coarse-grained models.[28, 88, 80, 81, 85, 55] It is certainly a useful outcome of the algorithm in so far as it reduces the necessary computational resources required to perform simulations. However, it opens the question as to whether all dynamical motions involving the retained dynamical variables—that is the coarse-grained ones—are accelerated uniformly or not. We test the use of two existing methods to map

the accelerated CG dynamics back to the rigorous PW dynamics and investigate whether different dynamical observables can be simultaneously attributed to the same renormalized time scales.

Time rescaling, as first developed by Maranas et al, [28] is a dynamical mapping method that has been successfully applied to studies of coarse-grained polymer dynamics. [88, 80, 55] In this method, any time interval in the CG dynamics is multiplied by a constant factor α ($\alpha > 1$) to recover the true timescales of the detailed model within this interval. Physically, time rescaling compensates for the accelerated rearrangement kinetics within the coarse-grained model as due to a reduction in the energy barrier for a dominant rearrangement process. Maranas and coworkers [28] showed that one can estimate the factor by which dynamics are accelerated in the coarse-grained polymer model from the mean squared displacements computed in the detailed model and in the coarse-grained model.

In the second dynamical mapping approach considered here, CG dynamics are coupled to a bath through a Langevin equation characterized by the friction constant η. [1, 93, 65] Physically, this coupling represents the energy dissipation and fluctuations of the CG coordinates resulting from the removal (or decimation) of the coordinates that were averaged over through the coarse-graining procedure. This technique has been suggested as a general solution to the accelerated dynamics of CG models[65] and has been successfully applied to several CG systems.[1, 93, 65] In general, η can be colored noise,[86, 139, 140] and even include nonstationarity depending on space,[77, 16, 78, 17, 23] time[58, 130, 126] or both.[57, 118, 56] Presently, we only consider uniform (in both space and time) Markovian memory friction kernels.

In this paper, we study the dynamics of our previously developed PW and CG models for DJ colloidal particles. In Section 5.2, we summarize the model and simulation methods that were previously developed in Ref. [52] as well as our methods for computing dynamic properties from simulation. Dynamical mapping methods to relate the accelerated CG dynamics to the PW dynamics are developed in Section 5.2.3. The numerical results of simulations and the dynamical mappings are presented in Section 5.3. Of particular significance, the dynamical mapping methods are found to successfully map the diffusion constants observed in the CG model to those found in the PW model, but fail to map the distributions of reversible bonds durations. A discussion of these results is presented in Section 5.4, including a possible explanation for why current dynamical mapping

methods work for some observables and not others. Additionally, we consider what may be needed in new dynamical mapping methods to address the dynamics of our CG model for DJ particles as well as the dynamics of other CG models.

5.2 Theory and methods

5.2.1 Models

This work builds upon our previous study of dipolar Janus colloids using the same rigorous pointwise (PW) and coarse-grained (CG) models as introduced in Ref. [52] and briefly summarized here. In the PW model, each particle has an isotropically repulsive soft core and an orientation dependent electrostatic interaction. The electrostatic term is approximated by a uniform pointwise decomposition of the particle surface into a set of point charges: each having the same magnitude and either a positive or negative sign. The strength of the pair interaction is modulated by the surface charge density σ across each particle's surface. In the PW model, uncharged ($\sigma = 0$) particles have a characteristic diameter of $l = 220\,\text{nm}$. Additionally, the PW pair interaction has a cutoff distance of $r = 230\,\text{nm}$ where r is the center-to-center separation distance of a pair.

A CG model is constructed from the PW model by Boltzmann averaging over pair orientations. This leads to an isotropic free energy profile $A(r)$ that serves as a potential of mean force in the limit that orientations are not correlated beyond the pair level. The minimum of this free energy profile A_p is taken as characteristic of pair affinity in both the CG and the PW models. There is a monotonic relationship between σ and A_p that was computed in earlier work.[52] We use both σ and A_p to quantify the strength of pair interactions in current work.

In both the PW and CG models, we initially study the dynamics of DJ particles in vacuum (i.e., no dissipative solvent is included.) Dissipative Langevin friction is introduced later to the CG model only so as to map the accelerated CG dynamics to those of the PW model. The effect of a dissipative solvent is not included in this current study so that the effects of the DJ interaction on dynamics can be isolated. Additionally, such simple vacuum models have played a key role in understanding features of colloid dynamics such as attractive melting. [99]

5.2.2 Simulation details

Simulations are performed using the LAMMPS molecular dynamics package [100] with a custom force field module for the PW electrostatics terms. Full details of our simulation methodology can be found in [52]. Simulations of $N = 1000$ particles are performed in a cubic periodic box with box volume V adjusted to reach the target volume fraction ϕ. This is defined from the diameter of the uncharged particles $l = 220\,\text{nm}$ by $\phi = \pi N l^3/6V$. As in earlier work, the integration algorithms "fix nvt/asphere" and "fix nve/asphere" are used for equilibration and sampling respectively. Additionally, the algorithm "fix langevin" is used in conjunction with "fix nve/asphere" in current work to perform Langevin dynamics. In all cases, an integration time step of $\Delta t = 1\,\text{ns}$ is used in the dynamics integration algorithms. All simulations are initialized from equilibrated configurations from our previous study and 5 ms trajectories are simulated for the sampling of dynamical quantities. As before, 50 different simulations are performed for each parameter combination (ϕ and σ) in each model and this allows an estimation of the uncertainty in computed quantities.

Both the velocity autocorrelation function (VACF)

$$C_{\vec{v}}(t) \equiv \langle \vec{v}(t_0) \cdot \vec{v}(t_0 + t) \rangle \tag{42}$$

and the mean squared displacement (MSD)

$$C_{\vec{R}}(t) \equiv \left\langle \left| \vec{R}(t_0 + t) - \vec{R}(t_0) \right|^2 \right\rangle \tag{43}$$

are computed in each simulation. Although formally these quantities are stationary —hence t_0 is arbitrary— the initial time t_0 has been specified for clarity in the presentation of the computational sampling methodology for time correlation functions (TCFs). Indeed, every configuration X_i (positions R_i or velocities v_i) obtained within a trajectory can serve as a reference t_o configuration for all subsequently sampled configurations. This is exploited to provide many samples of the dynamical correlation at each time interval t in the computed TCFs.

TCFs are computed at $(n_X + 1)$ uniform time intervals at rate of τ_X from 0 to a maximum time $n_X \tau_X$.Trajectories are initially integrated to create a history of the first n_X configurations while not accumulating statistics. For each subsequent configuration X_i, its correlation is calculated with itself and with each of the previous n_X configurations X_{i-j}. This provides a single sample of the TCF for

each of the correlation times $j\tau_x$. After calculating the correlations, each new configuration is added to the front of the configuration history sequence and the oldest configuration is discarded. The TCF samples at each time interval are summed throughout simulation and at the end of simulation each of the $n_X + 1$ sums is normalized by the number of contributions giving the average TCF as computed at each time interval. This TCF computation method provides an efficient way to calculate TCFs at a high resolution in time without the need to store large trajectories on disk; all analysis is performed during simulation.

The time intervals for each computed TCF are as follows: In computing the VACF, $C_{\vec{v}}(t)$, the time interval is $\tau_{\vec{v}} = 50\,\text{ns}$ and the number of intervals is $n_{\vec{v}} = 2000$ so that that the maximum time in the VACF is $100\,\mu\text{s}$. For the MSD, $C_{\vec{R}}(t)$, the parameters are $\tau_{\vec{R}} = 200\,\text{ns}$ and $n_{\vec{R}} = 2500$ with a maximum time of $500\,\mu\text{s}$. This leads to the determination of roughly 9×10^4 velocity correlation samples and 2×10^4 translational correlation samples from each 5 ms simulation. These values were chosen based on preliminary results that indicated the requisite short and long time lengths needed to capture the behavior of the TCFs. In computing $C_{\vec{R}}(t)$, the displacement distances takes into account the unmodulated trajectory on the periodic lattice.

As discussed in our previous paper, simulations are performed at constant energy in the NVE ensemble as initialized from NVT equilibration.[52] This is necessary to avoid dynamical artifacts as could arise from a thermostat. Consequently, multiple simulations from different initial conditions are needed to sample the Maxwell-Boltzmann distribution of kinetic energies for $T = 300\,K$. Each reported TCF is obtained by averaging the TCFs obtained from each simulation (each at a given fixed E). Error estimates are obtained from the distribution of observables across these simulations. The uncertainty is still quite small as quantified by

$$2\,\text{se}\left[C_{\vec{v}}(t)\right] / C_{\vec{v}}(t=0) < 0.01 \;\forall t$$

$$2\,\text{se}\left[C_{\vec{R}}(t)\right] / \text{mean}\left[C_{\vec{R}}(t)\right] < 0.02 \;\forall t$$

where $\text{se}(\cdot)$ is the standard error function and t denotes all times considered in TCF computations. Uncertainty is quantified by $2\,\text{se}(\cdot)$ for confidence intervals at the 95-th percentile. Similarly, error bars are calculated for all quantities derived from TCFs by first performing the calculation for each individual TCF and then calculating $2\,\text{se}(\cdot)$ for the distribution of values computed from the 50

different TCFs.

Diffusion constants are calculated from $C_{\vec{R}}(t)$ to quantify transport. This is accomplished by fitting the expression

$$C_{\vec{R}}(t) = 6Dt + r_0^2 \tag{44}$$

for $1\,\mu\text{s} < t \leq 500\,\mu\text{s}$ and r_0^2 accounts for inertial effects from $t \leq 1\,\mu\text{s}$. For internal consistency, D is also computed from VACFs by numerically integrating the Green-Kubo relationship for finite time

$$D = \frac{1}{3}\int_0^{t_{\max}} dt\, C_{\vec{v}}(t) \tag{45}$$

where $t_{\max} = 100\,\mu\text{s}$. The D's calculated from these two methods are found to agree within 0.3% in all cases and this is less than or comparable to the uncertainty in these quantities.

The distribution of reversible bond durations between pairs of particles is also computed as this quantity is taken to be sensitive to the details of microscopic particle dynamics. Comparing the distributions computed in both the PW and CG model can provide insight into the extent to which the detailed microscopic dynamics differ in the two models. A pair of particles are said to form a reversible bond when they are within each others interaction region as defined by a separation distance $r \leq r_{\text{bond}}$ with $r_{\text{bond}} = 230\,\text{nm}$. The set of reversible bonds in a simulation is monitored at 50 ns intervals and each bond duration t_{b} is obtained by noting the times at which the bond is formed and the time at which it is subsequently broken. Throughout the simulation, a histogram of reversible bond durations is constructed in the log scale. Specifically, a histogram of the quantity $l_{\text{b}} = \log(t_{\text{b}}/\text{s})$ is constructed with the range of $\log(5\times10^{-8}) \leq l_{\text{b}} \leq \log(1\times10^{-3})$ using 64 bins of uniform width. This results in the bond duration population $f(t_{\text{b}})$, defined by the frequency at which reversible bonds within a range of durations t_{b} are observed. This distribution is normalized by the total number of particles in simulation and the duration of simulation. Histogram bin width normalization is not performed.

5.2.3 CG dynamical mapping

The dynamics of the CG model are found to be accelerated relative to the PW model. We attempt to map the CG dynamics to that of the PW model by damping with Langevin friction. At present, we consider a uniform (in both space and time) friction η and test the extent to which this η can map the CG dynamics onto to the PW dynamics.

To calculate the mapping friction η, we propose first calculating the effective friction in the PW and CG models, η_{PW} and η_{CG} respectively, as experienced by each particle due to its interactions with the other particles. As the CG model has fewer degrees of freedom, it is anticipated that each particle will experience a weaker effective friction since there are fewer opportunities for energy exchange. The effective frictions are calculated from the VACFs computed in each model at the same conditions with an exponential approximation for the VACFs.

$$C_{\vec{v}}^{(\mathcal{M})}(t) = v_0^2 \exp\left(-\frac{\eta_{\mathcal{M}}}{m}t\right) \tag{46}$$

where $\mathcal{M}$ is either PW or CG, v_0^2 is the mean squared velocity of a particle and m its mass. The value of $\eta_{\mathcal{M}}$ is chosen to reproduce the diffusion constant computed from simulation for the respective model.

$$\frac{\eta_{\mathcal{M}}}{m} = \frac{v_0^2}{3D_{\mathcal{M}}} \tag{47}$$

The mapping friction η is then taken as the difference in the effective friction of the PW and CG models for one set of conditions.

$$\eta = \eta_{\mathrm{PW}} - \eta_{\mathrm{CG}} \tag{48}$$

The approximation of the VACFs by an exponential model may be too severe. Therefore η is also calculated by assuming it contributes an exponential decay to the CG VACF computed from simulation.

$$C_{\vec{v}}^{(\eta)}(t) = \exp\left(-\frac{\eta}{m}t\right) C_{\vec{v}}(t) \tag{49}$$

Numerical methods are used to find the value of η such that the new CG VACF $C_{\vec{v}}^{(\eta)}(t)$ gives rise to the same diffusion constant calculated in the PW model.

$$D_{\mathrm{PW}} = \frac{v_0^2}{3}\int_0^{t_{\max}} dt \, \exp\left(-\frac{\eta}{m}t\right) C_{\vec{v}}^{(\mathrm{CG})}(t) \tag{50}$$

This latter method will be referred to as the integrated exponential method for calculating η and the former method referred to as the single exponential method.

Langevin dynamics (LD) simulations of the CG model are performed to test this dynamical mapping. Langevin integration is performed using the LAMMPS algorithm "fix langevin",[100] which uses the method developed by Schneider and Stoll.[108] This method integrates the Langevin equations of motion in the Markovian limit, e.g. memory-less friction. The "fix langevin" algorithm

requires a characteristic relaxation time τ_r as input and this is related to the mapping friction through the relation, $\tau_r = m/\eta$. This algorithmic correction affects the propagation of the trajectory through Langevin equations of motion

$$m\ddot{q}(t) = F_{\text{pair}}[q(t)] - \eta\dot{q}(t) + F_s \tag{51}$$

for each degree of freedom q where F_{pair} is the deterministic force from pair interactions, F_s is the stochastic force, and η is the friction.

Rather than performing CG-LD simulations only for the predicted mapping frictions, simulations are performed for a range of η values across a fine grid. Interpolation is then used to determine the value of a computed quantity (such as a VACF) for any value of η within this range. Specifically, 17 different values in the range of $10^2\,\text{s}^{-1} \leq \eta/m \leq 10^7\,\text{s}^{-1}$ are simulated with a uniform separation on a log scale. All computed quantities are found to vary slightly between adjacent simulations and therefore linear interpolation is valid. The benefit of this method is that it allows us to determine the value of η, possibly different than those calculated from VACFs, that provides a best-fit dynamical mapping for each set of conditions. This optimal value of η is found by numerically inverting the interpolated monotonic function $D_{\text{CG-LD}}(\eta)$ using a binary search for η such that $D_{\text{CG-LD}}(\eta) = D_{\text{PW}}$.

5.3 Results

5.3.1 Dynamics of PW and naive-CG models

Dynamics are first quantified by computing the VACFs for particles in both the PW and CG models (Figure 28). The VACFs show standard behavior for attractive particle systems, with monotonic exponential decays for low-density weakly-attractive systems and faster non-monotonic decays for denser and stronger interacting systems. It is notable that the VACFs computed in the PW and CG models are not identical at higher densities and stronger pair interactions. These deviations cannot be discounted because they are larger than the uncertainty in the results. Specifically, the CG model exhibits stronger *dynamic* correlations for times $t \lesssim 1\,\mu$s. In contrast, the previously computed *static* pair correlations functions $h(r)$ for these systems were found to be identical in both models.[52] The stronger dynamical correlations in the CG model are consistent with the anticipation of accelerated dynamics in a coarse-grained model. The self-translational correlation function $C_{\vec{R}}(t)$ has also

been computed for each simulated system. All of these cases have been found to be diffusive with $C_{\vec{R}}(t) \propto t$ for $t \gtrsim 50\,\mu$s (not shown).

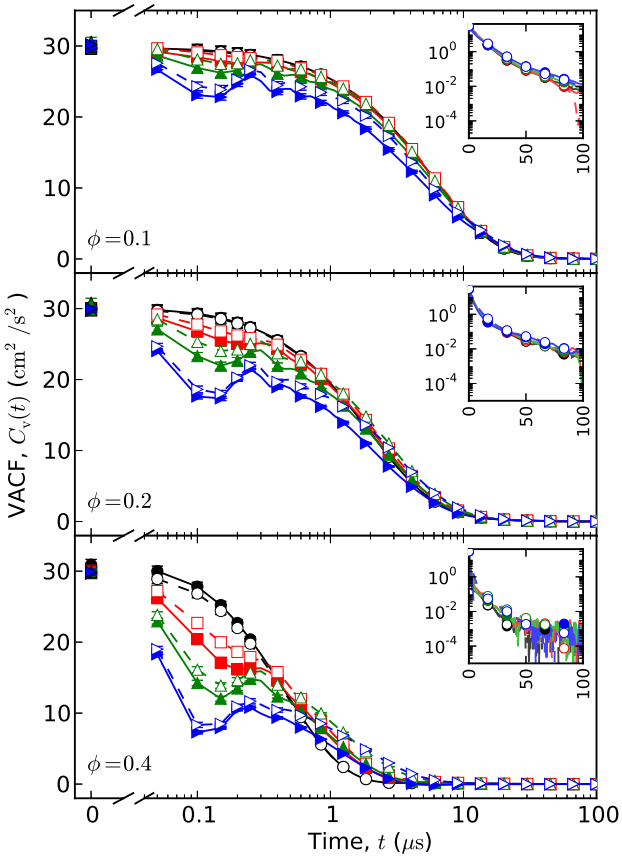

Figure 28: Velocity autocorrelation functions (VACFs) as computed in both the PW model (solid lines and solid markers) and the CG model (dashed lines and open markers). Each panel shows a different volume fraction as labeled on the plot and results are shown for four different charge densities: $\sigma = 0\,e_0/\mu\text{m}^2$ ($A_\text{p} = 0\,k_\text{B}T$) black circles, $\sigma = 19.29\,e_0/\mu\text{m}^2$ ($A_\text{p} = -1\,k_\text{B}T$) red squares, $\sigma = 20.92\,e_0/\mu\text{m}^2$ ($A_\text{p} = -2\,k_\text{B}T$) green up-triangles, and $\sigma = 22.18\,e_0/\mu\text{m}^2$ ($A_\text{p} = -3\,k_\text{B}T$) blue right-triangles. The zero time value is included by breaking the log-scale x-axis. VACF functions are computed at a resolution of $\Delta t = 50\,$ns and markers are only included at select data points to better distinguish the curves. Main axes show time on a log scale and VACFs on a linear scale and includes error bars at markers. The lines between early time markers are linear interpolations between points to guide the eye. The inset shows time on a linear scale and VACFs on a log scale to show that all VACFs at each volume fraction have similar long-time behavior.

The translational diffusion constants computed for DJ particle systems in each model are shown in Figure 29. Diffusion constants are significantly higher in the CG model than in the PW model at stronger pair interactions $A_\text{p} \lesssim -1\,k_\text{B}T$ for all investigated densities. This is consistent with the observation of stronger correlations for times $t \lesssim 1\,\mu$s in the VACFs computed for the CG model.

The non-monotonic trend of D vs σ observed in both models can be understood through the theory of attractive melting[99] wherein weak attractions increases the free volume and thereby the mobility of particles. It is notable that the attractive melting effects are observed to be stronger in the CG model than in the PW model.

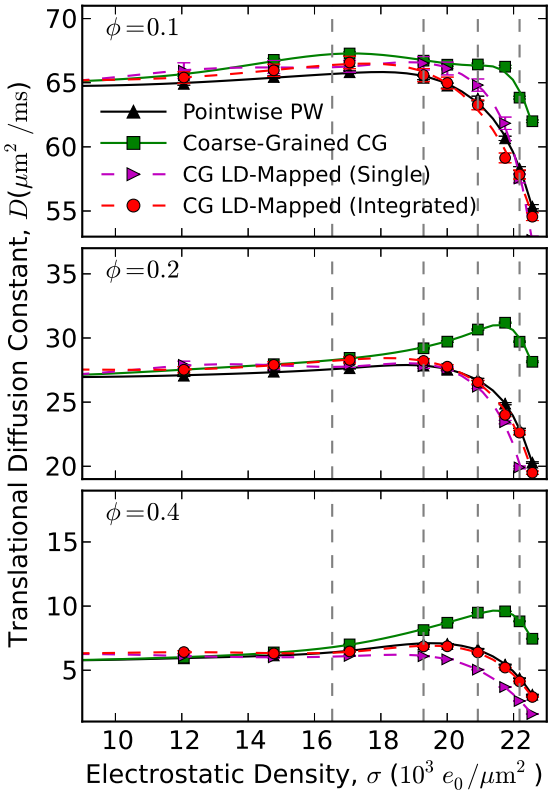

Figure 29: Translational diffusion constants are shown for the PW model (black up-triangles) and the CG model (green squares) as a function of electrostatic density. The diffusion constants for the CG model damped by Langevin dynamics (LD) employing different mapping frictions η are also shown. LD results are shown for damping friction η obtained from either the single exponential method or the integrated exponential method as shown by magenta right-triangles and red circles, respectively. Each panel corresponds to a different volume fraction ϕ as noted in the top left. Four vertical dashed lines denote the electrostatic densities corresponding to the following pair affinities in order left-to-right: $A_p = -0.01\,k_BT$, $A_p = -1\,k_BT$, $A_p = -2\,k_BT$, and $A_p = -3\,k_BT$. Markers denote computed results with error bars showing the uncertainty (in most cases they are smaller than the marker) and the lines are smoothing splines of data that are shown only to guide the eye.

A time rescaling factor α is calculated as the ratio of the diffusion constant in the CG model to that of the PW model

$$\alpha = D_{CG}/D_{PW} \tag{52}$$

Time rescaling factors are found to be on the order $1 \lesssim \alpha < 2.5$ and to vary with both volume fraction ϕ and particle charge density σ. In general, stronger time rescaling (larger α) is needed in denser systems and for stronger interactions. By construction, time rescaling succeeds in mapping the diffusion constant of the CG model onto that of the PW model.

The effect of time rescaling on the CG MSD is shown for one representative system—as specified by the choice of parameters detailed in the caption—in Figure 30. In both this and all others that we computed (though not shown) we find that time rescaling maps the CG MSD to that of the PW model. This could have been anticipated because the time rescaling factor is calculated from the diffusion constants computed in both models at the corresponding set of conditions. Similarly, the effect of time rescaling on the CG VACF is shown for the same representative system in Figure 31. In this instance, time rescaling is applied by multiplying t by α^{-1} in accordance with how time rescaling affects the diffusion constant computed from $C_{\vec{v}}(t)$. Time rescaling is found to improve the agreement of the CG VACF with the PW VACF for intermediate times of $0.3\,\mu\text{s} \lesssim t \lesssim 10\,\mu\text{s}$. In contrast, time rescaling causes both the short time ($t \lesssim 0.3\,\mu\text{s}$) and the long time ($t \gtrsim 10\,\mu\text{s}$) behavior of the CG VACF to deviate from that found for the PW model.

Figure 32 illustrates the bond duration populations computed in the PW and CG models for several interaction strengths at three selected volume fractions. As would be expected, increasing the interaction strength increases the rate at which longer duration reversible bonds are observed. The bond lifetime of $t_\text{b} \approx 0.4\,\mu\text{s}$ is found to occur with greatest frequency in the purely repulsive particle ($\sigma = 0$) systems and this is taken as the time scale of repulsive collisions. We will refer to bonds of this order of magnitude as short duration bonds that are associated with repulsive collisions. Longer duration bonds of the order $t_\text{b} \gtrsim 10\,\mu\text{s}$ are observed in DJ particle systems with non-trivial charge ($\sigma \gtrsim 19\,e_0/\mu\text{m}^2$) and we associate bonds of these durations with attractive pair collisions. We note that we also tested the effect of the bond length cutoff distance r_bond for one set of conditions: $\phi = 0.4$ and $A_\text{p} = -3\,k_\text{B}T$ in CG model (results not shown). Small changes of 5 nm below and above the cutoff (230 nm) employed throughout all other simulations in this work led to only a minor quantitative effect on the bond duration results. Decreasing the cutoff distance more dramatically to $r_\text{bond} = 215$ and 220 nm did give rise to qualitatively different bond duration populations as one might expect once significant numbers of bonds are no longer possible. This suggests that the

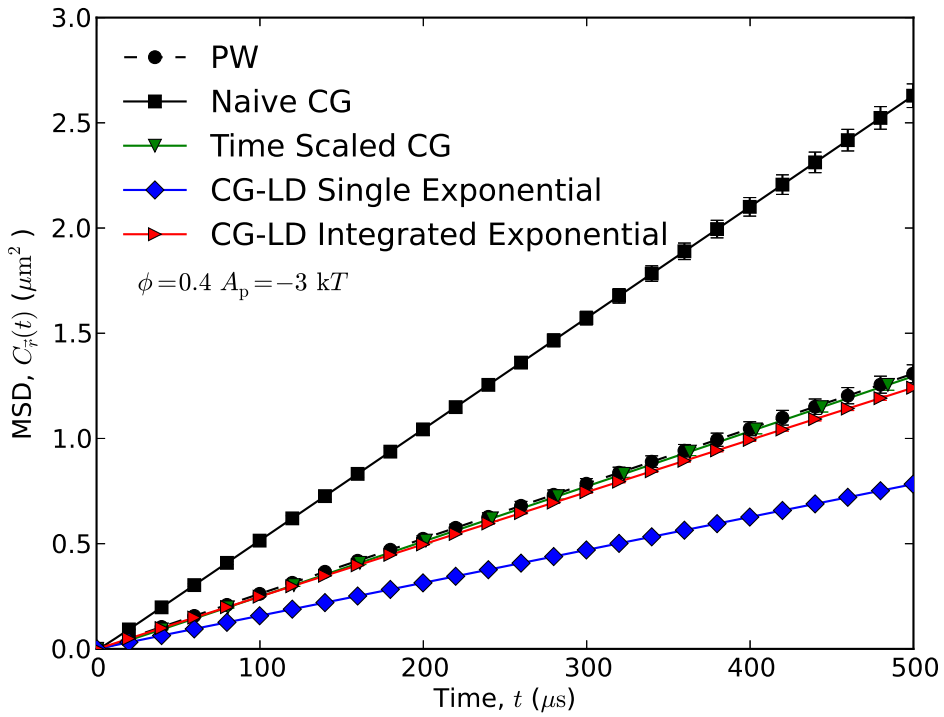

Figure 30: The effect of time rescaling and damping friction on the CG MSD for $\phi = 0.4$ $A_p = -3\,k_B T$. For reference, the PW MSD at these conditions is shown as a dashed black line with circles and the undamped CG MSD is shown with a solid black line with squares. The MSD found by time rescaling is shown by green down-triangles. The MSDs computed from the damped LD simulations are shown, where the mapping friction η is calculated using either the single exponential or the integrated exponential methods as shown by blue diamonds and red triangles, respectively. MSD functions are computed at a resolution of $\Delta t = 0.2\mu$s and markers are only included at select data points to better distinguish the curves and error bars are included at markers.

present results for bond dynamics should not be sensitive to small changes in the choice of r_{bond} given the cutoff distance that we use.

Different bond duration populations are observed in the PW and CG models. This is best shown by plotting the ratio of the bond durations population in the CG and PW model as shown in Figure 33. The CG model is found to have fewer short-duration bonds — bond durations on order of the repulsive collision time $t_b \lesssim 0.4\mu$s — as well as fewer longer-duration reversible bonds $t_b \gtrsim 10\mu$s. Furthermore, the CG model has more intermediate duration bonds $t_b \approx 1\mu$s than the PW model. These are significant qualitative differences in the bond duration populations.

It is simple to show that time rescaling cannot map the CG $f(t_b)$ onto that of the PW model.

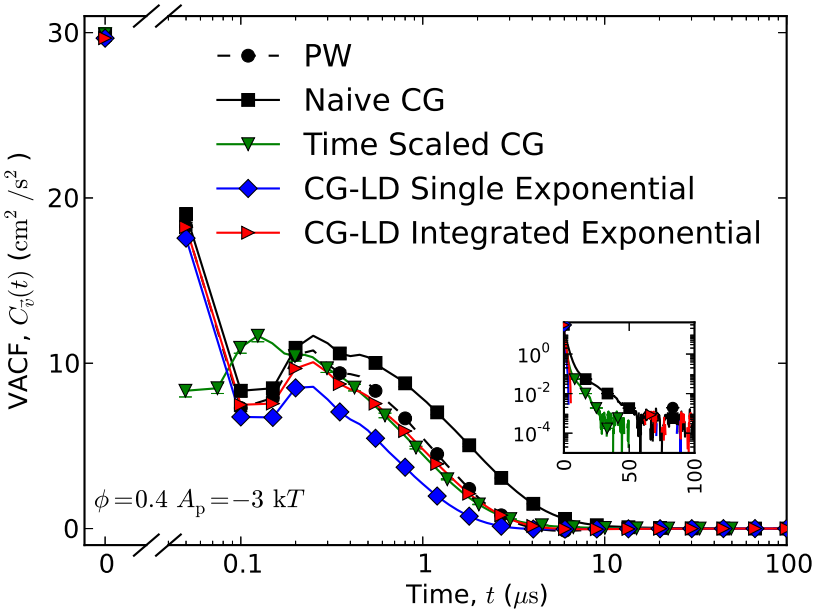

Figure 31: The effect of time rescaling and damping friction on the CG VACF for $\phi = 0.4$ $A_p = -3\,k_B T$. For reference, the PW VACF at these conditions is shown as a dashed black line with circles and the undamped CG VACF is shown with a solid black line with squares. The VACF found by time rescaling is shown by green down-triangles. The VACFs computed from the damped LD simulations are shown, where the mapping friction η is calculated using either the single exponential or the integrated exponential methods as shown by blue diamonds and red triangles, respectively. VACF functions are computed at a resolution of $\Delta t = 50\,\mathrm{ns}$ and markers are only included at select data points to better distinguish the curves. Error bars are included at markers and the lines between early time markers are linear interpolation between points to guide the eye. Uncertainty is comparable to plotting line width on the main axes. Inset has the VACF values on a log scale with time on a linear scale to show the slowly decaying long-time behavior is different for the time scaled VACF as opposed to the other four.

Time rescaling factors are found to be of the order $\alpha < 2.5$ and factors of this magnitude do not rescale time drastically enough to map the CG $f(t_b)$ onto that found in the PW model: the bond populations differ by orders of magnitude for some bond durations. Hence time rescaling methods are found to be inadequate for mapping the bonds dynamics of the CG model to that of PW model. In Sec. 5.3.2, we will test whether uniform damping friction can perform this dynamical mapping.

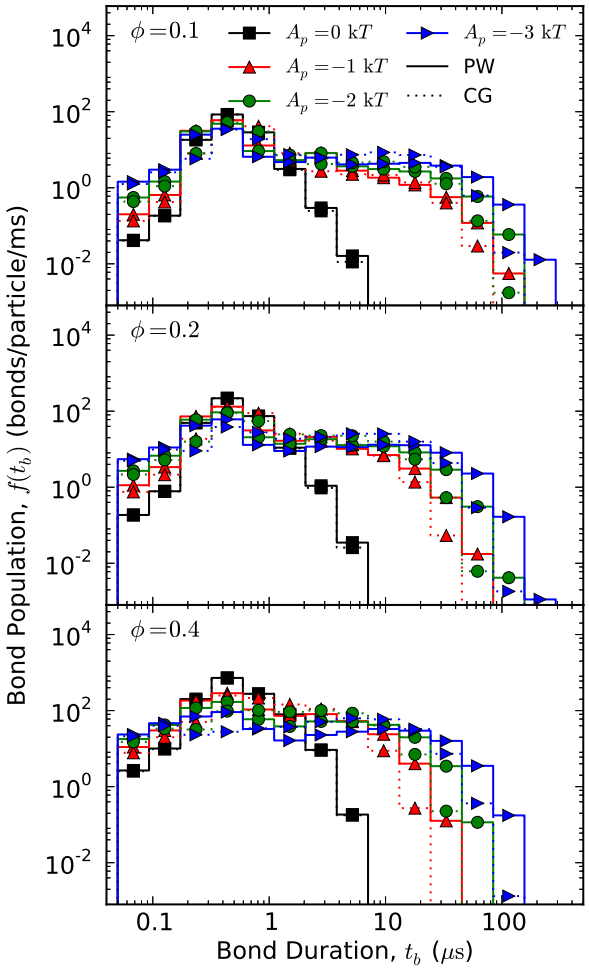

Figure 32: The frequency at which reversible bonds of different duration are observed — bond population $f(t_\mathrm{b})$ — in both the PW (solid lines) and CG (dashed lines) models. Each panel corresponds to a different volume fraction ϕ as labeled at the top left corner. Four charge densities are shown: $\sigma = 0\,e_0/\mu\mathrm{m}^2$ ($A_\mathrm{p} = 0\,k_\mathrm{B}T$) as black squares $\sigma = 19.29\,e_0/\mu\mathrm{m}^2$ ($A_\mathrm{p} = -1\,k_\mathrm{B}T$) as red up-triangles, $\sigma = 20.92\,e_0/\mu\mathrm{m}^2$ ($A_\mathrm{p} = -2\,k_\mathrm{B}T$) as green circles, and $\sigma = 22.18\,e_0/\mu\mathrm{m}^2$ ($A_\mathrm{p} = -3\,k_\mathrm{B}T$) as blue right-triangles. Uncertainty is less than plotting marker size.

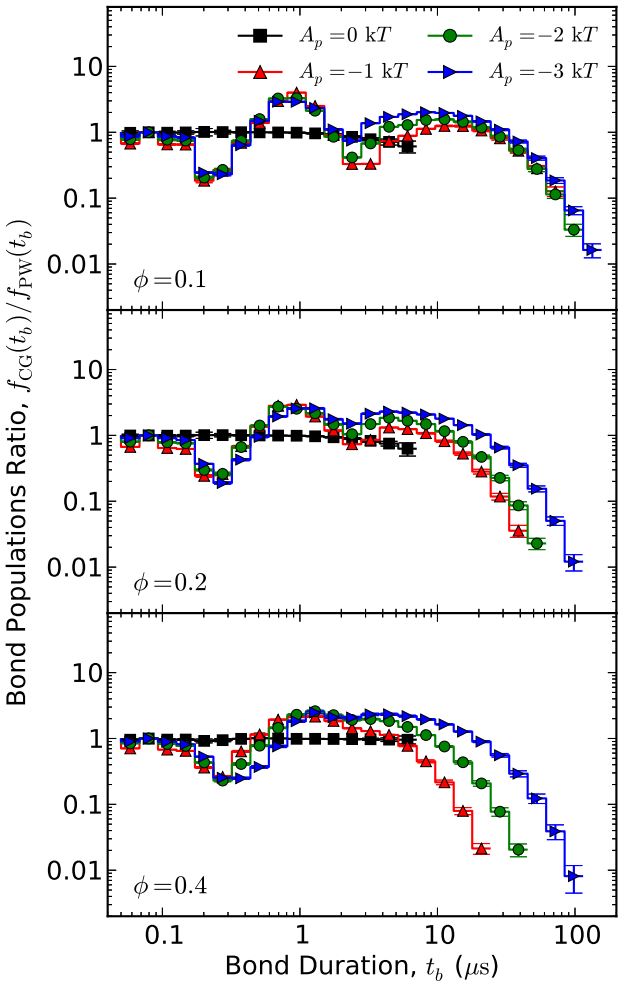

Figure 33: The ratio of bond populations in the CG model to that of the PW model. Error bars show uncertainty. Results are plotted as in Figure 32.

5.3.2 Dissipated-CG model dynamics

Dissipation of the CG model with Langevin dynamics is used in an attempt to map the accelerated CG dynamics back to the PW time scale. Calculation of the requisite friction η to damp the overall CG dynamics to the timescales of the PW model has been formulated through two different approaches in Sec. 5.2.3. The corresponding values of η calculated from the VACFs so as to map the CG dynamics to the PW model are shown in Figure 34. It is found that the values of η calculated from the single exponential method and the integrated exponential method are qualitatively similar although they do not agree to within the uncertainty of the results. For comparison, the optimal value of η required to map the translational diffusion constant D — found using the interpolated inverse search procedure described in Section 5.2.3 — is also shown. For higher values of η, the integrated exponential method appears superior to the single exponential method in that its predicted η values are closer to optimal value found from simulation. Therefore it is anticipated that the integrated exponential method will better predict η for dynamical mapping, although η computed from the single exponential method may be sufficient in some cases.

The effect of damping friction on the MSD for a representative system is shown in Figure 30 for $\phi = 0.4$ $A_{\mathrm{p}} = -3k_{\mathrm{B}}T$; the strongest interacting and densest system considered. Damping with Langevin friction improves the CG MSD relative to the naive CG model for mapping frictions calculated with both methods. Better agreement is found when η is computed with the integrated exponential method as opposed to the single exponential method. Similarly, the effect of damping friction on the VACF for the same representative system is shown in Figure 31. The LD damping with the η value calculated from the integrated method produces a VACF that agrees well with the VACF computed for the PW model. In contrast, the value of η computed from the single exponential model damps the dynamics too much and this leads to a faster decay in the VACF than that observed in the PW model. This is the general trend for all systems studied: the value of η calculated from the integrated exponential method better maps the VACF of the CG model to that of the PW model. The value of η found from the single exponential model generally damps the dynamics too much. The system shown here has the most severe extra damping such that in most studied systems the value of η found from the single exponential method does provides an improvement in the VACF

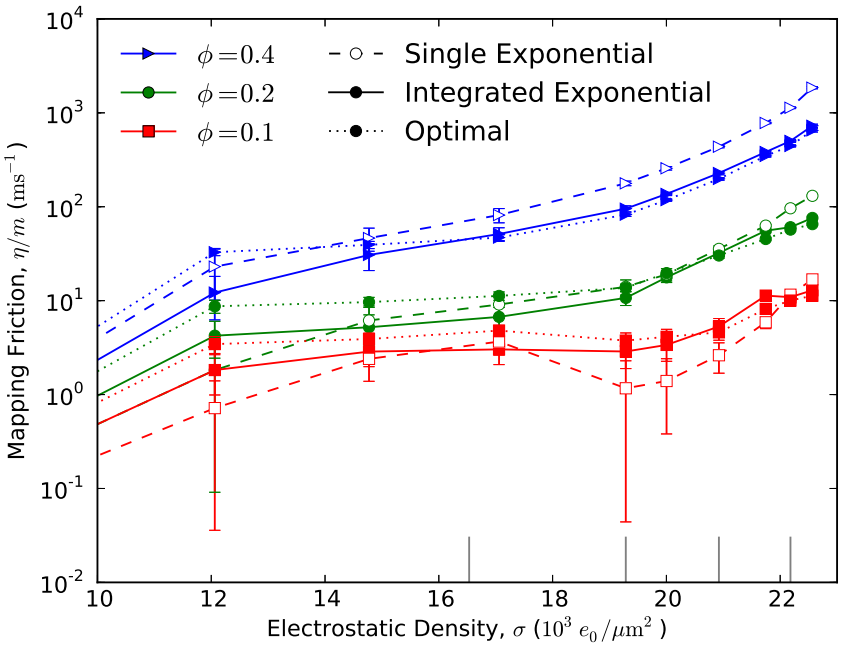

Figure 34: Friction η predicted to map the translational dynamics of the CG model to the PW model from VACF calculations as a function of electrostatic density for three different volume fractions ϕ as labeled on the plot. Friction is calculated either with the single exponential method (dashed lines and open markers) or with the integrated exponential method (solid lines and solid markers) The optimal mapping value of η — found by varying η in simulation — is shown by a dotted line with solid markers. Markers correspond to computed results with uncertainty shown by error bars and lines serve only to guide the eyes. Four ticks along the horizontal axis denote the electrostatic density corresponding to the following pair affinities in order left-to-right: $A_\mathrm{p} = -0.01\,k_\mathrm{B}T$, $A_\mathrm{p} = -1\,k_\mathrm{B}T$, $A_\mathrm{p} = -2\,k_\mathrm{B}T$, and $A_\mathrm{p} = -3\,k_\mathrm{B}T$.

relative to the undamped naive CG VACF.

The extent to which LD damping improves the simulated transport dynamics for all studied systems is shown in the computed diffusion constants (Figure 29). In all cases, damping is found to improve the diffusion constant: $D_\mathrm{CG-LD}$ is closer to D_PW than the undamped value D_CG. This is true regardless of which method is used to compute η. The value of η calculated by the integrated exponential method is found to produce a diffusion constant in the CG model that is closer to that found in the PW model as opposed to the value of η calculated by the single exponential method. For the lower density, $\phi = 0.1$, the single exponential method value of η provides slightly inadequate damping with D higher than that found in the PW model, although the difference is within the uncertainty of the diffusion computations. At the higher density, $\phi = 0.4$, the opposite is seen in

that the single exponential method predicts too strong of a damping friction and therefore D is consistently lower than that found in the PW model. This agrees with the observation that the single exponential method damping over suppresses the velocity autocorrelations at higher densities and stronger pair interactions.

As opposed to that seen for bulk transport proprieties, the LD damping does not reproduce reversible bond dynamics. Figure 35 shows bond duration $f(t_{\mathrm{b}})$ populations computed from the LD simulation of the CG model with η calculated using the integrated exponential method. The mapping friction η has not mapped the bond dynamics of the CG model onto that observed for the PW model. With comparison to Figure 33, the bond dynamics of original undamped CG model, it is seen that $f(t_{\mathrm{b}})$ in the damped CG simulations are comparable to undamped results. Hence, the same values of η that successfully maps the the diffusion constant are not successful at mapping the bond duration populations.

While the η values predicted from the VACFs do not map $f(t_{\mathrm{b}})$, it is possible that other values of η may provide better mappings. This is tested by studying the variation of $f(t_{\mathrm{b}})$ across the range of η values simulated and it is found that no value of η can provide a sufficient improvement in mapping the bond dynamics observed in the CG model onto that observed for the PW model. Representative results for $\phi = 0.4$ are shown in Figure 36. Lower values of η, comparable to that which map D, leave the bond duration population unchanged. Larger values of η give rise to qualitatively different bond duration populations. The $f(t_{\mathrm{b}})$'s found for the larger values of η have more longer duration bonds than the naive CG model, although not as many as found in the PW model. Additionally, the highly damped $f(t_{\mathrm{b}})$'s have significant deviations from the PW results for short and intermediate duration bonds. Therefore it appears that uniform and Markovian friction cannot map the CG bond dynamics, as quantified by $f(t_{\mathrm{b}})$, onto that of the PW model.

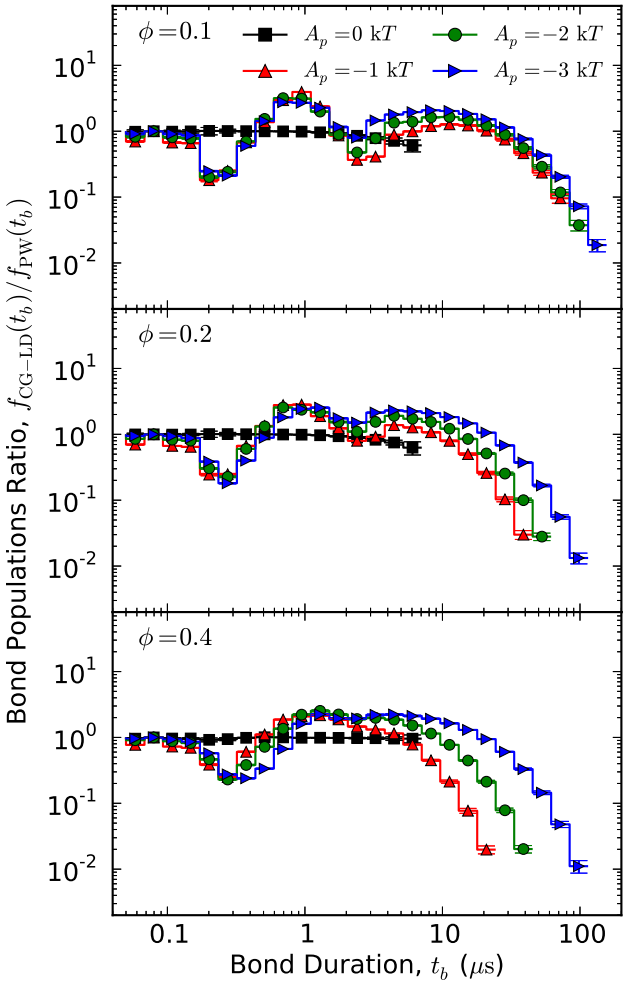

Figure 35: The ratio of bond populations in the LD damped CG model to that of the PW model. Mapping friction η is obtained using integrated exponential method. Results are plotted in same style as in Figure 33.

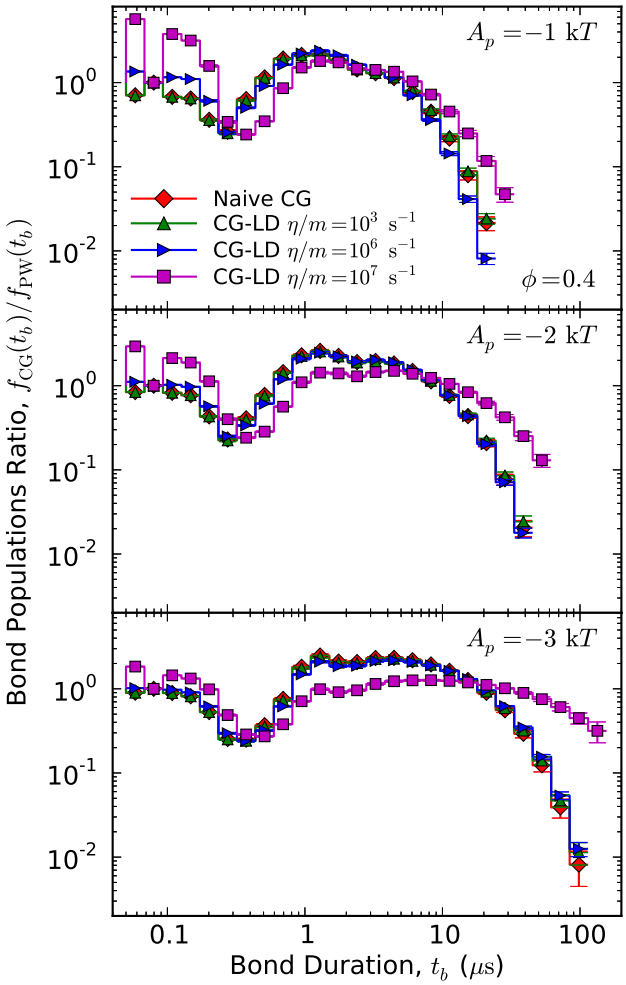

Figure 36: The ratio of bond population in the CG model to that of the PW model for both the naive (undamped) CG model and LD-CG model with one of three different frictions η. The naive CG results are shown by red diamonds while the the remaining curves show the bond duration populations for the CG model with one of three different values of mapping friction: $\eta/m = 10^5$ s green up-triangles, $\eta/m = 10^6$ s blue right-triangles, $\eta/m = 10^7$ s purple squares. All results are for volume fraction $\phi = 0.4$ and each panel shows results for a different pair interaction strength as labeled. Results are plotted as in Figure 33.

5.4 Discussion

The CG model fails to capture the dynamics of the PW model under conditions for which both models have near identical static properties. Specifically, the dynamics of the CG model are accelerated relative to the PW model as quantified by VACFs and diffusion constants. Additionally, the duration of reversible bonds between pairs has a significantly different distribution in the two models with the CG model having fewer long duration reversible bonds. These effects are amplified at stronger pair interaction strengths and higher densities. Therefore the naive CG model cannot be used to study dynamic properties of dipolar Janus (DJ) particles. As a physical corollary, one would anticipate dipolar Janus particles to have slower transport properties than comparable isotropically attractive particles for which the static properties of the two systems are similar. This could have important implications for the processing of dipolar Janus colloidal materials in that they may be more prone to the formation of amorphous phases as a consequence of their longer relaxation times. It is common for coarse-grained models to have accelerated dynamics relative to the detailed model from which they are derived [28, 88, 80, 81, 85, 55] and therefore various methods have been developed in the past to relate the CG dynamics to those of the underlying detailed models. Two such previously proposed methods are: (i) rescaling time uniformly *a posteriori* so as to match a coarse-grained dynamical observable time scale (e.g., the diffusion constant)[28, 55] and (ii) the addition of friction to the CG model using the Langevin Equation formalism or other dissipation mechanisms.[1, 93, 65] In this work, we have explored the use of these two methods in relating the dynamics of our CG model to the PW model so that the conceptually and computationally simpler CG model will be of use to study the dynamics of dipolar Janus particles. In current work, only uniformly Markovian friction is used to implement dissipative terms. The damping friction is calculated by comparison of the VACFs computed for the naive CG model and the PW model at each set of conditions.

Methods (i) and (ii) can adequately map the diffusion constant of the CG model onto that of the PW model for each set of conditions. These methods also produce a MSD and a VACF that are more similar to those of the PW model than those found in the naive CG model. In both methods, the mapping parameter (time scaling factor α or friction constant η) is not a universal constant, but instead varies with both pair interaction strength and particle density. Unfortunately, neither

method gives rise to a reversible bond duration distribution in the CG model that is similar to that of the PW model. This indicates that neither of these two methods are accurately reproducing the PW dynamics in the CG model for all time and length scales.

Other methods could be used to determine a non-uniform mapping friction $\eta(\vec{X})$ where $\vec{X}$ are the CG coordinates (e.g. friction tensor dependent on particle pair separation distances). [1, 93, 65] A non-uniform friction may better reproduce the microscopic dynamics of PW model within the CG model. However, there are reasons to believe that even a non-uniform friction will fail to reproduce the bond duration dynamics seen in the PW model within the CG model. The approach in method (ii) assumes the the primary effect of coarse-graining on the dynamics is to reduce momentum dissipation and energy fluctuations by way of eliminating degrees of freedom. In contrast, Depa and Maranas have proposed that coarse-graining also reduces the energy barriers to rearrangement.[28] They have explained the accelerated dynamics of a coarse-grained polymer model by the weaker intermolecular attraction in the coarse-grained model relative to the detailed model and therefore weaker attractive caging. A similar effect may be the cause of the dynamical disparity between the CG and PW models in the present work. This conjecture is supported by the reversible bond duration results. Namely, the PW model is observed to have significantly more longer-duration reversible bonds between pairs of particles than the CG model. We attribute this loss of longer duration reversible bond to a diminution in attractive caging upon coarse-graining. Such a reduction in attractive caging would explain the general acceleration of the CG model dynamics relative to the PW model.

Depa and Maranas's time rescaling approach is developed from consideration of changes in energy barriers for rearrangement upon coarse-graining.[28] The developed *a posterior* rescaling of time assumes that the accelerated dynamics can be attributed to a single dominant rearrangement process, of which the kinetics have been enhanced by a factor α as due to a change in the energy barrier for this rearrangement upon coarse-graining. This is the case for the time and length scales studied in coarse-grained polymer models. In contrast, time rescaling fails to map bond dynamics of our CG model to that of the PW model. This can be attributed to the existence of multiple rearrangement processes in the PW model and the kinetics of each process are affected by a different factor upon coarse-graining. Specifically, the energetics of each collision pair in the PW model are

dependent on the mutual orientation of the pair where as in the CG model there is only a single energetic profile associated with all collision pairs. In coarse-graining, the multiple rearrangement processes associated with collision pairs with different orientations are replaced by a single pair interaction. As a single rearrangement processes does not dominates the dynamics of the PW model, a single time rescaling factor cannot be applied *a posterior* to map the dynamics of the CG model onto that of the PW model for the time and length scales associated with reversible bonding. New methods may need developed to address time mapping in such systems and such methods will need to consider the change in energetics for multiple rearrangement processes. These methods would have application to other coarse-grained models in which the changing of the energetics for multiple rearrangement processes influence dynamical properties.

In summary, the primary finding of this work is the observation of different dynamical properties for the PW and CG models of dipolar Janus particles at conditions for which the two models have identical static properties. This is not entirely a negative result. With respect to real physical systems, it suggests the important conclusion that structuring colloids opens the possibility for new time-dependent (e.g. rheological and transport) material properties. It is also found that both time rescaling and uniform Markovian Langevin friction can map the diffusion constant of the CG model to the PW model. Unfortunately, these methods do not reproduce the reversible bond duration distribution in the CG model as observed in the PW model. To treat this and related dynamical properties, this suggests a need for new methods that treat the changes in the energy barriers for multiple rearrangement processes upon coarse-graining.

CHAPTER VI

DYNAMICAL SIMULATION OF ELECTROSTATIC STRIPED COLLOIDAL PARTICLES

6.1 Introduction

Anisotropic colloidal particles have received much attention in recent years motivated by the possibility of creating new colloidal materials. [98, 47, 51, 97, 31, 22, 113] One such family of particles is that of surface striped particles. It includes Janus,[123, 19, 62, 69] ternary, [89, 76, 22]. and higher-multiplicity striped[66, 68, 67] surface patterns. In this chapter, the static and dynamic properties of systems of striped particles with stripes of alternating electric charge are investigated through computer simulation.

There are several methods by which striped surfaces have been produced on colloidal and nano particles. [66, 89, 135, 68, 82, 67] Janus particles—2-striped particles with each hemisphere having a different surface chemistry—have been produced by several techniques [18, 123, 19, 20, 122, 62, 63, 113] all which take different approaches to protecting one hemisphere of the colloidal particle while the other hemisphere is chemically modified. Generalizing this approach to multi-step protection reactions allows for the fabrication of ternary particles with three stripes of differing chemistry.[76, 82, 22] In another approach,[89] a microfluidic technique is used to create both ternary and Janus particles with diameters on the order of $100\,\mu$m. Larger number of stripes can be achieved through particle lithography, resulting in the precise local patterning of colloidal particles with features on the order of 100 nm.[135] Additionally, ellipsoidal striped colloidal particles can be created from the self-assembly of diblock copolymers. [68, 67] This procedure creates striped domains over the particle surface with feature size on the order of 50 nm. At the nanoscale, striped architectures have been formed on the surface of gold nano particles using a coating of organic molecules that assembles into stripes of subnanometer thickness.[66] Therefore there are many approaches to fabricating striped colloidal particles with various number stripes.

There are currently challenges to producing large quantities of high-quality striped particles[22]

as would be needed for experimental characterization of these new colloidal materials. Therefore computer simulations have played an important role in predicting potential novel properties of striped colloidal systems to guide experimental investigation. [138, 26, 27, 48, 83, 49, 109, 110, 40, 107] In their ground-breaking simulation of patchy interactions, Glotzer and Zhang [138] discovered the large number of different self-assembled architectures that can be realized by different patchy motifs. The patchy interactions of amphiphilic Janus particles—hydrophobic particles with attractive patches—where simulated by Sciortino and coworkers. [109, 110, 40] They found that systems of amphiphilic Janus particles formed small isolated clusters. The occurrence of a cluster-rich phase was found to result in novel thermodynamic and phase behavior. [109] They also showed that particles with patchy tetrahedral interactions form network structures with anomalous dynamics in another simulation investigation. [26, 27] The dipolar Janus (DJ) architecture—in which the two hemispheres have different electronic charge—was studied by Hall and coworkers using dipole models. [48, 49, 107] Their results exhibit rich phase behavior by DJ particles with dipole-like interactions. A similar dipole model was simulated by Hansen and coworkers to study the gelation dynamics of DJ colloids. [83] They discovered a novel two-step gelation process in their simulations. In summary, these previous simulation studies have shown the potential for novel structure and dynamics in striped and patchy colloidal systems.

In previous work,[52, 53] we have studied the static and dynamic properties of dipolar Janus (DJ) colloids using molecular dynamics simulations. A pointwise (PW) model of DJ particles was developed to capture the short-range geometry dependent interactions. Such interactions were shown to be important in reproducing the experimental cluster structures of DJ colloidal particles by Granick and coworkers.[62] Our model reproduces these experimental cluster structures.[52] Additionally, we considered the extent to which DJ colloidal systems could be modeled by an isotropically attractive interaction determined from coarse-graining (CG) the interactions of an isolated pair of particles. Surprisingly, it was found that the fluid structure of DJ particle systems was well captured by the isotropic CG model.[52] In contrast, we found that the CG model had accelerated dynamics (e.g. larger transport coefficients) than the PW model.[53] Physically, this suggest DJ colloids will have slower dynamics than comparable isotropic colloids (e.g. depletion attracting colloids). It would be useful if the accelerated dynamics of the CG model could be related

back to the original PW time-scale. To this end, we explored two time mapping methods:[53] time rescaling[88, 28, 55] and damping with Langevin friction[1, 93, 65]. Both methods were found to improve time correlation functions and transport coefficients, but did not reproduce the bond dynamics of the PW model in the CG model.[53] These results show that current dynamical mapping methods do not address all time and length scales and new methods may need developed.

In current work, we generalize our dipolar Janus models and methods to n-striped particles. Molecular dynamics simulations are used to quantify the effect of stripe number n on the static and dynamic properties. In Section 6.2, we develop models and simulations methods for the study of striped particles systems. Simulation results of n-striped particle systems are presented in Section 6.3. Results include the approximate phase behavior of different n-striped systems (presented in Section 6.3.1) as well as equilibrium structure and dynamics of striped systems as presented in Secs. 6.3.2 and 6.3.3 respectively. A discussion of these results—including their relation to other studies and a summary of conclusions—is provided in Section 6.4.

6.2 Methods

6.2.1 Models

We model a system of identical colloidal particles in which each particle has n stripes of alternating electric charge. Particles interact through a pairwise potential which includes both a softly repulsive isotropic core and a geometry dependent electrostatic term. The electrostatic term is calculated using a pointwise (PW) representation of the striped particle surface by point charges that are uniformly distributed across the surface of a sphere. Each point has the same charge magnitude needed to produce a surface charge density of σ. Each points charge sign is specified to produce a striped pattern.

This is an adaption of our PW model for dipolar Janus particles—an $n = 2$ striped particle—from earlier work.[52, 53] A full specification of the PW model is given in Section 4.2.1 The predominant feature of this model is that it captures the short-range geometry dependence of striped electrostatic interactions. Electrostatics are modeled with simple Coulombic interactions between point charges and these interactions are truncated at 15% of the particle diameter to account for electrostatic screening. It has been shown that such short-range geometry-dependent interactions capture

the experimental cluster structures of micron-sized dipolar Janus particles.[62] Our PW model for dipolar Janus particles reproduces these experimentally observed cluster structures (Section 4.2.1) as demonstrated by the fact that it captures the predominate interactions in this example striped colloidal systems. In the PW model, uncharged ($\sigma = 0$) particles have a characteristic diameter of $l = 220\,\text{nm}$ as due to the repulsive core and the PW pair potential has a cutoff distance of $230\,\text{nm}$.

In this chapter, we consider striped particles with a net neutral charge. This entails an equal number of positive and negative point charges across the surface of each particle. Additionally, for each n-striped PW model the stripe pattern is constructed so that all stripes of the same sign charge have roughly the same surface area. This optimal charge distribution is achieved by use of a computer program that explores many possible point charge distributions for each number of stripes. The program chooses the point charge distribution in which all stripes of the same charge sign are closest to having the same surface area. Distribution used to model striped particles studied in this work are shown in Figure 37 The resolutions of these models—i.e. the number of point charges n_p—is considered in Appendix A.1. Specifically, these models are compared to higher resolution models with the computation of pair quantities. Results show that these models are of sufficiently high resolution.

We also consider the extent to which striped particles can be modeled by an effective isotropic pair interaction. An isotropic companion model is constructed for each n-striped PW model and varies with surface charge density σ. The isotropic interaction is determined by numerically computing the partition function for an isolated pair of PW particles in one-dimension as a function of their separation distance r. From this r-indexed partition function the isotropic free energy profile, $A(r)$, is computed. Details of partition function computation are given in reference [52]. This procedure is equivalent to coarse-graining over orientations at a pair level and hence this model is labeled as the CG model of striped particles. Example CG interaction profiles are shown in Figure 38. A key feature of the $A(r)$ profiles is that their length and energy scales are similar to the pair interactions of depletion attracting colloidal particles.[38, 104] The similarity of a system of n-striped particles to a system of depletion attracting particles is quantified by simulating particle systems in both the PW and CG models and comparing results.

These isotropic interaction profiles are also useful for quantifying the strength of striped particle

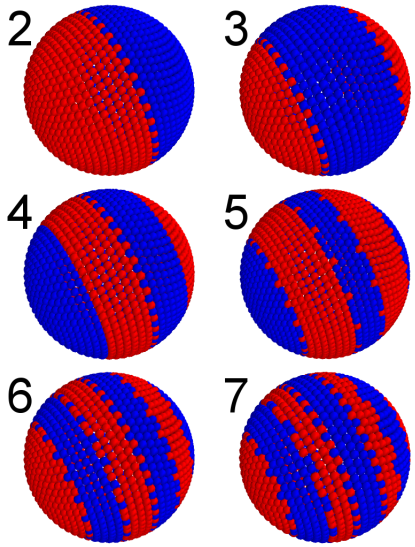

Figure 37: Point charge layouts for the PW model of n-striped particles in this work. Positive point charges are shown in blue and negative point charges in red. The number of point charges n_p used in each n-striped model is as follows: $n = 2$, $n_p = 1846$; $n = 3$, $n_p = 1652$; $n = 4$, $n_p = 1846$; $n = 5$, $n_p = 2248$; $n = 6$, $n_p = 1846$; and $n = 7$, $n_p = 1652$.

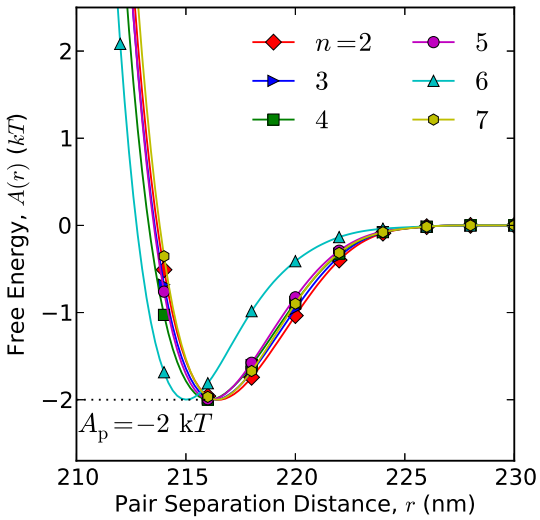

Figure 38: Free energy profiles for a pair of PW particles with different number of stripes n. For each n surface electrostatic density σ is specified to give a pair free energy minimum of $A_{\mathrm{p}} = -2\,k_{\mathrm{B}}T$ (see Table 3). These profiles are example isotropic interaction of the CG model. Units of y-axis are $k_{\mathrm{B}}T$ at $T = 300\,K$.

Table 3: Electrostatic charge densities, σ's, for the target pair affinities, A_p's, studied in current simulations. Charge density is given in units of $10^3\, e_0/\mu m^2$. The surface area of each striped particle in this model is $0.15\,\mu m^2$ such that the number of elemental charges (e_0) on each particle's surface is roughly one order of magnitude less than σ.

$-A_p$ (k_BT)	Number of Stripes, n					
	2	3	4	5	6	7
1	19.28	20.05	21.24	22.43	23.14	26.30
2	20.92	21.60	22.69	23.88	24.10	27.98
2.5	21.58	22.23	23.27	24.49	24.52	28.69
3	22.18	22.80	23.79	25.04	24.92	29.34
3.5	22.72	23.32	24.26	25.56	25.30	29.95
4	23.23	23.81	24.70	26.04	25.66	30.52

interactions in the both the PW and the CG models. The minimum of each free energy profile, A_p, is taken as characteristic of the pair interaction strength:

$$A_p = \min_r [A(r)]. \tag{53}$$

This quantity is related to the dimer equilibrium constant (as can be experimentally measured) and therefore it is a useful metric for comparison of future experiments with current results. The relationship between A_p and σ for each of the striped models considered in this work is shown in Figure 39. These functions $A_p(\sigma)$ are interesting in that they show how distributing the same charge density into a larger number of stripes does not always lead to weaker pair affinity. Specifically, deviations are seen for $n = 6$. We hypothesize that these deviations can be explained by on and off registry effects with respect to the alignment of the stripes between neighboring particles. These registry effects are explored in Appendix A.1. The results suggest that $n = 6$ particles have fewer unfavorable orientations at closer separation distances than other striped particles studied in this work. In simulation work we study different n-striped particles systems with common pair affinities on the order of $1\,k_BT \leq -A_p \leq 4.5\,k_BT$ for $T = 300\,K$.. The $A_p(\sigma)$ functions are inverted to specify the charge densities studied in simulation for these pair affinities. The charge densities simulated are listed in Table 3.

6.2.2 Simulation and analysis methods

Molecular dynamics simulations of striped particles are performed using the LAMMPS package[100] with a custom pair potential module for the PW electrostatics term. Simulation methods are adapted

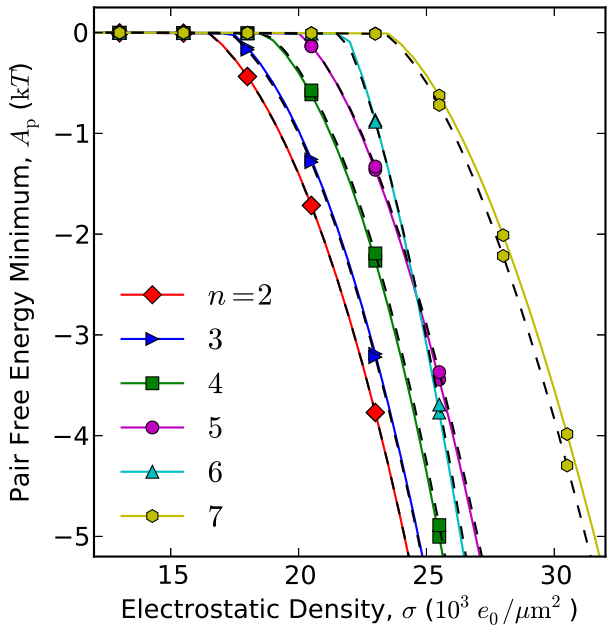

Figure 39: Relationship between the free energy minimum of a pair, A_p, and the electrostatic density σ across the surface of a *n*-striped particle. Results for different *n* are denoted by different plotting color and marker as labeled in the plot legend. Solid lines shows the results of computations for the point distributions used in simulations as shown in Figure 37. The results shown by dashed lines are computed with higher resolution models considered in Appendix A.1.

from our previous studies of dipolar Janus colloidal particles using the PW and CG models. The full details of these methods are given reference [52]. Each simulation consists on $N = 1000$ particles in a periodic cubic box. The dimensions of the box are adjusted to control the particle volume fraction ϕ. This is defined by the diameter of uncharged particles, $l = 220\,\text{nm}$, through

$$\phi = \pi N l^3 / 6V, \tag{54}$$

where V is the volume of the simulation box. In our earlier study of dipolar Janus particles,[52] we tested finite size effects on equilibrium observables by also performing simulations of $N = 4000$ particles for select conditions. Results were identical to those computed with $N = 1000$ suggesting that this system size is sufficiently large.

All simulation are initialized from a random and non-overlapping system of hard spheres of diameter l. The interactions of the PW or the CG model are introduced during thermal equilibration to a temperature of $T = 300\,K$ with a Langevin thermostat. This is accomplished using the LAMMPS algorithm "fix langevin" in conjunction with the "fix nve/asphere" algorithm. Thermal equilibration is performed with a time step of $\Delta t = 10\,\text{ns}$ and a thermostat relaxation time of $100\,\text{ns}$. Simulations are found to thermally equilibrate by $t \leq 10\,\text{ms}$ of simulation. Equilibration is quantified by a change in average excess internal energy of less than 1% over the last $2\,\text{ms}$ of simulation.

Equilibration trajectories are also used to investigate the conditions for which n-striped particle systems will form an equilibrated fluid state versus an arrested glass-like state. Each of these simulation is a nonequilibrium quench and we are interested in the progression of the internal energy with time $U(t)$. As will be discussed in Section 6.3.1 these quench results suggest phase transitions from a fluid state to a glass-like state with increasing pair interaction strength.

Additional simulation is used to compute the static and dynamic properties of particles systems that are found to equilibrate to a fluid state. In these production simulations, NVE molecular dynamics is performed starting from an equilibrated particle system. This accomplished using the LAMMPS algorithm "fix nve/asphere" with an integration time step of $\Delta t = 1\,\text{ns}$. For each set of conditions studied—(PW or CG model, ϕ, σ)—10 production trajectories are simulated. Each is initialized from a different equilibration trajectory. Production trajectories are of duration $2\,\text{ms}$ with

particle configurations sampled throughout. The present model does not include dissipation or hydrodynamics interactions due to the solvent. Such simple NVE models have provided key insight into colloidal dynamics: e.g. they have been used to study attractive melting.[99]

Static and dynamic properties of the particle systems are computed from the sampled configurations. These computations are performed during simulation—i.e. in real time—to avoid the need to store large trajectories on disk. Each quantity considered is computed by an algorithm that samples simulated configurations at a fixed interval of simulated time. Each algorithms averages multiple samples of each static or dynamic quantity throughout simulation to produce a single estimate at the end of simulation. Uncertainty in each computed property x is quantified from the distribution of x over the set of values, $\{x\}$, from the 10 different trajectories simulated. Error bars in figures show $2 \times \mathrm{se}(\{x\})$ where se is the standard error function. This show uncertainty estimates at the 95% confidence intervals.

The pair correlation function, $h(r)$, is computed to quantify equilibrium structure. This is accomplished by sampling particle configuration every $1\,\mu$s in production simulations. The separation distance r of each pair of particles in the configuration is computed using the minimal periodic image convention. These separation distances are histogramed throughout simulation using bin widths of $\Delta r = 1\,\mathrm{nm}$. This histogram is normalized at the end of simulation to give $h(r)$. The static structure factor, $S(k)$, is computed from $h(r)$ by

$$S(\vec{k}) = 1 + \rho \int \exp\left(-i\vec{k}\cdot\vec{r}\right) h\left(\vec{r}\right) \mathrm{d}\vec{r} \tag{55}$$

$$S(k) = 1 + \frac{4\pi\rho}{k} \int \sin(kr)\, h(r)\, r\, \mathrm{d}r \tag{56}$$

where ρ is the particle number density $\rho = N/V$.

The dynamics of simulated systems are quantified by computing time correlation functions. We consider both the mean squared displacement (MSD)

$$C_{\vec{R}}(t) \equiv \left\langle \left| \vec{R}(t_0 + t) - \vec{R}(t_0) \right|^2 \right\rangle_{t_0} \tag{57}$$

and the velocity autocorrelation function (VACF)

$$C_{\vec{v}}(t) \equiv \langle \vec{v}(t_0) \cdot \vec{v}(t_0 + t) \rangle_{t_0} \tag{58}$$

of particles. These time correlation functions are computed with multiple reference times, t_0, using the methods presented in reference [53]. MSDs are computed at a resolution of 200 ns up to a maximum time of 500 μs and VACFs are computed at a resolution of 50 ns up to 100 μs. These values were chosen from our previous study of dipolar Janus dynamics.[53] Additionally, the diffusion coefficients D are computed from these time correlation functions using the relationships

$$C_{\vec{R}}(t) = 6D_{\mathrm{MSD}}t + r_0^2 \tag{59}$$

and

$$D_{\mathrm{VACF}} = \frac{1}{3}\int_0^{t_{\max}} dt\, C_{\vec{v}}(t) \tag{60}$$

where $t_{\max} = 100\,\mu$s. The diffusion coefficients computed from both the MSDs and VACFs are comparable (within the error bars) in all cases. Reported values in results section are D_{MSD}.

The duration of reversible bonds between pairs of particles is also studied to more thoroughly understand the microscopic dynamics of striped particles in each model. A bond is defined as a pair of particles with a separation distance $r \leq r_{\mathrm{bond}}$ with $r_{\mathrm{bond}} = 230$ nm: i.e. the pair of particles is within the pair potential interaction range that is cutoff at 230 nm. The set of current bonds is tracked throughout simulation at a resolution of 50 ns. The duration of each reversible bond, t_{b}, is calculated by noting the time at which the bond is formed and the time at which it is subsequently broken. A histogram of bond durations is constructed throughout simulation. The histogram is normalized by the total number of particles in simulation and the duration of simulation to give the bond duration population, $f(t_{\mathrm{b}})$. This is the frequency at which reversible bonds within a range of durations t_{b} are observed.

6.3 Results

6.3.1 Approximate phase behavior

In computing the equilibrium structure of n-striped particle systems it is first necessary to determine the conditions for which molecular dynamics simulation of these models will equilibrate to fluid phases. This is in contrast to an arrested glass-like state as is found at stronger pair interactions and higher densities. From our earlier work with dipolar Janus colloids,[52] we had anticipated pair affinities on the order of $A_{\mathrm{p}} \approx -3\,k_{\mathrm{B}}T$ to equilibrate where as $A_{\mathrm{p}} \approx -4\,k_{\mathrm{B}}T$ would proceed towards

an arrested glass-like state for volume fractions of $\phi \leq 0.4$. We were surprised to find that this was not the case for all n-striped systems studied. For instance, $n = 3$ was found to form a collapsed and dynamically arrested state with pair affinities on the order of $A_p = -3k_BT$ at $\phi = 0.4$ (An example simulation configuration is shown in Figure 40.A). On the other hand, $n = 6$ was found to equilibrate to a fluid state with pair affinities as strong $A_p = -4.5k_BT$ at this same volume fraction (Figure 40.B). We note that both example configurations are for systems at the same volume fraction as clearly shows the collapsed structures with voids seen in snapshot A versus the more uniform distribution of particles in snapshot B. Additional configuration snapshots for all conditions studied are provided in Appendix A.1.

The conditions for fluid states are explored using nonequilibrium quench simulations. These simulations follow the equilibration procedure presented in Section 6.2.2. We are interested in the nonequilibrium relaxation of the excess internal energy with time, $U(t)$, in each of these quenches. For fluid states the quenches show a stabilization of $U(t)$ with time and particles are uniformly distributed throughout the simulation box. For the glass-like states, a collapsed and non-uniform particle structure is observed. The transition from fluid to glass-like with increasing pair affinities (larger magnitude A_p's) corresponds to a large drop in the excess internal energy which we take to correspond to a first order phase transition. We have reported this behavior earlier for $n = 2$ Janus particle.[52] The full set of $U(t)$ quench data is included in Appendix A.1 to show this behavior for each n-striped system.

We summarize the conditions for which we observe equilibrated fluid phases in our simulations using approximate phase diagrams shown in Figure 41. These diagrams detail the observation of fluid versus glass-like states at each set of conditions studied. Each diagram is for a different n-striped particle systems and results are shown for both the PW and the CG models. An approximation of the phase boundaries is shown in each panel with a red line corresponding to the PW model boundary and a green line showing that for the CG model. The CG model boundaries are generally comparable for the different n-striped systems. A deviation of these CG boundaries is seen for $n = 6$ as can be explained by the difference of the isotropic interaction for $n = 6$ versus the other striped models (Figure 38).

The PW boundary changes drastically across the different n's and in several cases a glass-like

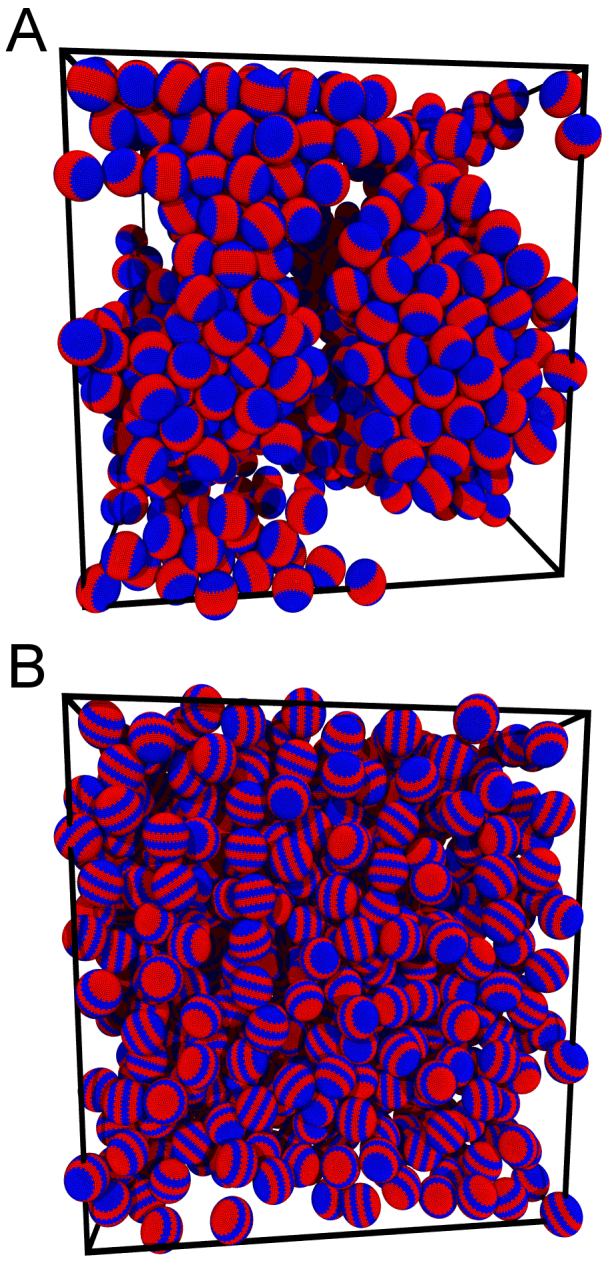

Figure 40: Example simulation snapshots from quench trajectories. Panel A show a configuration of a $n = 3$ stripe system at volume fraction $\phi = 0.4$, pair affinity $A_p = -3k_BT$, and quench time $t = 5.5\,\text{ms}$. This is a collapsed configuration with arrested dynamics (as seen in movies of the simulated system) and we consider these conditions to result in a glass-like state. Panel B is for a configuration of a $n = 6$ system at volume fraction $\phi = 0.4$, pair affinity $A_p = -4k_BT$, and quench time $t = 10\,\text{ms}$. This configuration is an equilibrated fluid state.

state is never observed in the PW model simulations. For $n = 2$ (Janus) the PW boundary is comparable to the CG boundary. This suggest dipolar Janus colloids will form arrested states at similar conditions for which arrest occurs in comparable depletion attracting colloid. In contrast, $n = 3$ (ternary) shows a substantially lower phase boundary with respect to pair affinity and this boundary is more strongly slopped with respect to volume fraction. These results suggest that ternary striped electrostatic particles will form glasses at higher temperatures than would be anticipated for depletion attracting colloids. This could be explained by the formation of particularly stable ordered structures in ternary particle systems. For $n = 4, 6, 7$ we do not observe glass-like states at any of the conditions studied. For $n = 5$ we only observe glass-like behavior at a single set of conditions: the highest volume fraction and strongest pair affinity considered. The resistance of these higher n-striped systems to arrest might be explained by structural frustration. It may be impossible to arrange such particles into energetically favored collapsed structures.

6.3.2 Equilibrium structure

We now consider the equilibrium structure of striped particle systems for conditions at which simulations equilibrate to a fluid. It is of particular interest to contrast the structure of the PW model to that of the CG model for each set of conditions. This contrasts the equilibrium structure of a striped colloidal particle system to that of a comparable isotropically attractive particle system. The structure factor, $S(k)$, is shown for three sets of conditions in Figure 42. Each panel of this figure shows results for a single volume fraction and pair affinity for all of the n-striped particles systems considered in both the PW and CG model. Surprisingly, all of the $S(k)$ function shown in each panel are comparable. Not only is the static structure comparable in different n-striped particle systems with the same pair affinities, but this structure is also captured by the CG models. This can be explained by the similarities of the isotropic CG interactions of different n-striped particle systems with similar pair affinities as quantified by A_{p}.

To show the striking similarities of the equilibrium structures of the PW and CG models for all conditions considered, we present the root-mean-squared (RMS) of structure factors in the two models

$$\sqrt{\langle (S_{\mathrm{PW}}(k) - S_{\mathrm{CG}}(k))^2 \rangle_k}. \tag{61}$$

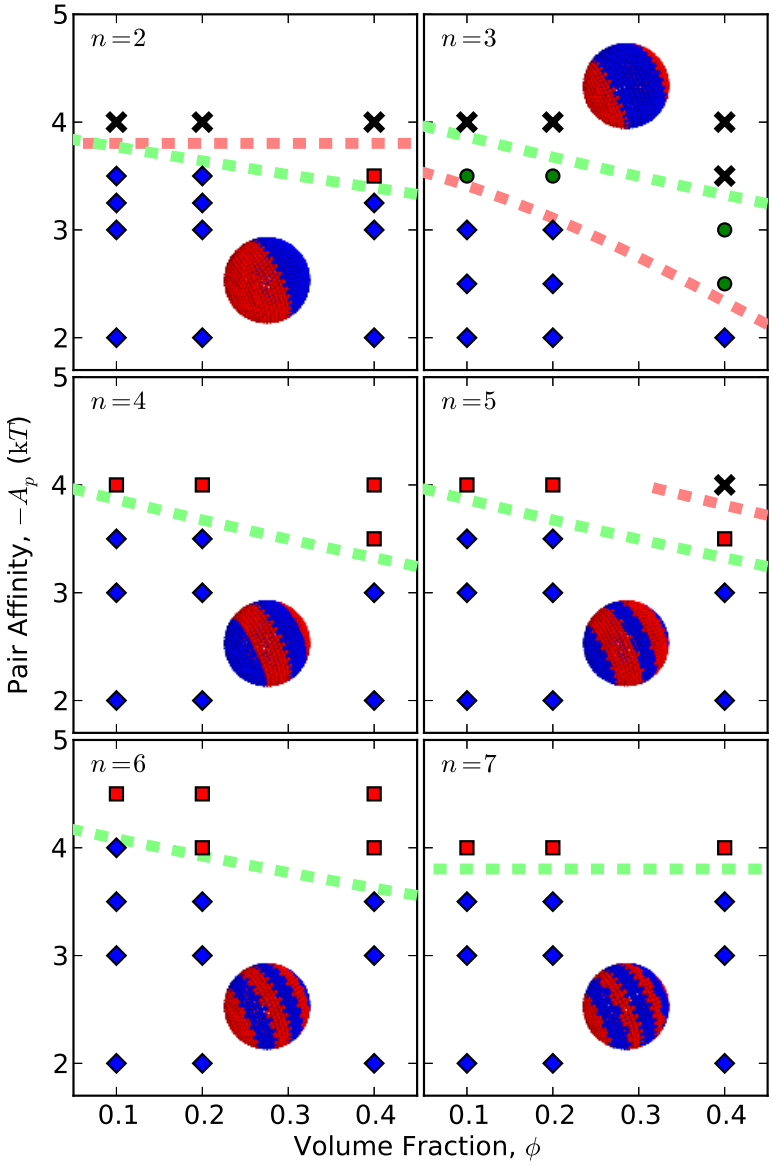

Figure 41: Approximation phase diagrams for striped particles with each panel showing results for a different number of stripes n. Markers denote whether nonequilibrium quench simulations suggest a glassy-like arrested state or an equilibrated fluid. Blue diamonds show conditions for which a fluid state is observed in both the PW and CG model. Black X's denote glass-like arrested states in both models. Red squares show conditions for which the fluid state is observed only for the PW model where as green circles show the opposite case where a fluid state is observed only for the CG model. The red and green lines lie approximately on the phase boundaries between fluid and glass-like states for the PW and CG models, respectively, and are shown so as to highlight these transition regions.

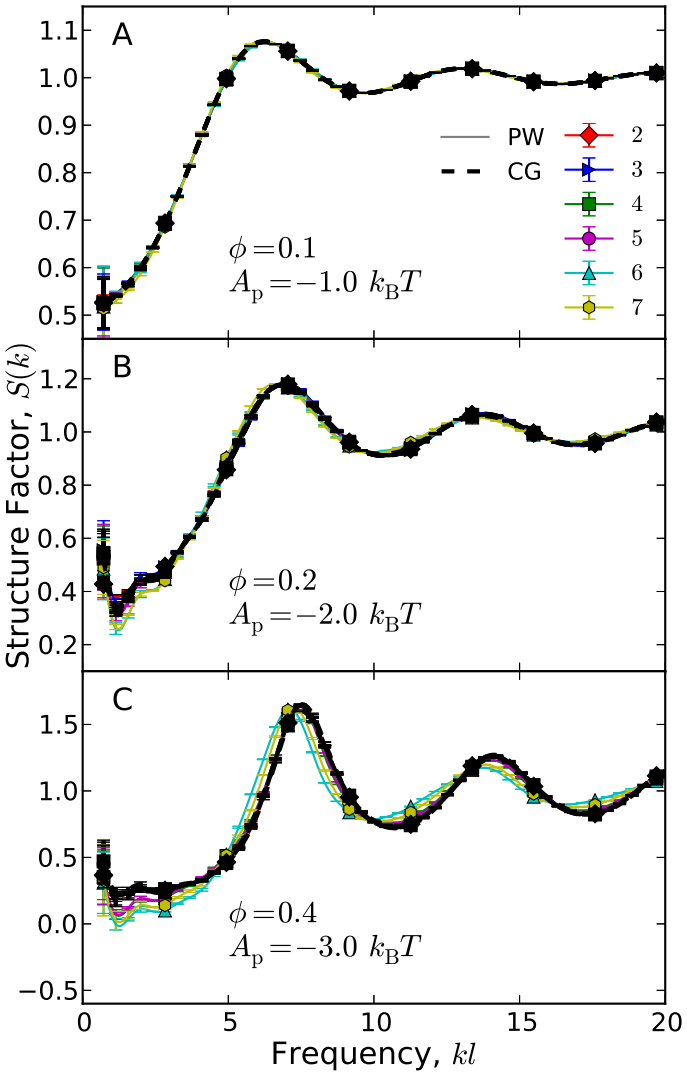

Figure 42: The structure factor $S(k)$ for different n-striped particle systems in both the PW and CG models. Each panel shows results at a different set of conditions: volume fraction ϕ and pair affinity A_p. Results of the PW model are shown with solid lines and the color of the line specifies the number stripes as labeled on the plot legend. CG model results are shown with dashed black lines. Plotting markers are included every 50 points to better denote the curves for different n stripes. Error bar are included every 10 points and most error bars are comparable to plotting line width. Panel C does not include results for $n = 3$ in the PW model as these simulations did not equilibrate to a fluid state.

This quantity is presented in Figure 43 for all conditions studied. The CG model well captures the structure of the PW model for all of these conditions with RMS differences in $S(k)$ on the order of 0.01. Since the CG models of different n-striped particle are similar, the different n-striped particles systems all have comparable equilibrium structure at the same ϕ and A_p conditions. These results suggest that pair affinity alone is the crucial quantity in determining the fluid structure of electrostatic striped colloidal particle systems. Further, this structure is similar to comparable isotropically attractive particles such as depletion attracting colloids. All of the $S(k)$ functions computed at different conditions are included in Appendix A.1.

6.3.3 Equilibrium dynamics

Our models and methods were specifically developed to allow for the study of the dynamics of striped particle systems. The dynamics of n-striped systems in the PW model are contrasted to dynamics of the CG model for the range of conditions consistent with an equilibrated fluid. These dynamics are quantified by time correlation functions. In general, results show that the CG model has accelerated dynamics relative to the PW model for the same range of conditions for which the two models had identical static structure. The mean squares displacement (MSD), $C_{\vec{R}}(t)$, for three set of conditions are shown in Figure 44. Each panel presents the MSDs for one sets of conditions (ϕ and A_p) and includes results for all of the n-striped systems studied in both the PW and CG models. At lower volume fraction and weaker pair interaction (Figure 44.A) all of the $C_{\vec{R}}(t)$ results are comparable. In contrast, at the highest volume fraction and strongest pair interactions considered (Figure 44.C) significant differences are seen. All of the CG MSDs at these conditions are comparable with $n = 6$ showing slightly faster dynamics. This can be explained by the difference of the isotropic interaction profile for $n = 6$ versus the other n-striped models. The PW MSDs show slower dynamics with a spread of $C_{\vec{R}}(t)$ results over the different n-striped systems. Janus particle ($n = 2$) are found to have the fastest dynamics where as $n = 5$ has the slowest. The MSD for other values of n are comparable.

The velocity autocorrelation functions (VACFs) are also computed as shown in Figure 45. As with the MSDs, the different VACFs are comparable at the lower volume fraction and pair affinity shown in panel A. Significant deviations between the PW and CG models are seen for the densest

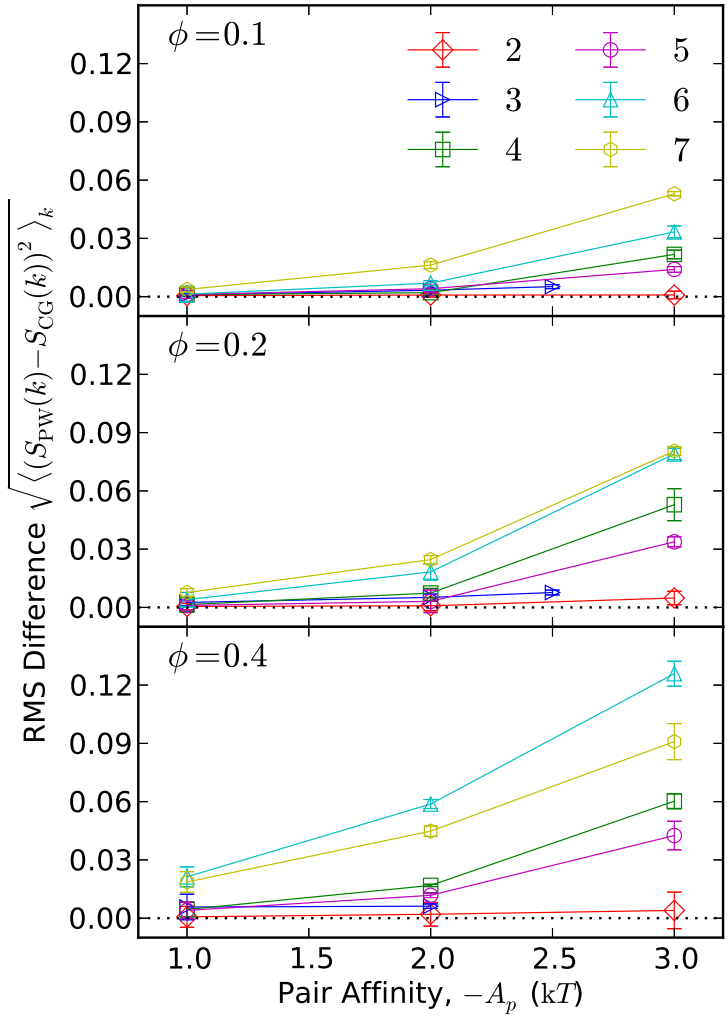

Figure 43: RMS difference of the structure factor, $S(k)$, of the PW model and the CG model as a function of pair affinity. Each panel shows results for a different volume fraction ϕ. Different curves are for different n-striped particle systems as denoted by color and marker as labeled on the plot. Markers show results with error bars. Line are included only to guide the eye.

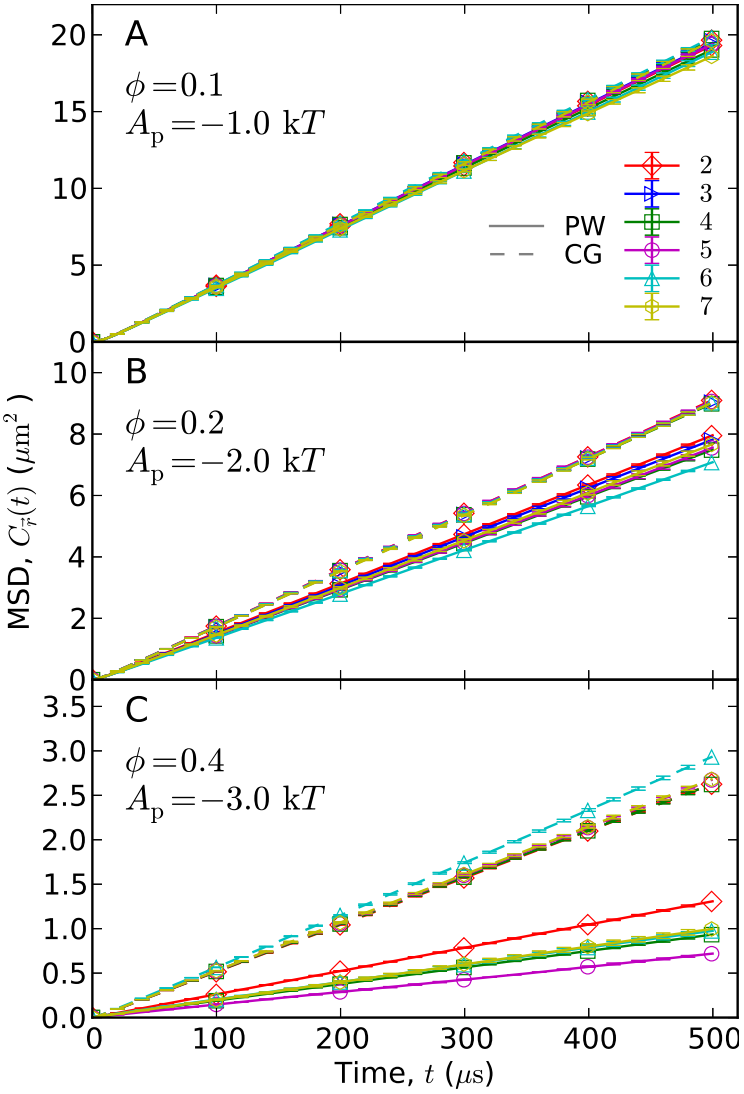

Figure 44: The mean squared displacement (MSD), $C_{\vec{R}}(t)$, for different n-striped particle systems in both the PW and CG models. Each panel shows results at a different volume fraction ϕ and pair affinity A_p. Results of the PW model are shown as solid lines and dashed lines show those for the CG model. Results for different n-striped system are shown in different colors as labeled on the plot legend. Plotting markers are included every 500 points to better denote the curves for different n stripes. Error bar are included every 100 points and in most cases they are comparable to plotting line width. Panel C does not include results for $n = 3$ in the PW model as these simulation did not equilibrate to a fluid state.

and strongest interacting conditions shown in panel C. The VACFs of the CG models for different n-striped particle systems are comparable with some deviation seen for $n = 6$. The PW VACFs are spread out with $n = 2$ having the strongest velocity correlations and $n = 5$ showing the weakest correlations for times of $1\,\mu\text{s} \lesssim t \lesssim 10\,\mu\text{s}$. These results are consistent with the MSD results. The general shape of $n = 6$ is different from all of the other VACFs. It has the strongest correlations for the times of $t \lesssim 0.5\,\mu\text{s}$ and these correlation quickly decay to be among the weakest for times of $t > 1\,\mu\text{s}$. This shows that $n = 6$ striped particles have different microscopic dynamics than other n-striped particle systems. The full set of MSD and VACF data for all conditions studied is provided in Appendix A.1.

The diffusion constants are computed to compare transport in different n-striped particles systems across the range of conditions studied. These results are shown in Figure 46. The general trends in these results are consistent with those of the time correlation functions. The diffusion constants in the CG models of different n-striped systems are comparable for most conditions. Some small deviations are seen for $n = 6$. Slower dynamics are observed in the PW model relative to the CG model for all conditions. Additionally, different n-striped PW systems have different diffusion constants for the same volume fraction and pair affinity. For the lowest volume fractions considered, $\phi = 0.1$, the diffusion constants for different n are comparable for pair affinities of $-A_\text{p} \leq 3\,k_\text{B}T$. Larger deviations are seen at the highest volume fraction of $\phi = 0.4$. In general, higher n-striped systems show slower diffusion at this higher volume fraction, although there are exceptions. For instance, $n = 5$ shows the slowest diffusion constant for $\phi = 0.4$ and $A_\text{p} = -3\,k_\text{B}T$. The diffusion of higher n-striped PW-systems continue to slow with increasing pair affinity of $-A_\text{p} \geq 3.5\,k_\text{B}T$. Such pair affinities did not equilibrate to fluid phases for the CG model nor for lower n's in the PW model.

A non-monotonic relationship between pair affinity and diffusion constant is found (Figure 46) where in the diffusion constant first increases with increasing pair affinity and then decreases with stronger pair affinities. This affect is strongest for the CG models at the higher volume fraction of $\phi = 0.4$. Similar behavior has been previously reported in both experimental and simulation studies of isotropically attractive colloidal particles. [99] This behavior has been explained through the theory of attractive melting wherein the introduction of weak attraction increases the free volume

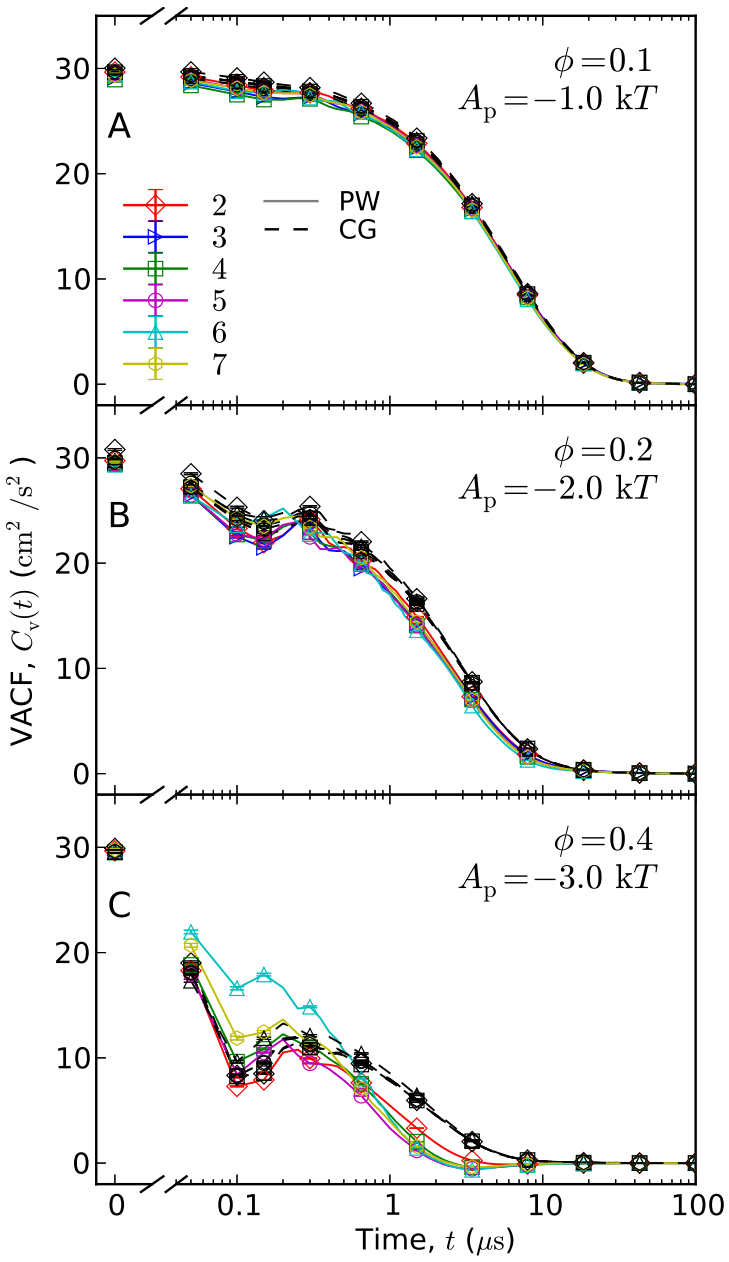

Figure 45: The velocity autocorrelation functions (VACF), $C_{\vec{v}}(t)$, for different n-striped particle systems in both the PW and CG models. Each panel shows results at a different volume fraction ϕ and pair affinity A_p. Results of the PW model are shown by solid lines and different line colors specify different n-striped systems as labeled on the plot legend. CG model results are shown with dashed black lines. The log-scale x-axis is broken to include the zero time value. VACF are computed at a time resolution of $\Delta t = 50$ ns and markers are only shown at select data points to better distinguish the curves. The lines between short time markers are linear interpolations to guide the eye. Panel C does not include results for $n = 3$ in the PW model as these simulation did not equilibrate to a fluid state.

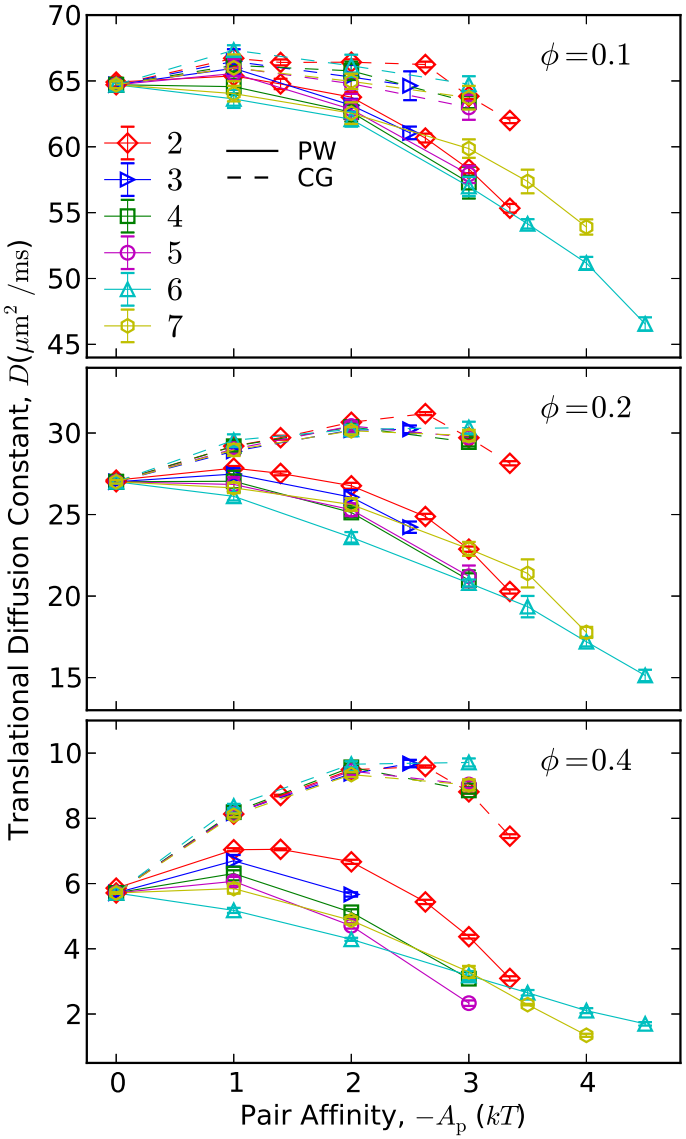

Figure 46: Diffusion constants in different n-striped particle systems. Each panel shows results for a different volume fraction and each curve is for a different n as denoted by plotting color and marker (labeled on the legend). Solid lines show the results of the PW model where as the CG model results are shown with dashed lines. Markers are computed results and include error bars. The lines serve only to guide the eye. The $A_p = 0 k_B T$ results correspond to the uncharged case ($\sigma = 0$) where particles are isotropically repulsive and the different models are identical. Addition data for $n = 2$ is provided from our earlier study of dipolar Janus particles.[53]

as enhances the mobility of particles. Stronger attraction diminishes the mobility through attractive bonding. We find stronger attractive melting effects in the CG model than in the PW model for all n studied. In fact, a strictly monotonically decreasing relationship between pair affinity and diffusion constant is found in the PW model for $n = 6$ at $\phi = 0.4$. Therefore striped electrostatic colloidal systems are predicted to have weaker attractive melting effects than comparable isotropically attractive colloidal systems.

To highlight the difference of the diffusion constants in the PW and CG models we plot their ratio, $D_{\mathrm{CG}}/D_{\mathrm{PW}}$, as the dynamical acceleration in the CG model (Figure 47). At lower volume fractions, $\phi = 0.1$, the dynamical accelerations is only on the order of 1.2 and it is comparable in all of different n-striped systems. For $\phi = 0.4$, dynamical accelerations as large as ≈ 4 are found. Further, the extent of dynamical acceleration varies with n. It is interesting that the largest dynamical acceleration, on the order of 4, is found to occur with $n = 5$. At these conditions, Janus particles ($n = 2$), only show a dynamical acceleration of roughly 2. The other n-striped system show comparable dynamical accelerations on the order 3. We again note that the CG models for different n have comparable diffusion constants at each set of conditions. Therefore these dynamical acceleration results highlights the extent to which different striped architectures can affect transport properties.

We also study the duration of reversible bonds, t_{b}, in the PW and CG models to gain addition insight into microscopic dynamics. The distribution of bond durations—the bond population $f(t_{\mathrm{b}})$—is shown in Figure 48 for three set of conditions. Similar bond population are found in both models and for all n at the lower density and weaker pair interactions shown in panel A. These $f(t_{\mathrm{b}})$'s show a peak near $t_{\mathrm{b}} \approx 0.4\,\mu$s. In our previous study of Janus particles using these models,[53] we identified this time scale as being characteristic of repulsive collisions. With the increased interaction strengths shown in panels B and C, broader tails are introduced for times of $t_{\mathrm{b}} \geq 5\,\mu$s and these longer duration reversible bonds are associated with attractive bonding. Additionally, a spread of $f(t_{\mathrm{b}})$'s are found in panels B and C. The bond populations of the CG models for the different n-striped systems are comparable at these conditions as is consistent with that observed for time correlation functions and diffusion constants. The PW models $f(t_{\mathrm{b}})$'s are substantially different from those of CG model and further they vary with n.

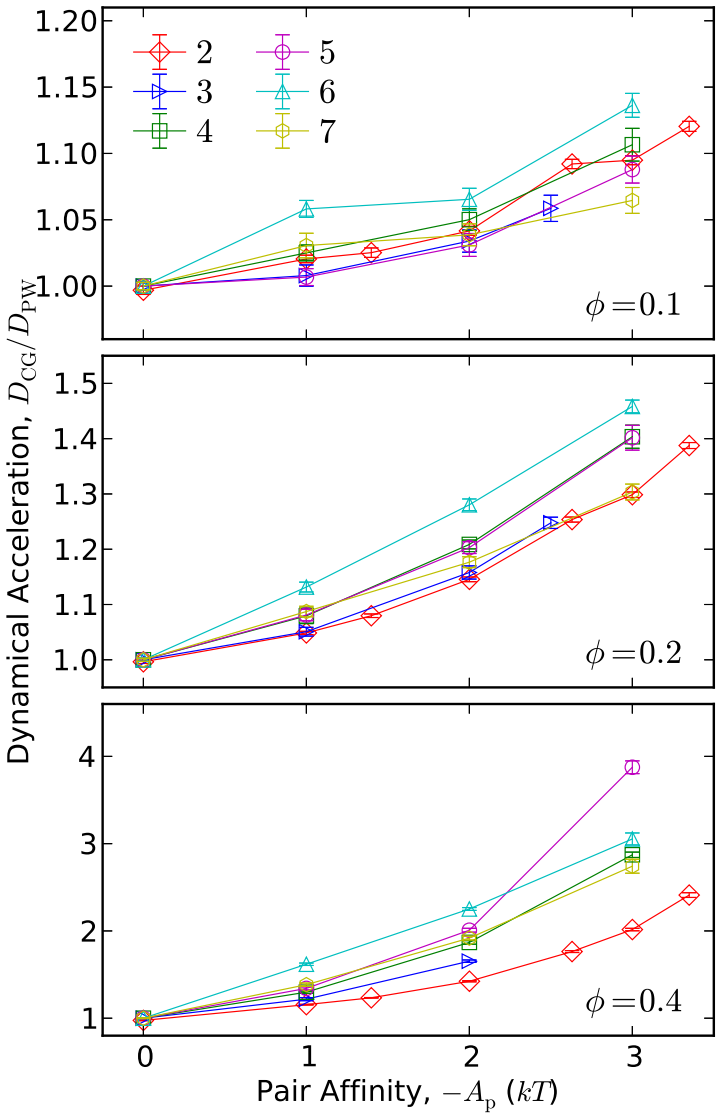

Figure 47: The dynamical acceleration, i.e. the ratio of diffusion constant in the CG model to that of the PW model, for the range of conditions studied. Results for different volume fraction are shown in different panels and are plotted as a function of pair affinity. The number of stripes, n, is denoted by different plotting color and markers as labeled on the plot legend. Markers show the results of simulation and include error bars. Lines are included only to guide the eye.

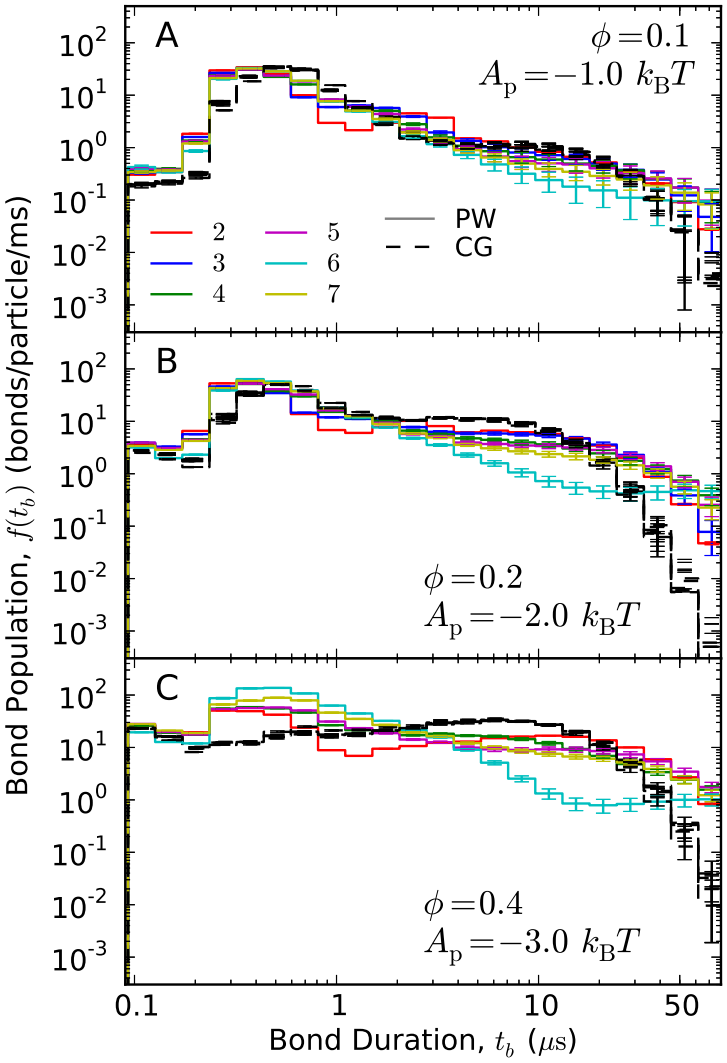

Figure 48: Bond population results: i.e. the frequency at which reversible bonds of duration t_b are observed in simulation. Each panel shows results for a different volume fraction ϕ and pair affinity A_p. Results of the PW model are shown as solid lines and different line colors specify different n-striped systems as labeled on the plot legend. CG model results are shown with dashed black lines. The CG results for different n are comparable and cannot be distinguished from each other. Bond populations are computed through the construction of a histogram of $\log(t_b)$ and plotting lines show bin widths. Error bars are included. Panel C does not include results for $n = 3$ in the PW model as these simulation did not equilibrate to a fluid state.

To highlight the difference in bond dynamics in the PW and CG models, we plot the ratios of bond populations in the two model, $f_{\mathrm{CG}}(t_{\mathrm{b}})/f_{\mathrm{PW}}(t_{\mathrm{b}})$, as shown in Figure 49. As the bond populations in the CG model are comparable for different n, these results also highlight the differences in bond durations for different n-striped systems in the PW model. In general, the PW model is found to have more short-duration bonds—bond durations on the order of $t_{\mathrm{b}} \lesssim 0.4\,\mu$s—as well as more long-duration bonds—$t_{\mathrm{b}} \gtrsim 10\,\mu$s—than the CG model. A deviation is observed for $n = 6$, which shows substantially fewer bonds of duration $5 \lesssim t_{\mathrm{b}} \lesssim 30$ than seen for other n-striped systems. The full set of bond population results for all system studied is provided in Appendix A.1.

The average number of bonds formed by each particle can provide insight into the simulated state of matter. If each particle only forms at most a single bond at each point in time then the system may be described as gas-like. For such conditions, it would not be surprising that the CG model adequately describes the system structure. With larger number of bonds—particularly the case where each particle forms bonds with multiple neighbors—the state of matter would be better described as a fluid. We have computed the number of bonded neighbors that a particles has on average for one example system at two densities (the lowest and highest densities studied). Specifically, we consider the Janus system ($n = 2$) in the PW model with particle charge densities of $\sigma_r = 22.18\,e_0/\mu\mathrm{m}^2$ ($A_{\mathrm{p}} = -3\,k_{\mathrm{B}}T$). For $\phi = 0.4$, each particle has 3.9 bonds on average and is far beyond the dilute gas limit. For $\phi = 0.1$, each particle has 0.90 bonds on average and therefore is the closest to the gas limit. However, even then, that number of bonds is far from the near-zero interactions typical of a gas. This suggests that the agreement between the CG model and the PW model is not the result of each particle rarely interacting with a neighboring particle. Instead, each particle interacts with multiple neighbors.

6.4 Discussion

The fluid structure of striped electrostatic particles in the PW models is captured well by the corresponding isotropic CG models. In contrast, the CG models have accelerated dynamics relative to the PW models as we also saw earlier in the case of Janus colloids. [52, 53] The accelerated dynamics of the CG model can be mostly attributed to the loss of longer duration reversible bonds

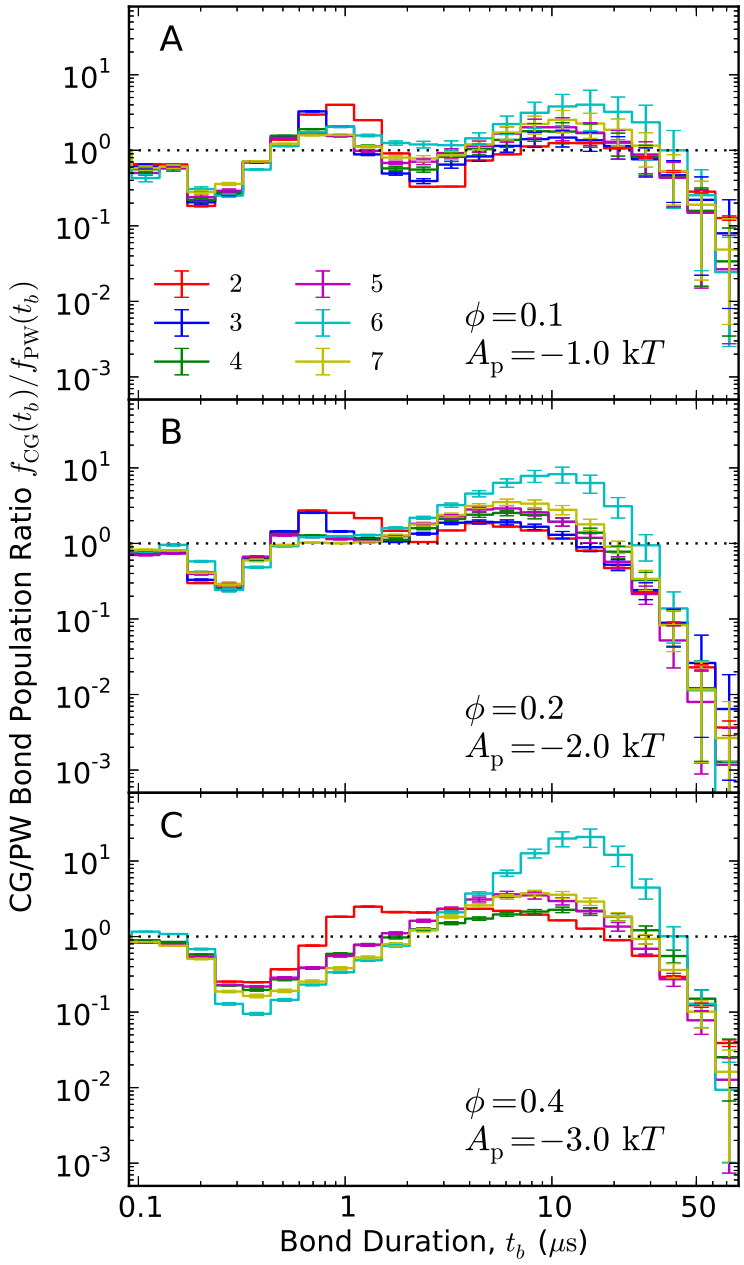

Figure 49: The ratio of bond population in the CG model to that of the PW model. Each panel shows different conditions as correspond to the panels in Figure 48. Results for different n-striped systems are shown by different color lines as labeled on the plot legend. Error bars are included. Panel C does not include results for $n = 3$ in the PW model as these simulation did not equilibrate to a fluid state.

between pairs of particles with the coarse-graining of the striped electrostatic interaction. Physically, this suggests striped electrostatic colloidal particles will exhibit the fluid structure of comparable isotropically attractive colloids—such as depletion attracting colloids—while having slower dynamics as a consequence of the longer-duration reversible bonds. A larger number of stripes generally leads to slower dynamics. This demonstrates a decoupling of static and dynamic properties with electrostatic striped interactions in that the dynamic properties can be tuned through a change in the number of stripes.

Although several observables of striped particle systems appear to follow trends with increasing number of stripes n, striped particles with $n = 6$ exhibited small deviations in both the PW and CG models. This includes a slight shift in the structure factor in both models (as seen in Figure 42), faster dynamics in the CG model than other n's at the same conditions (as seen in Figure 44 and 46), and qualitative differences in both the velocity autocorrelation functions (as seen in Figure 45) and the bond populations (as seen in Figure 49) in the PW model. The differences in the CG model can be explained by a shift in the pair free energy profile for $n = 6$ particles relative to other n's as shown in Figure 38 We attribute this shift to a difference in how pairs of $n = 6$ striped particles in PW model interact with each other. In particular, for a given pair separation distance, the relative number of favorable contacts between adjacent particles depends on the number of stripes on the colloids and the degree to which they are commensurate between the pairs. Further, the present results suggests that the $n = 6$ striped colloids have a slightly better degree of commensurability between the number of stripes and the degree of favorable contacts between stripes. By extension, these differences in the pair interactions may explain the dynamical differences of $n = 6$ systems in the PW model.

The phase behavior of striped particles is found to vary with the number of stripes. For ternary ($n = 3$) particles, glass-like states were observed for weaker pair affinities than that found for other n. This suggests that among the n-striped colloidal particles, the ternary electrostatic striped particles may form particularly stable structures. Additionally, these glass-like states at weak pair affinities were only observed in the PW model and not at all in the CG model. Therefore we predict ternary striped colloidal particles to form glass or gel states at higher temperatures than has been found for isotropically attractive colloidal particles (e.g. depletion attraction) with comparable pair affinities

as quantified by the dimer equilibrium constant. In contrast, the approximate phase diagram for Janus particles ($n = 2$) show similar fluid/glass-like boundary approximations in both the PW and CG model. This suggest that dipolar Janus particles form glasses and gels at similar conditions to those for of attractive colloidal particles. These predictions should be experimentally accessible in the near future as both Janus[123, 19, 62, 69] and ternary motifs[89, 76, 22] have been successfully fabricated. We find that striped particle systems with larger number of stripes, $n \geq 4$, are resistant to the formation of collapsed and arrested structures. For $n = 4$, 6, and 7, fluid-like states are observed with pair affinities as strong as $A_{\mathrm{p}} = -4\,k_{\mathrm{B}}T$ at volume fractions as high as $\phi = 0.4$. At these conditions the CG model is found to form arrested glass-like states. This suggests electrostatic striped colloidal particles will be resistant to arrested states at lower temperatures than comparable isotropically attractive colloidal particles. We attribute this behavior to structural frustration in that higher striped particles cannot be arranged into energetically favorable compact structures.

These simulations results for electrostatic striped colloidal particles can be contrasted to those of other structured colloidal particles. In the simulation of amphiphilic Janus particles, Sciortino and coworkers[109, 110, 40] found the formation of isolated clusters for comparable volume fractions including $\phi = 0.1$. The authors have explained the significance of clusters by the energetic stability of small micellar clusters of amphiphilic Janus particles as opposed to large structures.[110] This is not found to occur in simulations of dipolar Janus particles[52] as attributed to the net asymmetric distribution of charge in clusters of dipolar Janus particles[62]. These interactions favor the formation of larger structures as opposed to isolated small clusters. Current simulation of striped electrostatic particles show similar behavior to dipolar Janus particles in that isolated cluster structure are not observed. Instead, their fluid structure is comparable to isotropically attractive colloidal particles with a collapsed structure found at stronger pair interactions. It is possible that shape asymmetry (e.g. striped electrostatic ellipsoid particles) could change cluster structure as could lead to the formation of clusters in fluid phases. Such a change in cluster size and structure with shape asymmetry has been observed in simulations of ellipsoidal amphiphilic Janus particles. [79]

Other authors have simulated dipolar Janus particles ($n = 2$) using models with strong dipole character and the inclusion of long-range electrostatics.[48, 83, 49, 84] Hall and coworkers model consists of hard spheres with two embedded point charges.[48, 49] A dipolar dumbbell model was

used by Miller and coworkers.[83] Moghani and Khomami also used a pointwise surface model, a similar approach to our PW model, to study nanometer dimension Janus spheres and they further included long range electrostatic and electrostatic screening with the simulation of ions.[84] In all of these studies, significant chain structures were reported. [48, 83, 49, 84] We have previously shown chain structures do not occur in our PW model for dipolar Janus colloids, but instead compact clusters are found.[52] This highlights a difference in the long-range dipolar character models versus short-range geometry dependent models. Experimentally, both compact clusters[62, 137, 113] and chains[121, 70, 113] have been reported for dipolar Janus particles as shows that both types of models are need to describe different conditions. The transition between these two classes of structures with increasing solvent ionic strength—as screens the long-range electrostatic—has recently been observed in experimental study of amphiphilic Janus spheres and ellipsoids.[113] For small particles and weak ionic strength solvent the long-range dipole character should dominate where as for large particle and strong ionic strengths the short-range geometry dependence will dominate. Intermediate conditions may require a hybrid model that combines both the short-range and the long-range characters. Moghani and Khomami model for dipolar Janus particles does an excellent job capturing this behavior[84] as they have shown the transition from rings to chains and then to more compact structures with increasing solvent ionic strength. Their methods could be extended to electrostatic striped colloidal particles to study their structures at a range of screening conditions. Moghani and Khomami methods were developed to study dipolar Janus particles with diameters of 5 nm to 7.5 nm. It may be challenging to apply these methods for the simulation of larger colloidal particles as a prohibitively large number of ions would need simulated. To study systems of large striped colloidal particle at condition for which long-range electrostatics dominates, mutipole expansion methods of heterogeneous charge colloidal particles[8, 25] could be used. The results of such a study could be contrasted to this current study of striped particles when short-range electrostatics dominate.

In another direction, our nonequilibrium quench simulation could be extended to study the nonequilibrium behavior of electrostatic striped colloids. This would include simulation of the glasses and gels formed by striped colloidal particles. For isotropically attractive colloidal particles, such simulations have provided significant insight into the formation of glasses and gels.

[9, 37, 41, 102] As an example, Puertas, Fuchs, and Cates[102] simulation work has shown that aging of attractive colloidal glasses is similar to that of repulsive colloidal glasses. It would be interesting to contrast the aging of striped colloids gels to the aging of isotropically attractive colloidal gels. This could be accomplished by performing aging simulation of both the PW and CG models. As current work shows that the dynamics of the two models already differ at equilibrium conditions it would be anticipated that their aging under nonequilibrium conditions may differ substantially. In such a study, one would aim to perform long simulations to investigates the latest stages of aging that can be accessed in simulation. This may prove challenging for our current PW model as it is computationally expensive (roughly 100 times slower than the CG model). To address this issue, we are developing a tabulated version of the PW force field for such future long-duration simulations. Preliminary results suggests that the new force field can provide an order of magnitude improvement in computational efficiency. Another approach would be to relate the dynamics of the CG model to the time-scale of the PW model as would allow one to study the nonequilibrium behavior of striped colloidal particles with coarse-grained methods. Such time-mapping methods are considered in the subsequent discussion of dynamical acceleration of coarse-grained model.

The dynamical acceleration of the CG model relative to the PW model in this study is an instance of the general trend of coarse-grained models to have accelerated dynamics relative to the detailed model from which they are developed. This has been reported for various coarse-grained models, [80, 88, 28, 65, 81, 85, 55, 2] including models for polymers[88, 80, 28, 55] and water.[65, 85, 2] There is interest in relating the accelerated dynamics of the coarse-grained model to the original time scale of the detailed model using dynamical mapping methods.[1, 93, 88, 28, 65, 55] These methods allow for the study of dynamical properties using computationally efficient coarse-grained models. Such methods could be applied to the CG model of electrostatic striped particles developed in current work to study the dynamics of these systems with coarse-grained methods. This would be particularly useful in a nonequilibrium study of the glasses and gels formed by electrostatic striped colloidal particles as long-duration simulation are needed. Additionally, such mapping methods can provide insight into how the dynamics of electrostatic striped colloidal particles are related to the dynamics of isotropically attractive colloidal particles by explaining the dynamical mapping of the CG model to the PW time-scale. In our previous study of dipolar Janus dynamics[53] we

have applied two such dynamical mapping methods—time rescaling[88, 28, 55] and damping with Langevin friction[1, 93, 65]—to map the dynamics of the CG model for dipolar Janus particles to the time scales of the PW model. Both methods successfully mapped the diffusion constants of the CG model onto that of the PW model and improved the time correlation functions.[53] In contrast, these methods did not map the bond population results. Therefore these methods cannot be said to reproduce the PW dynamics in the CG model for all time and length scales. The deficiencies of these time mapping methods could have significant consequences in mapping the nonequilibrium behavior of the CG model to the PW time scales. New dynamical mapping methods may need developed for such studies.

In conclusion, we have constructed new pointwise (PW) models for striped electrostatic colloidal particles and investigated their static and dynamical properties with molecular dynamics simulations. Surprisingly, the fluid structure of striped particle systems is found to be well captured by isotropic coarse-grained (CG) models for the range of conditions studied. Therefore these systems are predicted to have structure similar to that of isotropically attractive colloids such as depletion attracting colloids. In contrast, the CG models are found to have accelerated dynamics relative to the PW models as suggests these systems will have slower dynamics than comparable isotropically attractive colloids. The slower equilibrium dynamics suggests the nonequilibrium behavior of striped electrostatic colloidal particles may be quite different from that of isotropically attractive particles. The nonequilibrium behavior of electrostatic striped particles may be the focus of future work.

CHAPTER VII

CONCLUDING REMARKS AND OUTLOOK

7.1 Concluding Remarks

In this thesis, methods have been developed for the dynamical simulation of structured colloidal systems. This includes new models for the novel interactions of structured colloidal particles. Simulation results demonstrate how the structured colloidal interactions influence particle order and dynamics. These static and dynamic results suggest novel materials properties for new colloidal technologies. The results of each structured particle project are briefly summarize in this chapter.

7.1.1 Gelation dynamics of electrostatically-stabilized depletion associating latex particles

In Chapter 3 we studied how radially-structured colloidal interactions influence the dynamics of colloidal gelation. The radially structured interaction occurs in electrostatically-stabilized depletion associating (ESDA) latex particles.[111, 114] The interaction includes short-range attraction and longer-range repulsion as creates an energetic barrier to pair association. It was previously unknown how this energetic barrier would affect the dynamics of flocculation for a non-dilute system of colloidal particles. In this thesis, we have explored this process using Brownian Dynamics computer simulations and analytic theory.

An Arrhenius-like time-rescaling theory is found to describe the effect of an energetic barrier on the gelation dynamics of dense colloids. Specifically, this theory explains the time-evolution of the extent of pair bonding throughout simulated gelation for different barrier heights. Pair bonding is quantified by the probability distribution of particle coordination numbers, $P_n(t)$; i.e. the probability that a particle forms n bonds with other particles. The scaling theory is found to describe the time-evolution of the this probability distribution throughout the simulated gelation of dense colloids.

At lower volume fractions, $\phi \lesssim 0.2$, the scaling theory does not adequately describe the gelation dynamics. This can be attributed to the importance of spatial diffusion at lower volume fractions as not accounted for in current theory. This is not an entirely negative result. It shows that there is a complicated relationship between the energetic barrier height and colloidal gelation dynamics

at lower volume fractions. Analysis of the gelation network structure in simulation suggests that different flocculation pathways are followed at different barrier heights. The difference in gelation structure at different barrier heights may be of interest for new colloidal technologies.

7.1.2 Modeling dipolar Janus colloids

In Chapter 4 of this thesis, new models were developed to capture the surface structured interactions of dipolar Janus (DJ) colloids. This includes the pointwise (PW) model (developed in Section 4.2.1) that captures the short-range geometry dependent interactions of DJ particles. Previous DJ models[48, 83, 49, 84] had focused on the long-range dipole character of DJ particles and were found to predict linear chain formation. While chains have been observed in some experiments of DJ particles, [121, 70, 113] other studies have found compact clusters.[62, 137, 113] Studies suggesting compact clusters include the rigorous experimental and simulation investigation of DJ cluster structures performed by Granick and coworkers.[62] They have stressed that DJ particles are too large to be modeled as dipoles and instead a pointwise surface-model is needed to capture the short-range geometry dependent DJ interactions. Our PW models builds off the work of Granick and coworkers. The key ingredient of our reformulation is to use only continuous terms in the PW model so as to facilitate molecular dynamics simulation. In Section 4.2.1 it was shown that the PW model accurately captures the short-range geometry dependent interactions of DJ particles in that it reproduces the cluster structures observed in the experimental work of Granick and coworkers.[62]

We have also considered the extent to which DJ particles can be modeled as isotropically attractive colloidal particles. This allows us to quantify the extent to which DJ colloidal systems are similar to conventional isotropically attractive colloids such as depletion attracting colloids. The isotropic interactions are determined by coarse-graining over the orientations of an isolated pair of PW particles as explained in Section 4.2.2. Hence, this model is labeled as the CG model of DJ particles. It is notable that the the length and energy scales important to Janus particles—as found through the isotropic CG model—are comparable to those of depletion attracting colloidal particles. [38, 104] Therefore DJ colloids may have much in common with depletion attracting colloids. This was tested by comparing the results of molecular dynamics simulations of DJ particle systems in

both the PW and CG models.

7.1.3 Static and thermodynamic properties of dipolar Janus colloids

We first considered the static and thermodynamic properties of dipolar Janus (DJ) colloidal particles systems in Chapter 4. Surprisingly, it was found that the static structure of DJ particles in the PW model was reproduced by the CG model for fluid conditions. This structural similarity was quantified by pair correlation function as presented in Section 4.4.1. These results further suggests that DJ colloids have the particle structure of comparable isotropically attractive colloids (e.g. depletion attracting colloids). By comparable me mean having similar dimerization equilibrium constants. Simulation of DJ particles with stronger pair integrations (or conversely lower temperatures) did not equilibrate to a fluid phase in either the PW or CG model. Instead a dynamically-arrested and collapsed glass-like state was observed. We therefore predict that DJ particles will have the structure of isotropically attractive colloidal particles for fluid conditions.

These results for DJ colloids can be contrasted to previous simulations of amphiphilic Janus colloids performed by Sciortino and coworkers. [109, 110, 40] In these studies, amphiphilic Janus colloids were found to form small isolated clusters as would alter material properties. In contrast, we did not observe small isolated clusters in any of our simulations of DJ colloids. Along the isochore for $\phi = 0.1$, amphiphilic Janus colloids were found to form isolated clusters with increasing interaction strengths (i.e. decreasing temperature). [109] In contrast, for DJ particles we observed a transition from a fluid to a collapsed state with increasing pair affinity. This shows a major difference in the dipolar Janus interaction versus the amphiphilic Janus interaction. The significance of clusters in amphiphilic Janus systems has been previously explained by the energetic stability of small miceullar clusters versus larger structures.[110] In contrast, we find that larger structures are energetically favorable in DJ systems.

While the translational structure of DJ particles was found to be similar to isotropically attractive colloids, additional order was observed in our PW simulations. This was seen in the anisotropic pair density correlation results of Section 4.4.2. These anisotropic density correlations result from a bias in how each particles prefers to orient itself within its neighbor shell. The translational structure of DJ particles is still comparable to that of isotropically attractive particles. Such biased orientations

might be important in the quenching of DJ particles in that the liquid structure already has initial orientation order. This initial order may influence the quenched structure of DJ particles in colloidal glasses and gels.

The thermodynamic similarity of DJ particles and isotropically attractive particles was demonstrated in Section 4.4.4. This was accomplished by rigorously computing the excess free energy of DJ particles in both the PW and CG models relative to a common standard. As with the isotropic structure, the CG model reproduces the excess free energy of the PW model for fluid conditions. Hence the fluid phase of DJ colloids should be thermodynamically favorable at similar conditions for which fluid is favored in isotropically attractive colloids. In contrast, the CG model does not reproduce the entropy/energy balance of free energy found in the PW model. The presence of fewer degrees of freedom in the CG model there in limits the extent to which it can store internal energy. Therefore dipolar Janus colloids are predicted to have larger heat capacities than comparable isotropically attractive colloids.

7.1.4 Dynamic properties of dipolar Janus colloids

A key feature of our DJ colloid model is that it includes only continuous potentials so as to accommodates molecular dynamics simulations. These methods have allowed us to compute the dynamical properties of DJ colloids in both the PW and CG models as studied in Chapter 5. It was found that the dynamics of the CG model are accelerated relative to the PW model for the same range of fluid conditions for which the models had identical static properties. This was quantified by the time correlation function results presented in Section 5.3.1. The velocity autocorrelation functions (VACF) showed stronger correlations for times $t \lesssim 1\,\mu$s in the CG model than in the PW model. Additionally the mean squared displacements (MSD) results showed faster transport in the CG model relative to the PW model. These results suggests that DJ colloids will have slower transport properties than comparable isotropically attractive colloids at conditions for which the two types of colloids have near identical static structure.

The accelerated dynamics of the CG model relative to the PW model can be understood through the differences in reversible pair bonding in the two models. It was found that coarse-graining the PW interaction to create the CG interaction leads to a diminution of longer-duration reversible

bonds in simulation. The loss of longer-duration reversible bonds decreases the extent of attractive caging in the CG model. This in turn enhances translational dynamics. These results suggests that attractive caging will be particularly important in the dynamics of dipolar Janus colloids and will result in reduced transport relative to isotropically attractive colloids.

7.1.5 Application of dynamical mapping methods to coarse-grained model of dipolar Janus colloids

The accelerated dynamics of the CG model relative to the PW model can be seen as an instance of a more general trend. Coarse-grained models generally have accelerated dynamics relative to the detailed model that they represent. [80, 88, 28, 65, 81, 85, 55, 2] Dynamical acceleration has also been previously reported in coarse-grained models of polymers[88, 80, 28, 55] and water.[65, 85, 2] It is of interest to map the accelerated dynamics of a coarse-grained model back to the original time scale. This would allow the simpler and computationally efficient coarse-grained model to be used in the simulation of dynamical properties. Dynamical mapping methods[1, 93, 88, 28, 65, 55] have been developed with this aim in mind.

In Section 5.3.2 we applied two dynamical mapping methods to our CG model to test their efficacy in reproducing the PW dynamics. The applied dynamical mapping methods are time rescaling[88, 28, 55] and damping with Langevin friction.[1, 93, 65] Both dynamical mapping methods are found to improve the velocity autocorrelation functions and the mean squared displacements of the CG model. Additionally, the diffusion constants computed from these dynamically-mapped time correlation functions are closer to those observed in the PW model. In contrast, neither dynamical mapping method improves the distribution of reversible bond duration. This demonstrates that current dynamical mapping methods can reproduce transport properties in coarse-grained models without reproducing the detailed dynamics for all time and length scales. Therefore current dynamical mapping methods may be insufficient for future simulations of DJ dynamics with the CG model. This is because attractive bonding plays an important role in the dynamics of DJ particles and it is not reproduced by current methods. New dynamical mapping methods may be needed to facilitate future simulations of DJ dynamics with the CG model. Such future simulations may include the proposed exploration of the nonequilibrium properties of DJ colloids as presented in the future work section of this thesis.

7.1.6 Dynamical simulation of electrostatic striped colloidal particles

Lastly, in Chapter 6 we have generalized the models and methods developed for dipolar Janus particles (DJ) in earlier chapters to the study of striped colloidal particles. We considered systems of identical colloidal particles where each particle has n stripes of alternating electric charge. The includes DJ particles with $n = 2$ stripes. We further consider striped particles for $3 \leq n \leq 7$ with the development of new PW models. As previously done in our DJ work, we also determined the extent to which striped electrostatic particles are similar to isotropically attractive colloidal particles by additionally modeling them with isotropic CG models.

The striped particles were found to exhibit many similarities to DJ particles. The static structure of striped particles systems is captured by the isotropically attractive CG models. Additionally, different n-striped particles system with comparable pair affinity (quantified by dimerization equilibrium constant) have similar static structure. This results from the fact that the CG interactions of different n-striped particles with comparable pair affinities are similar. Therefore pair affinity is predicted to be the crucial quantify in determining the extent of structure in electrostatic striped colloids. Further, the structure of these new colloidal systems is predicted to be near identical to more conventional isotropically attractive colloids with comparable pair affinity. The CG models of striped particles are found to have accelerated dynamics relative to the corresponding PW models. Such accelerated dynamics for the CG model was previously found in our study of DJ colloids. It is interesting that DJ ($n = 2$) particles have the smallest extent of dynamical acceleration for all n studied. Nearly twice as much dynamical acceleration is observed for other n (chiefly $n = 5$) than found for the DJ case. As with the DJ case, the dynamical acceleration of striped particles in the CG model is also explained by the loss of long-duration reversible.

Nevertheless, qualitative differences were seen between DJ particles ($n = 2$) and multi-striped ($n \geq 3$) particles. In general, particles with larger number of stripes are found to have slower dynamics at constant pair affinity (i.e. conditions at which the different n-striped systems had comparable static structure). This shows that the static and dynamic properties are decoupled in electrostatic striped colloids. Further, this suggests that one could tune the dynamical properties alone by changing the number of stripes. Such tunable dynamical properties of colloidal materials may be of

interest for new colloid technologies. Our results also suggest that different n-striped colloids will have different phase behavior.

We have approximated the phase diagram of each n-striped system studied by noting conditions at which collapsed and dynamically arrested states are observed in simulations. The CG models of different n-striped system are found to have similar phase behavior. This is explained the different CG models having similar interaction profiles at comparable pair affinities. In contrast, the phase behavior of the PW models is found to vary considerably across the different values of n studied. For DJ particles ($n = 2$) the approximate phase behavior of the PW model is similar to that of the CG model. This suggest dipolar Janus particles will form glasses and gels at similar conditions for which isotropically attractive colloids form glasses and gels. Ternary particles ($n = 3$) form glass-like states at much weaker pair affinities (or conversely higher temperatures). This is attributed to ternary particles forming particularly stable compact structures. In contrast, higher number of stripes ($n \geq 4$) were found to be resistant to the formation of collapsed glassy states. Structural frustration may inhibit the formation of energetically stable compact structures in such higher striped systems.

7.2 Future Work

The results of this thesis have answered many questions about structured colloids. They also raise new questions about the novel properties of these new colloidal materials. In this section we consider these new questions and discuss how they might be addressed in future work.

7.2.1 ESDA gelation dynamics with shearing

In Chapter 3, we considered the gelation of colloidal particles with an energetic barrier limiting pair association. This was accomplished with the development of the ESDA model for these radially-structured colloidal particles. As discussed in Section 3.5.4, shear forces are known to affect the gelation dynamics of strictly attractive colloidal particles. Shearing may have a stronger affect on ESDA particle gelation as shear forces could provide the energy to overcome the energetic barrier. This was demonstrated in the preliminary study of shear accelerated gelation performed in Section 3.5.4.

The preliminary study of Section 3.5.4 could be extended to a rigorous investigation of the effects of shear forces on the gelation of ESDA particles. This study would require the calculation

of longer duration simulation trajectories and a larger number of trajectories. Additionally, a better approximation of the hydrodynamic effect may be needed for better simulation of the shear. To this end, Stokesian Dynamics[10] or Dissipative Particle Dynamics[64] could be used to provide a better approximation of shear forces.

7.2.2 Adaptation of current methods to Janus and striped ellipsoidal colloids

Anisotropic colloidal particles can also be realized with non-spherical shapes. This includes ellipsoidal colloidal particles.[60, 91] Such shape asymmetry can be combined with surface patterning to create Janus[131, 94] and striped[68, 67] ellipsoidal colloidal particles. The new anisotropic interactions created by the combination of surface patterning and shape asymmetry could results in new colloidal material properties. Computer simulations can provide insight into these potential material properties. For instance, recent simulation by Liu et al.[79] have shown that amphiphilic Janus ellipsoids assemble into different cluster structures than amphiphilic Janus spheres. This could lead to new phase behavior with clusters-rich states favored at different conditions.

The models and simulation methods developed in this thesis could be adapted for the study of ellipsoids with stripes of alternating electric charge. This would include dipolar Janus ellipsoids. Adapting the pointwise (PW) model would require two changes: First, new point charge layouts would need to be constructed to model the patterned surfaces of striped ellipsoids. Second, the isotropically repulsive core would have to be replaced by a repulsive ellipsoidal core. To this end, the Gay-Berne potential[44] could be used. This potential has already been used extensively in the simulation of ellipsoidal colloidal particles with uniform surfaces. [6, 7, 39] Additionally, the Gay-Berne potential is already implemented in LAMMPS:[13] the molecular dynamics package used in current work. Therefore it would be straightforward to adapt the models and methods of the thesis to the study of striped ellipsoidal colloidal particles.

7.2.3 Nonequilibrium simulation of Janus and striped colloidal particles

Many colloid technologies harness the nonequilibrium properties of colloids in glasses and gels. [87, 136, 12] Previous computer simulations have provided valuable insight into nonequilibrium properties of isotropically attractive colloidal particles in glass and gel states. [9, 37, 41, 102] For instance, Puertas, Fuchs, and Cates[102] have shown that attractive colloidal glasses age through

similar processes by which repulsive colloidal glasses age. This thesis has shown that dipolar Janus and electrostatic striped colloids (Chapters 5 and 6 respectively) have slower dynamics than comparable isotropically attractive colloids at equilibrium. This suggests that their nonequilibrium aging may occur through different mechanisms. This would create a new type of colloidal glass.

The methods developed in this thesis for equilibrium simulation could be adapted to the nonequilibrium simulation of Janus and striped colloidal particles. Such a nonequilibrium simulation study would be challenging with current methods in that it would require a much larger amount of computing resources than current work. This is because the static and dynamic correlation functions computed in nonequilibrium simulation are time dependent (they vary with the extent of nonequilibrium simulation performed). Therefore these quantities cannot be time-averaged throughout each simulation trajectory and instead a much larger number of trajectories must be obtained. As the current PW model is computationally expensive (roughly 100 times slower than a Lennard-Jones potential) such a nonequilibrium simulation study would not be possible with current methods. To overcome this obstacle, tabulated methods could be used to compute the PW potential and gradients. If this approach can provide a significant improvement in computational efficiency, then nonequilibrium simulation of Janus and striped colloidal particles would be possible.

The computational efficiency challenge might also be addressed with the use of coarse-grained methods. The isotropic coarse-grained (CG) models of Janus and striped particles (developed in Chapter 4) are roughly 2 order of magnitude more computationally efficient (i.e. the simulations run 100 times faster) than the PW model. Unfortunately, the CG model does not reproduce the PW dynamics with conventional molecular dynamics simulation. Therefore it could not be used to study the time-dependent properties in nonequilibrium simulation with conventional methods. Time mapping methods could be used to address this deficiency as such methods would relate the CG dynamics back to original time scale of the PW model. Time mapping methods were applied to the CG model of DJ particles in Chapter 5 for equilibrium conditions. These methods were found to improve the time correlation functions and diffusion coefficients of the CG model: i.e. these results were closer to the time-scale of the PW model than the unmapped results. Unfortunately, the current time mapping methods were found to not reproduce the PW dynamics in the CG model for all time and lengths scales. This could prevent them from mapping the nonequilibrium dynamics of the CG

model to the original time scales. Therefore new dynamical mapping methods may be needed.

7.2.4 New dynamical mappings for coarse-grained models

In this thesis, it is shown that the isotropic coarse-grained (CG) model for dipolar Janus (Chapter 5) and striped (Chapter 6) colloids models were seen to contain accelerated dynamics relative to the corresponding detailed models for these systems. These results are instances of the general trend of coarse-grained models to exhibit faster dynamics than the detailed models that they correspond to. Such behavior has been reported for several coarse-grained models, [80, 88, 28, 65, 81, 85, 55, 2] including models for polymers[88, 80, 28, 55] and water.[65, 85, 2] It would be useful to relate the accelerated dynamics of coarse-grained models to the original time scale. To this end, dynamical mapping methods have been developed. [1, 93, 88, 28, 65, 55] These methods aim to allow for the investigation of dynamical properties with computationally efficient coarse-grained methods. Such methods would be useful for future simulations of the dynamics of structured colloidal systems with coarse-grained models.

In Section 5.3.2 of this thesis, two dynamical mapping methods were applied to the CG model of dipolar Janus particles. This was done to test whether these methods could relate the accelerated dynamics of the CG model back to the original time scale studied in the PW model. The dynamical mapping methods applied were time rescaling[88, 28, 55] and damping with Langevin friction.[1, 93, 65] Both of these methods were found to improve the velocity autocorrelation functions and mean squared displacements of the CG model for a range of conditions: i.e. the dynamically mapped time correlations function were closer to those of the PW model. Additionally, both methods also produced diffusion coefficients in the CG model that were closer to those of the PW model. These results demonstrate that both dynamical mapping methods could be applied in future simulations of the dynamics of structured colloidal particles in which the computation of similar equilibrium observables is sought.

In contrast, neither dynamical mapping method improved the distribution of reversible bond durations observed in the CG model: the mapped CG bond duration distribution were still quite different from those of the PW model. These results demonstrates a deficiency of current dynamical mapping methods. Neither dynamical mapping methods can be said to reproduce the PW dynamics

in the CG model for all time and length scales. Therefore these methods might not be applicable for the nonequilibrium investigation of structured colloidal particles proposed in Section 7.2.3. Attractive caging through particle bonding likely plays a key role in the nonequilibrium dynamics of these systems and current time mapping methods do not reproduce bond dynamics.

Therefore new dynamical mapping methods are needed. The results of this thesis suggest that certain physics must be addressed by these new methods. Specifically, in Section 5.4 it was shown that current time-rescaling methods[28] do not address the different changes in energetics of multiple rearrangement processes. Instead, time-rescaling assumes that there is single dominant rearrangement process and addresses the kinetic enhancement of this single process following coarse-graining. In dipolar Janus particles, there are multiple rearrangement processes corresponding to pair collisions with different orientations. These are replaced by a single pair collision profile in the isotropic CG model. Conventional time-rescaling does not account for the fact that each of these different rearrangement processes has a different energetic profile and therefore a different kinetic enhancement when replaced by coarse-grained interactions. New dynamical mapping methods could address the change in energetics for multiple rearrangement process. This might be accomplished by non-uniform time-rescaling in which different degrees of freedom can be rescaled by different factors. Such methods would facilitate the nonequilibrium studies of structured colloids with coarse-grained methods. Additionally, they might find use in other dynamical simulations with coarse-grained models.

APPENDIX A

ADDITIONAL RESULTS FOR DYNAMICAL SIMULATION OF ELECTROSTATIC STRIPED COLLOIDAL PARTICLES

A.1 PW model resolution

The pointwise (PW) model for striped particles can vary in the number of points, n_{p}, used to represent each striped particles surface. It is important to use sufficiently high resolution PW models—sufficiently large n_{p}—to accurately model the pair potential energy surface. We determine the sufficient resolution for each n-striped case considered by considering models of different resolution. It is found that roughly $n_{\mathrm{p}} \approx 2000$ models are of sufficiently high resolution to capture the potential energy surface in all n-striped cases. In this section we demonstrate these models to be of sufficiently high resolution to by comparing each of the simulated PW models to higher resolution PW models. These higher resolution comparison models are shown in Figure 50. For each n-striped case considered, the higher resolution model has roughly twice as many point charges as the model used in simulation. The specific values of n_{p} in each case are given in Tab. 4.

To compare the different resolution models, we compute the isotropic pair free energy profile computed in each resolution model. These computations discussed in Chapter 4 and Chapter 6. These isotropic pair free energy profiles provide a simple description of the pair interactions and the free energy minimum, A_{p}, quantifies pair affinity. Exam profiles for a range of pair affinities are shown in Figure 50. In each pane a single A_{p} is considered for all n-striped particle considered. The profile of the simulated resolution model and the comparison model are near identical in all cases. This shows the the simulated resolution models are of sufficiently high resolution.

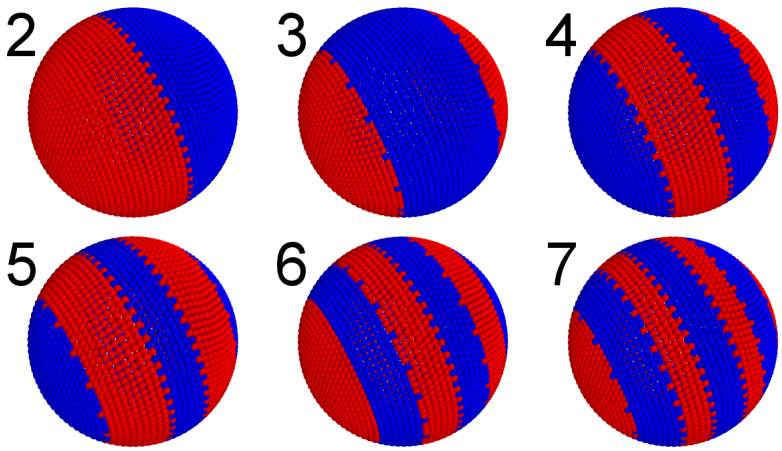

Figure 50: Higher resolution point charge layouts used for comparison with point charge layouts used in simulation. Positive point charges are shown in blue and negative point charges in red.

Table 4: The number of point charges, n_p, used to model striped particles in both the simulated PW models and the higher resolution comparison models.

n Stripes	n_p Simulated	n_p High Resolution
2	1846	4280
3	1652	4280
4	1846	4280
5	2248	3712
6	1846	4280
7	1652	4280

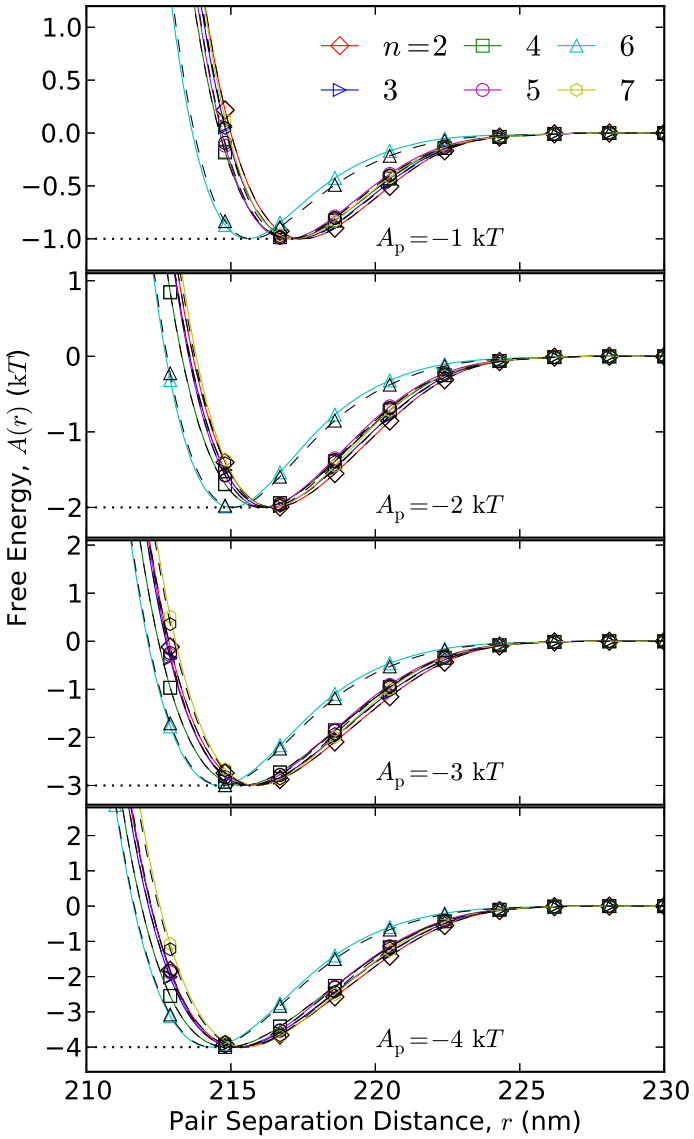

Figure 51: Comparison of pair free energy profiles with different resolution PW models. Each pane shows profiles of a single pair affinity, A_{p}, for each number of stripes n. The simulated resolution model profiles are shown by solid lines with different n-striped systems indicated by different colors (labeled on the plot). The free energy profiles of the higher resolution comparison models are shown by dashed black lines. These dashed black lines are near identical to the solid lines showing that in all cases the simulated resolution model gives the same free energy profile as the higher resolution comparison model. Markers are only included every 2 nm to better differentiate the curves which are calculated at a resolution of 0.1 nm.

A.2 Energetics of Pair Orientations

In Chapter 4, it was found $n = 6$ striped particles had different isotropic CG interactions than other striped particles considered at comparable pair affinities. This difference in pair interactions might be explained by on and off registry effects with the how stripes of a pair align. In this sections, we explore these registry effects by considering the energetics of pair of particles with different orientations. For each number of stripes n, we consider an isolated pair of particles at a fixed separation distance. The orientation of one particles is held constant while the particles is rotated. Energy is plotted as a function of rotation to explore how particle orientations are related to pair energetics for each number of stripes.

The results are shown in Fig. 52. The energy profile for the $n = 6$ curve shows broader energy wells and narrower energy hills than $n = 4$. Favorable alignment of stripes between pairs of $n = 6$ particles could explain these features. Such favorable alignment would explain why $n = 6$ particles can approach each other closer than other striped particles studied. These registry effects may be more thoroughly studied in future works by considering additional orientations. By exploring the 3-dimension potential energy surface across all orientations one could identify particularly favorable pair orientations for $n = 6$. We'd expect such favorable orientations to coincide for aligned stripes (i.e. on-registry effects).

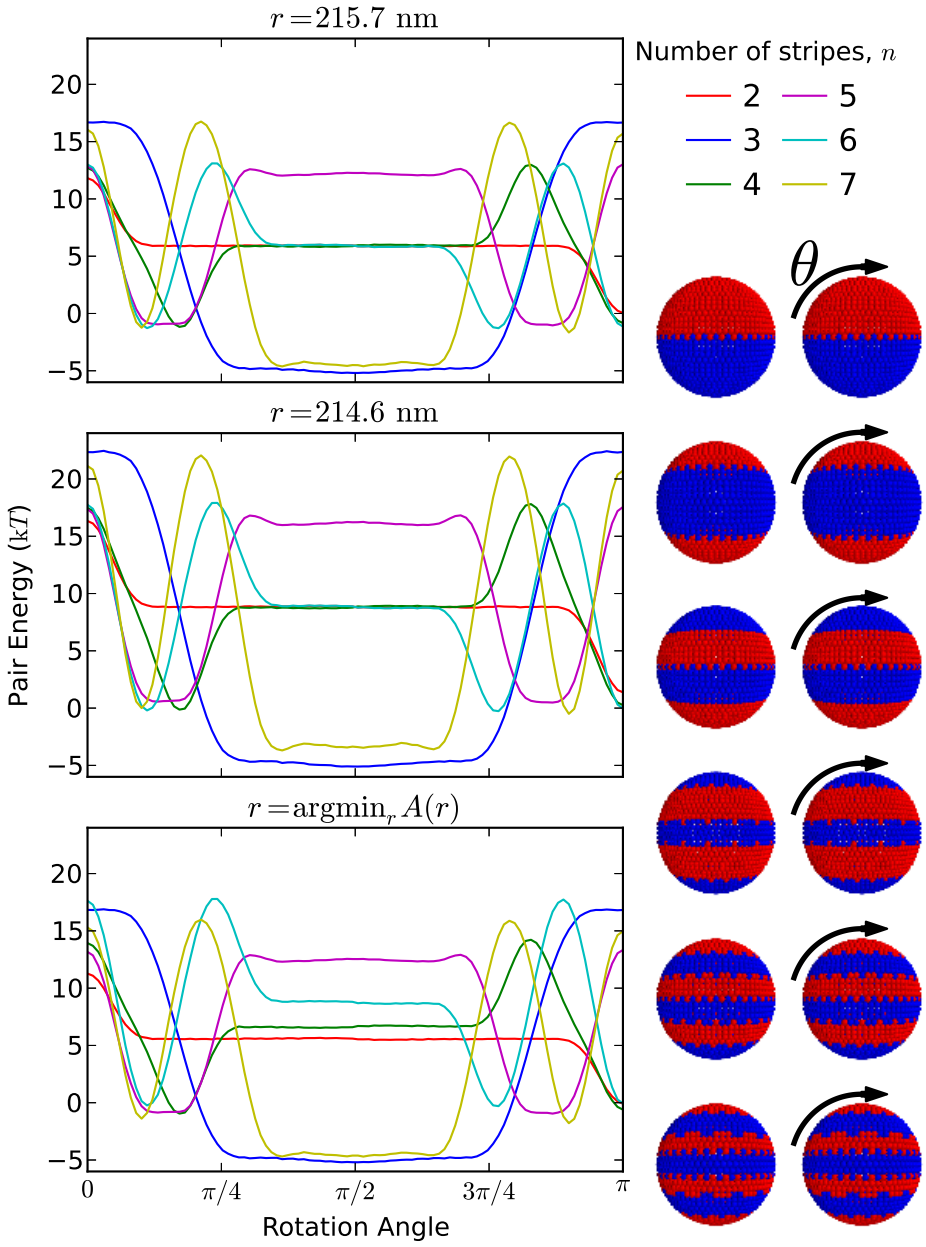

Figure 52: Results that show how the energetics of a pair changes as one of the particles is rotated. The orientation of the pair and the rotation considered is depicted on the schematics. The surface charge density of the particles in each pair is set to give a pair affinity of $A_{\mathrm{p}} = -3\,k_{\mathrm{B}}T$. Each panel shows results for all number of stripes considered as indicated in the plot legend. Panel A and B shows pairs at fixed separation distances of $r = 215.7\,\mathrm{nm}$ and $r = 214.6\,\mathrm{nm}$ respectively. In panel C, the separation distance is adjusted to be at the free energy minimum. These separation distances are (in nm): $n = 2$, $r = 215.9$; $n = 3$, $r = 215.7$; $n = 4$, $r = 215.4$; $n = 5$, $r = 215.6$; $n = 6$, $r = 214.6$; $n = 7$, $r = 215.9$. Potential has mirror symmetry about π (i.e. $U(\theta) = U(2\pi - \theta) \mathrm{for} \theta > \pi$).

A.3 Nonequilibrium quench trajectories

In Chp. 6 we noted that certain simulation failed to equilibrate to a fluid-like state, but instead formed a collapsed and arrested state as characteristic of a glass-like state. These glass-like states are characterized by a larger drop in internal energy during equilibration than observed for fluid-like state. In this section we show the progression of internal energy throughout equilibration for all simulations performed. As these simulation do not proceed towards an equilibrated state, these simulations are considered nonequilibrium quenches as initialized from a repulsive particle control state. These nonequilibrium quench simulation are further discussed in Chp. 6. Each of the figures, Figure 53 to Figure 58, shows the progression of internal energy for $n = 2$ to $n = 7$ respectively. Results for each colloid volume fraction are shown in a separate pane. In each pane, one can see the larger drops in internal energy that occur in stronger pair affinity systems (larger A_{p}) as correspond to observation of glass-like states in the simulation. These conditions for fluid-like vs. glass-like are summarized in Chp. 6 with approximate phase diagrams.

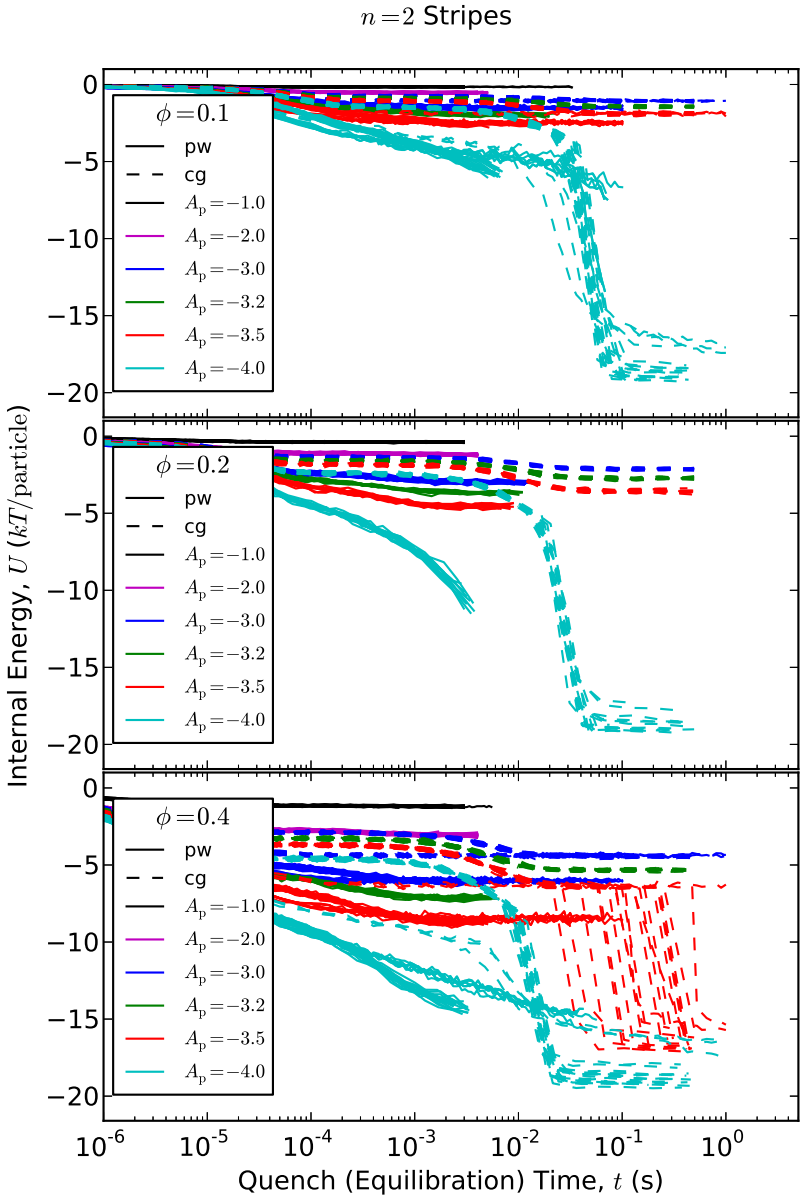

Figure 53: Potential energy as a function of equilibration time for the nonequilibrium quench of $n = 2$ striped particles. Each panel is for a different particle volume fraction ϕ as labeled on the plot legend. Different curves colors shows results for different pair affinity as quantified by A_p. Line style differentiates the two models studied with solid lines showing the results of the PW model and dashed lines for the CG model. This figure includes additional quench results from our previous study of dipolar Janus colloids.[52] These quench simulations were performed with a different thermostat and therefore show a different progression of internal energy with quench time.

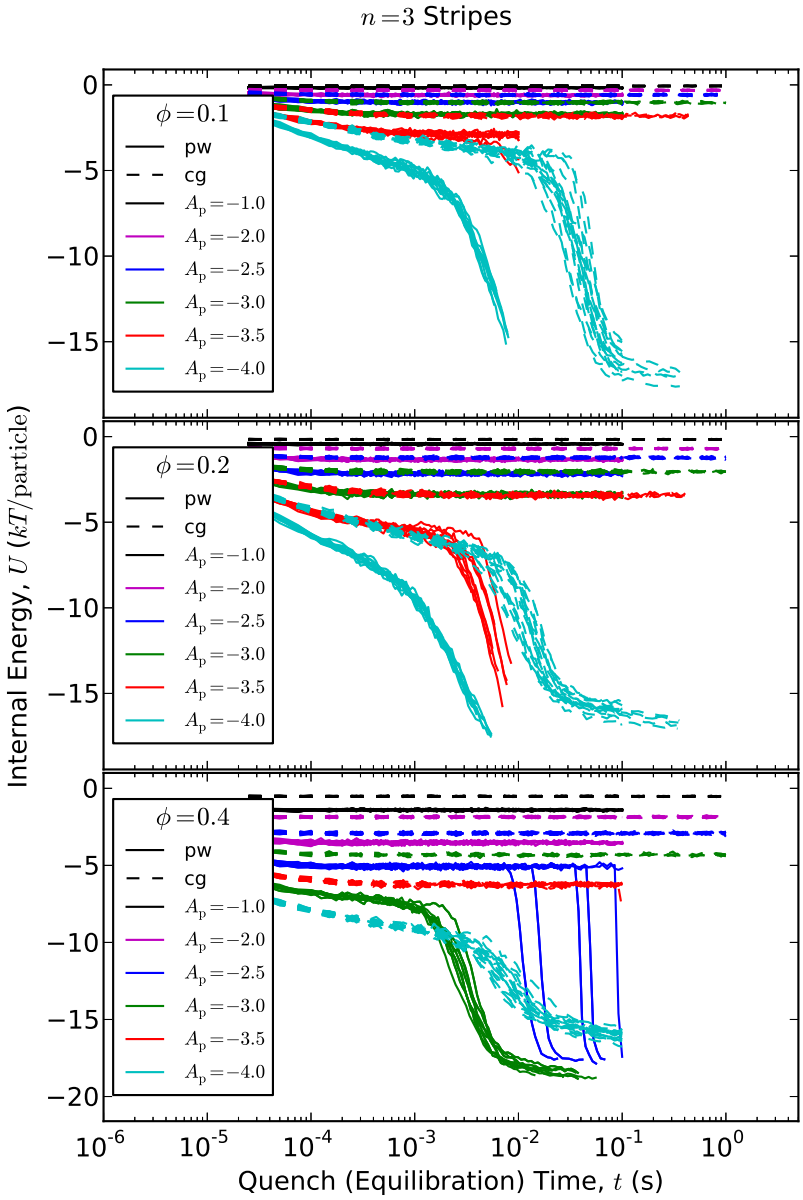

Figure 54: Quench results for $n = 3$ striped particles. Plotted in the same style as Figure 53.

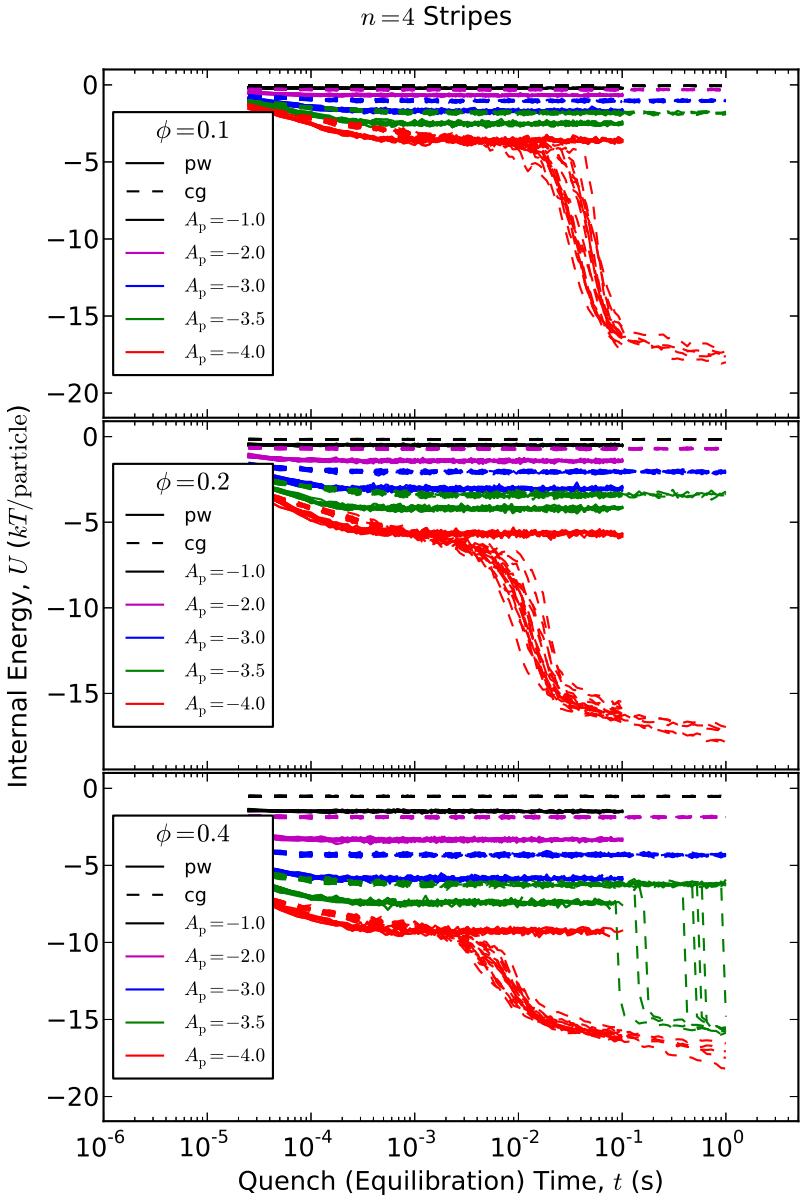

Figure 55: Quench results for $n = 4$ striped particles. Plotted in the same style as Figure 53.

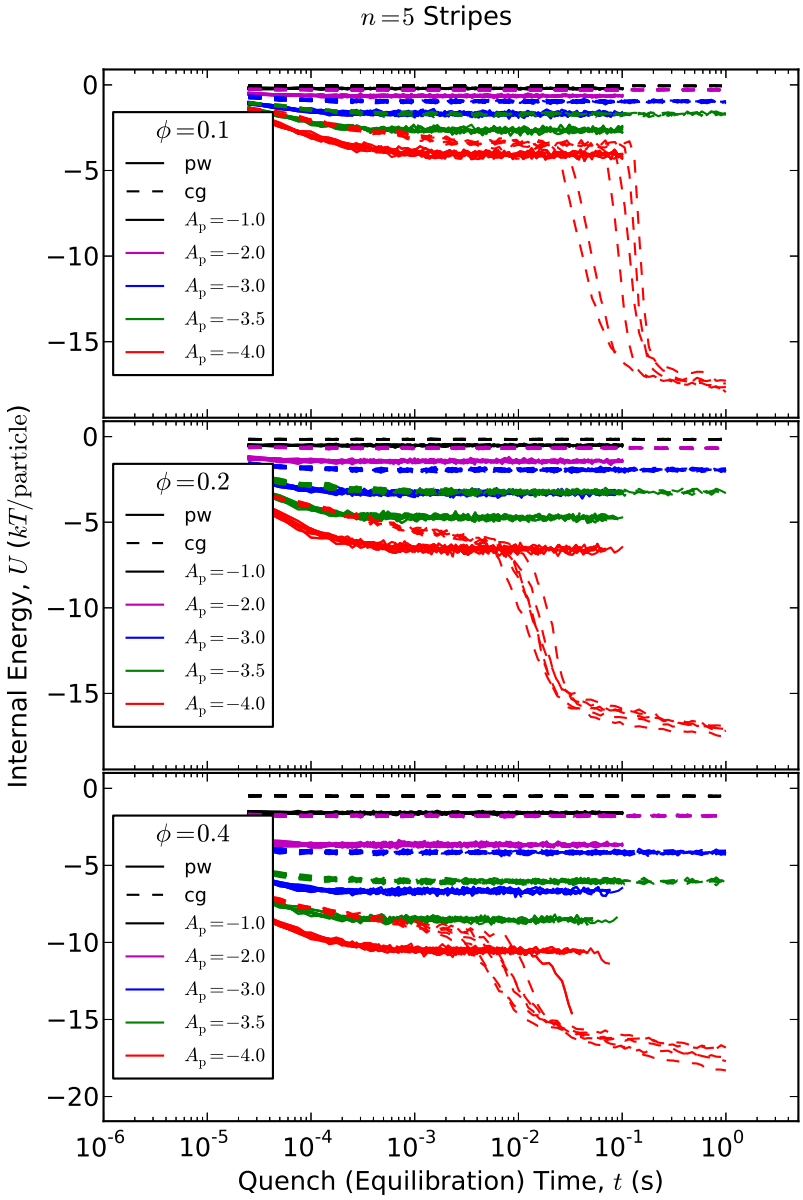

Figure 56: Quench results for $n = 5$ striped particles. Plotted in the same style as Figure 53.

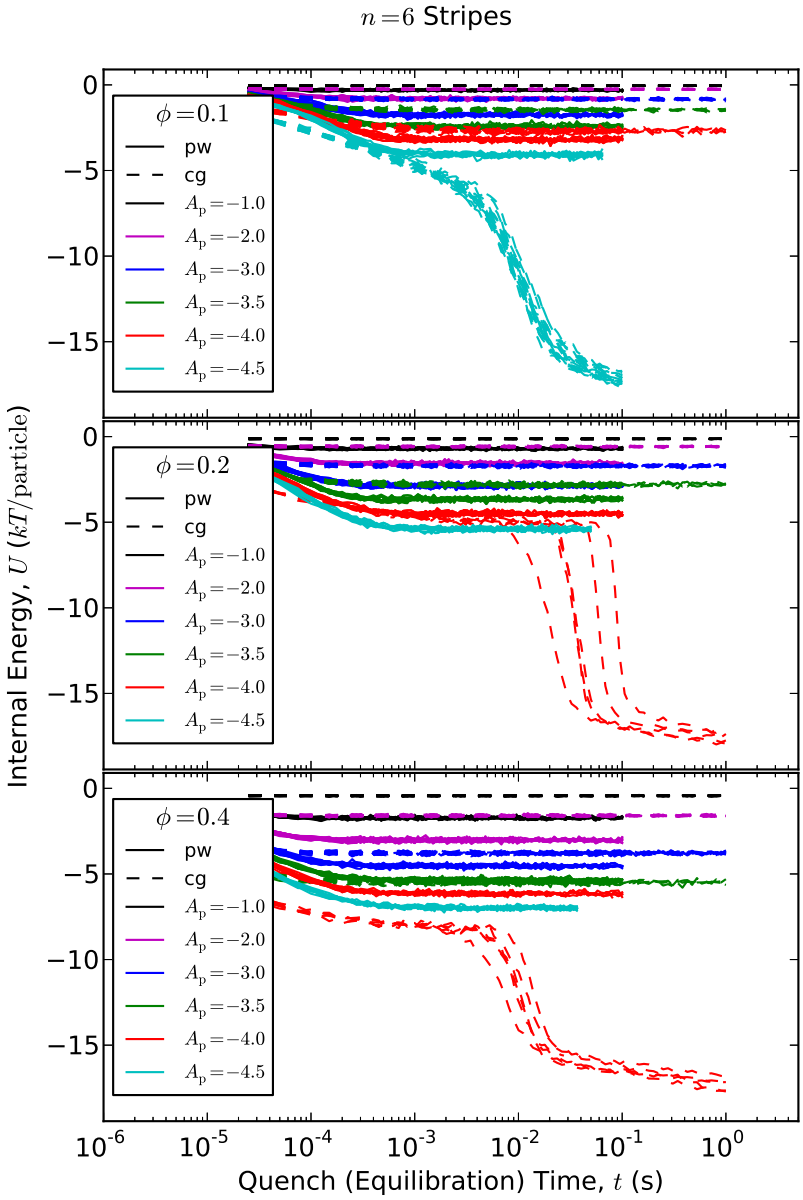

Figure 57: Quench results for $n = 6$ striped particles. Plotted in the same style as Figure 53.

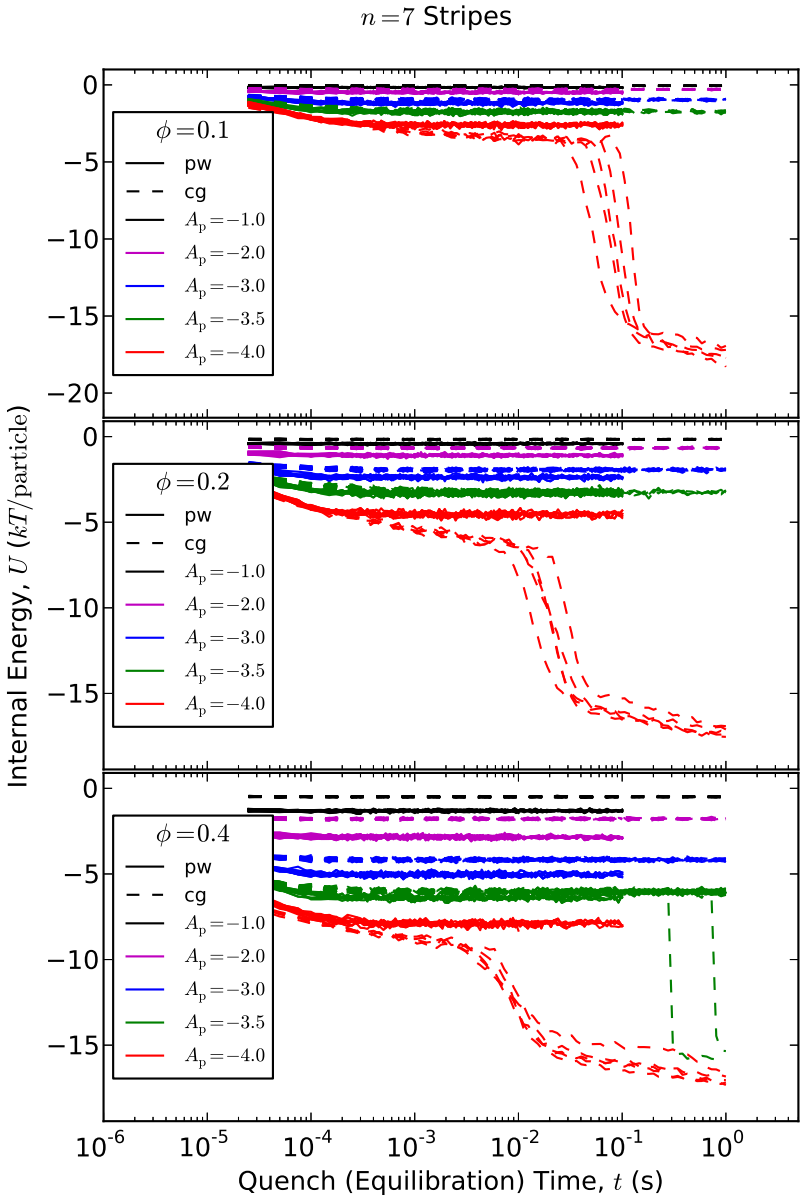

Figure 58: Quench results for $n = 7$ striped particles. Plotted in the same style as Figure 53.

A.4 Snapshots of at the end of quench/equilibration

This sections provides additional snapshosts of repressenative systems studied at the end of the quench/equilibration simulation. Each Figure, Figure 59 to Figure 70 to shows snapshots for one n-striped systems in either the PW or CG model.

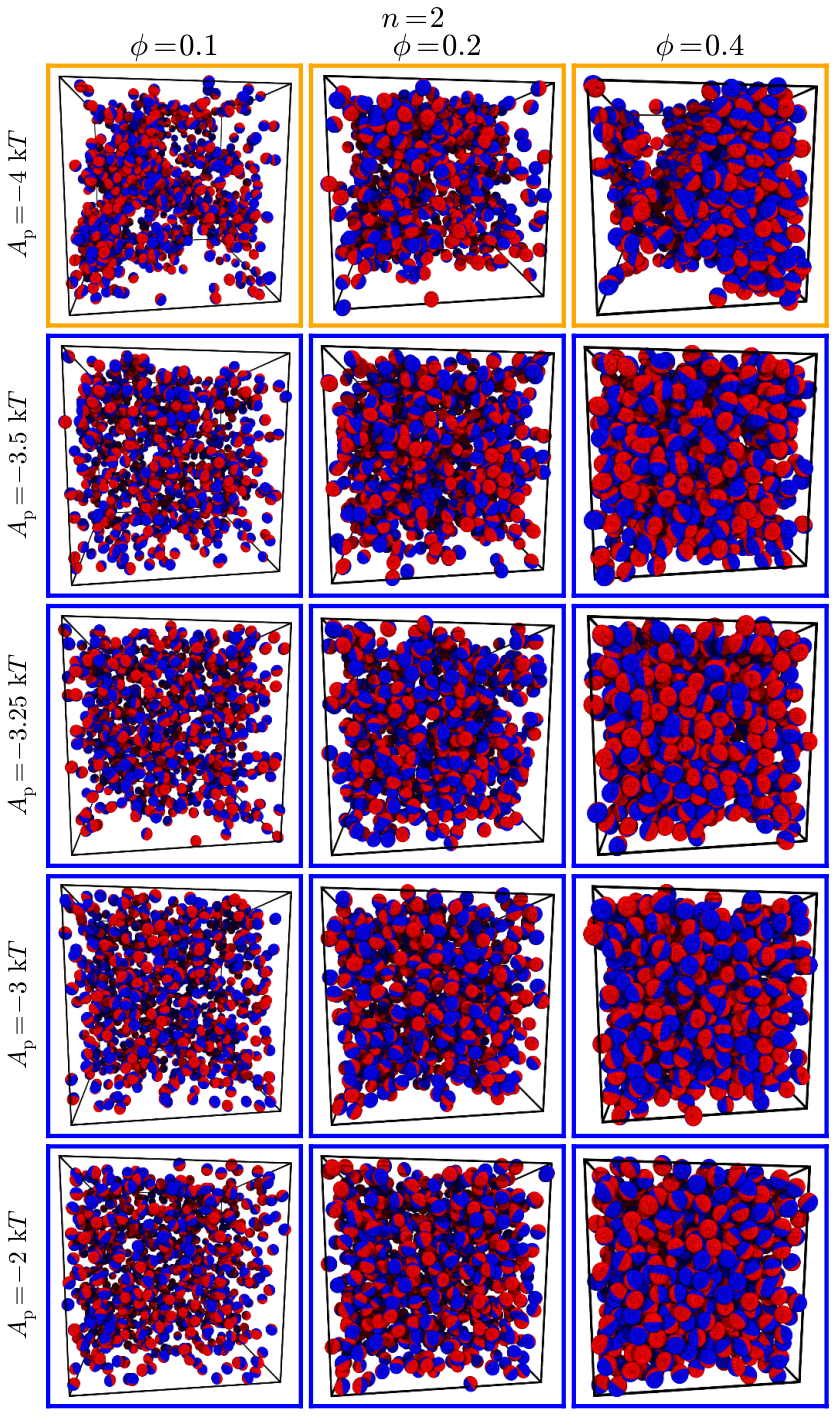

Figure 59: Repressentative snapshots of $n = 2$ PW system at the end of quench/equilibration simulation. Snapshots are shown for a range of pair affinities, A_p, and volume fractions, ϕ, as labeled on the figure. The border color of individual snapshosts indicates whether these conditions are considered to equilibrate to a fluid state (blue border) or glass-like state (orange border).

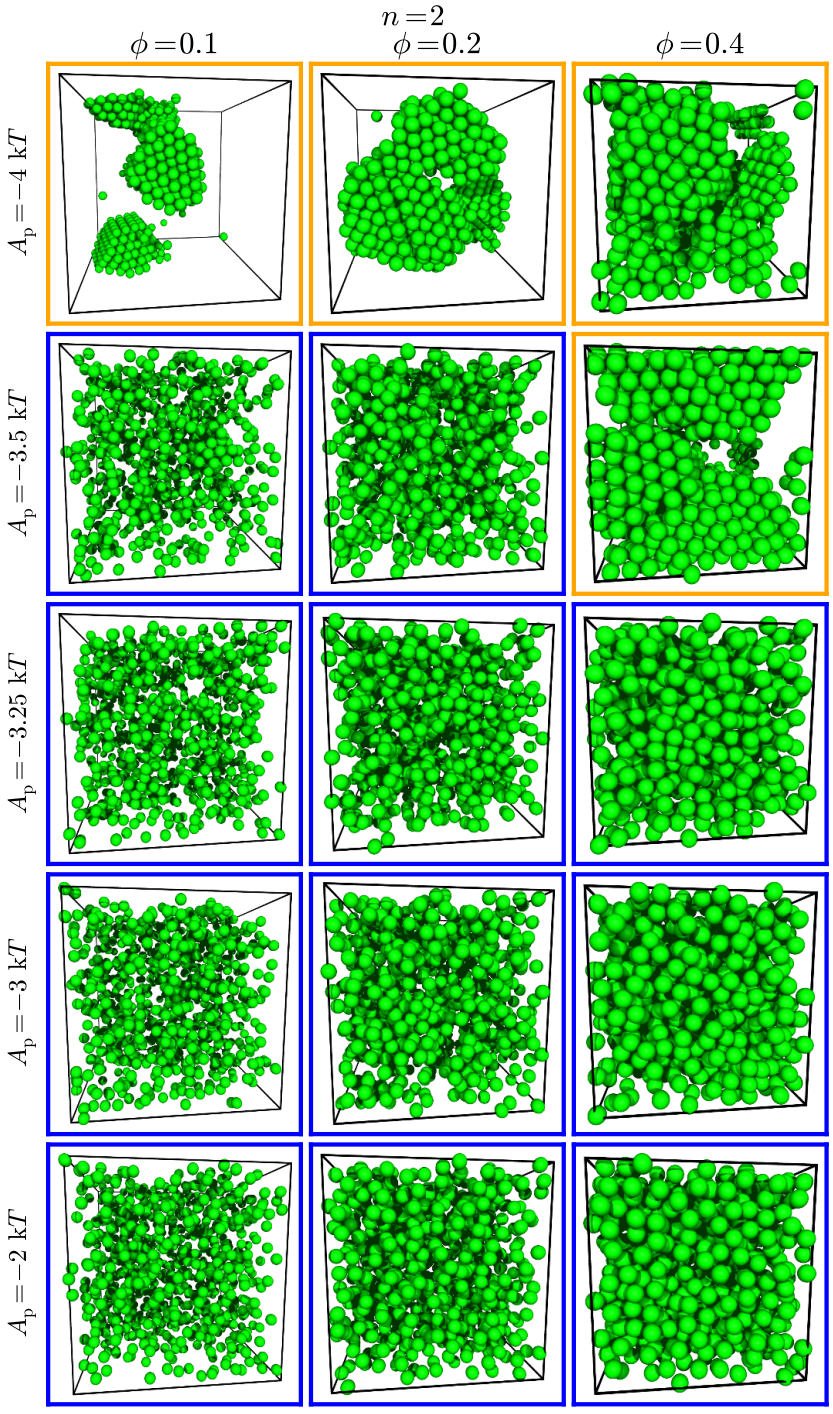

Figure 60: Repressentative snapshosts for $n = 2$ CG systems at the end of quench/equilibration simulations. Presented in the same style as Figure 59.

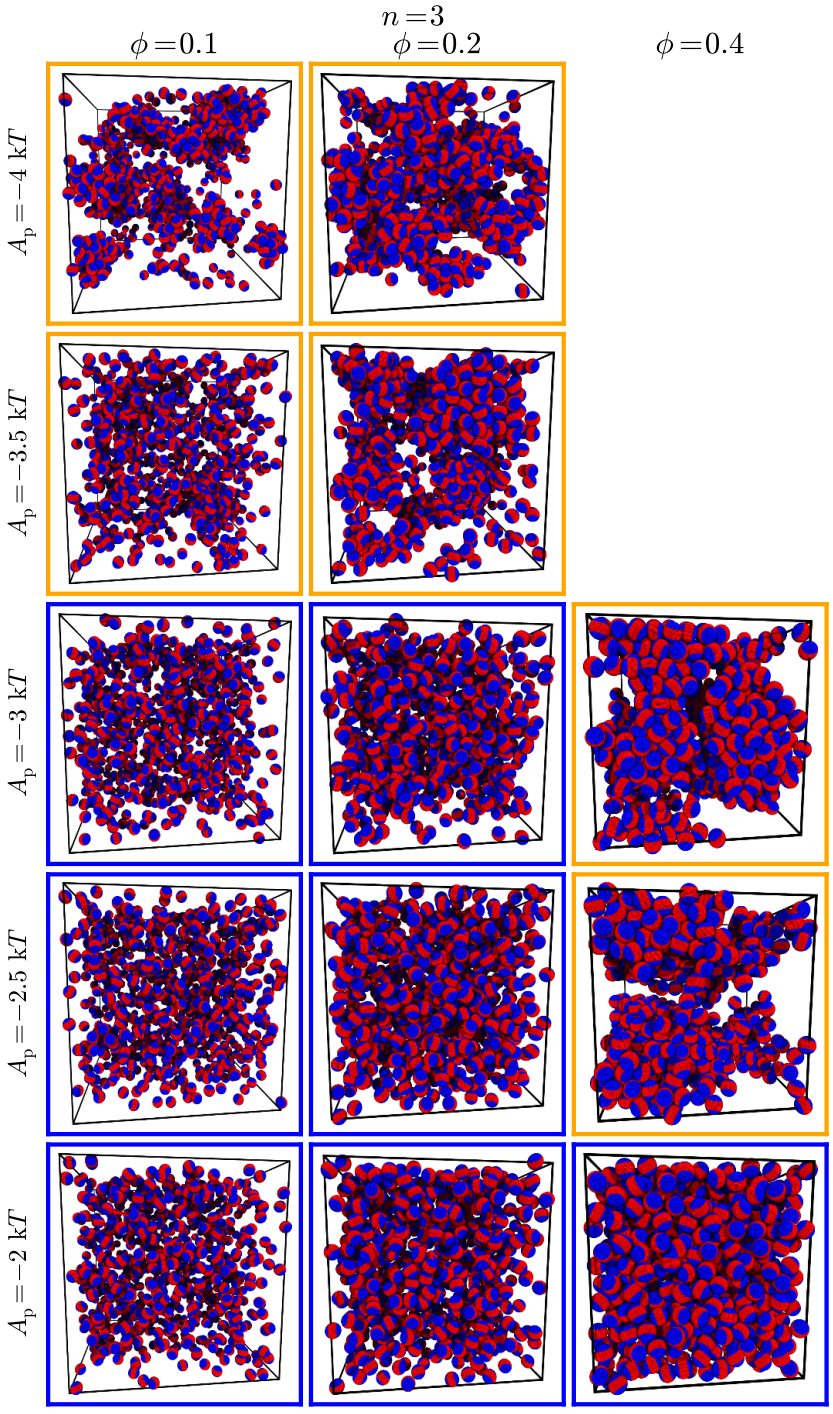

Figure 61: Repressentative snapshosts for $n = 3$ PW systems at the end of quench/equilibration simulations. Presented in the same style as Figure 59.

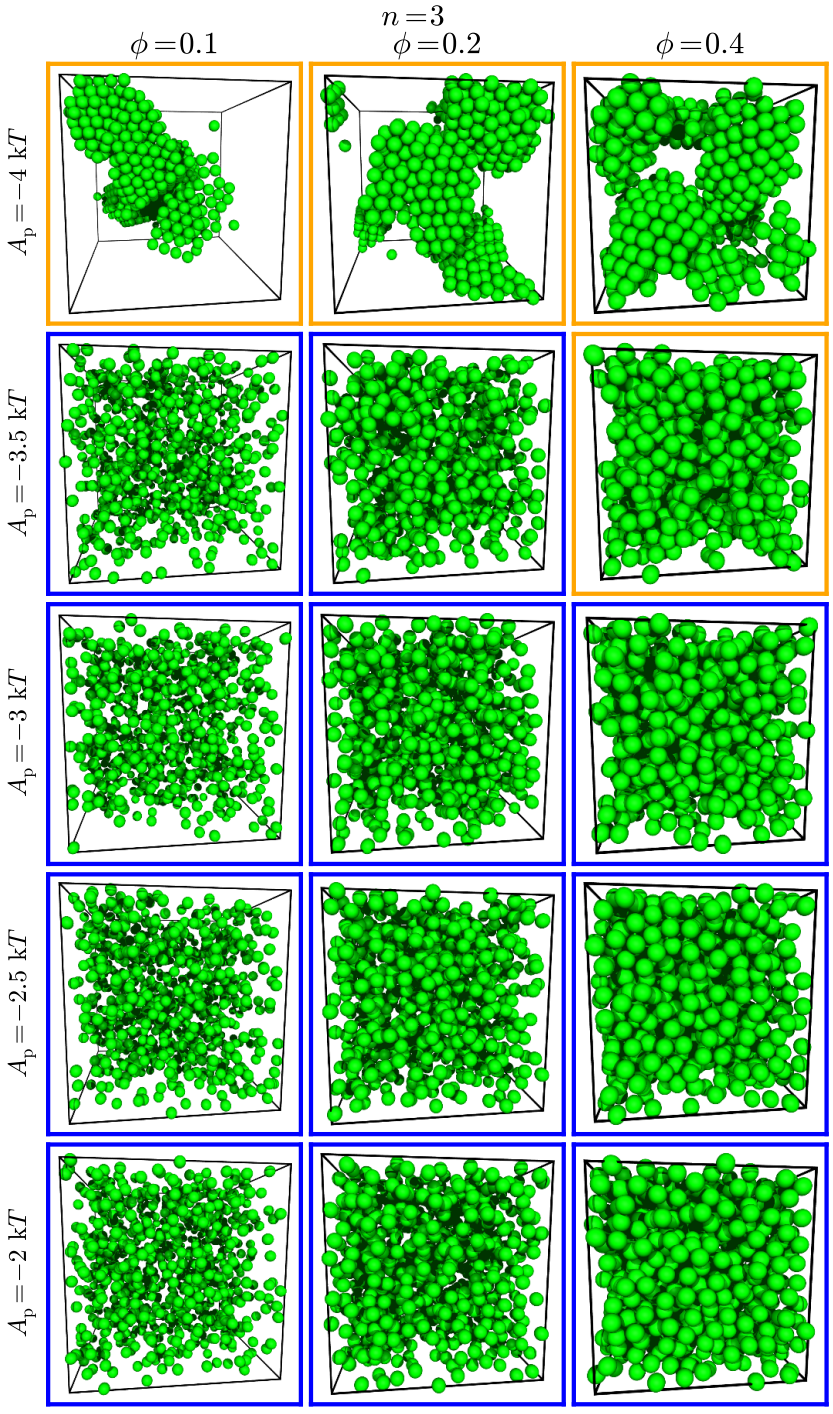

Figure 62: Repressentative snapshosts for $n = 3$ CG systems at the end of quench/equilibration simulations. Presented in the same style as Figure 59.

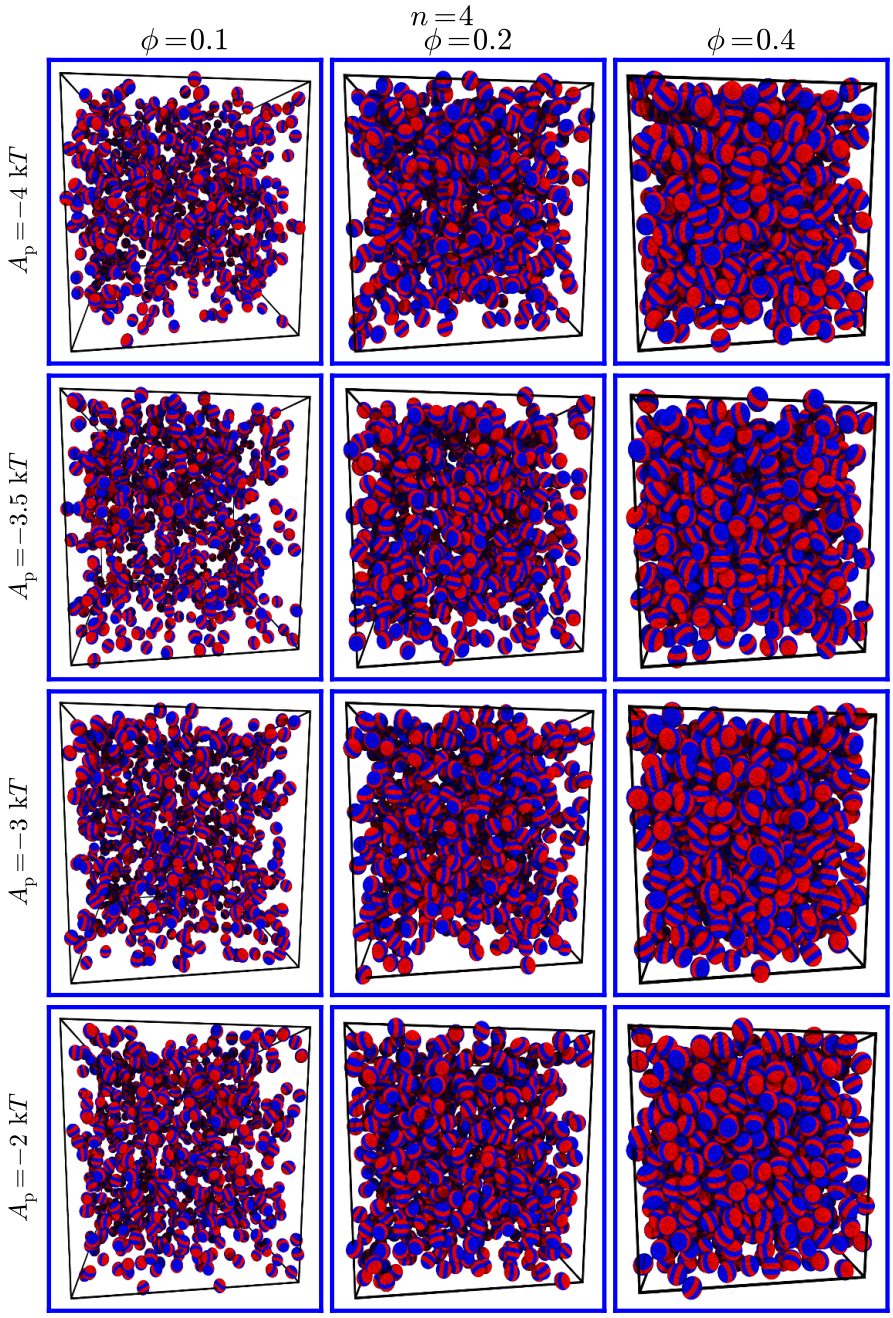

Figure 63: Repressentative snapshosts for $n = 4$ PW systems at the end of quench/equilibration simulations. Presented in the same style as Figure 59.

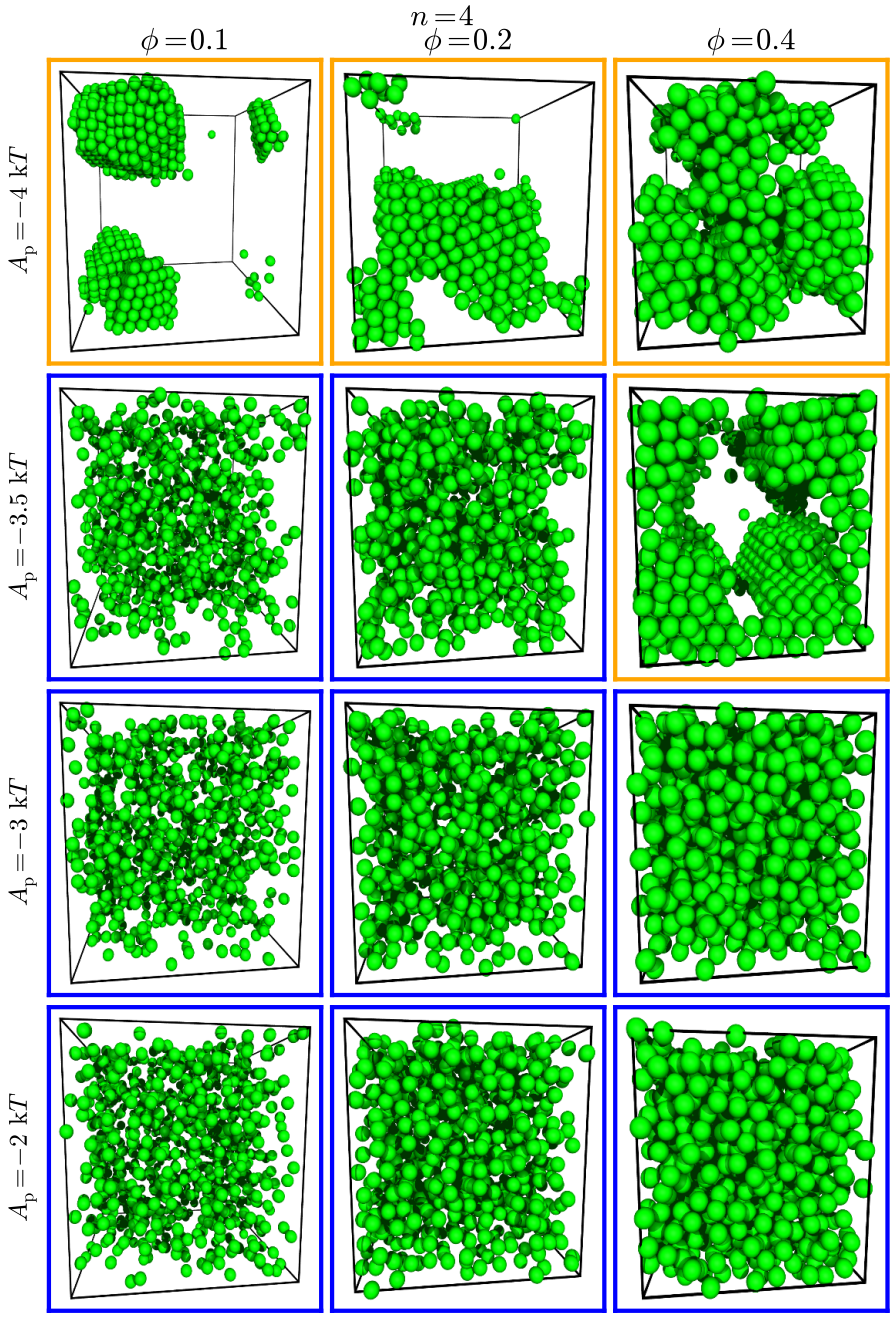

Figure 64: Repressentative snapshosts for $n = 4$ CG systems at the end of quench/equilibration simulations. Presented in the same style as Figure 59.

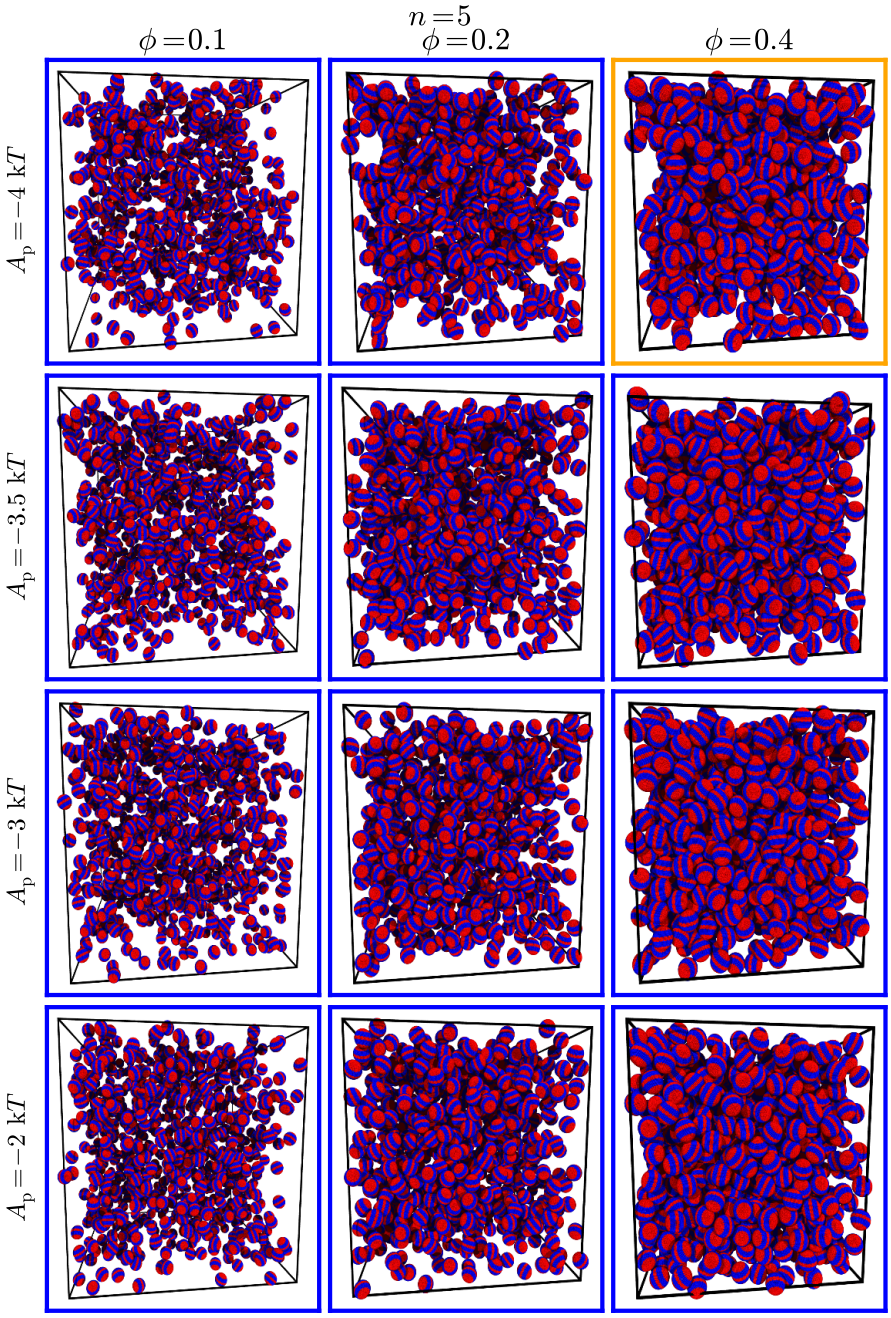

Figure 65: Repressentative snapshosts for $n = 5$ PW systems at the end of quench/equilibration simulations. Presented in the same style as Figure 59.

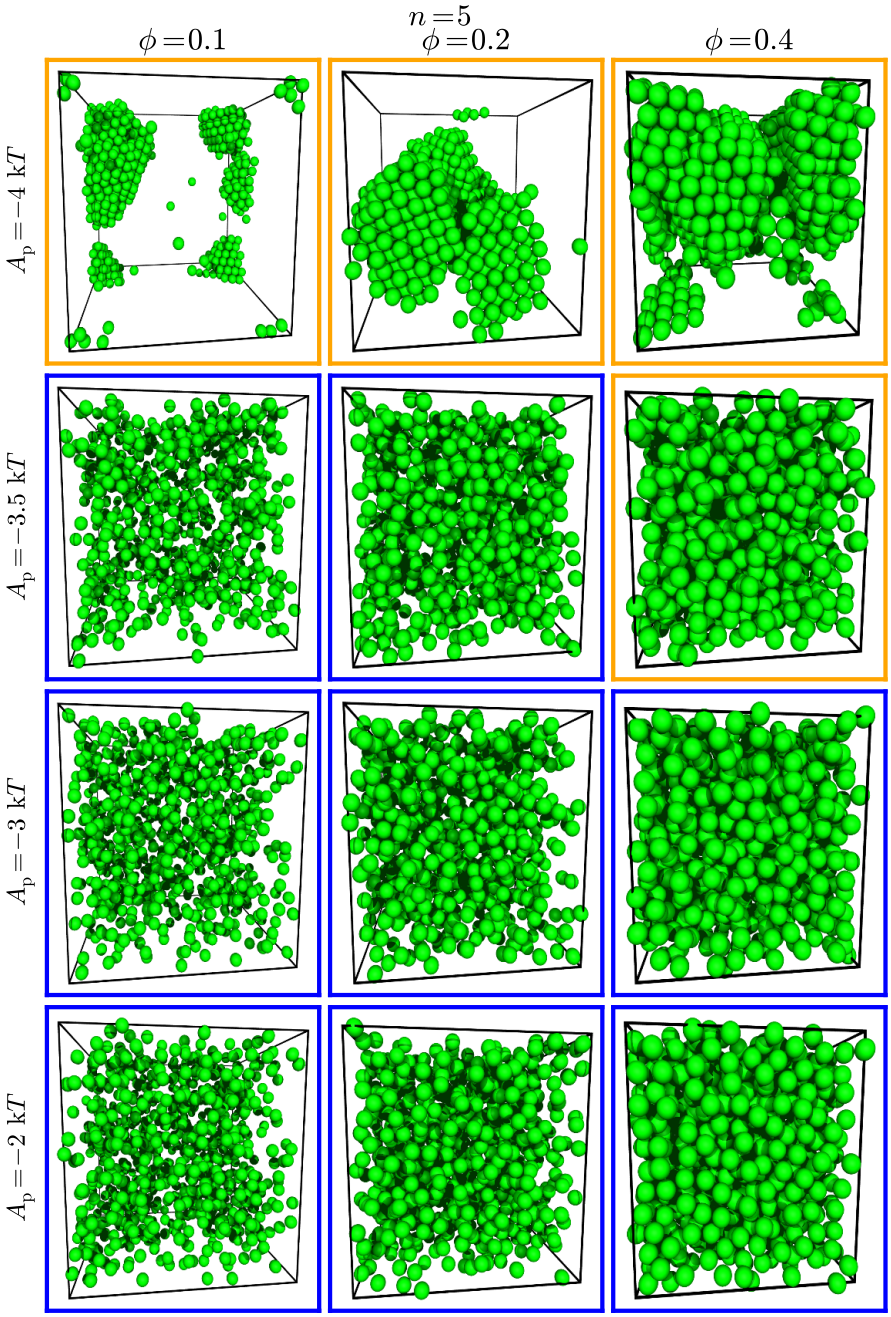

Figure 66: Repressentative snapshosts for $n = 5$ CG systems at the end of quench/equilibration simulations. Presented in the same style as Figure 59.

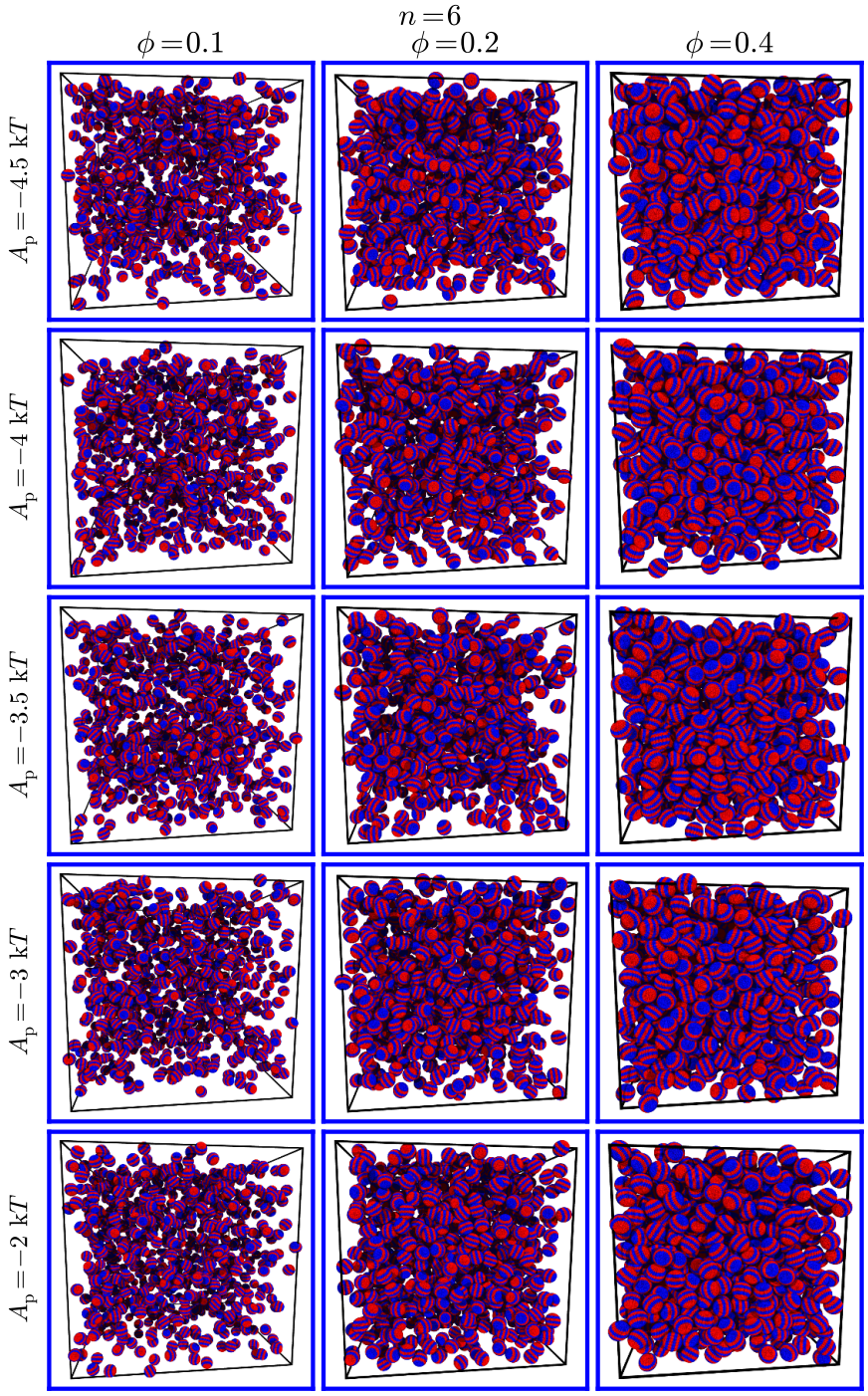

Figure 67: Repressentative snapshosts for $n = 6$ PW systems at the end of quench/equilibration simulations. Presented in the same style as Figure 59.

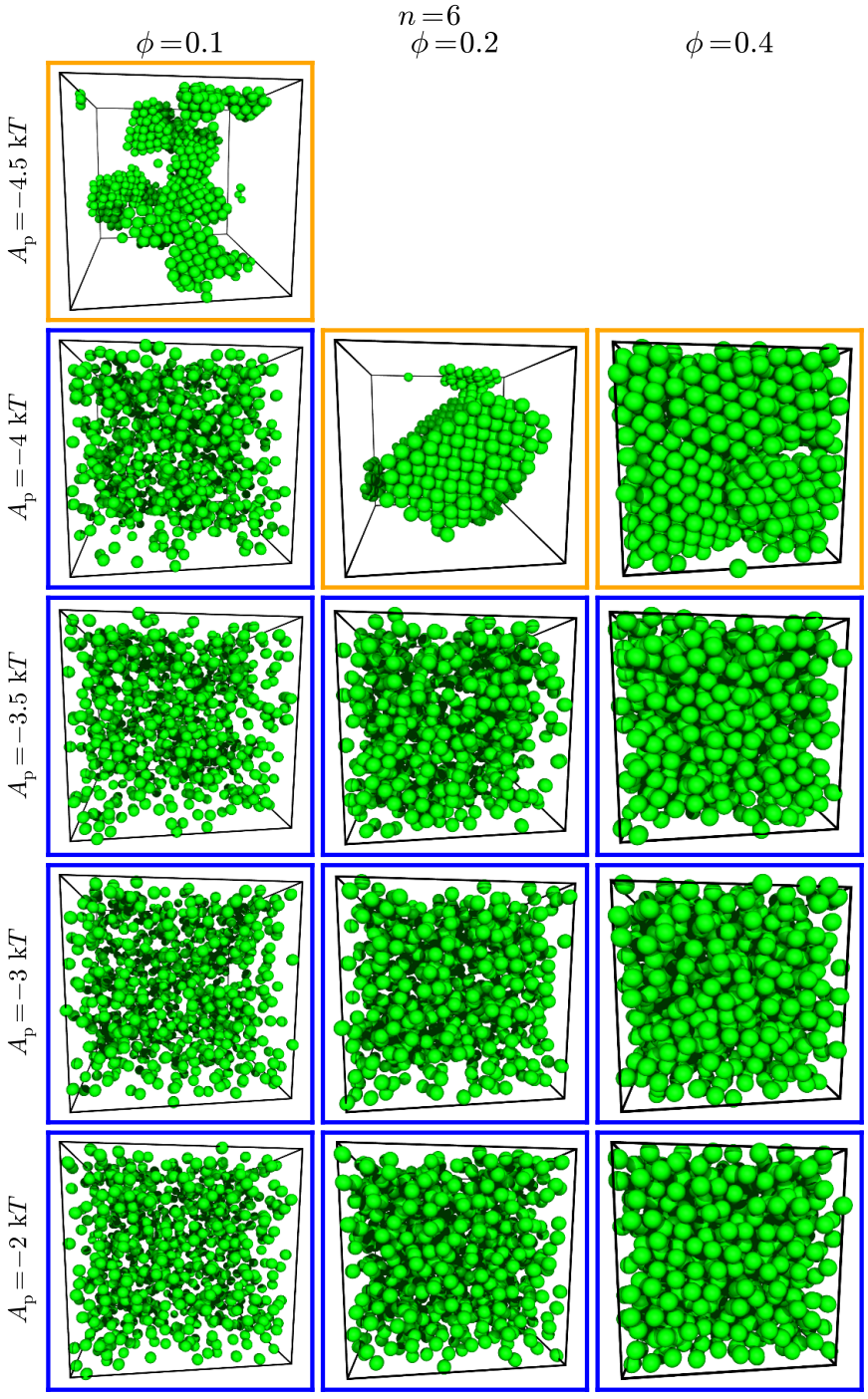

Figure 68: Repressentative snapshosts for $n = 6$ CG systems at the end of quench/equilibration simulations. Presented in the same style as Figure 59.

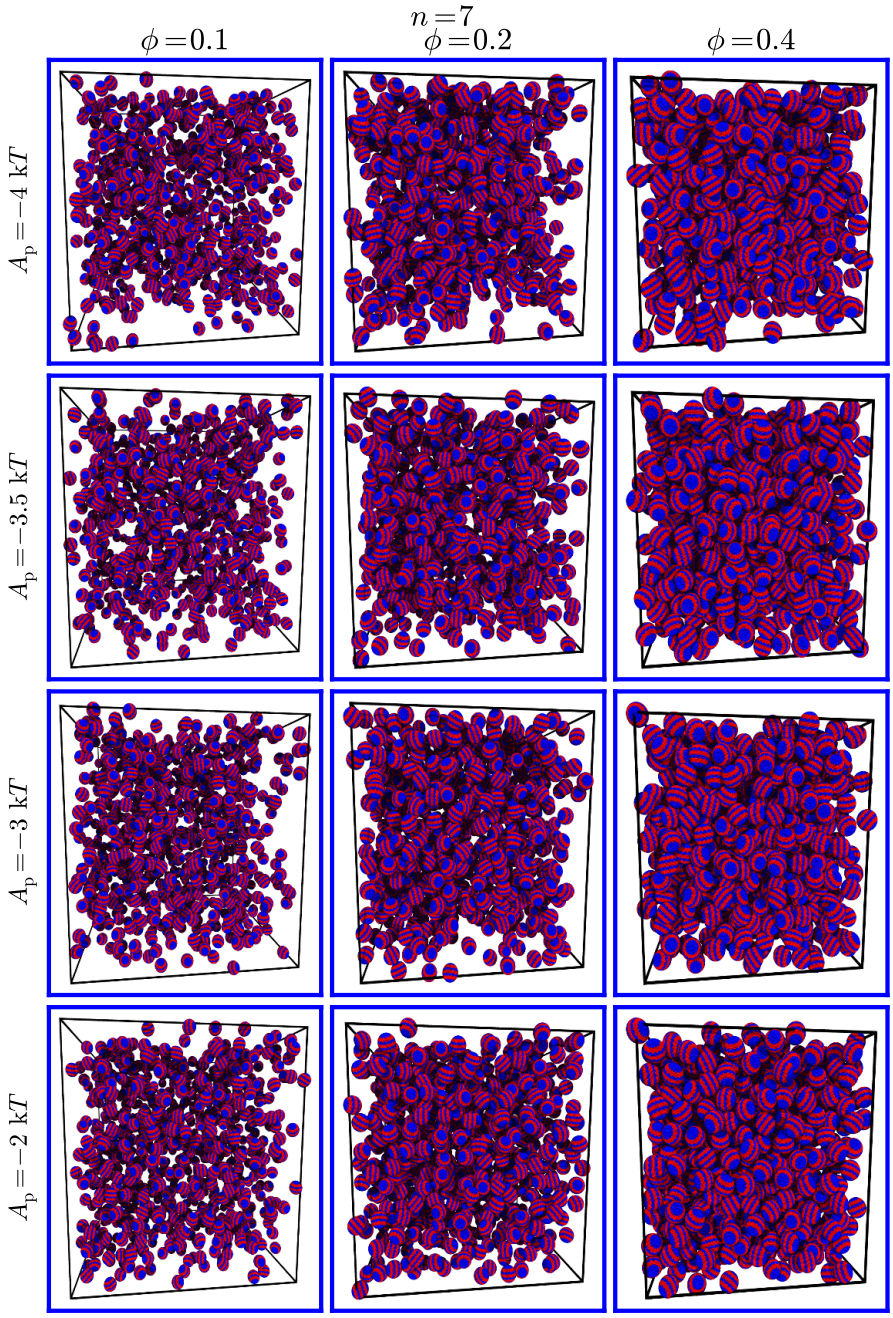

Figure 69: Repressentative snapshosts for $n = 7$ PW systems at the end of quench/equilibration simulations. Presented in the same style as Figure 59.

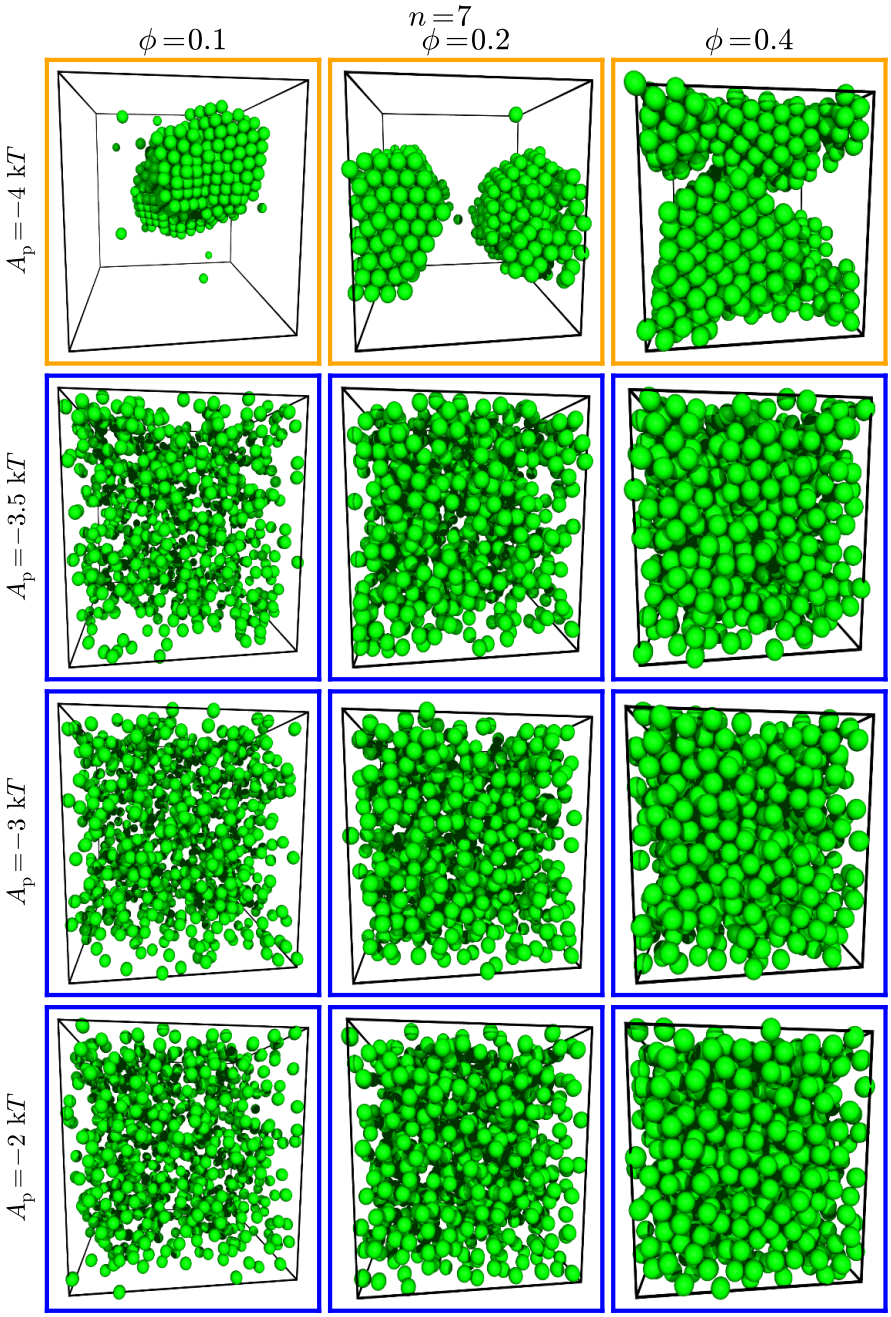

Figure 70: Repressentative snapshosts for $n = 7$ CG systems at the end of quench/equilibration simulations. Presented in the same style as Figure 59.

A.5 Additional structure factor results

This sections provides the additional structures factors for all systems considered. Each of the Figures, Figure 71 to Figure A.5, shows the static structure for a single pair affinity from $A_{\mathrm{p}} = 1\,k_{\mathrm{B}}T$ to $A_{\mathrm{p}} = 4.5\,k_{\mathrm{B}}T$.

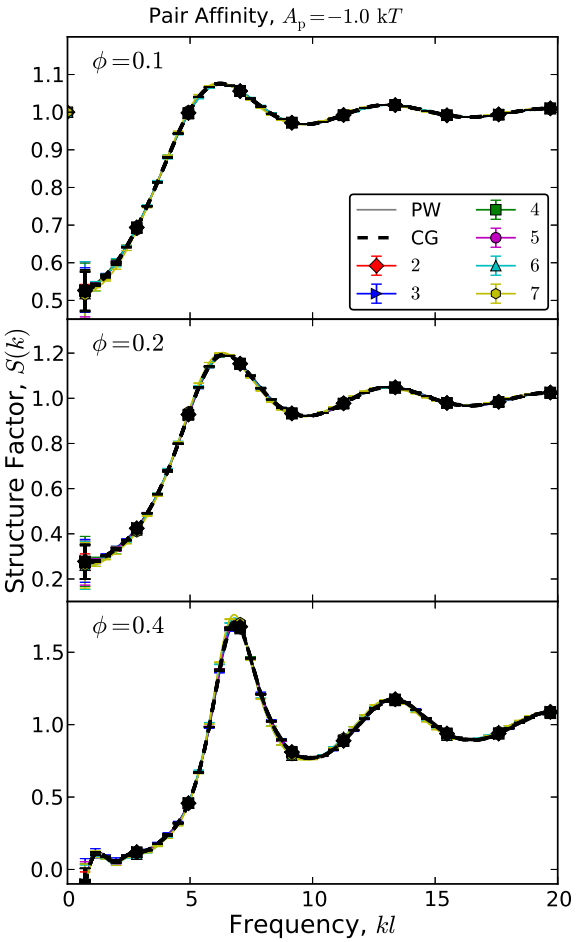

Figure 71: The structure factor $S(k)$ for different n-striped particle systems in both the PW and CG models with pair affinities of $A_{\mathrm{p}} = -1\,k_{\mathrm{B}}T$. Each pane shows results for a different particle volume fraction ϕ. Results of the PW model are shown with solid lines and the color of the line specifies the number stripes as labeled on the plot legend. CG model results are shown with dashed black lines. Plotting markers are included every 50 points to better denote the curves for different n stripes. Error bar are included every 10 points and in most cases the error bar is comparable to plotting line width.

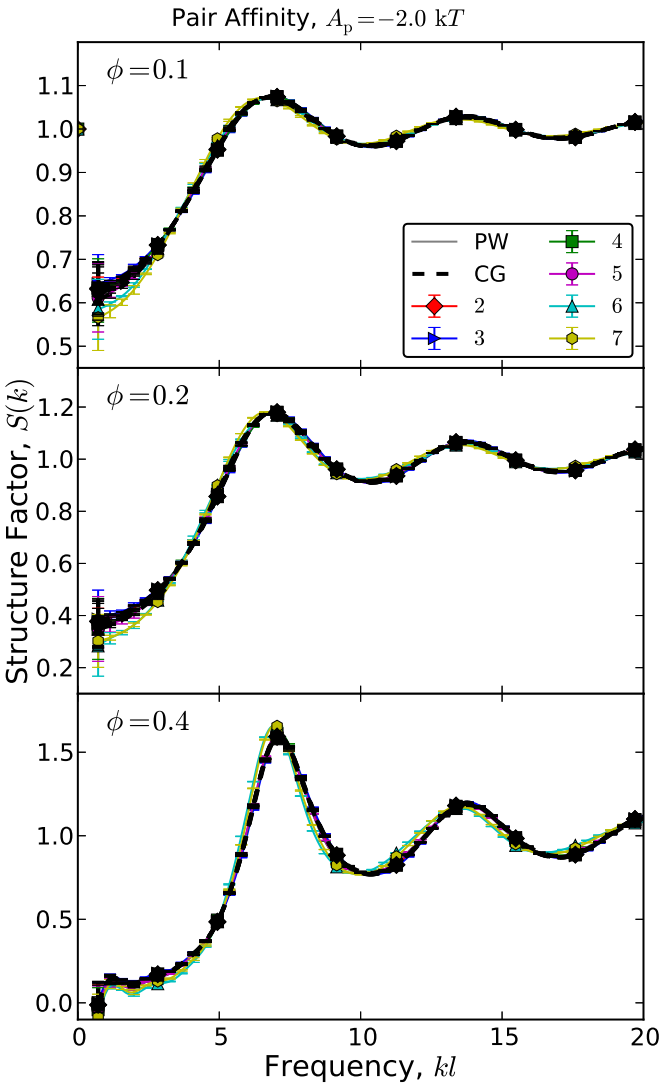

Figure 72: The structure factors for pair affinities of $A_p = -2k_BT$. Plotted in the same style as Figure 71.

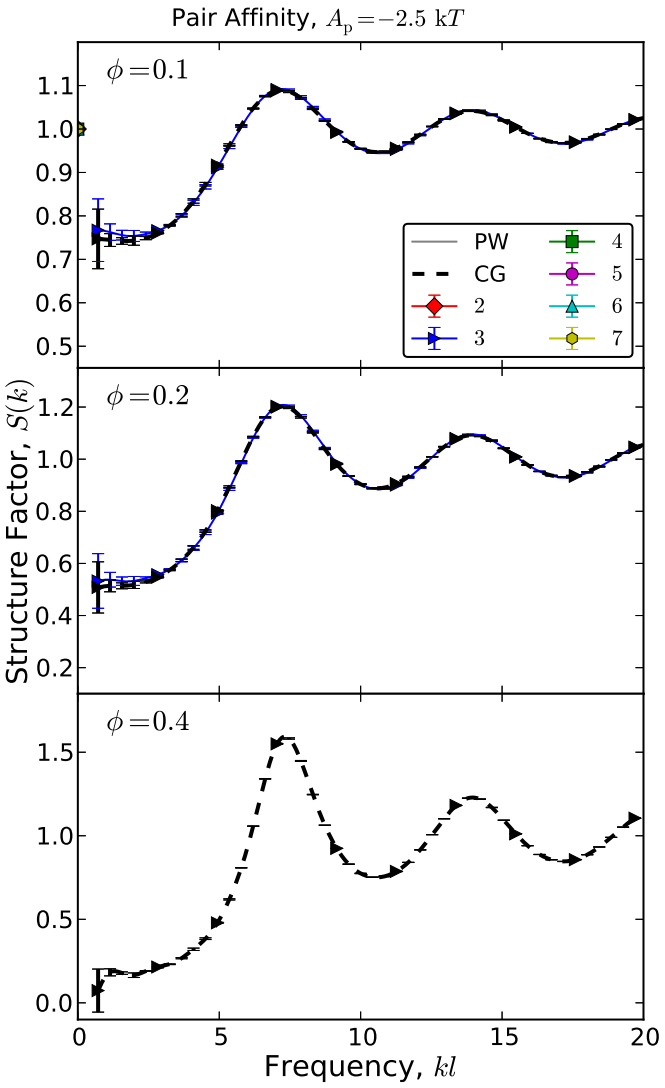

Figure 73: The structure factors for pair affinities of $A_p = -2.5\,k_B T$. Plotted in the same style as Figure 71.

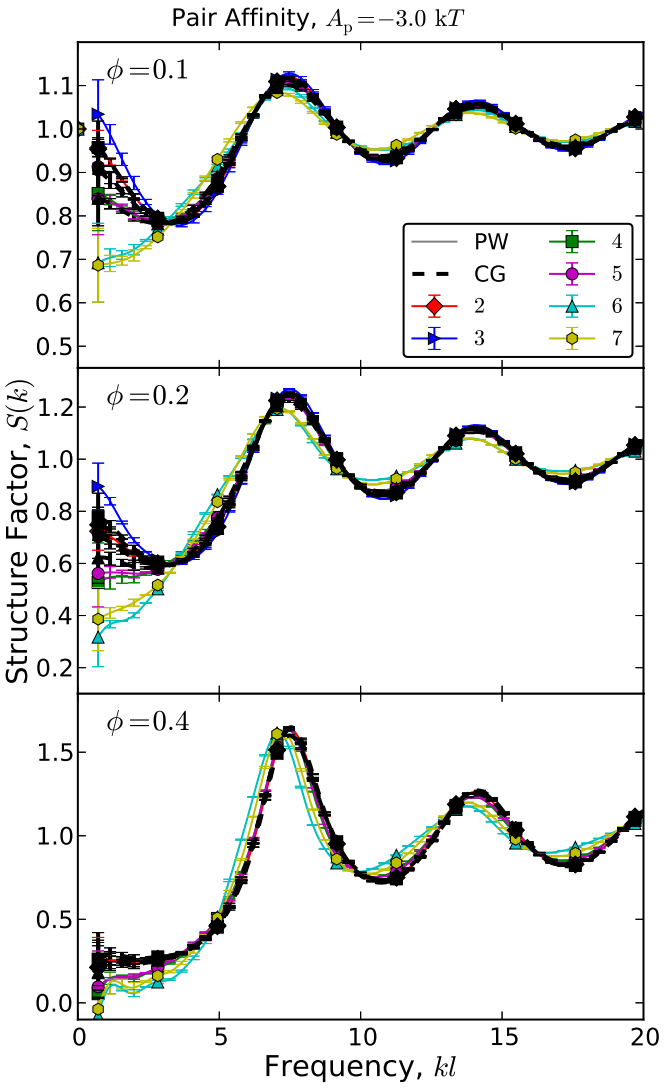

Figure 74: The structure factors for pair affinities of $A_p = -3 k_B T$. Plotted in the same style as Figure 71.

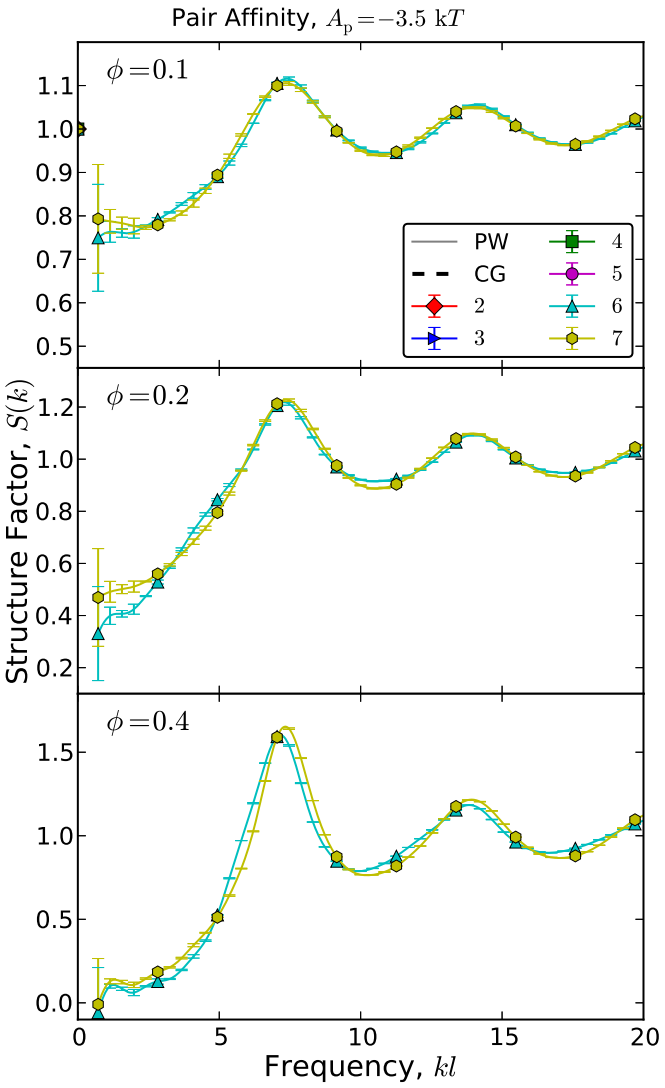

Figure 75: The structure factors for pair affinities of $A_p = -3.5\,k_B T$. Plotted in the same style as Figure 71.

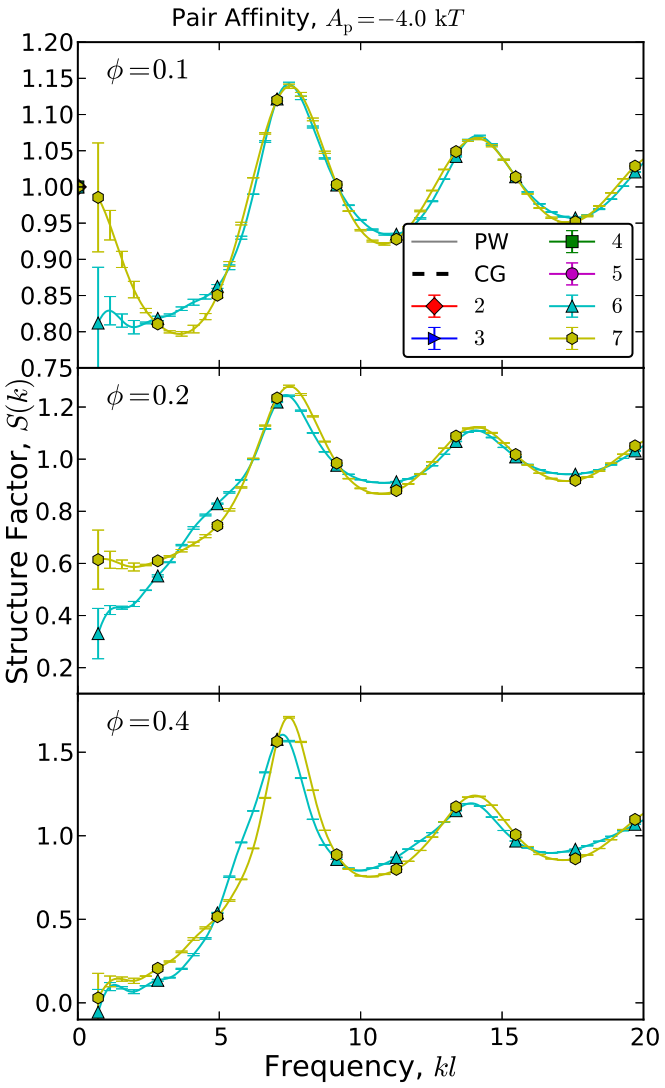

Figure 76: The structure factors for pair affinities of $A_p = -4k_BT$. Plotted in the same style as Figure 71.

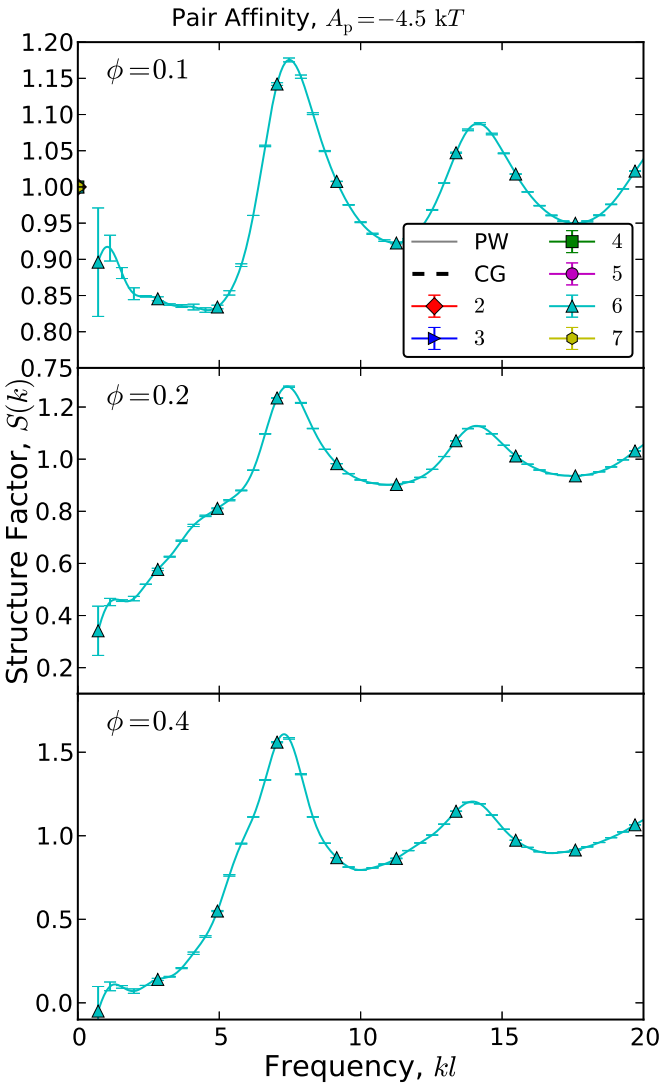

Figure 77: The structure factors for pair affinities of $A_p = -4.5\,k_B T$. Plotted in the same style as Figure 71.

A.6 Additional mean squared displacement (MSD) results

This sections provides the additional mean squared displacement results for all systems considered. Each of the Figures, Figure 78 to Figure 84, shows the static structure for a single pair affinity from $A_\mathrm{p} = 1\,k_\mathrm{B}T$ to $A_\mathrm{p} = 4.5\,k_\mathrm{B}T$.

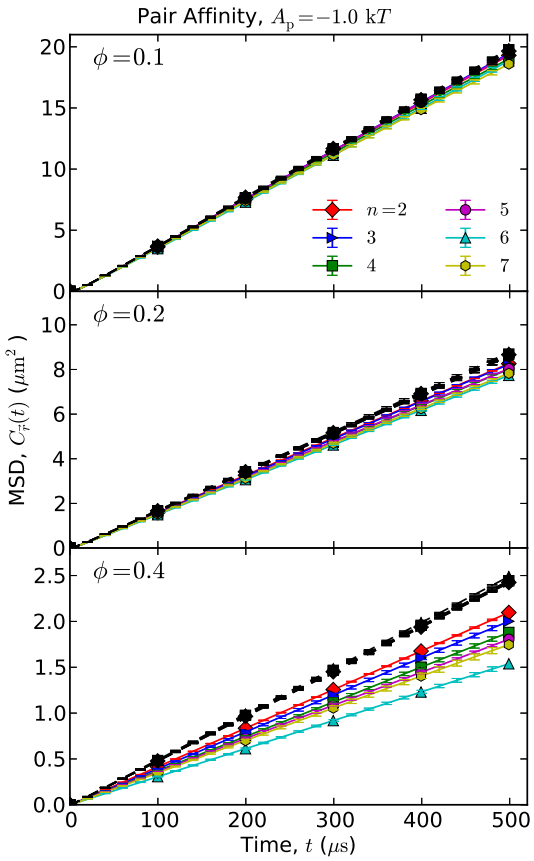

Figure 78: The mean squared displacement (MSD) for different n-striped particle systems in both the PW and CG models with pair affinities of $A_\mathrm{p} = -1\,k_\mathrm{B}T$. Each pane shows results for a different particle volume fraction ϕ. Results of the PW model are shown with solid lines and the color of the line specifies the number stripes as labeled on the plot legend. CG model results are shown with dashed black lines. Plotting markers are included every 500 points to better denote the curves for different n stripes. Error bar are included every 100 points and in most cases they are comparable to plotting line width.

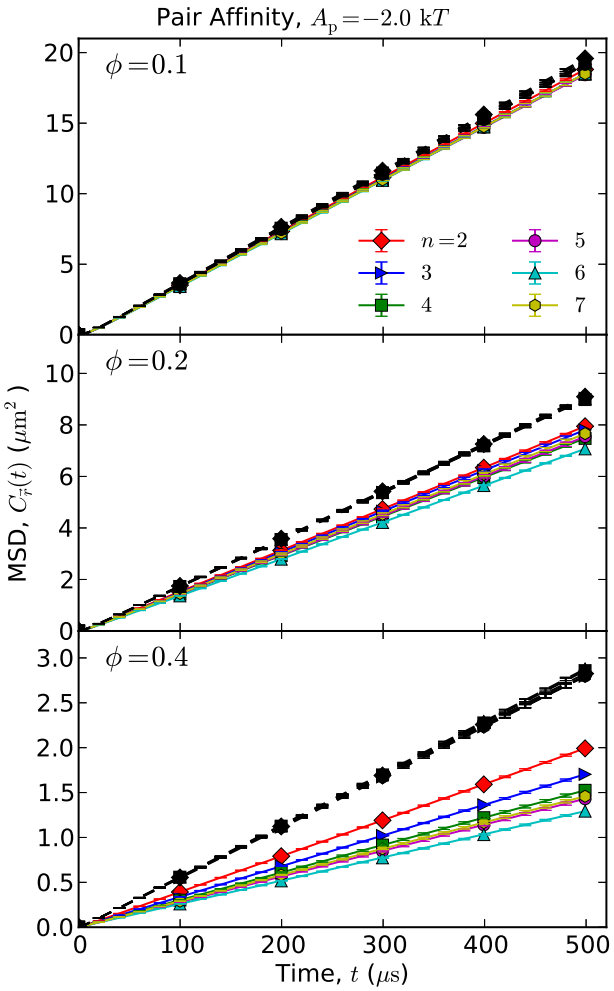

Figure 79: The mean squared displacement (MSD) for pair affinities of $A_p = -2k_BT$. Plotted in the same style as Figure 78.

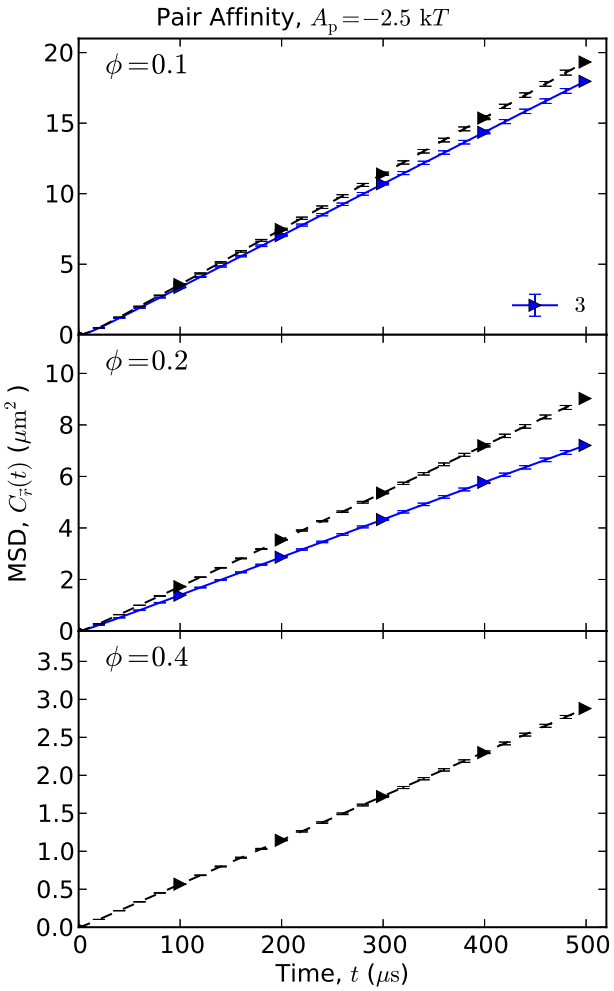

Figure 80: The mean squared displacement (MSD) for pair affinities of $A_p = -2.5 k_B T$. Plotted in the same style as Figure 78.

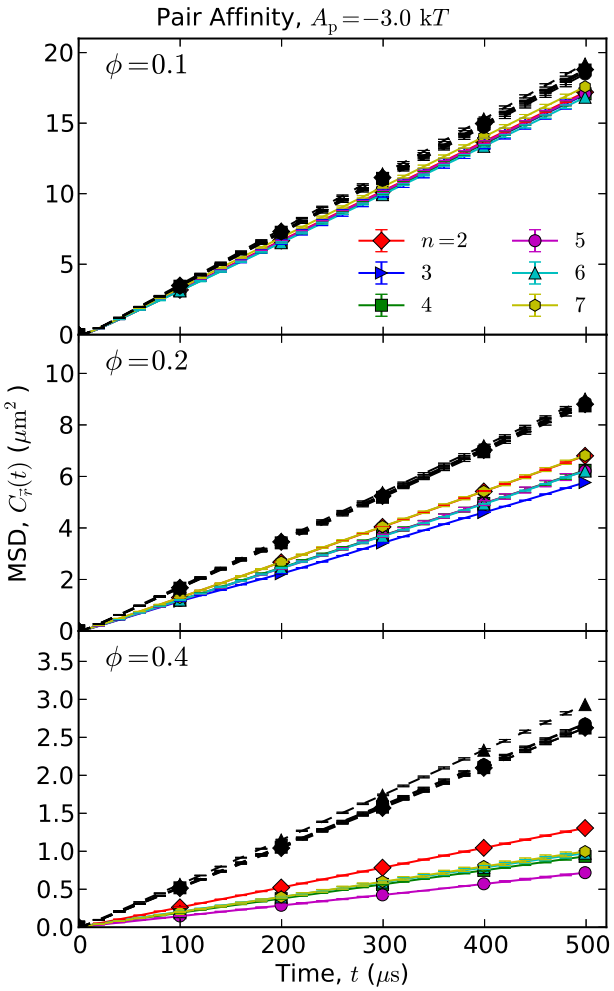

Figure 81: The mean squared displacement (MSD) for pair affinities of $A_p = -3\,k_B T$. Plotted in the same style as Figure 78.

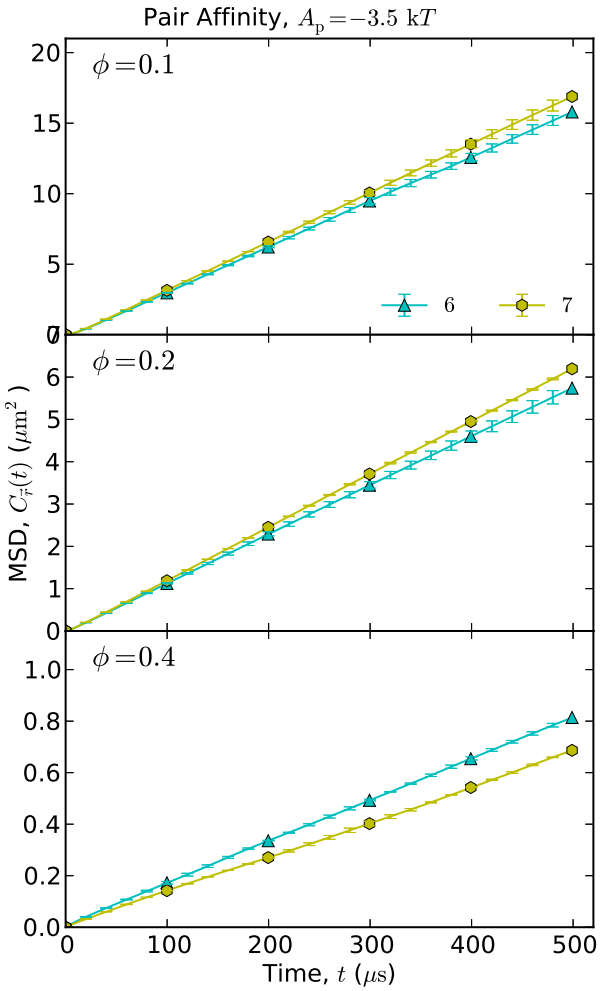

Figure 82: The mean squared displacement (MSD) for pair affinities of $A_p = -3.5 k_B T$. Plotted in the same style as Figure 78.

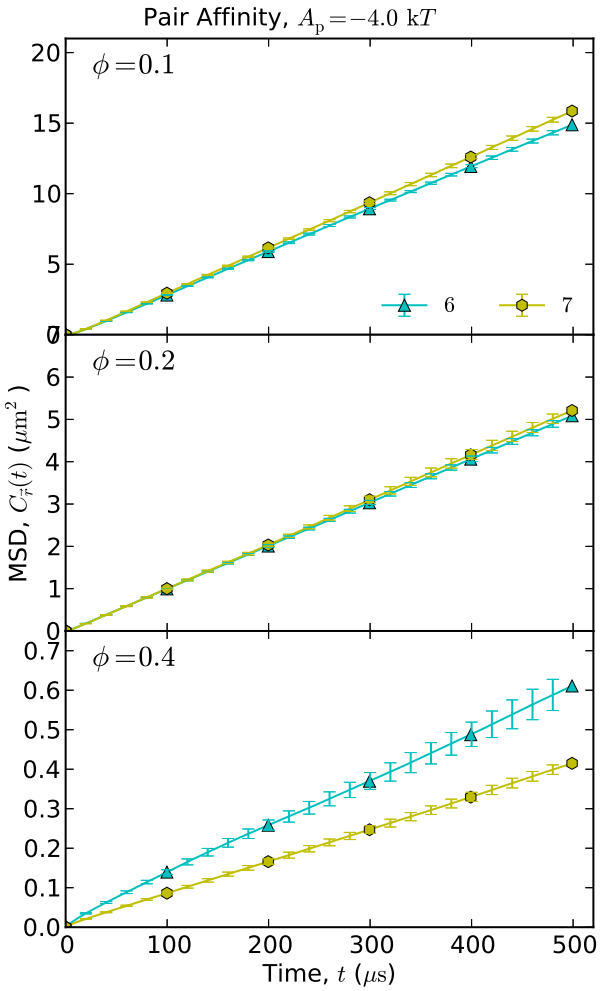

Figure 83: The mean squared displacement (MSD) for pair affinities of $A_p = -4k_BT$. Plotted in the same style as Figure 78.

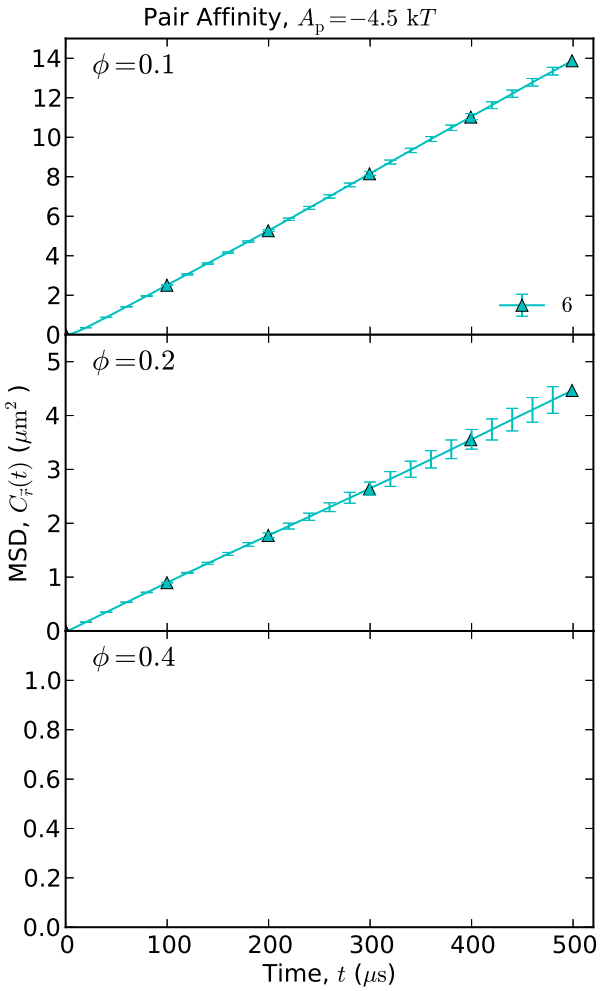

Figure 84: The mean squared displacement (MSD) for pair affinities of $A_p = -4.5 k_B T$. Plotted in the same style as Figure 78.

A.7 Additional velocity autocorrelation function (VACF) results

The additional velocity autocorrelation functions for all systems studied are provided in this sections. Each of the Figures, Figure 85 to Figure 91, shows the velocity autocorrelation function for a single pair affinity from $A_\mathrm{p} = 1\,k_\mathrm{B}T$ to $A_\mathrm{p} = 4.5\,k_\mathrm{B}T$.

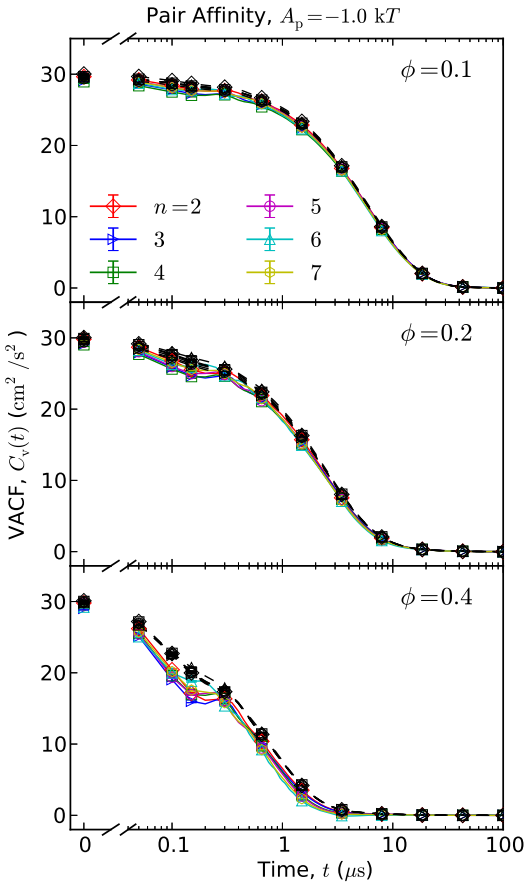

Figure 85: The velocity autocorrelation function (VACF) for different n-striped particle systems in both the PW and CG models with pair affinities of $A_\mathrm{p} = -1\,k_\mathrm{B}T$. Each pane shows results for a different particle volume fraction ϕ. Results of the PW model are shown with solid lines and the color of the line specifies the number stripes as labeled on the plot legend. CG model results are shown with dashed black lines. The log-scale x-axis is broken to include the zero time value. VACF are computed at a time resolution of $\Delta t = 50\,\mathrm{ns}$ and markers are only shown at select data points to better distinguish the curves. The lines between short time markers are linear interpolations to guide the eye.

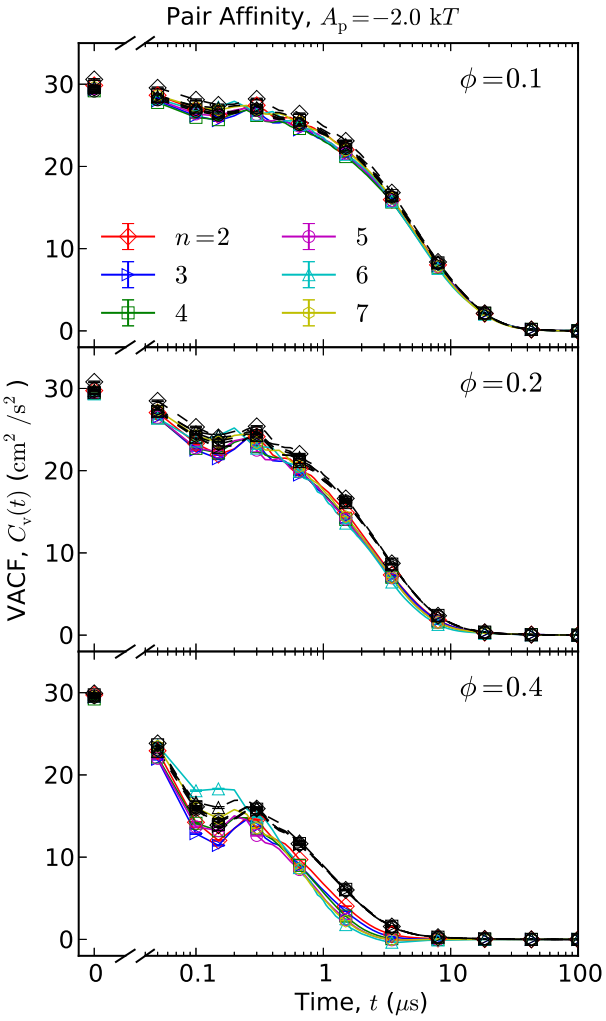

Figure 86: The velocity autocorrelation functions (VACF) for pair affinities of $A_p = -2k_BT$. Plotted in the same style as Figure 85.

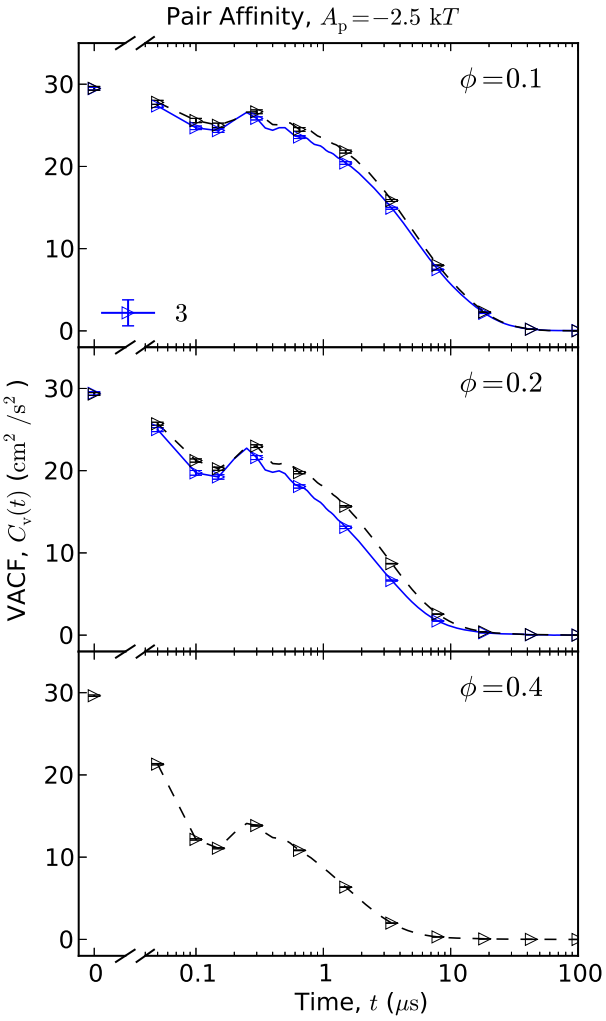

Figure 87: The velocity autocorrelation functions (VACF) for pair affinities of $A_p = -2.5 k_B T$. Plotted in the same style as Figure 85.

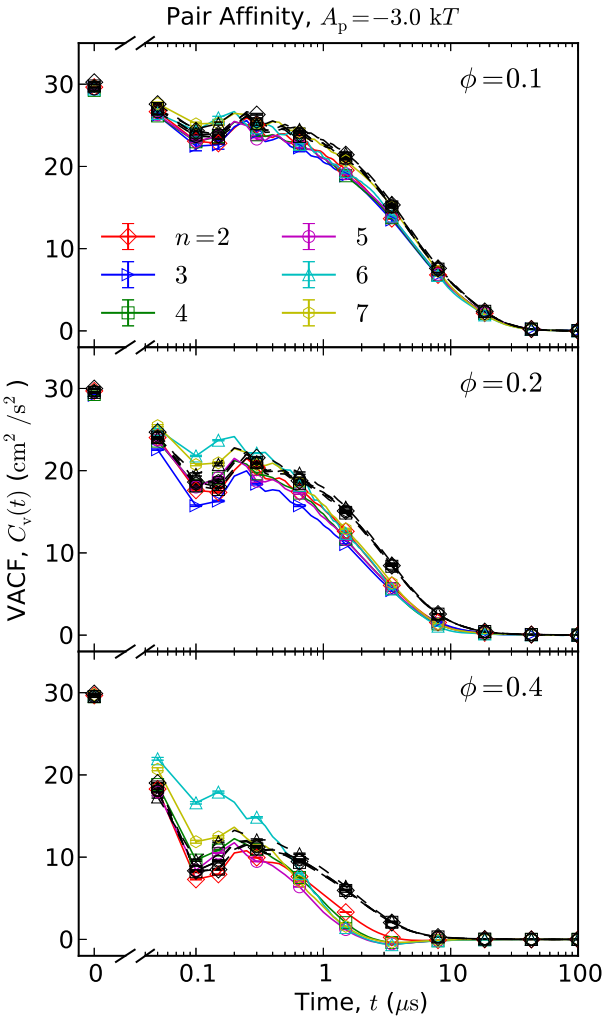

Figure 88: The velocity autocorrelation functions (VACF) for pair affinities of $A_p = -3k_BT$. Plotted in the same style as Figure 85.

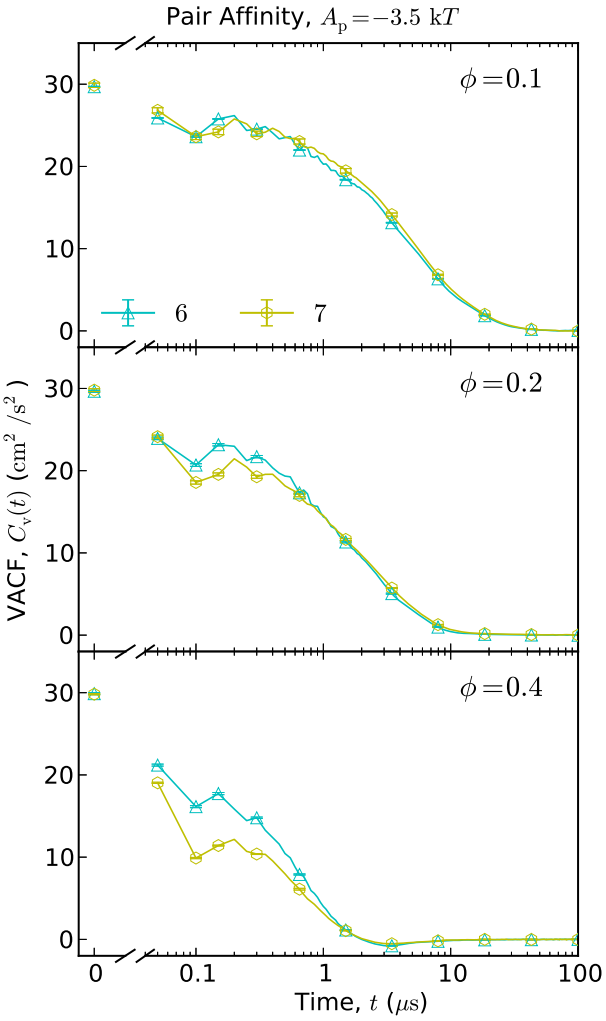

Figure 89: The velocity autocorrelation functions (VACF) for pair affinities of $A_p = -3.5 k_B T$. Plotted in the same style as Figure 85.

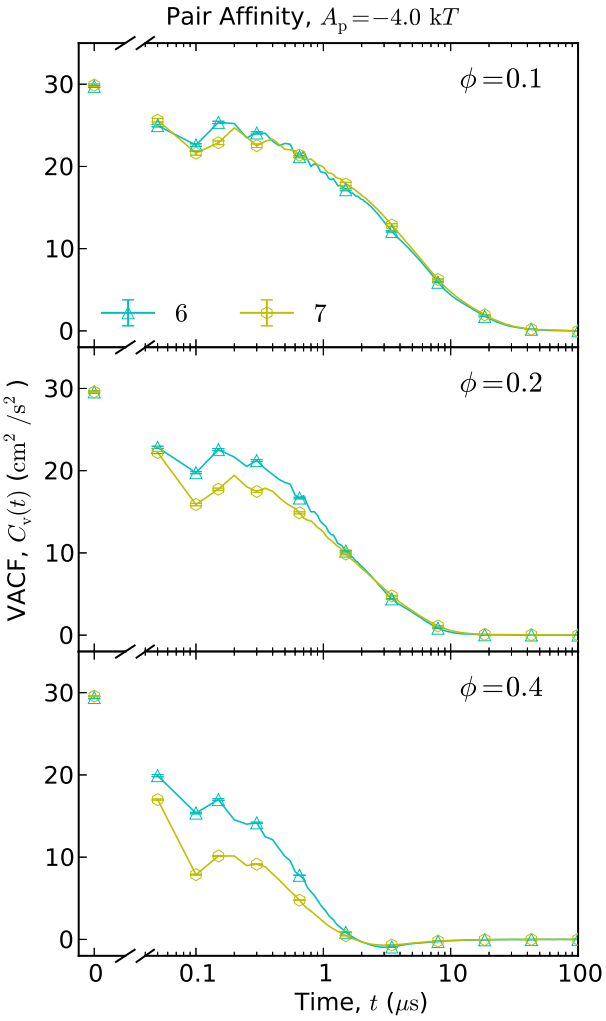

Figure 90: The velocity autocorrelation functions (VACF) for pair affinities of $A_p = -4k_BT$. Plotted in the same style as Figure 85.

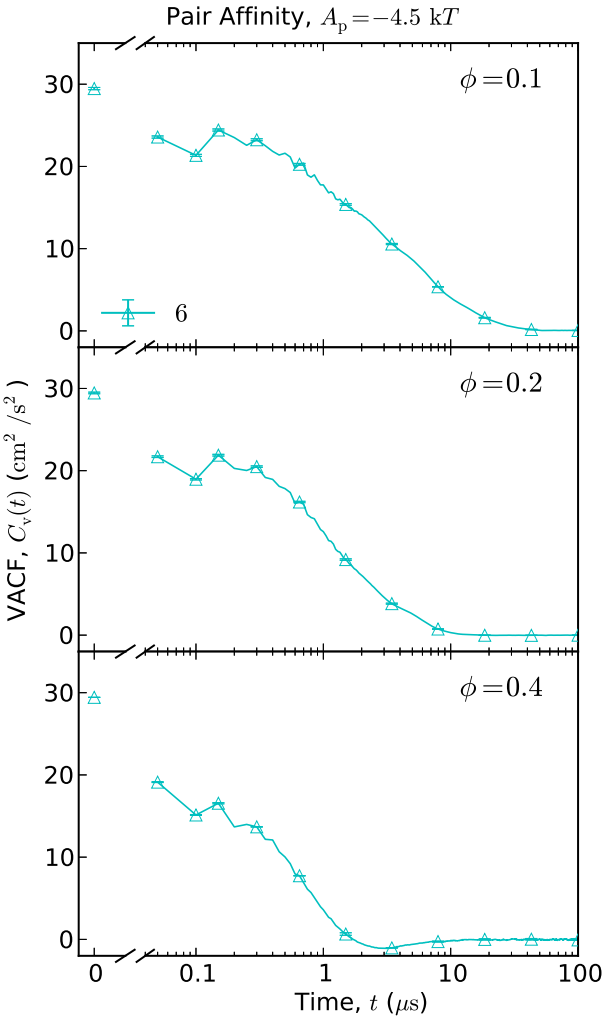

Figure 91: The velocity autocorrelation functions (VACF) for pair affinities of $A_p = -4.5 k_B T$. Plotted in the same style as Figure 85.

A.8 Additional bond duration populations resolution

This sections provides the additional bond duration results for all systems studied. The bond durations are provided in Figures, Figure 92 to Figure 98, for a single pair affinity from $A_p = 1\,k_B T$ to $A_p = 4.5\,k_B T$. Additional, the ratio of bond population in the CG model to that of the PW model are provided in Figures Figure 99 to Figure 102.

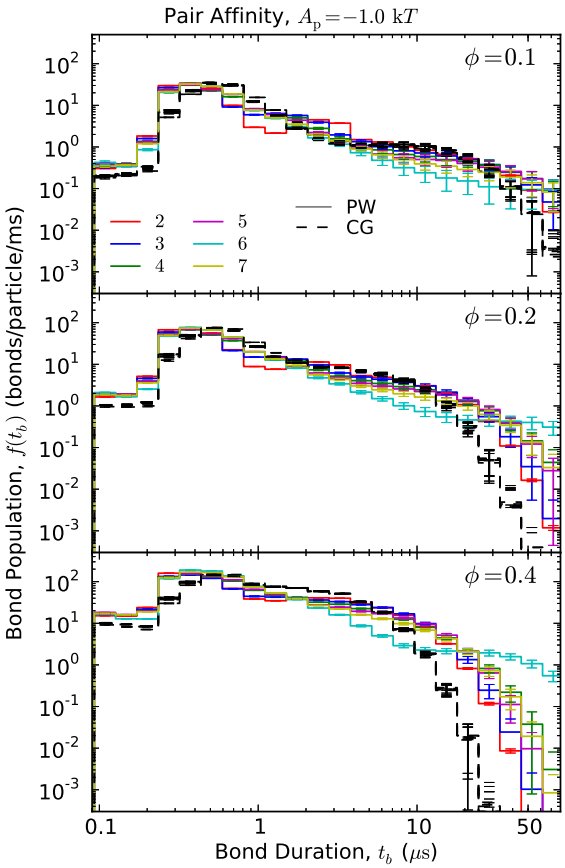

Figure 92: Bond population results: i.e. the frequency at which reversible bonds of duration t_b are observed in simulation. Each pane shows results for a different particle volume fraction ϕ. Results of the PW model are shown with solid lines and the color of the line specifies the number stripes as labeled on the plot legend. CG model results are shown with dashed black lines. The CG results for different n are comparable and cannot be distinguished from each other. Bond population is computed through construction of a histogram of $\log(t_b)$ and plotting lines show bin widths. Error bars are included.

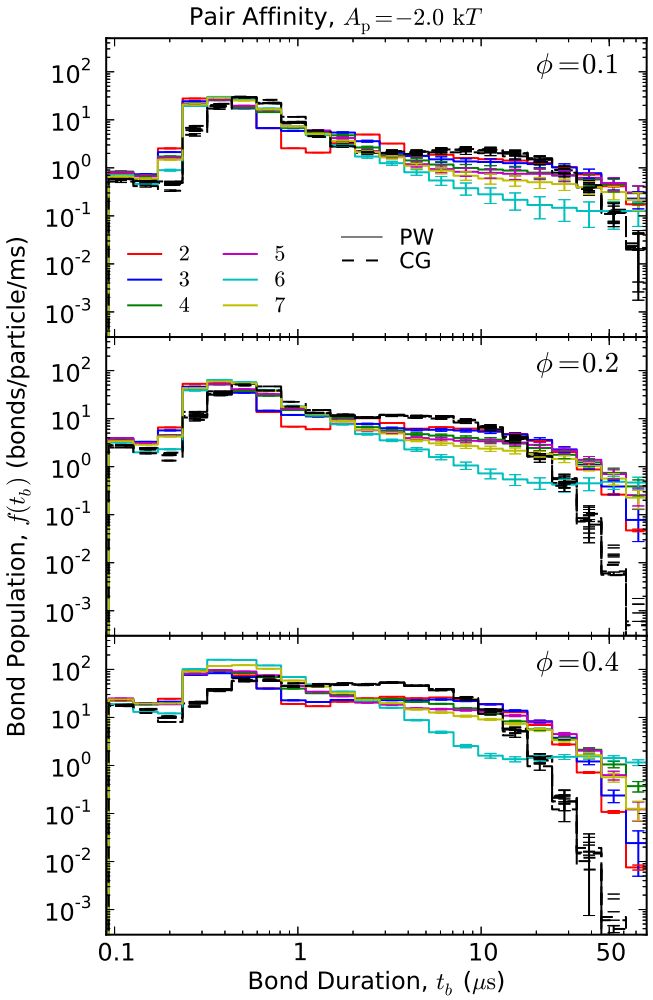

Figure 93: The bond populations for pair affinities of $A_p = -2k_BT$. Plotted in the same style as Figure 92.

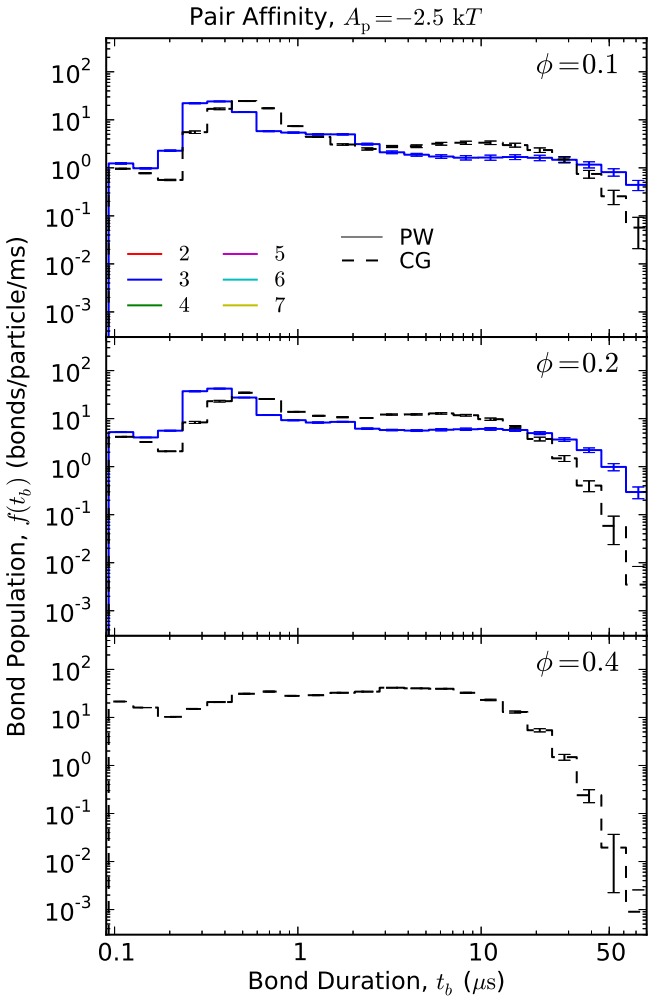

Figure 94: The bond populations for pair affinities of $A_p = -2.5\,k_B T$. Plotted in the same style as Figure 92.

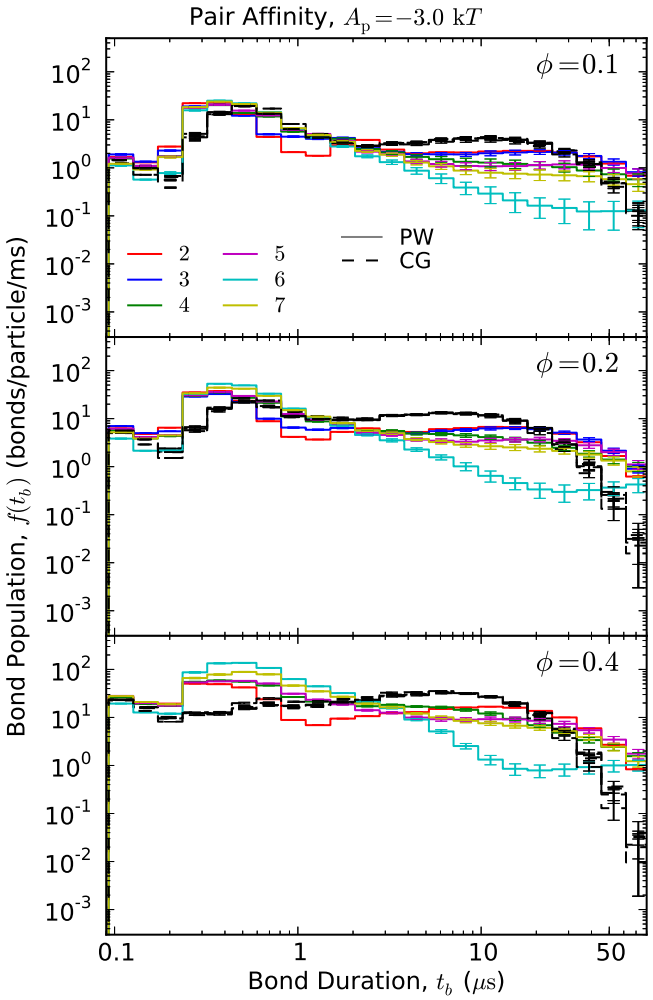

Figure 95: The bond populations for pair affinities of $A_p = -3.0 k_B T$. Plotted in the same style as Figure 92.

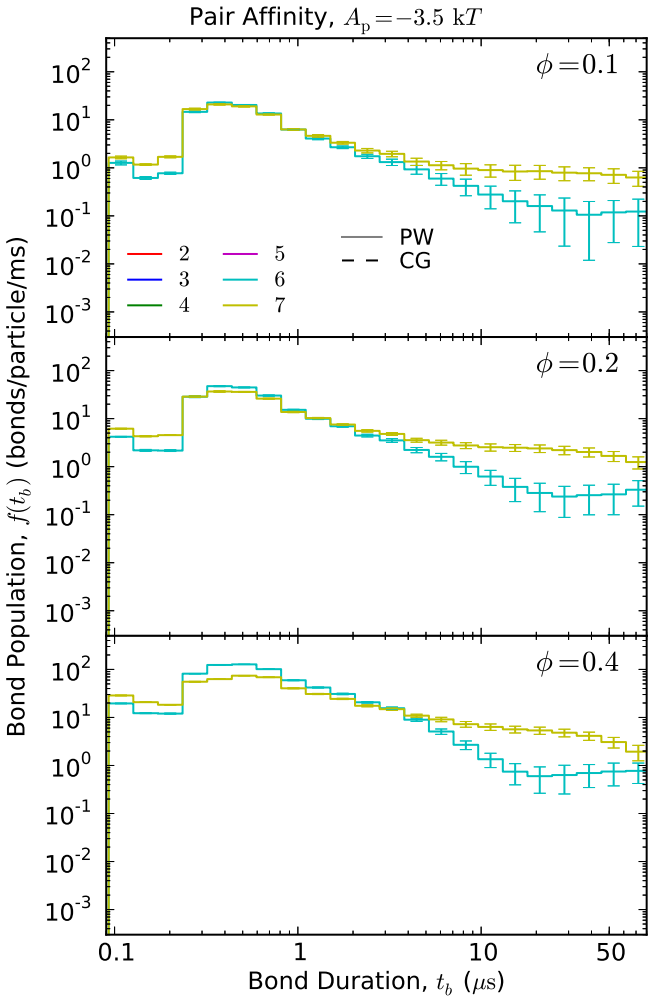

Figure 96: The bond populations for pair affinities of $A_p = -3.5\,k_B T$. Plotted in the same style as Figure 92.

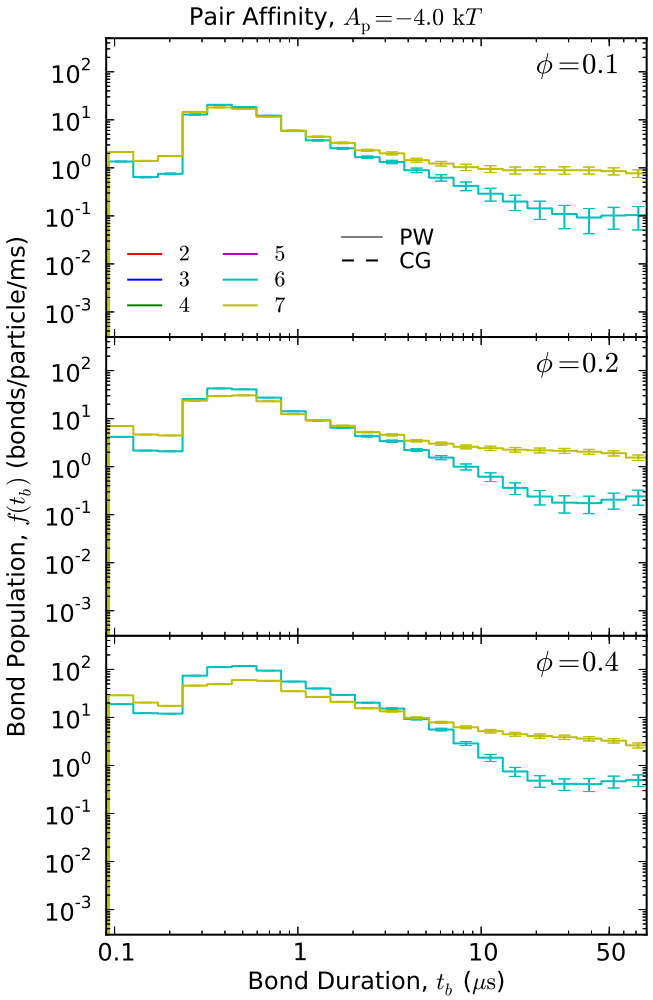

Figure 97: The bond populations for pair affinities of $A_p = -4.0 k_B T$. Plotted in the same style as Figure 92.

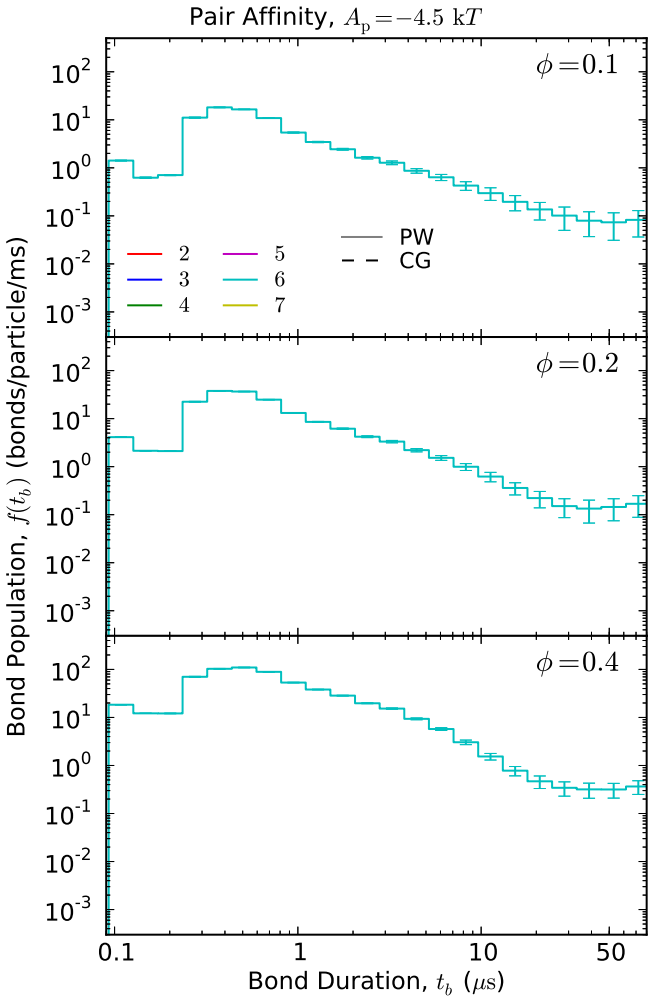

Figure 98: The bond populations for pair affinities of $A_p = -4.5\,k_B T$. Plotted in the same style as Figure 92.

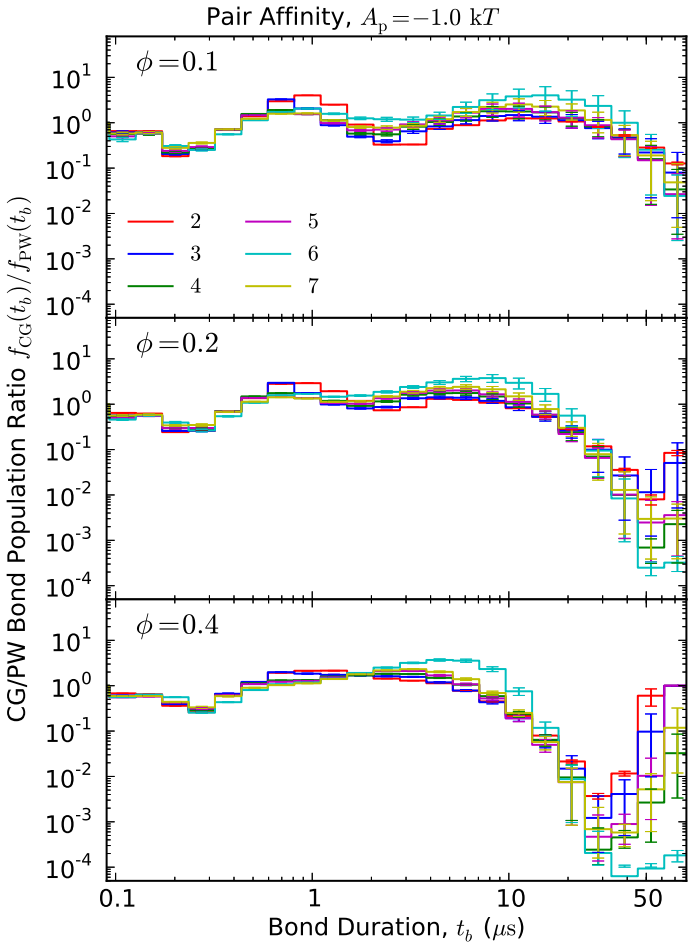

Figure 99: The ratio of bond population in the CG model to that of the PW model for pair affinities of $A_p = -1\,k_B T$. Each pane shows results for a different particle volume fraction ϕ. Results for different n-striped systems are shown by different color lines as labeled on the plot legend. Error bars are included.

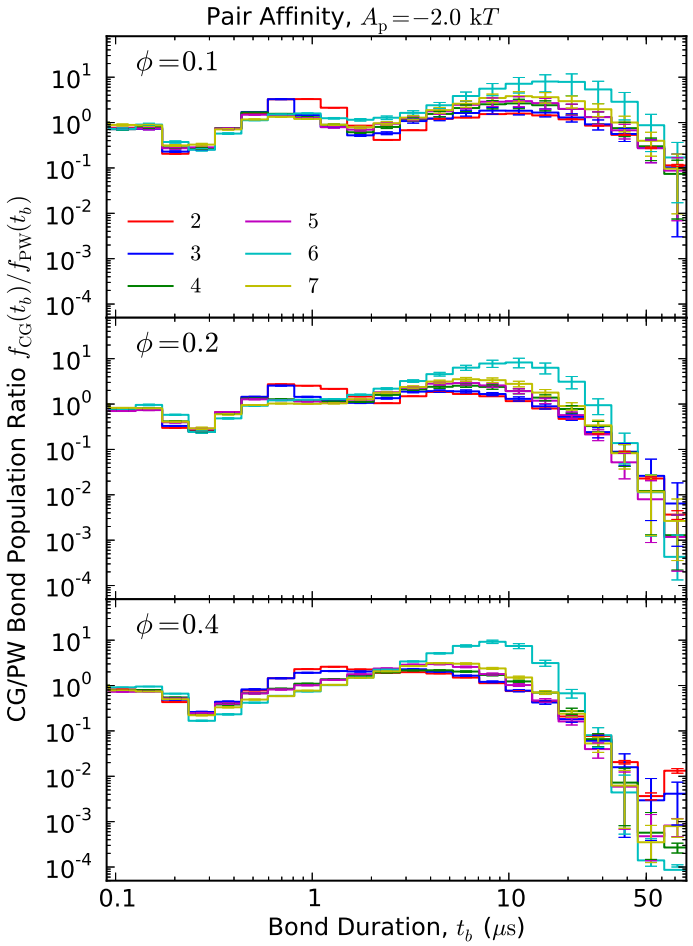

Figure 100: The ratio of bond population in the CG model to that of the PW model for pair affinities of $A_p = -2k_BT$. Plotted in the same style as Figure 99.

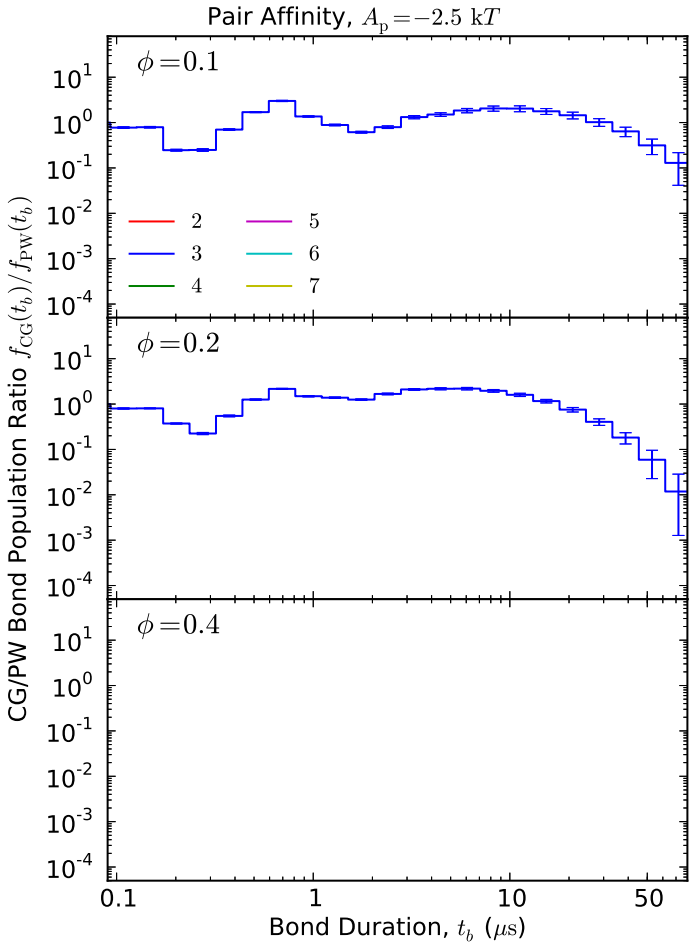

Figure 101: The ratio of bond population in the CG model to that of the PW model for pair affinities of $A_p = -2k_BT$. Plotted in the same style as Figure 99.

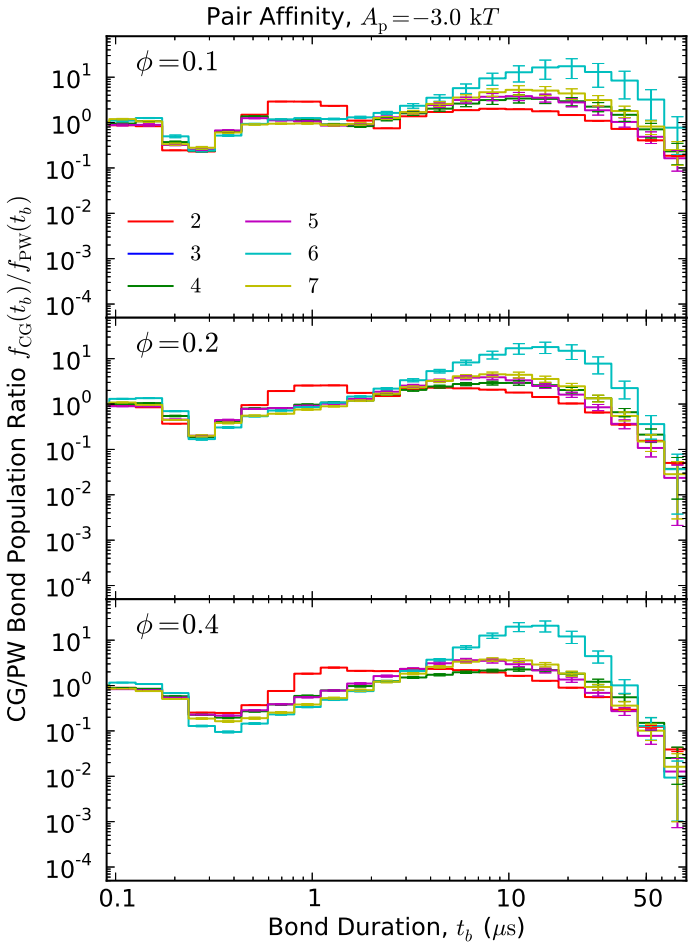

Figure 102: The ratio of bond population in the CG model to that of the PW model for pair affinities of $A_p = -2k_BT$. Plotted in the same style as Figure 99.

REFERENCES

[1] AKKERMANS, R. L. C. and BRIELS, W. J., "Coarse-grained dynamics of one chain in a polymer melt," *J. Chem. Phys.*, vol. 113, p. 6409, 2000.

[2] ARMSTRONG, J. A., CHAKRAVARTY, C., and BALLONE, P., "Statistical mechanics of coarse graining: Estimating dynamical speedups from excess entropies," *J. Chem. Phys.*, vol. 136, p. 124503, 2012.

[3] AUER, S. and FRENKEL, D., "Prediction of absolute crystal-nucleation rate in hard-sphere colloids," *Nature*, vol. 409, no. 6823, pp. 1020–1023, 2001.

[4] BELLONI, L., "Colloidal interactions," *J. Phys.: Condens. Matter*, vol. 12, no. 46, p. R549, 2000.

[5] BENNETT, C. H., "Efficient estimation of free energy differences from monte carlo data," *J. Comput. Phys.*, vol. 22, no. 2, pp. 245–268, 1976.

[6] BERARDI, R. and ZANNONI, C., "Do thermotropic biaxial nematics exist? a monte carlo study of biaxial gay–berne particles," *J. Chem. Phys.*, vol. 113, p. 5971, 2000.

[7] BILLETER, J. L. and PELCOVITS, R. A., "Defect configurations and dynamical behavior in a gay-berne nematic emulsion," *Phys. Rev. E*, vol. 62, no. 1, p. 711, 2000.

[8] BOON, N., GALLARDO, E. C., ZHENG, S., EGGEN, E., DIJKSTRA, M., and VAN ROIJ, R., "Screening of heterogeneous surfaces: charge renormalization of janus particles," *J. Phys.: Condens. Matter*, vol. 22, no. 10, p. 104104, 2010.

[9] BOS, M. T. A. and VAN OPHEUSDEN, J. H. J., "Brownian dynamics simulation of gelation and aging in interacting colloidal systems," *Phys. Rev. E*, vol. 53, no. 5, pp. 5044–5050, 1996.

[10] BRADY, J. F. and BOSSIS, G., "Stokesian dynamics," *Annu. Rev. Fluid Mech.*, vol. 20, pp. 111–157, 1988.

[11] BRINKER, C. J. and SCHERER, G. W., *Sol-gel science: the physics and chemistry of sol-gel processing*. Academic Pr, 1990.

[12] BRINKER, C. J. and SCHERER, G. W., *Sol-gel science: the physics and chemistry of sol-gel processing*. Access Online via Elsevier, 1990.

[13] BROWN, W. M., WANG, P., PLIMPTON, S. J., and THARRINGTON, A. N., "Implementing molecular dynamics on hybrid high performance computers–short range forces," *Comp. Phys. Comm.*, vol. 182, no. 4, pp. 898–911, 2011.

[14] BUTLER, B. and HANLEY, H., "Aggregation in quenched systems interacting through a short-range attractive, long-range repulsive potential," *J. Sol-Gel Sci. Technol.*, vol. 15, no. 2, pp. 161–166, 1999.

[15] CAMP, P. J., SHELLEY, J. C., and PATEY, G. N., "Isotropic fluid phases of dipolar hard spheres," *Phys. Rev. Lett.*, vol. 84, no. 1, pp. 115–118, 2000.

[16] CARMELI, B. and NITZAN, A., "Non-markoffian theory of activated rate processes," *Phys. Rev. Lett.*, vol. 49, pp. 423–426, 1982.

[17] CARMELI, B. and NITZAN, A., "Theory of activated rate processes: Position dependent friction," *Chem. Phys. Lett.*, vol. 102, pp. 517–522, 1983.

[18] CASAGRANDE, C., FABRE, P., RAPHAEL, E., and VEYSSIE, M., "Water/oil interfaces.," *Europhys. Lett.*, vol. 9, no. 3, pp. 251–255, 1989.

[19] CAYRE, O., PAUNOV, V. N., and VELEV, O. D., "Fabrication of asymmetrically coated colloid particles by microcontact printing techniques," *J. Mater. Chem.*, vol. 13, no. 10, pp. 2445–2450, 2003.

[20] CAYRE, O., PAUNOV, V. N., and VELEV, O. D., "Fabrication of dipolar colloid particles by microcontact printing," *Chem. Comm.*, vol. 39, no. 18, pp. 2296–2297, 2003.

[21] CHANDLER, D., WEEKS, J. D., and ANDERSEN, H. C., "Van der waals picture of liquids, solids, and phase transformations," *Science*, vol. 220, no. 4599, pp. 787–794, 1983.

[22] CHEN, Q., YAN, J., ZHANG, J., BAE, S. C., and GRANICK, S., "Janus and multiblock colloidal particles," *Langmuir*, vol. 28, no. 38, pp. 13555–13561, 2012.

[23] CORTÉS, E., WEST, B. J., and LINDENBERG, K., "On the generalized Langevin equation: Classical and quantum mechanical," *J. Chem. Phys.*, vol. 82, pp. 2708–17, 1985.

[24] DE GENNES, P. G. and PINCUS, P. A., "Pair correlations in a ferromagnetic colloid," *Z. Phys. B.*, vol. 11, no. 3, pp. 189–198, 1970.

[25] DE GRAAF, J., BOON, N., DIJKSTRA, M., and VAN ROIJ, R., "Electrostatic interactions between janus particles," *J. Chem. Phys.*, vol. 137, p. 104910, 2012.

[26] DE MICHELE, C., GABRIELLI, S., TARTAGLIA, P., and SCIORTINO, F., "Dynamics in the presence of attractive patchy interactions," *J. Phys. Chem. B*, vol. 110, no. 15, pp. 8064–8079, 2006.

[27] DE MICHELE, C., TARTAGLIA, P., and SCIORTINO, F., "Slow dynamics in a primitive tetrahedral network model," *J. Chem. Phys.*, vol. 125, p. 204710, 2006.

[28] DEPA, P. and MARANAS, J., "Speed up of dynamic observables in coarse-grained molecular-dynamics simulations of unentangled polymers," *J. Chem. Phys.*, vol. 123, p. 094901, 2005.

[29] DERJAGUIN, B., "On the repulsive forces between charged colloid particles and on the theory of slow coagulation and stability of lyophobe sols," *Trans. Faraday Soc.*, vol. 35, pp. 203–215, 1940.

[30] DHONT, J. K., *An introduction to dynamics of colloids*. Access Online via Elsevier, 1996.

[31] DU, J. and O'REILLY, R. K., "Anisotropic particles with patchy, multicompartment and janus architectures: preparation and application," *Chem. Soc. Rev.*, vol. 40, no. 5, pp. 2402–2416, 2011.

[32] EGGEN, E. and VAN ROIJ, R., "Poisson-boltzmann cell model for heterogeneously charged colloids," *Phys. Rev. E*, vol. 80, no. 4, p. 041402, 2009.

[33] ELIMELECH, M., JIA, X., GREGORY, J., and WILLIAMS, R., *Particle deposition & aggregation: measurement, modelling and simulation*. Butterworth-Heinemann, 1998.

[34] ELLSON, J., GANSNER, E., KOUTSOFIOS, L., NORTH, S. C., and WOODHULL, G., "Graphviz-open source graph drawing tools," in *Graph Drawing*, pp. 483–484, Springer, 2002.

[35] ERDMANN, T., KRÖGER, M., and HESS, S., "Phase behavior and structure of janus fluids," *Phys. Rev. E*, vol. 67, no. 4, p. 041209, 2003.

[36] ERMAK, D., "A computer simulation of charged particles in solution. I. Technique and equilibrium properties," *J. Chem. Phys.*, vol. 62, p. 4189, 1975.

[37] ERRINGTON, J. R., DEBENEDETTI, P. G., and TORQUATO, S., "Quantification of order in the lennard-jones system," *J. Chem. Phys.*, vol. 118, p. 2256, 2003.

[38] EVANS, D. F. and WENNERSTROM, H., *The colloidal domain*. Wiley-VCH, 1994.

[39] EVERAERS, R. and EJTEHADI, M., "Interaction potentials for soft and hard ellipsoids," *Phys. Rev. E*, vol. 67, no. 4, p. 041710, 2003.

[40] FANTONI, R., GIACOMETTI, A., SCIORTINO, F., and PASTORE, G., "Cluster theory of janus particles," *Soft Matter*, vol. 7, no. 6, pp. 2419–2427, 2011.

[41] FOFFI, G., MICHELE, C. D., SCIORTINO, F., and TARTAGLIA, P., "Scaling of dynamics with the range of interaction in short-range attractive colloids," *Phys. Rev. Lett.*, vol. 94, no. 7, p. 078301, 2005.

[42] FRIES, P. H. and PATEY, G. N., "The solution of the hypernetted-chain approximation for fluids of nonspherical particles. a general method with application to dipolar hard spheres," *J. Chem. Phys.*, vol. 82, p. 429, 1985.

[43] FUJIMOTO, K., NAKAHAMA, K., SHIDARA, M., and KAWAGUCHI, H., "Preparation of unsymmetrical microspheres at the interfaces," *Langmuir*, vol. 15, no. 13, pp. 4630–4635, 1999.

[44] GAY, J. and BERNE, B., "Modification of the overlap potential to mimic a linear site–site potential," *J. Chem. Phys.*, vol. 74, p. 3316, 1981.

[45] GIACOMETTI, A., LADO, F., LARGO, J., PASTORE, G., SCIORTINO, F., and OTHERS, "Phase diagram and structural properties of a simple model for one-patch particles," *J. Chem. Phys.*, vol. 131, no. 17, p. 174114, 2009.

[46] GLOTZER, S. C., "Some assembly required," *Science*, vol. 306, no. 5695, p. 419, 2004.

[47] GLOTZER, S. C. and SOLOMON, M. J., "Anisotropy of building blocks and their assembly into complex structures," *Nature Mater.*, vol. 6, no. 8, pp. 557–562, 2007.

[48] GOYAL, A., HALL, C. K., and VELEV, O. D., "Phase diagram for stimulus-responsive materials containing dipolar colloidal particles," *Phys. Rev. E*, vol. 77, no. 3, p. 031401, 2008.

[49] GOYAL, A., HALL, C. K., and VELEV, O. D., "Self-assembly in binary mixtures of dipolar colloids: Molecular dynamics simulations," *J. Chem. Phys.*, vol. 133, p. 064511, 2010.

[50] GRAY, C. G. and GUBBINS, K. E., *Theory of molecular fluids*, vol. 1. Clarendon Press Oxford, 1984.

[51] GRZELCZAK, M., VERMANT, J., FURST, E. M., and LIZ-MARZN, L. M., "Directed self-assembly of nanoparticles," *ACS Nano*, vol. 4, no. 7, pp. 3591–3605, 2010.

[52] HAGY, M. C. and HERNANDEZ, R., "Dynamical simulation of dipolar janus colloids: Equilibrium structure and thermodynamics," *J. Chem. Phys.*, vol. 137, p. 044505, 2012.

[53] HAGY, M. C. and HERNANDEZ, R., "Dynamical simulation of dipolar janus colloids: Dynamical properties," *J. Chem. Phys.*, vol. 138, p. 184903, 2013.

[54] HANSEN, J. P. and MCDONALD, I. R., *Theory of simple liquids*. Academic press, 2006.

[55] HARMANDARIS, V. and KREMER, K., "Predicting polymer dynamics at multiple length and time scales," *Soft Matter*, vol. 5, no. 20, pp. 3920–3926, 2009.

[56] HERNANDEZ, R., "The projection of a mechanical system onto the irreversible generalized Langevin equation (igle)," *J. Chem. Phys.*, vol. 111, pp. 7701–7704, 1999.

[57] HERNANDEZ, R. and SOMER, F. L., "Stochastic dynamics in irreversible nonequilibrium environments. 1. The fluctuation-dissipation relation," *J. Phys. Chem. B*, vol. 103, pp. 1064–1069, 1999.

[58] HERSHKOVITS, E. and HERNANDEZ, R., "Fast numerical integrator for stochastic differential equations with nonstationary multiplicative noise," *J. Phys. Chem. A*, vol. 105, pp. 2687–2693, 2001.

[59] HIMMELHAUS, M. and TAKEI, H., "Cap-shaped gold nanoparticles for an optical biosensor," *Sens. Actuators, B*, vol. 63, no. 1-2, pp. 24–30, 2000.

[60] HO, C., KELLER, A., ODELL, J., and OTTEWILL, R., "Preparation of monodisperse ellipsoidal polystyrene particles," *Colloid Polym. Sci.*, vol. 271, no. 5, pp. 469–479, 1993.

[61] HONG, L., JIANG, S., and GRANICK, S., "Simple method to produce janus colloidal particles in large quantity," *Langmuir*, vol. 22, no. 23, pp. 9495–9499, 2006.

[62] HONG, L., CACCIUTO, A., LUIJTEN, E., and GRANICK, S., "Clusters of charged janus spheres," *Nano Lett.*, vol. 6, no. 11, pp. 2510–2514, 2006.

[63] HONG, L., CACCIUTO, A., LUIJTEN, E., and GRANICK, S., "Clusters of amphiphilic colloidal spheres," *Langmuir*, vol. 24, no. 3, pp. 621–625, 2008.

[64] HOOGERBRUGGE, P. and KOELMAN, J., "Simulating microscopic hydrodynamic phenomena with dissipative particle dynamics," *Europhys. Lett.*, vol. 19, no. 3, p. 155, 1992.

[65] IZVEKOV, S. and VOTH, G. A., "Modeling real dynamics in the coarse-grained representation of condensed phase systems," *J. Chem. Phys.*, vol. 125, p. 151101, 2006.

[66] JACKSON, A. M., MYERSON, J. W., and STELLACCI, F., "Spontaneous assembly of subnanometre-ordered domains in the ligand shell of monolayer-protected nanoparticles," *Nature Mater.*, vol. 3, no. 5, pp. 330–336, 2004.

[67] JANG, S. G., AUDUS, D. J., KLINGER, D., KROGSTAD, D. V., KIM, B. J., CAMERON, A., KIM, S.-W., DELANEY, K. T., HUR, S.-M., KILLOPS, K. L., and OTHERS, "Striped, ellipsoidal particles by controlled assembly of diblock copolymers," *J. Am. Chem. Soc.*, 2013.

[68] JEON, S.-J., YI, G.-R., and YANG, S.-M., "Cooperative assembly of block copolymers with deformable interfaces: toward nanostructured particles," *Adv. Mater.*, vol. 20, no. 21, pp. 4103–4108, 2008.

[69] JIANG, S., CHEN, Q., TRIPATHY, M., LUIJTEN, E., SCHWEIZER, K. S., and GRANICK, S., "Janus particle synthesis and assembly," *Adv. Mater.*, vol. 22, no. 10, pp. 1060–1071, 2010.

[70] JIANG, S., SCHULTZ, M. J., CHEN, Q., MOORE, J. S., and GRANICK, S., "Solvent-free synthesis of janus colloidal particles," *Langmuir*, vol. 24, no. 18, pp. 10073–10077, 2008.

[71] KERN, N. and FRENKEL, D., "Fluid–fluid coexistence in colloidal systems with short-ranged strongly directional attraction," *J. Chem. Phys.*, vol. 118, p. 9882, 2003.

[72] KOSTANSEK, E. C., "The role of hydrophobicity in latex stability," *Trends Polym. Sci.*, vol. 4, no. 11, pp. 383–387, 1996.

[73] KRAMERS, H. A., "Brownian motion in a field of force and the diffusional model of chemical reactions," *Physica (Utrecht)*, vol. 7, pp. 284–304, 1940.

[74] LATTUADA, M. and HATTON, T. A., "Synthesis, properties and applications of janus nanoparticles," *Nano Today*, vol. 6, no. 3, pp. 286–308, 2011.

[75] LEVESQUE, D. and VERLET, L., "Computer" experiments" on classical fluids. iii. time-dependent self-correlation functions," *Phys. Rev. A*, vol. 2, no. 6, p. 2514, 1970.

[76] LIN, C.-C., LIAO, C.-W., CHAO, Y.-C., and KUO, C., "Fabrication and characterization of asymmetric janus and ternary particles," *ACS Appl. Mater.*, vol. 2, no. 11, pp. 3185–3191, 2010.

[77] LINDENBERG, K. and SESHADRI, V., "Dissipative contributions of internal multiplicative noise," *Physica A*, vol. 109A, pp. 483–499, 1981.

[78] LINDENBERG, K., SHULER, K. E., SESHADRI, V., and WEST, B. J., "Langevin equations with multiplicative noise: Theory and applications to physical processes," in *Probabilistic Analysis and Related Topics* (BHARUCHA-REID, A. T., ed.), vol. 3, pp. 81–125, San Diego: Academic Press, 1983.

[79] LIU, Y., LI, W., PEREZ, T., GUNTON, J. D., and BRETT, G., "Self assembly of janus ellipsoids," *Langmuir*, vol. 28, no. 1, pp. 3–9, 2011.

[80] LYUBARTSEV, A., KARTTUNEN, M., VATTULAINEN, I., and LAAKSONEN, A., "On coarse-graining by the inverse monte carlo method: Dissipative particle dynamics simulations made to a precise tool in soft matter modeling," *Soft Matter*, vol. 1, no. 1, pp. 121–137, 2002.

[81] MARRINK, S. J., RISSELADA, H. J., YEFIMOV, S., TIELEMAN, D. P., and DE VRIES, A. H., "The martini force field: coarse grained model for biomolecular simulations," *J. Phys. Chem. B*, vol. 111, no. 27, pp. 7812–7824, 2007.

[82] MCCONNELL, M. D., KRAEUTLER, M. J., YANG, S., and COMPOSTO, R. J., "Patchy and multiregion janus particles with tunable optical properties," *Nano Lett.*, vol. 10, no. 2, pp. 603–609, 2010.

[83] MILLER, M. A., BLAAK, R., LUMB, C. N., and HANSEN, J. P., "Dynamical arrest in low density dipolar colloidal gels," *J. Chem. Phys.*, vol. 130, p. 114507, 2009.

[84] MOGHANI, M. M. and KHOMAMI, B., "Self-assembly of spherical janus particles in electrolytes," *Soft Matter*, 2013.

[85] MOLINERO, V. and MOORE, E. B., "Water modeled as an intermediate element between carbon and silicon," *J. Phys. Chem. B*, vol. 113, no. 13, pp. 4008–4016, 2009.

[86] MORI, H., "Transport, collective motion, and Brownian motion," *Prog. Theor. Phys.*, vol. 33, pp. 423–455, 1965.

[87] MUKHERJEE, S., "Sol-gel processes in glass science and technology," *J. Non-Cry. Solids*, vol. 42, no. 1, pp. 477–488, 1980.

[88] MÜLLER-PLATHE, F., "Coarse-graining in polymer simulation: From the atomistic to the mesoscopic scale and back," *ChemPhysChem*, vol. 3, no. 9, pp. 754–769, 2002.

[89] NIE, Z., LI, W., SEO, M., XU, S., and KUMACHEVA, E., "Janus and ternary particles generated by microfluidic synthesis: design, synthesis, and self-assembly," *J. Am. Chem. Soc.*, vol. 128, no. 29, pp. 9408–9412, 2006.

[90] NUR, H., IKEDA, S., and OHTANI, B., "Phase-boundary catalysis: a new approach in alkene epoxidation with hydrogen peroxide by zeolite loaded with alkylsilane-covered titanium oxide," *Chem. Comm.*, vol. 19, no. 22, pp. 2235–2236, 2000.

[91] OCAÑA, M., MORALES, M. P., and SERNA, C. J., "The growth mechanism of α-fe2o3 ellipsoidal particles in solution," *J. Colloid Interface Sci.*, vol. 171, no. 1, pp. 85–91, 1995.

[92] OVERBEEK, J. T. G., "Recent developments in the understanding of colloid stability," *J. Colloid Interface Sci.*, vol. 58, no. 2, pp. 408–422, 1977.

[93] PADDING, J. T. and BRIELS, W. J., "Time and length scales of polymer melts studied by coarse-grained molecular dynamics simulations," *J. Chem. Phys.*, vol. 117, p. 925, 2002.

[94] PARK, B. J. and LEE, D., "Equilibrium orientation of nonspherical janus particles at fluid–fluid interfaces," *ACS Nano*, vol. 6, no. 1, pp. 782–790, 2011.

[95] PASHLEY, R. and KARAMAN, M., *Applied colloid and surface chemistry*. Wiley, 2005.

[96] PATEY, G. N. and VALLEAU, J. P., "Dipolar hard spheres: A monte carlo study," *J. Chem. Phys.*, vol. 61, p. 534, 1974.

[97] PAWAR, A. B. and KRETZSCHMAR, I., "Fabrication, assembly, and application of patchy particles," *Macromol. Rapid Commun.*, vol. 31, no. 2, pp. 150–168, 2010.

[98] PERRO, A., RECULUSA, S., RAVAINE, S., BOURGEAT-LAMI, E., and DUGUET, E., "Design and synthesis of janus micro-and nanoparticles," *J. Mater. Chem.*, vol. 15, no. 35-36, pp. 3745–3760, 2005.

[99] PHAM, K., PUERTAS, A., BERGENHOLTZ, J., EGELHAAF, S., MOUSSAID, A., PUSEY, P., SCHOFIELD, A., CATES, M., FUCHS, M., and POON, W., "Multiple glassy states in a simple model system," *Science*, vol. 296, no. 5565, p. 104, 2002.

[100] PLIMPTON, S., "Fast parallel algorithms for short-range molecular dynamics," *J. Comput. Phys.*, vol. 117, no. 1, pp. 1–19, 1995.

[101] POTANIN, A. A., "On the computer simulation of the deformation and breakup of colloidal aggregates in shear flow," *J. Colloid Interface Sci.*, vol. 157, no. 2, pp. 399–410, 1993.

[102] PUERTAS, A. M., FUCHS, M., and CATES, M. E., "Aging in attraction-driven colloidal glasses," *Phys. Rev. E*, vol. 75, no. 3, p. 031401, 2007.

[103] ROSENTHAL, G., GUBBINS, K. E., and KLAPP, S. H. L., "Self-assembly of model amphiphilic janus particles," *J. Chem. Phys.*, vol. 136, no. 17, p. 174901, 2012.

[104] RUDHARDT, D., BECHINGER, C., and LEIDERER, P., "Direct measurement of depletion potentials in mixtures of colloids and nonionic polymers," *Phys. Rev. Lett.*, vol. 81, no. 6, pp. 1330–1333, 1998.

[105] RUEB, C. and ZUKOSKI, C., "Viscoelastic properties of colloidal gels," *J. Rheol.*, vol. 41, p. 197, 1997.

[106] SANTOS, P., CAMPANELLA, O., and CARIGNANO, M., "Brownian dynamics study of gel-forming colloidal particles," *J. Phys. Chem. B*, vol. 114, no. 41, pp. 13052–13058, 2010.

[107] SCHMIDLE, H., HALL, C. K., VELEV, O. D., and KLAPP, S. H., "Phase diagram of two-dimensional systems of dipole-like colloids," *Soft Matter*, vol. 8, no. 5, pp. 1521–1531, 2012.

[108] SCHNEIDER, T. and STOLL, E., "Molecular-dynamics study of a three-dimensional one-component model for distortive phase transitions," *Phys. Rev. B*, vol. 17, no. 3, p. 1302, 1978.

[109] SCIORTINO, F., GIACOMETTI, A., and PASTORE, G., "Phase diagram of janus particles," *Phys. Rev. Lett.*, vol. 103, no. 23, p. 237801, 2009.

[110] SCIORTINO, F., GIACOMETTI, A., and PASTORE, G., "A numerical study of one-patch colloidal particles: from square-well to janus," *Phys. Chem. Chem. Phys.*, vol. 12, no. 38, pp. 11869–11877, 2010.

[111] SEEBERGH, J. E. and BERG, J. C., "Depletion flocculation of aqueous, electrosterically-stabilized latex dispersions," *Langmuir*, vol. 10, no. 2, pp. 454–463, 1994.

[112] SEGRE, P., MEEKER, S., PUSEY, P., and POON, W., "Viscosity and structural relaxation in suspensions of hard-sphere colloids," *Phys. Rev. Lett.*, vol. 75, no. 5, p. 958, 1995.

[113] SHAH, A. A., SCHULTZ, B., KOHLSTEDT, K. L., GLOTZER, S. C., and SOLOMON, M. J., "Synthesis, assembly, and image analysis of spheroidal patchy particles," *Langmuir*, vol. 29, no. 15, pp. 4688–4696, 2013.

[114] SHARMA, A. and WALZ, J. Y., "Direct measurement of the depletion interaction in a charged colloidal dispersion," *J. Chem. Soc., Faraday Trans.*, vol. 92, no. 24, pp. 4997–5004, 1996.

[115] SHIH, W.-H., SHIH, W. Y., KIM, S.-I., LIU, J., and AKSAY, I. A., "Scaling behavior of the elastic properties of colloidal gels," *Phys. Rev. A*, vol. 42, no. 8, p. 4772, 1990.

[116] SHIRTS, M. R., BAIR, E., HOOKER, G., and PANDE, V. S., "Equilibrium free energies from nonequilibrium measurements using maximum-likelihood methods," *Phys. Rev. Lett.*, vol. 91, no. 14, p. 140601, 2003.

[117] SMIT, B., WILLIAMS, C., HENDRIKS, E., and DE LEEUW, S., "Vapour-liquid equilibria for stockmayer fluids," *Mol. Phys.*, vol. 68, no. 3, pp. 765–769, 1989.

[118] SOMER, F. L. and HERNANDEZ, R., "Stochastic dynamics in irreversible nonequilibrium environments. 3. Temperature-ramped chemical kinetics," *J. Phys. Chem. A*, vol. 103, pp. 11004–11010, 1999.

[119] SOMOZA, A. M., CHACÓN, E., MEDEROS, L., and TARAZONA, P., "A model for membranes, vesicles and micelles in amphiphilic systems," *J. Phys.: Condens. Matter*, vol. 138, p. 5753, 1995.

[120] STELL, G., "Sticky spheres and related systems," *Journal of statistical physics*, vol. 63, no. 5-6, pp. 1203–1221, 1991.

[121] SUZUKI, D., TSUJI, S., and KAWAGUCHI, H., "Janus microgels prepared by surfactant-free pickering emulsion-based modification and their self-assembly," *J. Am. Chem. Soc.*, vol. 129, no. 26, pp. 8088–8089, 2007.

[122] TAKAHARA, Y. K., IKEDA, S., ISHINO, S., TACHI, K., IKEUE, K., SAKATA, T., HASEGAWA, T., MORI, H., MATSUMURA, M., and OHTANI, B., "Asymmetrically modified silica particles: a simple particulate surfactant for stabilization of oil droplets in water," *J. Am. Chem. Soc.*, vol. 127, no. 17, pp. 6271–6275, 2005.

[123] TAKEI, H. and SHIMIZU, N., "Gradient sensitive microscopic probes prepared by gold evaporation and chemisorption on latex spheres," *Langmuir*, vol. 13, no. 7, pp. 1865–1868, 1997.

[124] TUCKER, A. K. and HERNANDEZ, R., "Observation of a trapping transition in the diffusion of a thick needle through fixed point scatterers," *J. Phys. Chem. B*, vol. 114, pp. 9628–9634, 2010.

[125] TUCKER, A. K. and HERNANDEZ, R., "Absence of enhanced diffusion in the dynamics of a thick needle through three-dimensional fixed point scatterers," *J. Phys. Chem. B*, vol. 115, pp. 4412–4418, 2011.

[126] TUCKER, A. K. and HERNANDEZ, R., "Diffusion of a spherical probe through static nematogens: Effect of increasing geometric anisotropy and long-range structure," *J. Phys. Chem. B*, vol. 116, pp. 1328–1334, 2012.

[127] VERLET, L., "Computer" experiments" on classical fluids. i. thermodynamical properties of lennard-jones molecules," *Phys. Rev.*, vol. 159, no. 1, p. 98, 1967.

[128] VERLET, L., "Computer" experiments" on classical fluids. ii. equilibrium correlation functions," *Phys. Rev.*, vol. 165, no. 1, p. 201, 1968.

[129] VERWEY, E. J. W. and OVERBEEK, J. T. G., *Theory of the stability of lyophobic colloids*. Courier Dover Publications, 1999.

[130] VOGT, M. and HERNANDEZ, R., "An idealized model for nonequilibrium dynamics in molecular systems," *J. Chem. Phys.*, vol. 123, p. 144109, 2005.

[131] WALTHER, A. and MÜLLER, A. H., "Janus particles," *Soft Matter*, vol. 4, no. 4, pp. 663–668, 2008.

[132] WEEKS, J. D., CHANDLER, D., and ANDERSEN, H. C., "Role of repulsive forces in determining the equilibrium structure of simple liquids," *J. Chem. Phys.*, vol. 54, no. 12, p. 5237, 1971.

[133] WEIS, J. J. and LEVESQUE, D., "Chain formation in low density dipolar hard spheres: A monte carlo study," *Phys. Rev. Lett.*, vol. 71, no. 17, pp. 2729–2732, 1993.

[134] WERTHEIM, M. S., "Exact solution of the mean spherical model for fluids of hard spheres with permanent electric dipole moments," *J. Chem. Phys.*, vol. 55, p. 4291, 1971.

[135] YAKE, A. M., SNYDER, C. E., and VELEGOL, D., "Site-specific functionalization on individual colloids: Size control, stability, and multilayers," *Langmuir*, vol. 23, no. 17, pp. 9069–9075, 2007.

[136] ZELINSKI, B. and UHLMANN, D., "Gel technology in ceramics," *J. of Phys. and Chem. of Solids*, vol. 45, no. 10, pp. 1069–1090, 1984.

[137] ZHANG, L. and ZHU, Y., "Directed assembly of janus particles under high frequency ac-electric fields: Effects of medium conductivity and colloidal surface chemistry," *Langmuir*, vol. 28, no. 37, pp. 13201–13207, 2012.

[138] ZHANG, Z. and GLOTZER, S. C., "Self-assembly of patchy particles," *Nano Lett.*, vol. 4, no. 8, pp. 1407–1413, 2004.

[139] ZWANZIG, R., "Ensemble method in the theory of irreversibility," *J. Chem. Phys.*, vol. 33, pp. 1338–1341, 1960.

[140] ZWANZIG, R., *Nonequilibrium statistical mechanics*. London: Oxford University Press, 2001.